Title
Electrostatic Turbulence and Transport in the Field-Reversed Configuration

Author
Lau, Calvin

Publication Date
2017

UNIVERSITY OF CALIFORNIA,
IRVINE

Electrostatic Turbulence and Transport in the Field-Reversed Configuration

DISSERTATION

submitted in partial satisfaction of the requirements
for the degree of

DOCTOR OF PHILOSOPHY

in Physics

by

Calvin K Lau

Dissertation Committee:
Professor Zhihong Lin, Chair
Professor Toshiki Tajima
Professor William W. Heidbrink

2018

DEDICATION

To my unconditionally loving parents;
my brother who I've always looked up to;
and the love of my life and pillar of support, Cyan Lokelani Kiyoko Curtis.

TABLE OF CONTENTS

LIST OF FIGURES

Page

LIST OF TABLES

ACKNOWLEDGMENTS

I would like to thank a lot of people. For me to get to this point of my life requires the help of many, many individuals. I do not want to leave out a single person I can think of, but if I do, it is because of rules, regulations, and my poor biologically limited brain. I'll start with the grants and funding to get it out of the way.

This work was carried out at University of California, Irvine with the support of the Norman Rostoker Fellowship and Tri Alpha Energy subcontract (Grant No. TAE- 200441). Simulations used the resources of DOE Office of Science User Facilities: Oak Ridge Leadership Computing Facility at Oak Ridge National Laboratory (DOE Contract No. DE-AC05-00OR22725) and National Energy Research Scientific Computing Center (DOE Contract No. DE-AC02-05CH11231). Thank you to L. Schmitz, S. Dettrick, M. Binderbauer, and the TAE team at Tri Alpha Energy, Inc., for equilibrium data, experimental comparisons, and ongoing insights and collaboration.

I need to thank my advisor, Prof. Z. Lin, and my unofficial mentor, Prof. T. Tajima. Without their expertise and guidance during this time, I would still be drowning in my own incompetence. In addition, I need to thank Profs. Heidbrink, McWilliams, Dollar, and Chen whose various areas of expertise keep me striving to learn.

Next, I need to thank four specific teachers from my grade school years whose interactions with me were essential to the current path I walk: Mrs. A. Stuart, my 4th grade teacher who mentioned nuclear fusion. I didnt know what these meant in 4th grade, but my brain dutifully stored the phrase in memory, leading me to plasma physics; Mr. J. Risk, the coach of the MathCounts team (which I unwillingly joined because my mom voluntold me to join). I didn't like math as a kid because classes moved too slow for me to be interested but Mr. Risk's enthusiasm infected me, leading me to like maths, to question the validity of ideas of terrible teachers, and to trust my own mathematical instinct; Mr. B. Cooley, my first physics teacher. I only joined his class because I saw physics as great cruising class, but Mr. Cooleys enthusiasm for physics infected me. Before his class, I had wanted to be a history major, eventually becoming a journalist to support my real love of writing fiction novels. Then this guy came crashing in and destroyed that dream by injecting physics into my life; Mr. Bruce Cohen, my calculus teacher. He taught the fundamentals so well that I was able to coast in the first (and second) year of undergrad. I never had that moment of whoa, college is harder than high school because he was such a great teacher that I never felt a moment of being unprepared. Plus, he was hilarious, like most math and physics people are. Actually, I also have a lot of appreciation for many of my teachers and want to thank: Mrs. Sher, Mrs. Jobin, Mr. Richards, Mr. Talsky, Mrs. Turner, Mrs. Takemoto, Mrs. Chin, Mrs. Lubenow, and Mr. Schwarz.

Education does not come just from teachers. My peers have also been very essential to my current path.

First, I need to thank T. Barrella, whose brilliance and dedication made me realize that I needed to work much harder to catch up and become his peer again. Luckily, hes in particle physics so theres no direct competition for those of you who already want to hire him instead.

Thank you to the graduate students whose coattails I rode on until I could run myself and who suffered my non-stop bursts of random noises: Z. Wang, P. Jiang, O. Luk, J. Bao, Y. Liu, D. Fulton, J. McClenaghan, L. Stagner, C. Pitcher, Y. Hwang, S. Taimourzadeh, D. Farinella, S. Nicks, S. Hakimi, T. Nguyen. They are more than just lab-mates and mentors; they are my friends, and they made this lab group more than just a lab group for me. In addition, D. Fulton, J. Bao, and I. Holod are especially important because without their help, the numerical capabilities for FRC physics would probably not be ready.

Life is not just about education, teachers, seniors, colleagues. There is also life outside of the university and work.

Thank you to W. Do, whose easy (to me, not to him, oops) physics homework prompted me to take physics as cruising class in high school and is pretty much the reason I ended up in physics. Also, to my friends outside of physics, W. Chau, J. Hiura, L. Shum, K. McEvoy, V. Chu, K. Chu, C. Liu, H. Ajel, T. Mar, N. Romig, S. Bairamian, B. Pourhamzeh, D. Giberti, K. Truong, J. Cheung.

Finally, I must thank people in my family.

I first must thank my late grandparents who watched over me as a kid. I miss them very much, and I can only hope they would have been proud of my work.

Thank you to my best friend, Nuri Chang, who I have known since the second grade and is essentially my brother. He is brilliant, lucid, and able to separate the different regions of his life apart. I always seek his views because he doesn't shy from tough questions. He is always willing to help me with issues, and I am always willing to help him with his issues.

Thank you to my older brother, Wilson. I have always wanted to be as good as my brother or better in everything that we do. Whenever I seem friendly or charming, I am simply channeling and imitating my brothers natural personality. I thank him for putting up with me as a kid, but also for many things he did and does for me, despite the little jerkwad I was.

Thank you to my parents whose greatest gift to me is freedom. Many Asian immigrant parents have specific routes and paths for their kids to go through. Doctor. Lawyer. Engineer. Businessman (what does that even mean?!). My parents realized that I dont like to be told what to do early on. They never pushed me in one direction, never tried to make me into something specific. They just tried to give me whatever resources I might need (like pushing me to join MathCounts, to read books, etc.). When I told them I wanted to be a physicist, they were supportive and they trusted me to be able to do it, despite having no idea what a physicist does, because they believed in me. I thank my parents for the freedom and the support they have given me and still give me.

And finally, thank you to my best friend and the woman I want to spend my life with, Cyan Lokelani Kiyoko Curtis, who I have known since middle school wherein a teacher (mistakenly) punished me by placing me next to her (because I had to ask someone next to me to tell me what was on the board as I was near-sighted without glasses). Needless to say, his punishment was ruined because Cyan is one of the best people I have met in my life. She is always supportive and encouraging, despite my self-questioning. She supported me through some of the worst times of my life, attending to my rants and complaints. She supported me as I went through some of the best times of my life, listening to my endless speeches about myself and my minor successes. I try my best to be as good a friend to her as she is to me because she is not only my best friend, but also someone whose work and life make me proud to even be associated with her. We've been in the same city and we've been separated by an ocean and a time-zone difference; it doesn't matter because I know I will always be able to depend on her for strength and I will always be ready for her to do the same.

CURRICULUM VITAE

Calvin K Lau

EDUCATION

Doctor of Philosophy in Physics **2018**
University of California, Irvine *Irvine, California*

Master of Science in Physics **2015**
University of California, Irvine *Irvine, California*

Bachelor of Science in Physics **2012**
University of California, Los Angeles *Los Angeles, California*

RESEARCH EXPERIENCE

Graduate Research Assistant *with Dr. Zhihong Lin* **2012–2017**
University of California, Irvine *Irvine, California*

Undergraduate Research Assistant *with Dr. Hong Wen Jiang* **2010–2012**
University of California, Los Angeles *Los Angeles, California*

Undergraduate Research Assistant *with Dr. Troy Carter* **2009–2010**
University of California, Los Angeles *Los Angeles, California*

TEACHING EXPERIENCE

Teaching Assistant **2012–2014, 2016**
University of California, Irvine *Irvine, California*

Graduate Student Mentor **2015–2016**
University of California, Irvine *Irvine, California*

PEER-REVIEWED PUBLICATIONS

Ponderomotive Acceleration by Relativistic Waves — Feb 2015

C.K. Lau, P.C. Yeh, O. Luk, J. McClenaghan, T. Ebisuzaki, and T. Tajima.

Phys. Rev. Spec. Topics: Accel. and Beams 18, 024401 (2015)

Gyrokinetic Particle Simulation of a Field Reversed Configuration — Jan 2016

D.P. Fulton, **C.K. Lau**, L. Schmitz, I. Holod, Z. Lin, T. Tajima, M.W. Binderbauer, and the TAE team.

Phys. Plasma 23, 012509 (2016)

Gyrokinetic Simulation of Driftwave Instability in Field Reversed Configuration — May 2016

D.P. Fulton, **C.K. Lau**, I. Holod, Z. Lin, and S. Dettrick.

Phys. Plasma 23, 056111 (2016)

High Energy Photon Emission From Wakefields — July 2016

D.M. Farinella, **C.K. Lau**, X.M. Zhang, J.K. Koga, S. Taimourzadeh, Y. Hwang, K. Abazajian, N. Canac, T. Ebisuzaki, P. Taborek, and T. Tajima.

Phys. Plasma 23, 073107 (2016)

Suppressed Ion-scale Turbulence in a Hot High- Plasma — Dec 2016

L. Schmitz, D. P. Fulton, E. Ruskov, **C. Lau**, B. H. Deng, T. Tajima, M. W. Binderbauer, I. Holod, Z. Lin, H. Gota, M. Tuszewski, S. A. Dettrick, and L. C. Steinhauer.

Nat. Comm. 7, 13860 (2016)

Drift-wave Stability in the Field-reversed Configuration — Aug 2017

C. K. Lau, D. P. Fulton, I. Holod, Z. Lin, M. Binderbauer, T. Tajima, and L. Schmitz.

Phys. Plasma 24, 082512 (2017)

MANUSCRIPTS IN PREPARATION

Electrostatic Turbulence in the Field-Reversed Configuration — 2017

C.K. Lau, D.P. Fulton, I. Holod, Z. Lin, M. Binderbauer, T. Tajima, and L. Schmitz

A New Code (ANC): global, cross-separatrix turbulent transport — 2017

D.P. Fulton, **C.K. Lau**, J. Bao, I. Holod, Z. Lin, T. Tajima

Wakefield Simulation of Solid State Plasma **2017**

S. Hakimi, T. Nguyen, D. Farinella, **C.K. Lau**, H. Wang, P. Taborek, F. Dollar, and T. Tajima

submitted

TALKS

Electrostatic Turbulence in the Field-Reversed Configuration **Aug 2017**

C.K. Lau, D. Fulton, J. Bao, Z. Lin, T. Tajima, L. Schmitz.

Science Panel Meeting 2017 at Tri Alpha Energy, Foothill Ranch, California

Linear and Non-linear Electrostatic Turbulence **May 2017**

C.K. Lau, D. Fulton, J. Bao, Z. Lin, T. Tajima, L. Schmitz.

FRC Transport Workshop 2017 at Tri Alpha Energy, Foothill Ranch, California

Electrostatic Driftwaves in the Field-Reversed Configuration: destabilized in the scrape-off layer, robustly stabilized in the core **Aug 2016**

C.K. Lau, D. Fulton, J. Bao, I. Holod, Z. Lin, M. Binderbauer, T. Tajima, L. Schmitz.

US-Japan Workshop on Compact Tori 2016 at Irvine, California

Field-Reversed Configuration: understanding turbulence in an unconventional approach to fusion energy **Apr 2016**

C.K. Lau, D. Fulton, I. Holod, Z. Lin, M. Binderbauer, T. Tajima, L. Schmitz.

Associated Graduate Student (AGS) Symposium 2016 at Irvine, California

CONFERENCES

Cross-separatrix Coupling in Nonlinear Global Electrostatic Turbulent Transport in C-2U **Oct 2017**

C.K. Lau, D. Fulton, J. Bao, Z. Lin, D. Fulton, M. Binderbauer, T. Tajima, and L. Schmitz.

Poster presented at APS Division of Plasma Physics 2017 at Milwaukee, Wisconsin

Parallel Transport with Sheath and Collisional Effects in Global Electrostatic Turbulent Transport in FRCs

J. Bao, **C.K. Lau**, A. Kuley, Z. Lin, D. Fulton, and T. Tajima.

Poster presented at APS Division of Plasma Physics 2017 at Milwaukee, Wisconsin

Fully-kinetic Ion Simulation of Global Electrostatic Turbulent Transport in C-2U

D. Fulton, **C.K. Lau**, J. Bao, Z. Lin, and T. Tajima

Poster presented at APS Division of Plasma Physics 2017 at Milwaukee, Wisconsin

Whole Device Modeling of Compact Tori: Stability and Transport Modeling of C-2W

S. Dettrick, D. Fulton, **C.K. Lau**, Z. Lin, F. Ceccherini, L. Galeotti, S. Gupta, M. Onofri, and T. Tajima.

Poster presented at APS Division of Plasma Physics 2017 at Milwaukee, Wisconsin

Separatrix $E \times B$ Shear Flows and Turbulence Propagation in the C-2U FRC; Reflectometry Upgrades for C-2W

L. Schmitz, D. Fulton, **C.K. Lau**, I. Holod, Z. Lin, B. Deng, H. Gota, T. Tajima, and M. Binderbauer.

Poster presented at APS Division of Plasma Physics 2017 at Milwaukee, Wisconsin

Wakefield simulation of solid state plasma

S. Hakimi, T. Nguyen, D. Farinella, **C.K. Lau**, H. Wang, P. Taborek, and T. Tajima.

Poster presented at APS Division of Plasma Physics 2017 at Milwaukee, Wisconsin

---

Development of a First-Principles Simulation Model of Turbulent Transport in Compact Tori — May 2017

D. Fulton, **C.K. Lau**, J. Bao, A. Kuley, Z. Lin, T. Tajima, and the GTC and TAE Teams.

Poster presented at Sherwood Fusion Theory Conference 2017 at Annapolis, Maryland

---

Global simulation of field-reversed configuration using fully kinetic ion and drift kinetic electron — Oct 2016

C.K. Lau, D. Fulton, A. Kuley, J. Bao, Z. Lin, M. Binderbauer, T. Tajima, L. Schmitz.

Poster presented at APS Division of Plasma Physics 2016 at San Jose, California

Absence of Ion-scale Core Turbulence and Transport Barrier Formation with Passive/active Divertor Biasing in the C-2/C-2U Field Reversed Configuration

M. Tuszewski, D. Fulton, **C.K. Lau**, I. Holod, Z. Lin, B.H. Deng, H. Gota, T. Tajima, M. Binderbauer, L. Schmitz.

Poster presented at APS Division of Plasma Physics 2016 at San Jose, California

Simulation of drift wave instability in field-reversed configurations using global magnetic geometry

D. P. Fulton, **C.K. Lau**, Z. Lin, T. Tajima, I. Holod.

Poster presented at APS Division of Plasma Physics 2016 at San Jose, California

Global particle in cell simulation of radio frequency waves in tokamak

A. Kuley, Z. Lin, J. Bao, **C.K. Lau**, G.Y. Sun.

Poster presented at APS Division of Plasma Physics 2016 at San Jose, California

---

Electrostatic Drift-wave Instability in the Field Reversed Configurations **Apr 2016**

C.K. Lau, D.Fulton, I.Holod, Z.Lin, S.Dettrick, T.Tajima, L.Schmitz.

Poster presented at Sherwood Fusion Theory Conference 2016 at Madison, Wisconsin

---

Electrostatic Drift-Wave Instability in Field-Reversed Configuration **Nov 2015**

C. Lau, D. Fulton, I. Holod, Z. Lin, M. Binderbauer, T. Tajima, L. Schmitz.

Poster presented at APS Division of Plasma Physics 2015 at Savannah, Georgia

Suppressed Ion-scale Turbulence and Critical Density Gradient in the C-2 Field Reversed Configuration

L. Schmitz, D. Fulton, **C. Lau**, I. Holod, Z. Lin, E. Ruskov, B. Deng, H. Gota, T. Tajima, M. Binderbauer, D. Gupta, J. Douglass.

Poster presented at APS Division of Plasma Physics 2015 at Savannah, Georgia

High Energy Photon Emission from Wakefields and its Signatures in Astrophysical Blazars

D. Farinella, X. Zhang, **C. Lau**, S. Taimourzadeh, Y. Hwang, J. Koga, T. Ebisuzaki, T. Tajima.

Poster presented at APS Division of Plasma Physics 2015 at Savannah, Georgia

---

Suppressed Ion-scale Turbulence and Critical Density Gradient in the C-2 Field Reversed Configuration **Aug 2015**

L. Schmitz, **C. Lau**, D. Fulton, I. Holod, Z. Lin, E. Ruskov, B. Deng, H. Gota, T. Tajima, M. Binderbauer, D. Gupta, J. Douglass, and the Tri Alpha Energy team.

Talk presented by L. Schmitz at Norman Rostoker Symposium August 2015 at Irvine, California

---

Turbulence Physics Update (C-2): Recent Experimental and Simulation Results **Mar 2015**

L. Schmitz, **C. Lau**, D. Fulton, I. Holod, Z. Lin, T. Tajima, M. Binderbauer, H. Gota, B. Deng, D. Gupta, D. Osin, and the Tri Alpha Energy team.

Talk presented by L. Schmitz at Science Panel Meeting March 2015 Tri Alpha Energy, Inc, California

Electrostatic Driftwave Instabilities in Field Reversed Configurations

C. K. Lau, D.Fulton, I.Holod, Z.Lin, S.Dettrick, T.Tajima, L.Schmitz.

Poster presented at Sherwood Fusion Theory Conference 2015 at New York City, New York

---

Ponderomotive Acceleration by Relativistic Waves **Oct 2014**
C.K. Lau, P.C. Yeh, O. Luk, J. McClenaghan, T. Ebisuzaki, T. Tajima.

Poster presented at APS Division of Plasma Physics 2014 at New Orleans, Louisiana

Kinetic Particle Simulation of Turbulence in an FRC Geometry
D. Fulton, **C.K. Lau**, I. Holod, Z. Lin, S. Dettrick, M. Binderbauer, T. Tajima.

Poster presented at APS Division of Plasma Physics 2014 at New Orleans, Louisiana

SOFTWARE

Gyrokinetic Toroidal Code (GTC) `https://bitbucket.org/uciplasmatheory/gtc/`
Fortran particle-in-cell code developed with UCI theory group for turbulence and transport studies in magnetized plasmas.

A New Code (ANC) `https://bitbucket.org/danfulton/anc/`
Fortran particle-in-cell code developed with D. Fulton for turbulence and transport studies in global field-reversed configuration geometry.

A Remapping Code (ARC) `https://bitbucket.org/danfulton/anc/`
Fortran code developed to re-map kinetic information from particle-in-cell codes to phasespace distribution function.

ABSTRACT OF THE DISSERTATION

Electrostatic Turbulence and Transport in the Field-Reversed Configuration

By

Calvin K Lau

Doctor of Philosophy in Physics

University of California, Irvine, 2018

Professor Zhihong Lin, Chair

Recent drastic improvement of plasma stability and confinement in the high performance C-2 advanced beam-driven field-reversed configuration (FRC) experiment at Tri Alpha Energy, Inc. (TAE) has led to consistently reproducible stable plasmas suitable for transport study. To understand and support the ongoing efforts towards an FRC-based reactor, the sources of the fluctuations and the mechanisms of the transport must first be identified such that a suitable transport scaling may be found and applied toward predicting confinement performance in larger, hotter, and denser FRC plasmas.

In the first half of this thesis, a mature, well-benchmarked turbulence simulation code, the Gyrokinetic Toroidal Code (GTC), has been extended and applied to a system with experimentally realistic C-2 parameters. Using GTC, local electrostatic drift-wave stabilities in the core and scrape-off layer (SOL) regions of C-2 have been characterized and compared to experimental findings. The drift-wave is found to be stable in the core. On the other hand, in the SOL, a class of ion-to-electron scale instabilities is observed. These simulation results are consistent with density fluctuation measurements in C-2.

Since experimental measurements show that fluctuations exist in the core, the discovery of the robust stability of the core suggests that the fluctuations may originate from the SOL. In the second half of this thesis, a new turbulence simulation code, A New Code (ANC), has been developed to study nonlocal phenomenon. Using ANC, the linear propagation and nonlinear spreading of a single-mode instability from the SOL to the core has been characterized. It is shown that nonlocal effects, due to the ion finite Larmor radius (FLR) effect and ion polarization drift, allows for the coupling of different drift-surfaces and for the instability in the SOL to spread into the core. The phase velocities of the instability is consistent with experimental measurements of radial propagation. The nonlinear saturation of the instability shows that the saturated mode amplitude in the SOL is higher than in the core, again, consistent with experimental measurements.

In addition, the first turbulent transport simulation in the FRC SOL has also been performed using gyrokinetic ions and adiabatic electrons. Self-consistent ion heat flux is calculated from these simulations to be $\sim 6[\mathrm{kW/m^2}]$ while an upper bound for the electron heat flux is calculated to be $\sim 4[\mathrm{MW/m^2}]$ through electron test particles, though the self-consistent electron heat flux is expected to be lower. An inverse spectral cascade is also observed, with unstable shorter wavelength modes feeding into stable or damped long wavelength modes.

Chapter 1

Introduction

The idea of nuclear fusion has been known since the early 1900s when it was proposed as the process which powers the stars. The concept of nuclear fusion was later applied to enhance the destructive capabilities of nuclear weapons by chaining fission reactions to drive fusion reactions within the hydrogen bomb. During the later half of the twentieth century, research on nuclear fusion energy also began in earnest and early optimism underestimated the complexity of confining plasmas, the state of matter in which nuclear fusion is achieved.

Plasma is made up of charged particles which generate electric and magnetic fields, and plasma dynamics are most correctly described by nonlinear equations due to the long-range effects of these fields. Because of the nonlinear nature, perturbations in the plasma can have positive feedback and grow in amplitude; these are plasma instabilities.

”Macro-instabilities” cause immediate and violent disruptions. They must be first suppressed before any hope of fusion reactors is possible, and for the type of fusion reactor considered in this thesis, Tri Alpha Energy (TAE) has shown that they have the ability to suppress or mitigate the macro-instabilities of their devices.

"Micro-instabilities" are more subtle and reduce confinement quality, ie. reduce the economic viability of fusion reactors. They do so by driving turbulence which are field fluctuations that can give charged particles "kicks" out of the plasma, beyond what is expected for charged particles colliding into each other, ie. classical transport. This enhanced transport of particles and energy was known as anomalous transport.

Due to the nonlinear equations which describe the plasma dynamics, to adequately understand micro-turbulence and transport requires the aid of numerical simulations. In general, numerical transport studies have several objectives:

1. Identification and characterization of instabilities that cause fluctuations.
2. Having identified the mechanism, discovery of a reactor regime or operation scheme in which the fluctuations are sufficiently small.
3. If such a regime cannot be found, then estimates of enhanced transport rates must be calculated for potential reactor regimes to determine the feasibility of the reactor design.

Using numerical tools described in later chapters, this thesis aims to study transport in the field-reversed configuration, an approach to magnetic confinement which has significantly progressed thanks to the research efforts of TAE and is described in the next section.

1.1 Background

1.1.1 Field-reversed configuration (FRC)

A field-reversed configuration (FRC) is an elongated prolate compact toroid (CT) with purely poloidal magnetic fields. The FRC consists of two regions separated by a separatrix: an inner, closed field-line core region and an outer, open field-line scrape-off layer (SOL) region.

In magnetic confinement fusion (MCF) research, the standard confinement approach is the tokamak while the FRC has received much less attention since its initial discovery in the 1960s due to the extremely successful confinement times shown by the tokamak. However, research interest in the FRC persists because of potential reactor benefits: (1) the FRC is a plasma with β (the ratio of plasma pressure to magnetic energy density) near unity which suggests less magnetic energy investment and less cyclotron radiation than low β approaches such as the tokamak; (2) the compact nature of the plasma simplifies the construction of the confinement vessel and external magnetic field coils; (3) engineering is also aided by the SOL, which naturally connects to the divertor.

1.1.2 Recent experimental progress by TAE

It was suggested by Rostoker *et al.*[59, 58] that adding a significant energetic ion population via neutral beam injection (NBI) would improve FRC macro-stability while preserving the FRC's favorable transport properties[59, 7, 4, 49, 35, 30] due to the large ion Larmour radius relative to the plasma size[56, 49]. In 2008, Tri Alpha Energy, Inc. (TAE) launched a campaign on the FRC experiment, C-2[6]. With the use of NBI, electron gun biasing, and magnetic end plugs, the C-2 experiments have succeeded in suppressing the major MHD instabilities, the rotational ($n = 2$), wobble, and tilt[26] ($n = 1$) modes (where n is

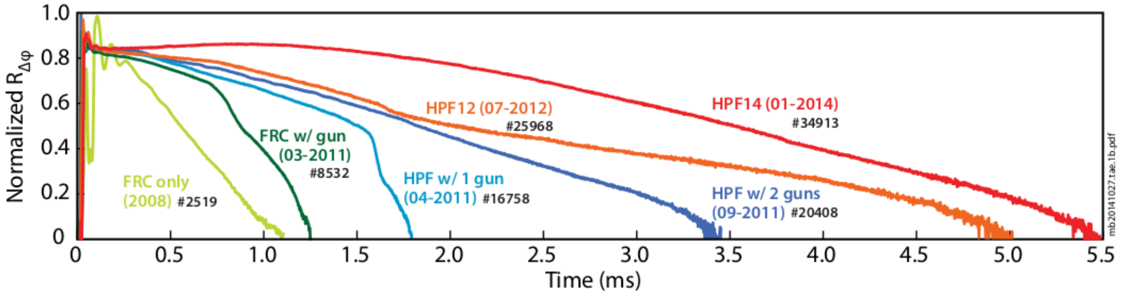

Figure 1.1: From Binderbauer *et al*[8], the normalized size of FRCs for various experiments is plotted against time. With a variety of experimental controls, TAE has shown that the FRC can now be sustained for longer than MHD time-scales and is now in the transport-limited regime.

the toroidal mode number), and increasing FRC confinement times to the order of several milliseconds[66, 26, 8] as seen in Fig. 1.1. This achievement has pushed the FRC to the transport-limited regime.

1.1.3 Past transport research

In early experiments of FRCs, besides the fact that many FRCs may not have reached the transport-limited regime, the transport studies have showed relatively short confinement times. In these experiments, particle[29, 65], flux[33], and energy confinement were well identified as anomalous. Possible electrostatic micro-instabilities have been investigated[12, 68, 9, 25], with the lower hybrid drift instability (LHDI) theoretically identified as the most linearly unstable. However, experiments found that the LHDI saturates at levels two orders of magnitude below oft-predicted values[12]. Electromagnetic modes such as the electron temperature gradient driven electromagnetic micro-tearing modes may also be present in FRCs[24]. Confinement is significantly affected by radial diffusion through the edge[47, 32], where particles move from the closed field-lines of the core to the open field-lines of the SOL. A number of analytical studies have been made of classical transport in simple equilibria[2, 50, 16, 15] and using quasi-steady 1-D plasma profiles[1, 55, 28]. Numerical models of transport have been made to include more details using both simple 1-D and 2-D equilibria [29, 33, 54, 11, 67, 61].

However, the high performance advanced beam-driven FRC plasmas in C-2 and C-2U[66, 26, 8, 5] clearly reached the transport-limited regime, have considerably lengthed transport times[8], and show markedly different properties of fluctuations[60]. In these FRC shots, the Q1D fluid transport code[27], based on the CFRX code[36], has been developed and employed for transport analysis of C-2 plasma conditions.

1.1.4 Measured density fluctuations

Schmitz *et al.*[60] found that, while the plasma in the SOL shows robust fluctuations driven by micro-instabilities, the level of fluctuations in the FRC core is less than in the SOL by 1∼2 orders of magnitude. The fluctuation spectrum is shown in Fig. 1.2. The level of fluctuations are reduced when the neutral beam injection commences. An appropriately applied end voltage bias can further reduce the level of fluctuations. These are strong indications that fluctuations are strongly dependent on the plasma density, temperature, presence of large orbit particles, and shear flows, which may influence stability properties of micro-instabilities. Taking inspiration from these observations, this thesis studies the properties of the microscopic drift-wave instabilities in the FRC plasma, both in the core and in the SOL.

1.2 Overview of the thesis

In early work in slab geometry, drift-waves were shown to be always unstable without particular thresholds, thus called "universal instability"[48, 63]. In the same slab geometry with the addition of finite magnetic shear, however, drift-waves were then found to become

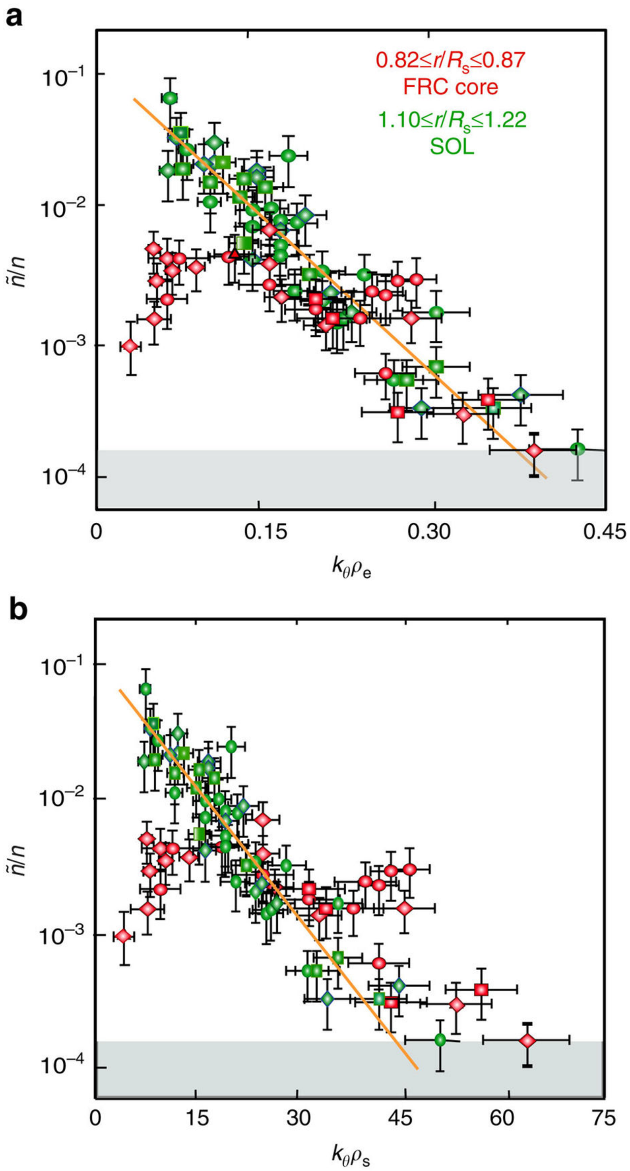

Figure 1.2: From Schmitz *et al*[60], normalized density fluctuation $\tilde{n}/n$ level versus toroidal wavenumber normalized to the (a) electron gyroradius $k_\theta \rho_e$ and (b) normalized to the ion sound gyroradius $k_\theta \rho_s$, in the FRC core and SOL (shots #2958729610; #2975029802). The Doppler Backscattering sensitivity limit is indicated in the figure (grey bar), and error bars represent the typical standard deviation (s.d.) of the measurements. An inverted core wavenumber spectrum is observed for $k_\theta \rho_e < 0.05$ ($k_\theta \rho_s < 7$) indicating that long wavelength (ion) modes are not present. The SOL spectrum shows the highest fluctuation levels at low wavenumber, and the fluctuation level decays exponentially with increasing wavenumber.

completely stabilized[52, 57, 64, 62]. The inclusion of electron non-linearity, however, can de-stabilize the drift wave[31]. Investigations of toroidal coupling, in toroidal geometries such as the tokamak, then lead to the de-stabilization of drift-waves yet again[14, 13, 17]. In toroidal geometry, the addition of shear flow was then found to be partially stabilizing for the drift-wave instabilities[41, 39]. In the last two decades, the paradigm has been dominated by the understanding of zonal flow generation as a non-linear mechanism of regulation for the drift-wave instabilities[44]. Within the work of this thesis, I address the new aspect of drift-wave stability in the FRC geometry which is found to be quite distinct from those in tokamaks.

By identifying and studying transport mechanisms, a suitable transport scaling may be found and applied toward predicting confinement performance in larger, hotter, and denser FRC plasmas. To our knowledge, first-principles simulation of turbulent transport in FRC geometry has not been previously carried out. To fill this gap in theoretical understanding, and, in support of ongoing experiments at TAE, a mature, well-benchmarked turbulence simulation code, the Gyrokinetic Toroidal Code (GTC)[34, 44], was extended to a system with C-2-like geometry and parameters[21, 22, 60]. In addition, a newer, slimmed-down code, A New Code (ANC)[20], has also been developed in collaboration with Dr. D. Fulton for simulation of FRCs. Using these simulation codes, the work of this thesis focuses on drift-wave stabilities and turbulence in the FRC.

1.2.1 Outline of the thesis

The rest of the thesis is organized as follows.

Chapter 2 presents the basics of the FRC simulation model used in this thesis, including FRC geometry, gyrokinetics and the simulation model of the codes.

Chapter 3 describes the simulation code, A New Code (ANC), which has been developed in collaboration with Dr. Daniel Fulton and is used for the cross-separatrix sections of this thesis. Specifically, I emphasize the developmental work that I put into ANC (and into GTC): the Poisson equation, toroidal wedge domain and other boundary tools, divergence-free calculation of magnetic fields, physical benchmarks, and the new field-aligned mesh version of ANC.

Chapter 4 details the results of local drift-wave stability simulations in the FRC where the drift-wave was found to be locally stable in the core and unstable in the scrape-off layer. This chapter draws heavily from Lau *et al.*, 2017[40].

Chapter 5 explores the linear propagation and nonlinear turbulence spreading of a single unstable mode from the SOL to the core. In addition to confirmation of turbulence spread, it is shown that the saturated mode amplitude is lower in the core than the SOL, consistent with experimental observations.

Chapter 6 examines the nonlinear turbulence and transport of multiple unstable modes in the SOL. An inverse spectral cascade is observed after saturation.

Chapter 7 summarizes the main findings of this thesis and comments on future directions.

Punishingly technical detail and derivations have been relocated to the appendix.

Chapter 2

FRC simulation model

The FRC simulation model used within this thesis is based on gyrokinetics. Gyrokinetics is an important tool for understanding turbulence and transport in confined plasmas. It averages over the fast gyro-motion of charged particles so that the slower turbulence time-scales can be resolved. Analytically solving the gyrokinetic equations is not easy, and so, an effective approach is to employ the particle-in-cell method for plasma simulations. Gyrokinetics and particle-in-cell simulations are powerful tools which have been used to advance understanding of turbulence and transport in tokamak plasmas in the past few decades. In this thesis, I use these tools to advance our understanding of turbulence in FRC plasmas and, in this chapter, I present the basics of the FRC geometry, gyrokinetics, and computational model of our approach.

2.1 Geometry of the field-reversed configuration

The FRC is a compact toroid, meaning that there is no external coil in the center of the configuration. Ideally, its magnetic fields have little to no toroidal components, ie. its magnetic field-lines are dominantly in the poloidal direction. It is composed of two coupled but distinct regions: a closed field-line core region and an open field-line scrape-off layer (SOL) region.

2.1.1 Coordinate systems

In this thesis, I use two different coordinate systems in both equations and simulations.

In the local GTC simulations of chapter 4, magnetic Boozer coordinates ($\hat{\psi} \times \hat{\theta} \parallel \hat{\zeta}$) are used where $\hat{\theta}$ is the poloidal direction and is the direction parallel to the magnetic field-lines, $\hat{\psi}$ is the radial direction and is the direction of decreasing pressure, and $\hat{\zeta}$ is the toroidal direction and is perpendicular to both the poloidal and radial directions. These directions are shown in Fig. 2.1.

In the nonlocal ANC simulations of chapters 5 and 6, cylindrical coordinates ($\hat{R} \times \hat{Z} \parallel \hat{\zeta}$) are used where $\hat{Z}$ is the axial direction and is parallel to the machine axis, $\hat{R}$ is the radial direction with respect to the machine axis, and $\hat{\zeta}$ is the toroidal direction, unchanged from the previous. Note that the cylindrical coordinates of ANC are not the conventional $\hat{R} \times \hat{\zeta} \parallel \hat{Z}$ so it is technically left-handed when considering the usual conventions.

2.1.2 Differences between core and SOL

The magnetic field strength of a typical C-2 FRC is shown in Fig. 2.1. Note the differences between the core and SOL in the magnitude of the magnetic field, the shape of the field-lines, and distances from the machine axis. Since the two regions are quite different, it is instructive to look at several effects and their differences between the core and SOL.

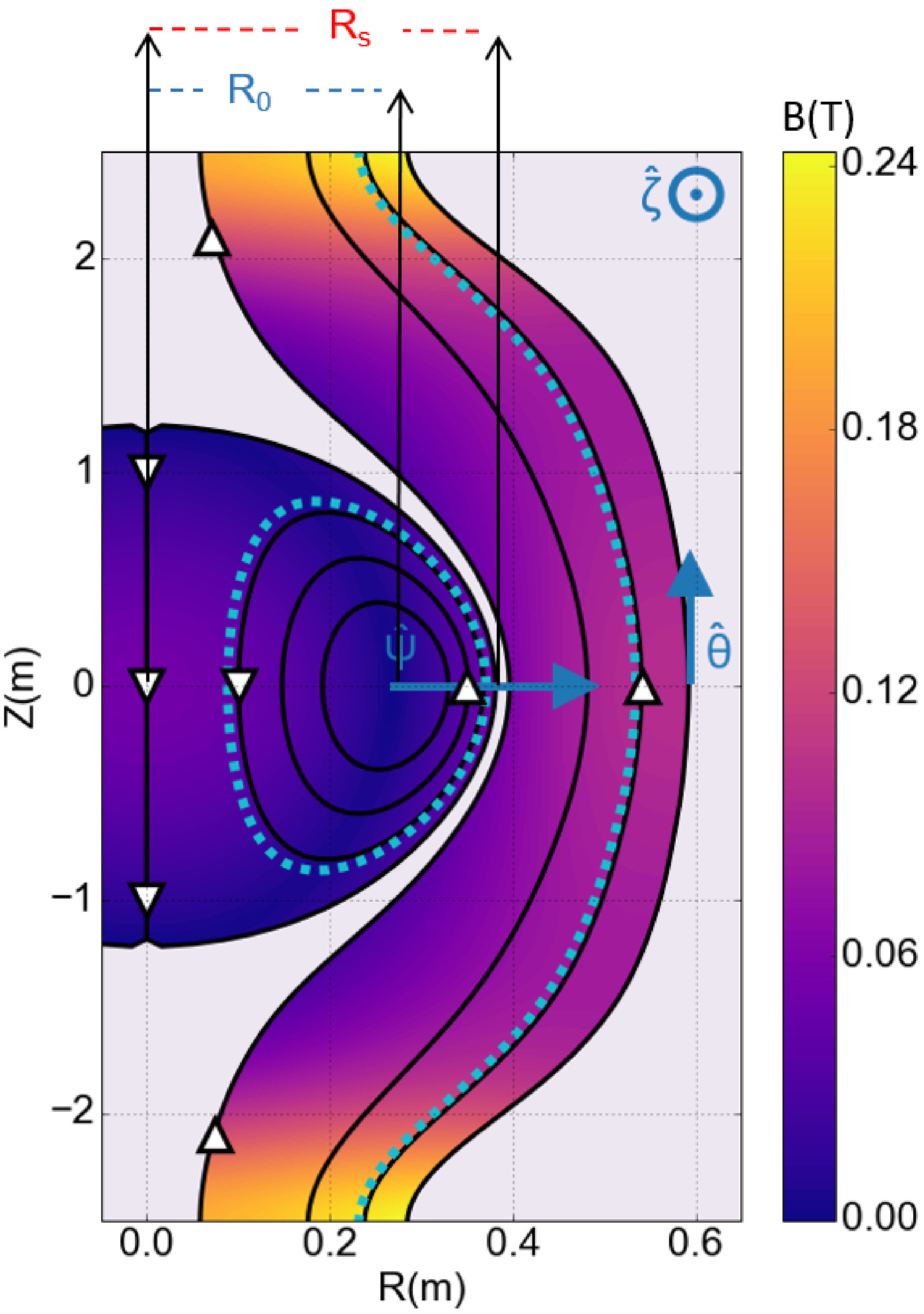

Figure 2.1: The field-aligned mesh on a poloidal plane of a typical C-2 FRC discharge is plotted along with the magnitude of the magnetic field represented by color. The flux surfaces used in simulations are represented by dashed cyan lines. Note that the axes are not proportionally scaled. Arrows denote the directions of the magnetic Boozer coordinate system.

Non-uniform magnetic field

A non-uniform magnetic field has curvature and grad-B. The inverse radius of curvature, $1/R_c$, and inverse scale-length of the magnetic field, $1/L_B$, (normalized by the distance from the machine axis to the null-point, R_0) are shown in Fig. 2.2.

In the core, curvature is strongest in the turning points as expected and grad-B is strong everywhere except near the turning points. This leads to sharply changing drift-motions which is almost zeroed out when field-line averaged. In the SOL, curvature is overall weaker because of the much straighter field-lines while grad-B is similar strength until the point where the magnetic field becomes relatively flat. This leads to a much more uniform drift-motion dominated by the grad-B drift compared to the core.

Finite Larmor radius (FLR) effects

The finite Larmor radius (FLR) effect is the effect of gyro-averaging. A simplified picture of this can be found by ignoring the radial direction and keeping only the toroidal components of the mode, ie. $k_\perp^2 = k_\psi^2 + k_\zeta^2 \to k_\zeta^2$. Then, the FLR effect can be simplified to just a simple multiplication by the squared Bessel function $J_0^2(k_\zeta \rho_i)$ where $k_\zeta = n/R$ and $\rho_i = (T_i/m_i)^{1/2}\Omega_{c,i}^{-1}$. This factor is plotted for three different toroidal mode numbers for a case of uniform temperature in Fig. 2.3 and for a case of non-uniform temperature (radially decreasing) in Fig. 2.4.

In the uniform temperature case, the FLR effect in the core would reduce the amplitude of modes more strongly on the outer midplane than in the inner midplane (red being higher amplitude and blue/purple being lower amplitude). On the other hand, in the SOL, the FLR effect is relatively uniform until much higher toroidal mode numbers such as $n = 150$

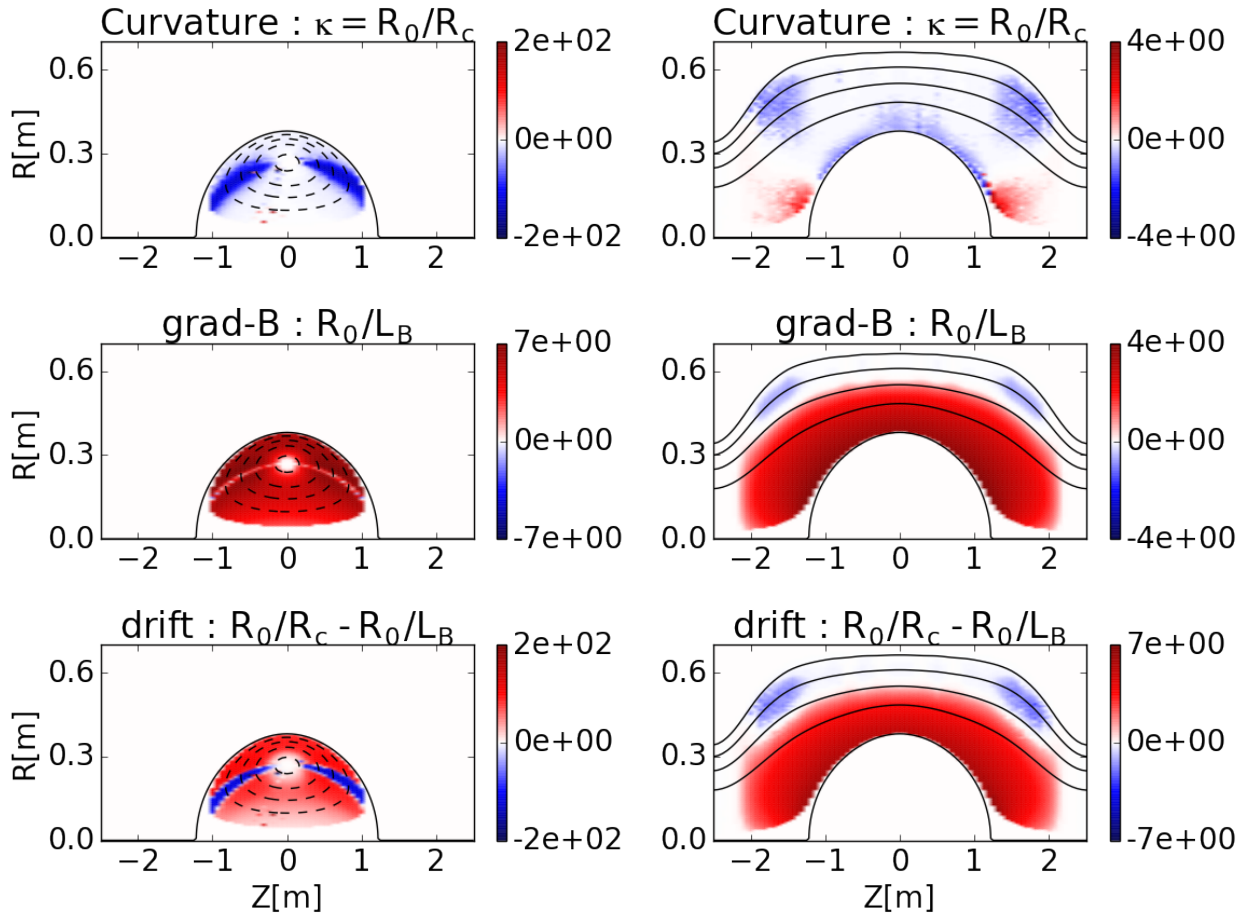

Figure 2.2: Scale-lengths for curvature and grad-B are plotted in the R-Z plane for the core and SOL separately. The positive direction (red) is correlated with stabilizing effects relative to the diamagnetic drift while the negative direction (blue) is correlated with destabilizing effects. The bottom row represents the combined effects of both curvature and grad-B.

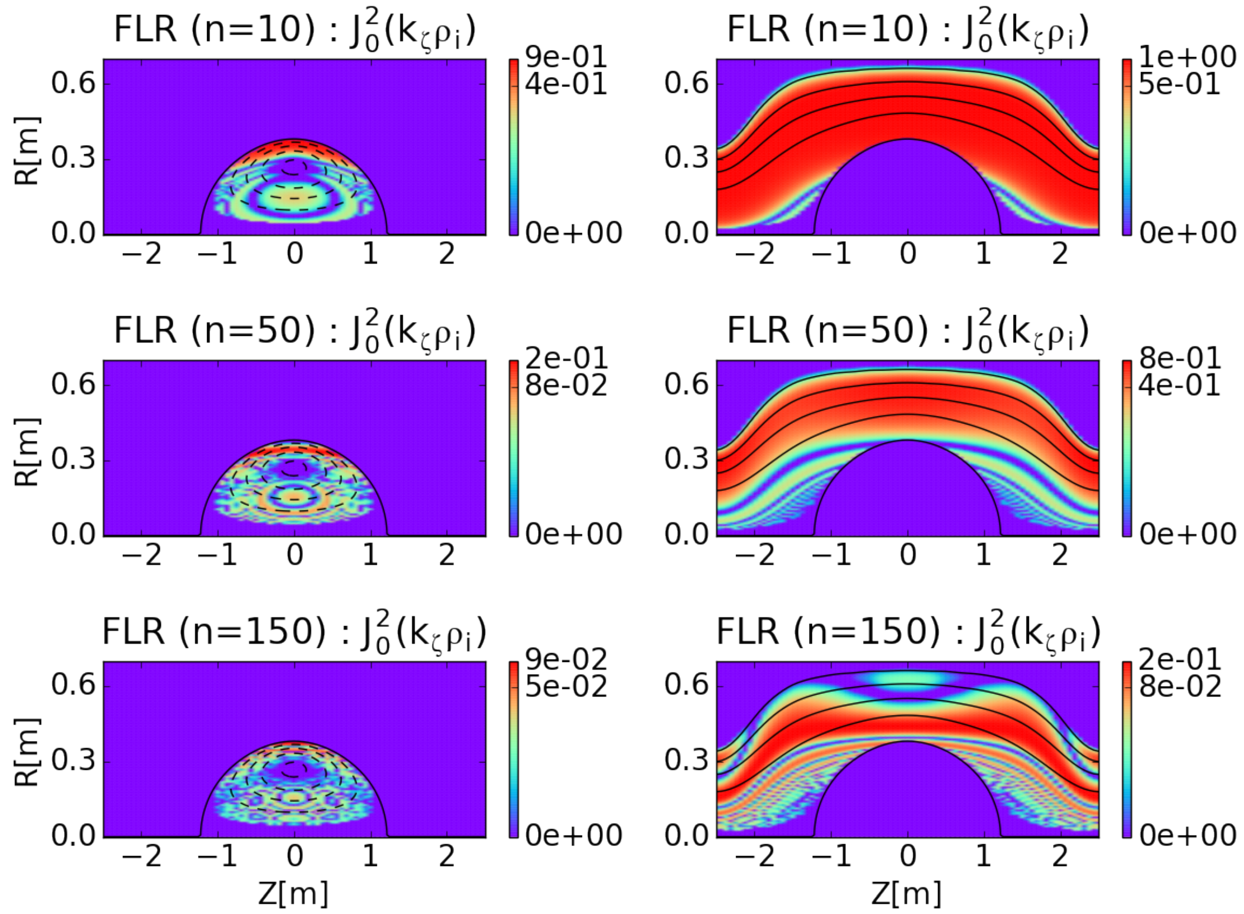

Figure 2.3: The simplified FLR effect ($J_0^2(k_\zeta \rho_i)$) is plotted using a uniform temperature for $n = 10$ (top), $n = 50$ (middle), $n = 150$ (bottom).

in the bottom panel. The interesting features on the axial ends in the bottom panel are due to the magnetic field strength which is quite large towards $Z = \pm 2.5$m.

In the non-uniform radially decreasing temperature case, the FLR effect in the core still suggests a ballooning mode structure, and the FLR effect in the SOL still is more uniform than in the core. The interesting features in the bottom panel is delayed to even higher toroidal mode numbers since the temperature is much lower towards outer field-lines.

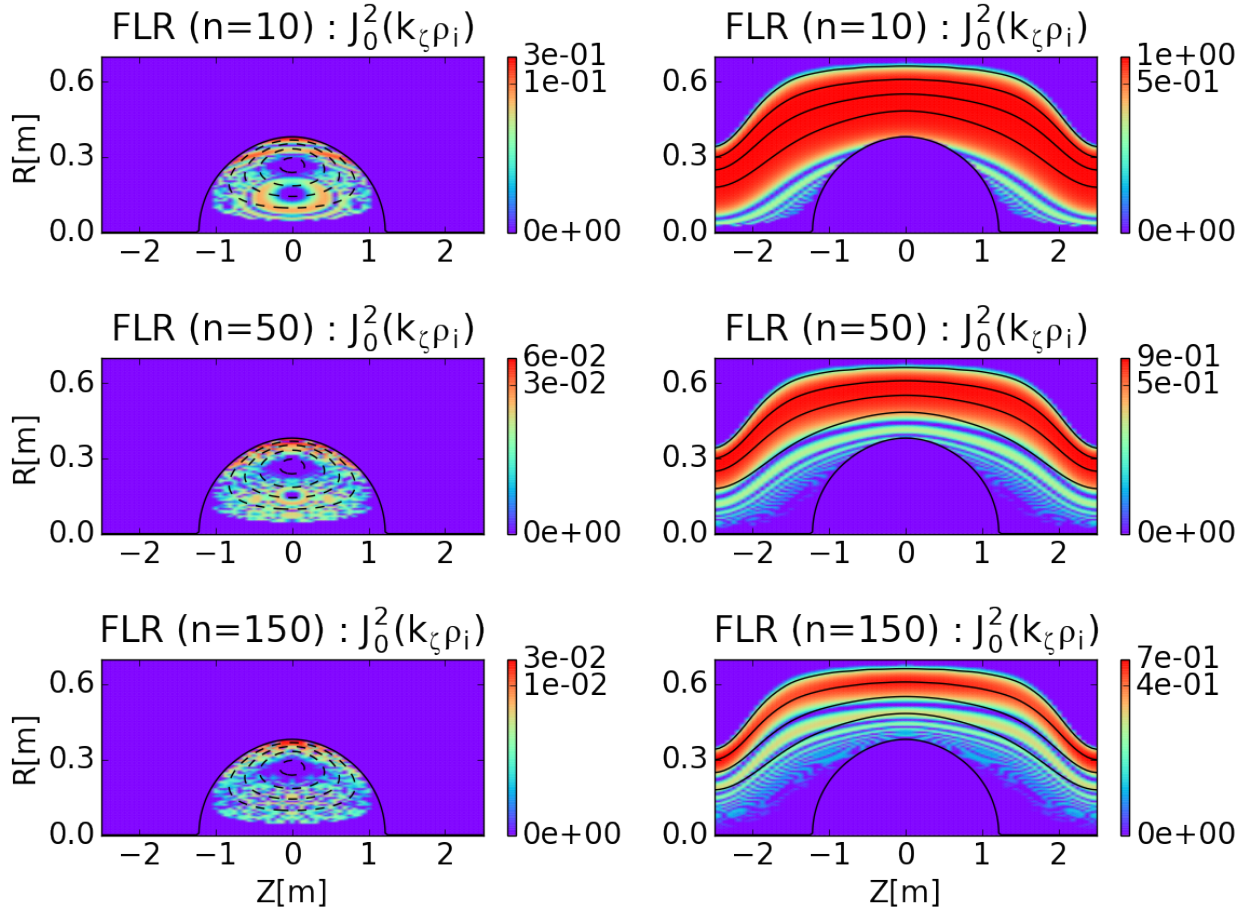

Figure 2.4: The simplified FLR effect ($J_0^2(k_\zeta \rho_i)$) is plotted using a non-uniform temperature which is radially decreasing for $n = 10$ (top), $n = 50$ (middle), $n = 150$ (bottom).

Field-line length

Electrostatic modes are stabilized by parallel electron motion when electrons are able to freely move to cancel space charge along the field-line. The effectiveness of this stabilization is related to how the mode frequency compared to the transit frequency, ie. whether the electron motion is fast enough to cancel space charge perturbation ($\omega < k_{\parallel} v_{th,e}$). The short field-line length also increases the sound wave and Alfven wave frequencies, increasing the difficulty to excite these waves.

Radial plots of arc length and lowest $k_{\parallel}$ (longest possible wavelength) are shown in Fig. 2.5. The arc length is shorter in the core and becomes relatively constant in the SOL. This relatively constant length in the SOL is partially due to the simulation domain cut-off, but it actually holds true even as the simulation domain is extended farther out (although the actual arc length itself will increase). The inverse of the arc length is the lowest possible finite $k_{\parallel}$, and it is clear from the plot that the stabilizing effect of short electron transit lengths will be stronger deeper into the core.

2.1.3 Differences between FRC and tokamak geometry

It is insightful to highlight some of the differences between the FRC and the more researched tokamak. These differences are listed in table 2.1 and further described below.

Table 2.1: Differences between FRC and tokamak geometry

	Feature	FRC	Tokamak
a.	β	$\mathcal{O}(1)$	$\mathcal{O}(1^{-2})$
b.	Toroidal coupling	no	yes
c.	Steep gradient region (pedestal)	outside of separatrix	inside of separatrix
d.	Field-line length	shorter	longer
e.	Curvature	always bad	bad in outer (relative to machine axis) re
f.	$\lvert B\rvert$	radially increasing	radially decreasing

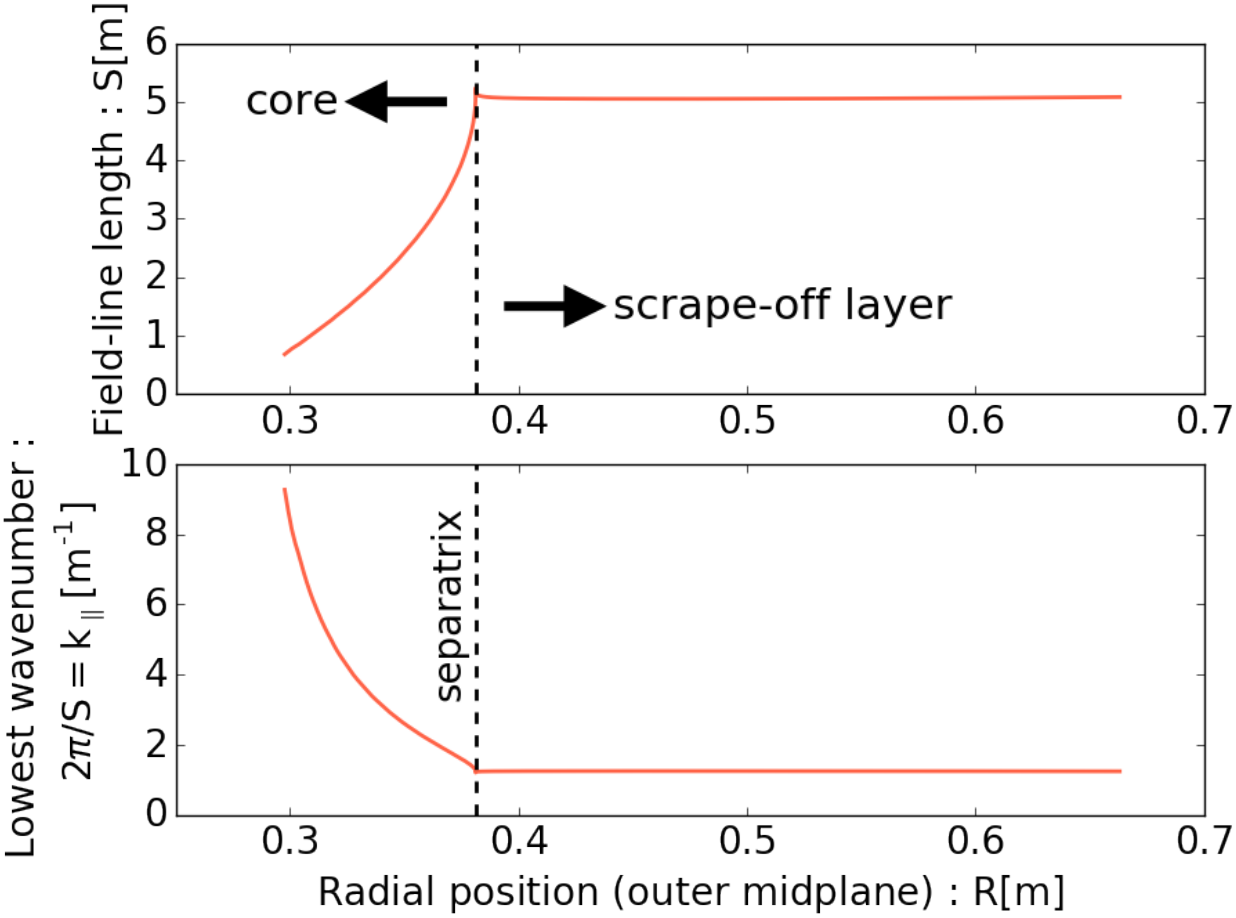

Figure 2.5: The arc length and lowest finite $k_{\parallel}$ are plotted in red. The dashed black line denotes the separatrix which separates the core (left region) from the SOL (right region). Note that the longest wavelength in the realistic SOL can be even longer than indicated here due to the artificial cut-off in simulation domain.

(a) β is the ratio of plasma energy density to magnetic energy density. A higher β suggests cheaper magnetic energy costs (valuable for an economically feasible reactor) and larger ion Larmor radii (stabilizing for instabilities). High β also suggests that electromagnetic modes may be of importance and that is a future line of research once electrostatic modes are understood.

(b) Historically, the stability of drift-waves has crossed the threshold between stable and unstable many times. In slab geometry with finite magnetic shear, drift-waves are completely stabilized[52, 57, 64, 62]. Toroidal coupling leads to de-stabilization of drift-waves[14, 13, 17]. For tokamaks, this toroidal coupling allows modes to exist in just the bad curvature region. In addition, finite q allows for much longer field-lines.

(c) The location of the pedestal changes where instabilities exist. In tokamaks, there has been much progress made by electrostatic simulations of just the core plasma because the core is inherently unstable. In FRCs, however, for progress to be made, we must instead start from the SOL and advance to coupled-core-SOL simulations.

(d) Electrostatic modes are stabilized by parallel electron motion when electrons are able to move to cancel space charge along the field-line. The effectiveness of this stabilization is related to how the mode frequency compares to the transit frequency, ie. whether the motion of the electrons fast enough to cancel space charge due to the perturbation, $k_\parallel v_{th,e} > k_\parallel C_s, k_\parallel v_A > \omega^*$. A short field-line ensures that any finite $k_\parallel$ at all will be quite large so that the condition is fulfilled.

(e) Curvature is considered "good" or "bad" relative to the pressure gradient. One simple way to think of this is that the plasma fluid will experience a force directed from the high pressure region to the low pressure region. If the magnetic field-line is bent such that the inertial force of a particle moving along the field-line, ie. centrifugal force, is in the same direction and reinforces the motion, then it is "bad" curvature; otherwise, it is "good" curvature. In the FRC, the core and the SOL region near the core only have ”bad” curvature. In the tokamak, curvature is ”bad” on the outside and ”good” on the inside. The difference stems from the dominant magnetic field being poloidal in the FRC and toroidal in the tokamak.

(f) The other geometric effect is the non-uniformity of the magnetic field strength. In the tokamak, the magnetic field decreases with increasing radial distance from the magnetic axis; in the FRC, the magnetic field increases with increasing radial distance from the magnetic axis. A radially increasing magnetic field induces a drift that opposes the diamagnetic drift; therefore, in the FRC core, the $\nabla|B|$ is stabilizing and counters the ”bad” curvature.

2.2 Gyrokinetics

Because of costs in computing resources and time, computational physicists need to solve exact equations approximately or solve approximate equations exactly. Gyrokinetics is an approximation which averages out the gyro-motion, ie. the fast circular motion of a charged particle in a magnetic field. It is a set of approximate equations which are valid when the gyrokinetic ordering is fulfilled, ie.

$$\frac{\omega}{\Omega_i} \sim \frac{\rho_i}{L_B} \sim \frac{e\phi}{T} < 1, \ \frac{k_\parallel}{k_\perp} \ll 1 \tag{2.1}$$

where ρ_i is the ion gyro-radius, $L_B = \frac{1}{B}\frac{\partial B}{\partial r}$ is the magnetic field scale length, and ϕ is the perturbed electrostatic potential.

The benefit of gyrokinetics is in the separation of the fast gyro-motion from the slower drift and parallel motions while still retaining finite Larmour radius (FLR) effects. Solving the full dynamics, as in the kinetic portion of section A, in complex magnetic geometry is extremely difficult and costly; therefore, when valid, gyrokinetics is used for understanding physics which exist on longer time-scales than cyclotron periods such as turbulence and transport. Here, I present some of the basic gyrokinetic equations as well as justification for the use of gyrokinetics in the FRC geometry.

2.2.1 Gyrokinetic equations

The ion gyrocenter distribution, f_i, is governed by

$$\frac{df_i}{dt} \equiv \frac{\partial f_i}{\partial t} + \dot{\vec{X}} \cdot \nabla f_i + \dot{v}_\parallel \frac{\partial f_i}{\partial v_\parallel} = 0 \tag{2.2}$$

where $\dot{\vec{X}}$ is the gyrocenter position, and $v_\parallel$ is the velocity parallel to the magnetic field. The motion of the gyrocenter is a combination of the parallel motion and the perpendicular drifts,

$$\begin{aligned} \dot{\vec{X}} &= v_\parallel \hat{b}_0 + \vec{v_E} + \vec{v_d} \\ v_\parallel &= -\frac{1}{m_i} \frac{\vec{B}^*}{B_0} \cdot \left(\mu \nabla B_0 + Z_i \nabla \delta\phi\right) - \frac{Z_i}{m_i} \frac{\partial \delta A_\parallel}{\partial t} \end{aligned} \tag{2.3}$$

where m_i is the ion mass, Z_i is ion charge normalized by e, and μ is the magnetic moment. The term marked in blue is the $\vec{E} \times \vec{B}$ drift

$$\vec{v_E} = \frac{c\vec{B}_0 \times \nabla \delta\phi}{B_0^2} \tag{2.4}$$

which is dropped during linear simulations. The other part of the perpendicular drifts is due to the magnetic geometry, ie. the curvature and grad-B drifts

$$\begin{aligned}\vec{v_d} &= \vec{v}_{curv} + \vec{v}_{\nabla B}\\ \vec{v}_{curv} &= \frac{v_\parallel^2}{\Omega_{c,i}}\nabla\times\hat{b}_0\\ \vec{v}_{\nabla B} &= \frac{\mu}{m_i\Omega_{c,i}}\hat{b}_0\times\nabla B_0.\end{aligned} \tag{2.5}$$

The term marked in red in Eq. (2.3) is the modification to the parallel motion due to induction. This is an electromagnetic term which is dropped from the current electrostatic simulations. Similarly, the magnetic field used,

$$\vec{B}^* = \vec{B}_0 + \frac{B_0 v_\parallel}{\Omega_{c,i}}\nabla\times\hat{b}_0 + \delta\vec{B}, \tag{2.6}$$

also has an electromagnetic term, the perturbed magnetic field, which is dropped.

Perturbative δf simulation

While the previous gyrokinetic equations can be implemented as is, a more efficient approach is to split the distribution function into equilibrium and perturbed parts, ie. $f = f_0 + \delta f$. Defining particle weight to be $W_i \equiv \delta f_i / f_i$, Eq. (2.2) is transformed into the weight equation

$$\begin{aligned} \frac{dW_i}{dt} = (1 - W_i)\Bigg[& - \left(v_\parallel \frac{\delta \vec{B}}{B_0} + \vec{v_E} \right) \cdot \frac{\nabla f_{i,0}}{f_{i,0}} \\ & + \left(\mu \frac{\delta \vec{B}}{B_0} \cdot \nabla B_0 + Z_i \frac{\vec{B}^*}{B_0} \cdot \nabla \phi + \frac{Z_i}{c} \frac{\partial A_\parallel}{\partial t} \right) \frac{1}{m_i} \frac{1}{f_{i,0}} \frac{\partial f_{i,0}}{\partial v_\parallel} \Bigg] \end{aligned} \tag{2.7}$$

where, again, I have put electromagnetic terms in red and the parallel nonlinearity in blue.

When a drift-kinetic model is used for the electrons, the governing equations are similar with the exception that the perturbed electric field is not gyro-averaged. When an adiabatic model is used for the electrons, ie. Boltzmann electrons, the electron response simply becomes Eq. (A.1).

2.2.2 Poisson equation

The gyrokinetic Poisson equation is

$$\frac{Z_i^2 e n_{i,0}}{T_i} \left(\phi - \tilde{\phi} \right) = Z_i \bar{\delta} n_i - \delta n_e \tag{2.8}$$

where the bar denotes a gyro-averaged quantity, δn is the perturbed density, $n_{i,0}$ and T_i are the equilibrium ion density and temperature, respectively. The term on the left-hand side is the polarization term where ϕ is the electrostatic potential and $\tilde{\phi}$ is the ”second gyro-averaged” potential. In both the GTC and ANC simulations, the Padé approximation is used for the second gyro-averaged potential such that the gyrokinetic Poisson equation becomes

$$\begin{aligned} \tilde{\phi} &\approx \frac{1}{1-\rho_i^2\nabla_\perp^2}\phi \\ \rightarrow \frac{Z_i^2 e n_{i,0}}{T_i}\left(\phi - \frac{1}{1-\rho_i^2\nabla_\perp^2}\phi\right) &= Z_i\bar{\delta} n_i - \delta n_e \\ \rightarrow \frac{Z_i^2 e n_{i,0}}{T_i}\left(-\rho_i^2\nabla_\perp^2\phi\right) &= \left(1-\rho_i^2\nabla_\perp^2\right)\left(Z_i\bar{\delta} n_i - \delta n_e\right). \end{aligned} \tag{2.9}$$

Another approximation that is later used in ANC is the adiabatic electron model, ie. Eq. (A.2). Replacing $\delta n_e = n_0\frac{e\phi}{T_e}$ in the gyrokinetic Poisson equation,

$$\begin{aligned} \frac{Z_i^2 e n_0}{T_i}\left(-\rho_i^2\nabla_\perp^2\phi\right) &= \left(1-\rho_i^2\nabla_\perp^2\right)\left(Z_i\bar{\delta} n_i - n_0\frac{e\phi}{T_e}\right) \\ \rightarrow \left[\left(\frac{Z_i^2 e n_0}{T_i} + {\color{red}\frac{e n_0}{T_e}}\right)\left(-\rho_i^2\nabla_\perp^2\right) + {\color{red}\frac{e n_0}{T_e}}\right]\phi &= \left(1-\rho_i^2\nabla_\perp^2\right) Z_i\bar{\delta} n_i \end{aligned} \tag{2.10}$$

where the subscript on the equilibrium density has been dropped since $Z_i n_{i,0} = n_{e,0}$ and the adiabatic contributions are colored red.

2.2.3 Gyrokinetics in FRC geometry

For the FRC magnetic geometry, there may be a concern in the use of gyrokinetics. In the localized GTC simulations, the simulated drift-surfaces *do not* include the magnetic null-point, allowing the guiding-center approximation to remain valid[10]. For the simulated drift

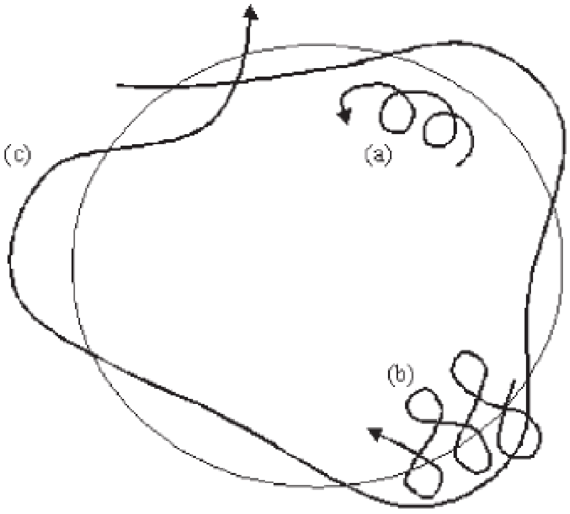

Figure 2.6: Visualization from Yumi *et al*[69] of three different kinds of particle orbits in the FRC: (a) cyclotron, (b) figure-8, and (c) betatron.

surfaces, the average gyro-kinetic parameter is $\rho_i/L_B \simeq 0.2$ in the core and $\rho_i/L_B \simeq 0.006$ in the SOL which are gyro-kinetically valid (about 1.3% difference between the guiding-center and orbit-averaged positions in the case of $\rho_i/L_B \simeq 0.2$ as shown by Brizard[10]).

In the ANC simulations, the particle boundary is set such that there are no fluctuations in the region near the magnetic null-point, allowing simulations to avoid the areas where gyrokinetics may not apply. Additionally, in the field-aligned version of ANC, the region near the magnetic null-point is similarly cut out of the simulation domain.

A possible valid concern is that the gyro-averaging operator in our model only captures the confined cyclotron orbits in the FRC. For the betatron type of motion, ANC has a fully kinetic particle model in place as well. For the figure-8 trajectories, a future step is to expand the gyro-averaging operator to correctly capture the FLR effects of this type of motion. The classification between these trajectories can be found through the energy and canonical momentum (H, P_θ)[69], and a graphical representation of these orbits from Yumi *et al* is shown in Fig. 2.6.

2.3 Simulation model

Simulations presented in this thesis have been conducted with the Gyrokinetic Toroidal Code (GTC) and A New Code (ANC), detailed in chapter 3. These are closely related particle-in-cell (PIC) microturbulence simulation codes using an electrostatic perturbative δf model[63, 19, 51, 45, 34]. Although there are other ways to solve the same kinetic equations, such as continuum simulations or semi-Lagrangian simulations, for phase-space dimensions numbering more than four (three spatial, one velocity), the PIC method is the most capable of taking advantage of the massively parallel supercomputers. In this section, an overview of the PIC method and some of the more general simulation model details are described. Since different simulations use slightly different models, more specific details about the simulations will be described before each result in the later chapters.

2.3.1 Particle-in-cell method

The particle-in-cell method is conceptually very simple. The basic idea is to represent physical particles (numbering more than 10^{18} particles when estimating with a cylinder of radius 30cm, axial length of 5m, and average density of 10^{12}cm^{-3}) with simulation particles (numbering around 10^9). Effectively, each simulation particle samples a volume element of the phase space. These simulation particles are moved according to the Maxwell's equations and the electromagnetic fields generated by the particles themselves and whatever external fields. Different models can be used; for instance, the gyrokinetic equations from section 2.2 are used to move simulation gyrocenters representing physical particles. Fluid quantities can be calculated by taking moments of the distribution functions represented by the simulation particles.

The core particle-in-cell cycle is pretty simple:

(1) Particles are interpolated onto grid to calculate density (and flow, which is used for electromagnetic simulations or an alternate numerically stable method[3] to calculate density).

(2) Density is used in Poisson equation to calculate electrostatic potential. (The flow can also be used in Ampere's law to calculate the vector potential for electromagnetic simulations.)

(3) Potential is used to calculate self-consistent electric fields which are interpolated onto particles.

(4) Fields are used to push particles and update particle weights.

(5) Repeat from step (1) until relevant time scales have been achieved.

This cycle can be modified for more complex numerical schemes. For example, the mentioned alternate scheme in (1) would require the calculation of flow to calculate density. Numerical smoothing of the grid quantities is also performed to ensure that unphysical instabilities due to aliasing or other numerical effects do not affect the physics. The end goal (5) is vague because it depends on the type of physics which is important. In laser-plasma interactions, for example, simulations may run until the laser pulse has been depleted. In the turbulence simulations of this thesis, linear simulations are run until the growth-rates and frequencies can be identified, while non-linear simulations are run until, at least, mode saturation or longer.

2.3.2 Toroidal wedge

In the ideal FRC, there is no toroidal coupling, and it is simple to take advantage of the toroidal periodicity. A larger number of simulations is enabled by the reduction of the simulation domain from a full torus $[0,\ 2\pi]$ to a partial torus $[0,\ 2\pi/n]$ where n is the

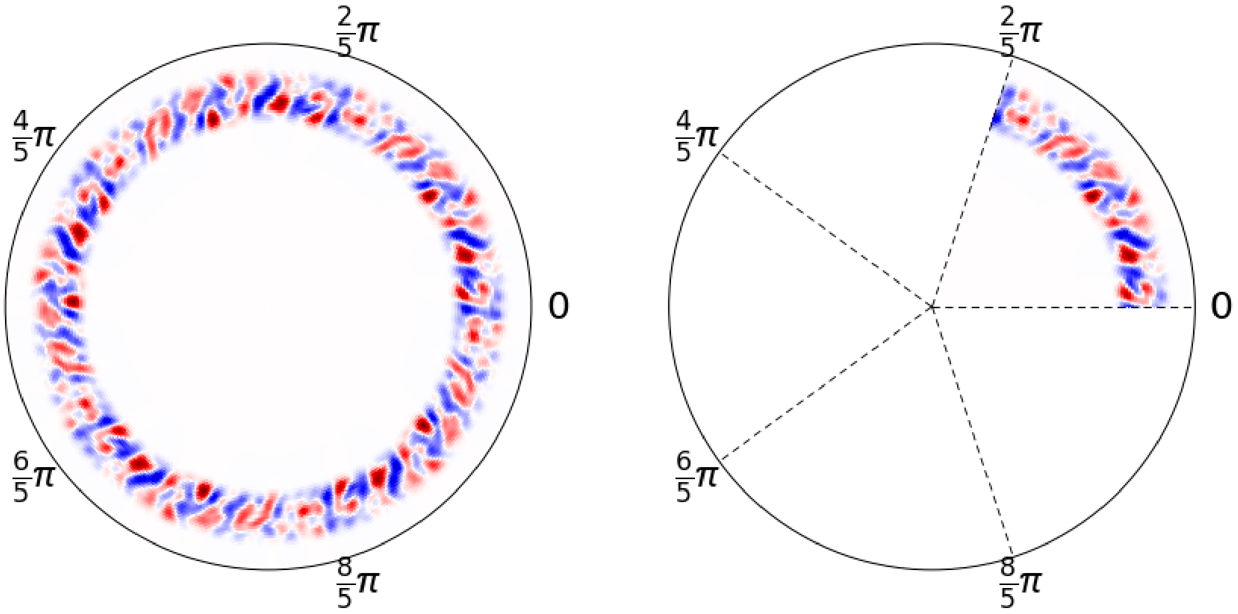

Figure 2.7: A plot of electrostatic turbulence, looking down the Z-axis, showing the reduction from the full torus (left) to the partial torus (right).

particular toroidal mode number of interest. Initially, this was only used for the single-n simulations. However, in ANC, this partial torus domain reduction is extended to use the lowest common denominator, n, for multiple-n non-linear simulations such as the one shown in Fig. 2.7.

2.3.3 Flux-tube domain

In the early simulations, the focus of the study was to characterize the local linear properties of FRC instabilities in the core and SOL *separately*. In those simulations, the toroidal wavelength is assumed to be much shorter than the radial wavelength of the instabilities, ie. $k_\psi \ll k_\zeta$.

This allows the radial domain to be localized to a single drift-surface. The local simulations of this thesis were localized to the surfaces where $R = 37$cm in the core and $R = 52$cm in the scrape-off layer as shown in Fig. 2.1. As mentioned in section 2.2, these drift-surfaces *do* *not* include the magnetic null-point, allowing the guiding-center approximation to remain valid[10]. The average gyro-kinetic parameter is $\rho_i/L_B \simeq 0.2$ in the core and $\rho_i/L_B \simeq 0.006$ in the SOL which are gyro-kinetically valid[10].

As mentioned, in gyrokinetic simulations[42], dynamics faster than the ion gyro-period are averaged out while ion and electron finite Larmour radius (FLR) effects are retained through accurate representation of gyro-averaging on particles via direct calculations of Bessel functions for the scattering of charge onto the grid and in the gathering of fields onto the charge. In the local simulations, due to the neglect of radial gyro-averaging, growth-rates were expected to be higher when compared to non-local simulations. Later non-local simulations found this expectation to be correct and will be discussed in chapter 5.

2.4 Summary

In this chapter, I have presented the basics of the FRC geometry and its differences from the more studied magnetic confinement approach, ie. the tokamak. Some differences are advantageous such as the stabilizing influence of large FLR, ∇B, short field-lines, and lack of toroidal coupling (in the ideal FRC), or the economic potential of high β and simple geometry. Some differences are less promising such the ever-present "bad" curvature or need for different research approaches due to the importance of the open field-line region. Despite these differences, gyrokinetics is still an important and valid tool for understanding basics physics of turbulence and transport in the FRC, and thus, an overview of gyrokinetics has also been presented. Keeping these differences in mind, GTC and ANC have been developed to further push the capabilities of turbulence simulations in the FRC. Although some of the basics of the simulation model have been presented in this chapter, chapter 3 will go further into excruciating details of some of the specific implementations I have developed.

Chapter 3

Cross-separatrix simulations: A New Code (ANC)

Within this thesis, I present physics based on results from both the the Gyrokinetic Toroidal Code (GTC) and A New Code (ANC). These are closely related particle-in-cell (PIC) microturbulence codes using a first-principles model[1,2].

GTC was originally developed by Prof. Z. Lin two decades ago, with contributions from a large international collaboration of physicists and developers since then. It is well established in the tokamak and stellerator community, with extensive cross code verification[3,4,5,6] and validation[7,8] studies. It was the first fusion production code to hit a teraflop on NERSC Seaborg in 2001[9] and a petaflop on ORNL Jaguar in 2008[10].

While GTC is a robust multi-physics suite, capable of simulating a variety of magnetic geometries, it was originally built for tokamak geometry. Due to the stark differences of the FRC geometry as mentioned in section 2.1, there are different computational considerations such as parallelization and different physical needs such as cross-separatrix coupling. To that end, ANC is a smaller code built to address the unique requirements of FRC physics, including zero toroidal field magnetic geometry, fully kinetic ion orbits, and closely coupled closed field-line and open field-line physics. ANC was originally developed by Dr. D. Fulton, with assistance from Dr. I. Holod, for overcoming the issue of describing the separatrix in magnetic Boozer coordinates (in which the original GTC is based in).

Initially, I developed and implemented the Poisson equation for GTC as well as other efforts to increase computational efficiency. With this experience with GTC development, I then focused on developing ANC, including modifications to the Poisson equation, development of toroidal wedge domain and other boundary tools, implementation of divergence-free magnetic fields, validation against theory, and the development of the field-aligned mesh. I describe my contributions to both codes in this chapter with more focus on my contributions to ANC. More technical details such as verification and numerical tools are shown in section B and section C.

3.1 Divergence-free magnetic field

One of the benefits of magnetic Boozer coordinates is that the divergence of the magnetic field is guaranteed to be zero ($\nabla \cdot \vec{B} = 0$). In the cylindrical coordinate system, there may be non-zero divergence due to numerical representations of the continuous derivatives. Within simulations, the non-zero divergence would present itself as numerical heating or cooling.

To solve this issue, the key is to bypass numerical differentiation when calculating magnetic field quantities, including magnetic field derivatives, by using analytic differentiation through spline functions instead. In ANC, the magnetic field is represented by the analytic differentiation of the poloidal flux function

$$\begin{aligned} B_R = -&\frac{1}{R}\frac{\partial\psi(R,Z)}{\partial Z} \\ B_Z = &\frac{1}{R}\frac{\partial\psi(R,Z)}{\partial R} \end{aligned} \tag{3.1}$$

where the poloidal flux function itself is represented by cubic splines. The forms of the poloidal flux function and the magnetic field are

$$\begin{aligned} \psi(R,Z) &= \left(\sum_{i=0}^{3} a_i \Delta_R^i\right)\left(\sum_{j=0}^{3} b_j \Delta_Z^j\right) \\ B_R(R,Z) &= -\frac{1}{R}\left(\sum_{i=0}^{3} a_i \Delta_R^i\right)\left(\sum_{j=1}^{3} b_j j \Delta_Z^{j-1}\right) \\ B_Z(R,Z) &= \frac{1}{R}\left(\sum_{i=1}^{3} a_i i \Delta_R^{i-1}\right)\left(\sum_{j=0}^{3} b_j \Delta_Z^j\right) \end{aligned} \tag{3.2}$$

where $\Delta_R = R - R_B$, $\Delta_Z = Z - Z_L$, and (R_B, Z_L) are the respective nearest grid point locations with values lower than the sample point position, (R, Z). The divergence is minimized to machine precision as seen in Fig. 3.1, and the magnetic field can be seen in Fig. 3.2. Sample trajectories from trapped and passing particles are shown in Fig. 3.3 and Fig. 3.4.

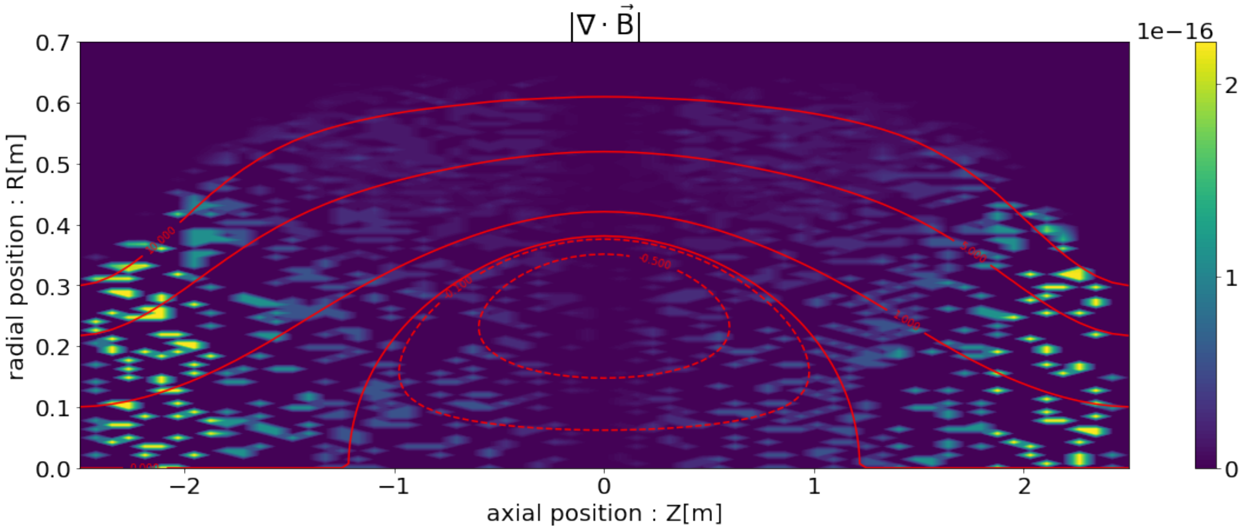

Figure 3.1: Divergence of the magnetic field calculated within ANC is minimized to machine precision, ie. effectively zero. Several field-lines are plotted for reference in red.

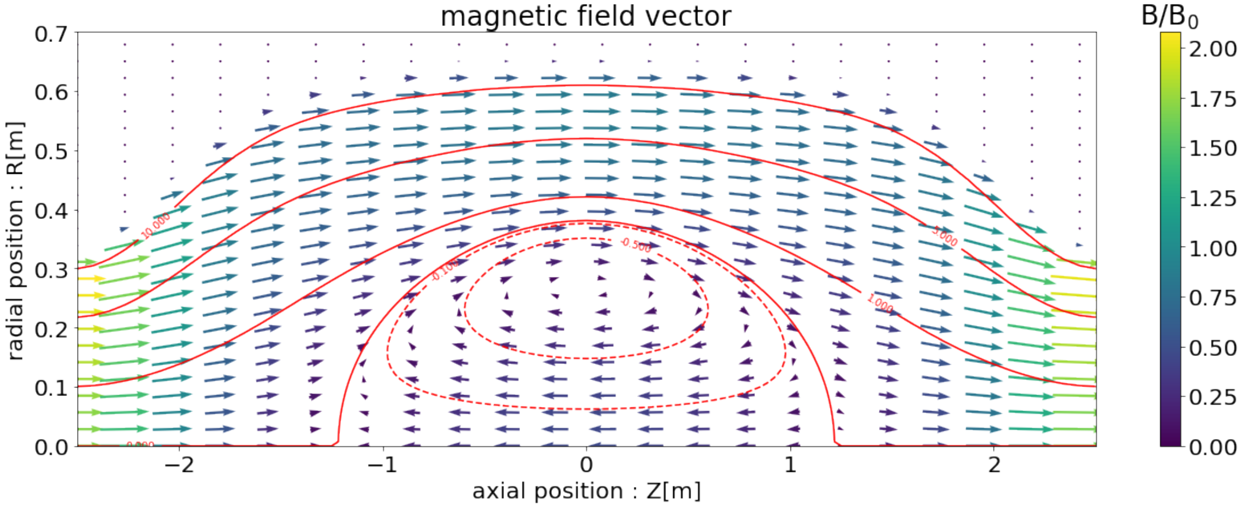

Figure 3.2: The magnetic field is plotted as a vector field with color and arrow size determined by the magnetic field strength. Several field-lines are plotted in red for reference.

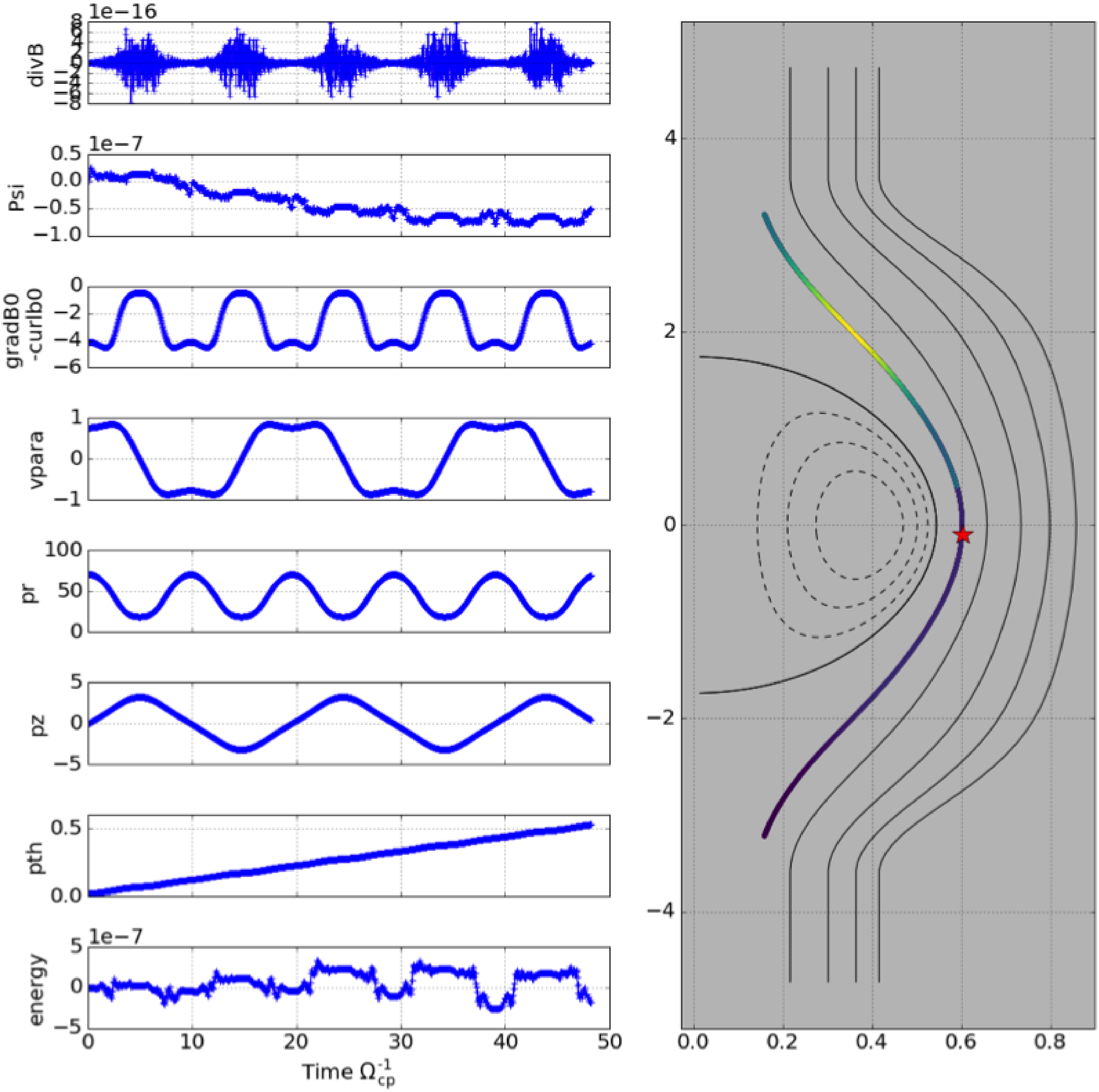

Figure 3.3: A sample trajectory of a trapped particle is plotted. The time histories on the left show that divergence remains near zero, that the particle stays on the field-line as expected (ψ difference is about $\mathcal{O}(1^{-7})$), ie. canonical momentum is conserved, and energy is conserved (difference is about $\mathcal{O}(1^{-7})$).

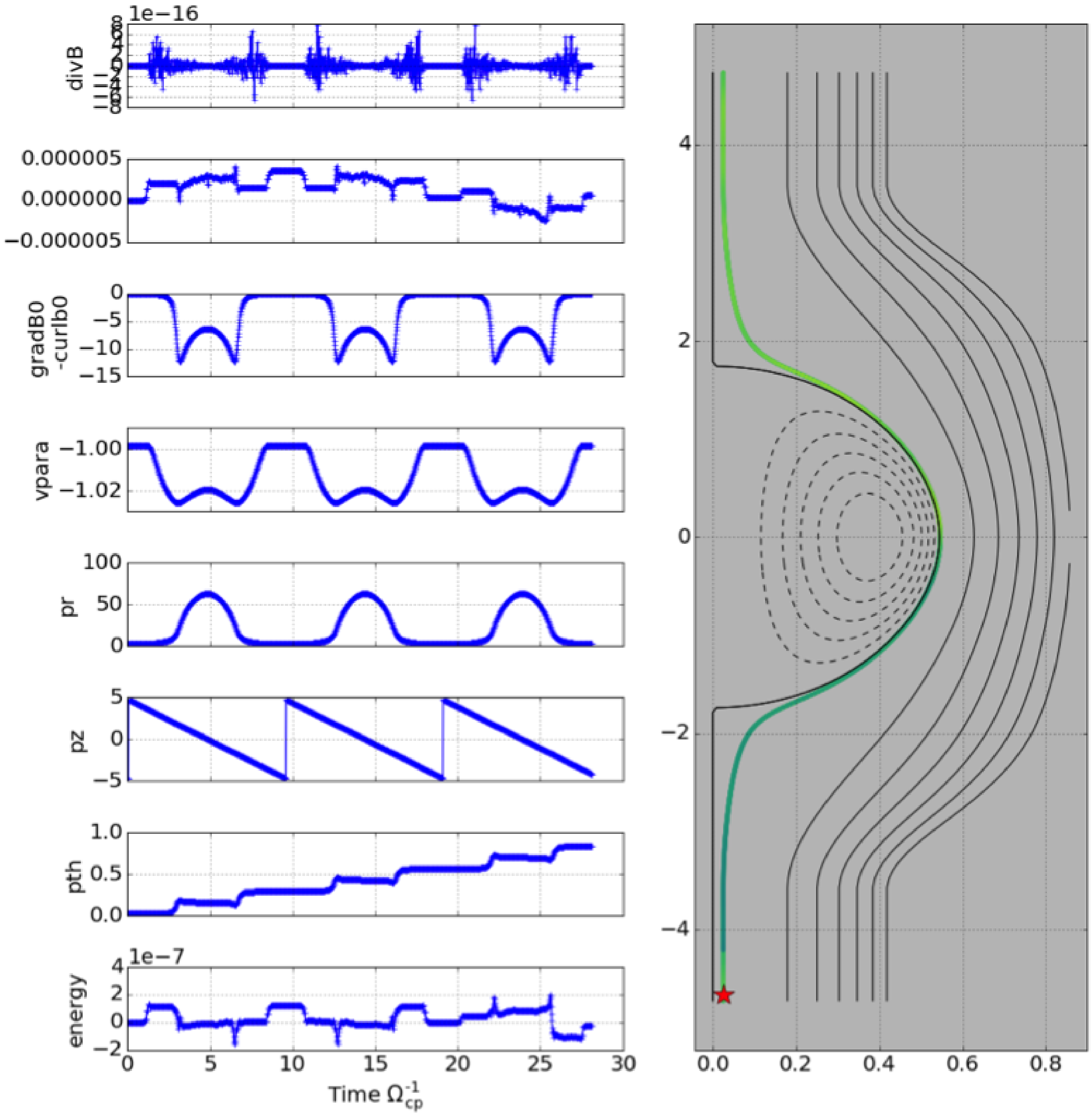

Figure 3.4: A sample trajectory of a passing particle near the separatrix is plotted. The time histories on the left show that divergence remains near zero, that the particle stays on the field-line as expected (ψ difference is about $\mathcal{O}(1^{-6})$), ie. canonical momentum is conserved, and energy is conserved (difference is about $\mathcal{O}(1^{-7})$).

3.2 Poisson Equation

As stated in section 2.3.1, the particle-in-cell cycle is pretty simple: (1) particles are interpolated onto a grid as density, (2) density is used in the Poisson equation to calculate the electrostatic potential, (3) self-consistent electric fields are calculated from the potential and interpolated onto particles, (4) particles are moved and particle weights are updated, and (5) repeat from step (1) until relevant time-scales have been achieved. Clearly, the Poisson equation is an integral part of the process, and careful consideration of the physics can lead to a substantial difference in the computational efficiency of solving the Poisson equation. Aside from the field-aligned mesh and benchmarks, much of my computational development has been focused on the Poisson equation in both GTC and ANC. Here, I detail the methods used in the GTC simulations, in the ANC simulations, and in the recently developed field-aligned version of ANC.

3.2.1 GTC semi-spectral solver

Initial GTC FRC simulations were extremely inefficient in solving the Poisson equation because GTC and its computational parallelism was originally designed for tokamak and stellerator geometry. One major difference is in the parallel direction of the magnetic field which is mainly in the toroidal direction in the tokamak and stellerator but is purely in the poloidal direction in the FRC.

Originally, the Laplacian matrix was based purely on finite difference

$$\begin{aligned} \nabla_\perp^2 f &= g^{\psi\psi}\frac{\partial f}{\partial \psi} + g^{\zeta\zeta}\frac{\partial f}{\partial \zeta} \\ \rightarrow \nabla_\perp^2 f &= g^{\psi\psi}\frac{f_{i-1,j} - 2f_{i,j} + f_{i+1,j}}{2\Delta\psi} + g^{\zeta\zeta}\frac{f_{i,j-1} - 2f_{i,j} + f_{i,j+1}}{2\Delta\zeta}. \end{aligned} \tag{3.3}$$

Taking advantage of the simple symmetries in the FRC, I introduced a semi-spectral Poisson solver with a partial torus domain (noting that $f \rightarrow \hat{f}$ means that f is now spectrally decomposed in the toroidal direction)

$$
\begin{aligned}
\nabla_\perp^2 f &= g^{\psi\psi}\frac{\partial f}{\partial \psi} + g^{\zeta\zeta}\frac{\partial f}{\partial \zeta} \\
\rightarrow \nabla_\perp^2 f &= g^{\psi\psi}\frac{\hat{f}_{i-1} - 2\hat{f}_i + \hat{f}_{i+1}}{2\Delta\psi} + g^{\zeta\zeta}(-n^2\hat{f}_i)
\end{aligned}
\tag{3.4}
$$

which was able to reproduce the same mode structures, growth-rates, and frequencies while, at the same time, significantly reducing the computational costs related to inefficient computational parallelization schemes based on tokamak geometry. A quick comparison of sample mode structures between the semi-spectral method and the original GTC method is shown in Fig. 3.5.

The personal computing hours I spent on Oak Ridge's Titan supercomputer is shown in Fig. 3.6, essentially a factor of about 26 in terms of the average computing hours spent. In reality, the efficiency improvement goes beyond that because this does not reflect how many more simulations I was able to perform due to the lower wait in queue time. The efficiency mainly comes from the reduction in the domain. Since I was interested in simulations of a single toroidal mode at a time, I only needed to simulate a bounded domain of $[0, 2\pi/n]$ instead of the full $[0, 2\pi]$ as described in section 2.3. This reduced the Poisson matrix size and the total number of simulation particles required. In addition, the semi-spectral solver was cleaner than the finite-difference solver, further reducing the grid-resolution needs, and the spectral decomposition required was already performed for the filtering process so no additional overhead was required.

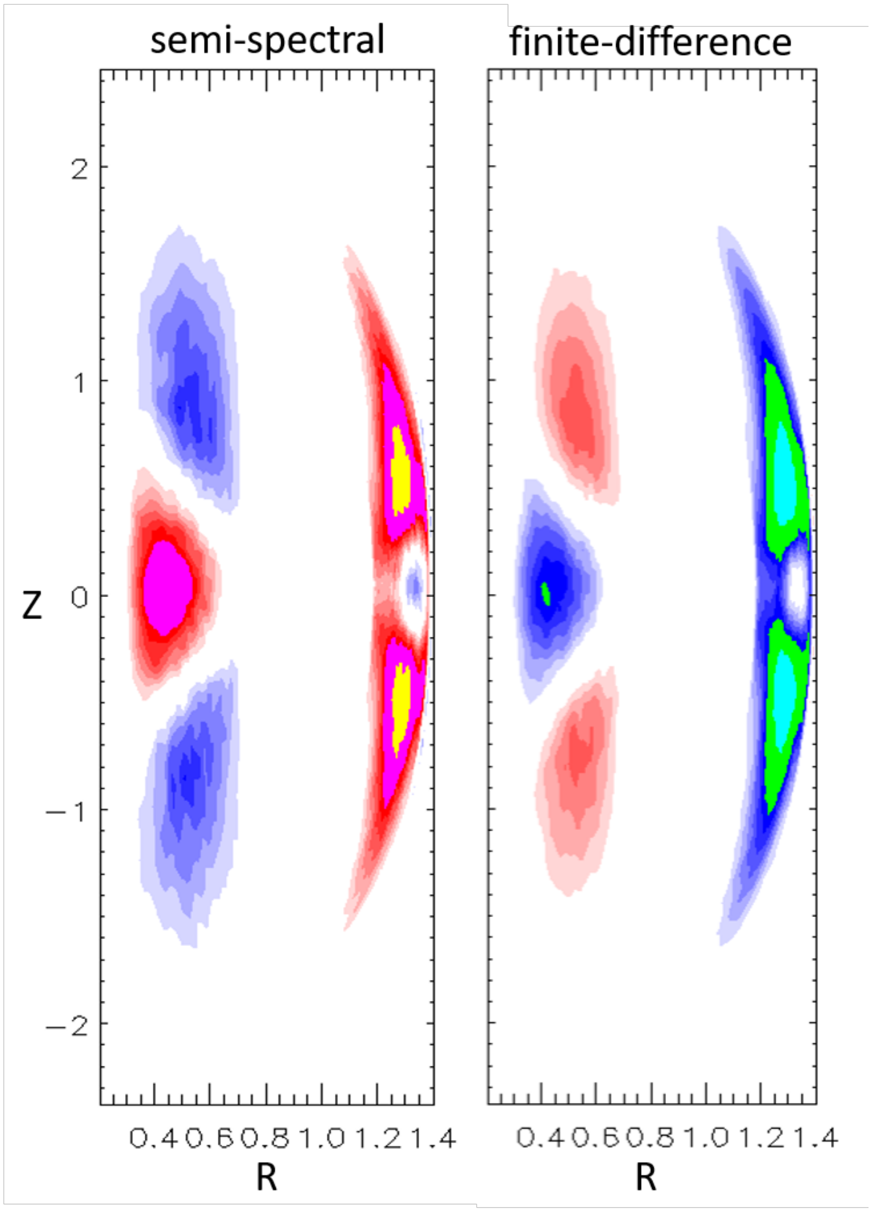

Figure 3.5: Poloidal mode structures from the semi-spectral (my implementation, left panel) and the finite-difference (original, right panel) methods.

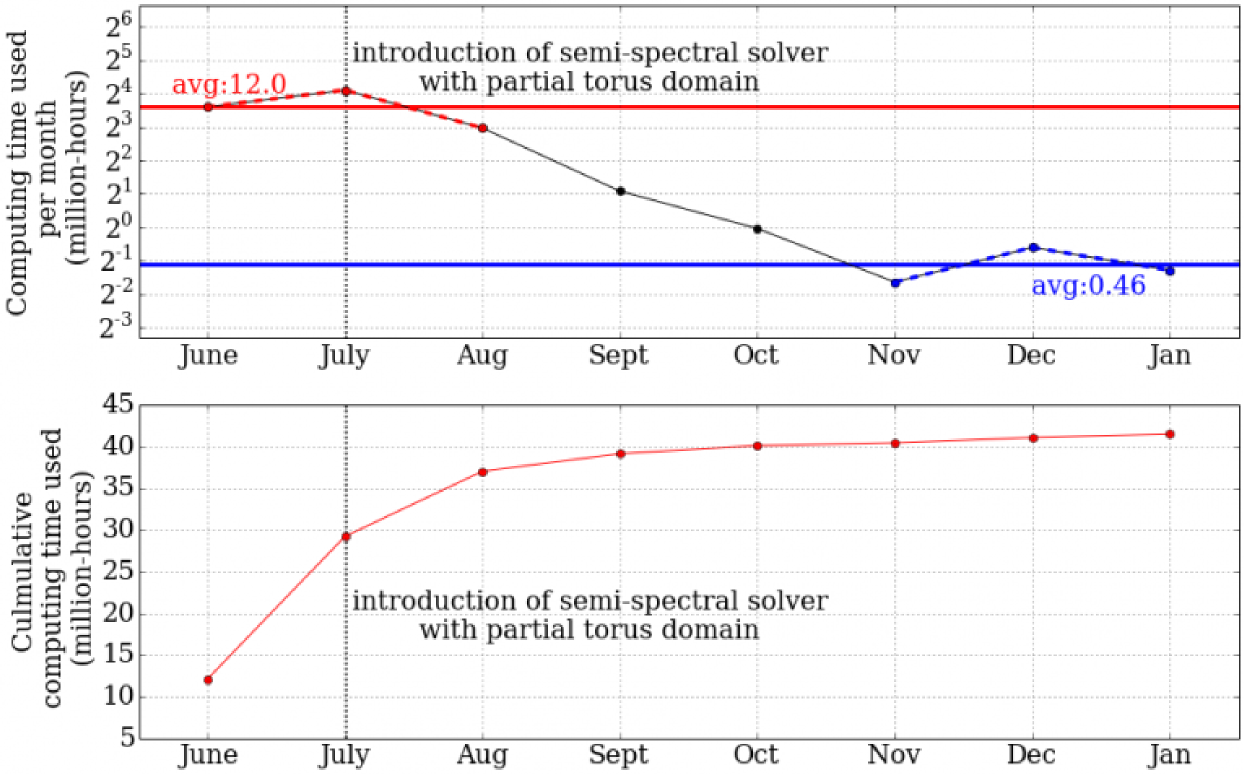

Figure 3.6: The amount of computing hours I personally used on the Oak Ridge Titan supercomputer in 2014.

Eventually, I took this a step further by localizing the simulations to a single drift-surface

$$\begin{aligned}\nabla_\perp^2 f &= g^{\psi\psi}\frac{\partial f}{\partial\psi} + g^{\zeta\zeta}\frac{\partial f}{\partial\zeta}\\ \rightarrow \nabla_\perp^2 f &= g^{\zeta\zeta}(-n^2\hat{f}_i)\end{aligned} \tag{3.5}$$

as explained in section 2.3, which further reduced the computational needs allowing for simulations over a wide range of parameters.

3.2.2 ANC semi-spectral solver

In ANC, the metric tensor is not calculated. Instead, the perpendicular Laplacian can be constructed from the equilibrium magnetic field unit vector through

$$\nabla_\perp^2 f = \nabla\cdot\left(\hat{b}_0\times\hat{b}_0\times\nabla f\right). \tag{3.6}$$

Using the identities

$$\begin{aligned}\nabla f &= \frac{\partial f}{\partial R}\hat{R} + \frac{\partial f}{\partial Z}\hat{Z} + \frac{1}{R}\frac{\partial f}{\partial\zeta}\hat{\zeta}\\ \nabla\cdot\vec{A} &= \frac{1}{R}\frac{\partial(RA_R)}{\partial R} + \frac{\partial(A_Z)}{\partial Z} + \frac{1}{R}\frac{\partial(A_\zeta)}{\partial\zeta}\\ \hat{b}_0 &= b_R\hat{R} + b_Z\hat{Z}\end{aligned} \tag{3.7}$$

the cross product of the magnetic field unit vector and the gradient is

$$\begin{aligned}\hat{b}_0 \times \hat{b}_0 \times \nabla f &= \hat{b}_0 \times \left(\left(b_Z \frac{1}{R} \frac{\partial f}{\partial \zeta} \right) \hat{R} + \left(-b_R \frac{1}{R} \frac{\partial f}{\partial \zeta} \right) \hat{Z} + \left(b_R \frac{\partial f}{\partial Z} - b_Z \frac{\partial f}{\partial R} \right) \hat{\zeta} \right) \\ &= b_Z \left(b_R \frac{\partial f}{\partial Z} - b_Z \frac{\partial f}{\partial R} \right) \hat{R} - b_R \left(b_R \frac{\partial f}{\partial Z} - b_Z \frac{\partial f}{\partial R} \right) \hat{Z} + \left(-\frac{b_R^2 + b_Z^2}{R} \frac{\partial f}{\partial \zeta} \right) \hat{\zeta}.\end{aligned} \tag{3.8}$$

The perpendicular Laplacian can then be re-written as

$$\begin{aligned}\nabla_\perp^2 f &= \nabla \cdot \left(\hat{b}_0 \times \hat{b}_0 \times \nabla f \right) \\ &= \frac{1}{R} \frac{\partial (R \left(b_Z b_R \frac{\partial f}{\partial Z} - b_Z^2 \frac{\partial f}{\partial R} \right))}{\partial R} - \frac{\partial \left(b_R^2 \frac{\partial f}{\partial Z} - b_R b_Z \frac{\partial f}{\partial R} \right)}{\partial Z} - \left(\frac{b_R^2 + b_Z^2}{R^2} \right) \frac{\partial^2 f}{\partial \zeta^2}.\end{aligned} \tag{3.9}$$

Discretization

This perpendicular Laplacian can then be discretized using the semi-spectral approach for the toroidal direction and central finite differencing for the $R - Z$ directions. The nine-element matrix associated with one grid-point is shown

$$\nabla_\perp^2 f_{i,j} = \begin{bmatrix} \frac{b_R b_Z}{2\Delta_R \Delta_Z} & \frac{b_Z^2}{2R\Delta_R} + \frac{b_Z^2}{\Delta_R^2} & -\frac{b_R b_Z}{2\Delta_R \Delta_Z} \\ \frac{b_R b_Z}{2R\Delta_Z} + \frac{b_R^2}{\Delta_Z^2} & -\frac{2b_R^2}{\Delta_R^2} - \frac{2b_Z^2}{\Delta_Z^2} - \frac{n^2}{R^2} & -\frac{b_R b_Z}{2R\Delta_Z} + \frac{b_R^2}{\Delta_Z^2} \\ -\frac{b_R b_Z}{2\Delta_R \Delta_Z} & -\frac{b_Z^2}{2R\Delta_R} + \frac{b_Z^2}{\Delta_R^2} & \frac{b_R b_Z}{2\Delta_R \Delta_Z} \end{bmatrix} f_{i,j} \tag{3.10}$$

with spectral component colored in red. For simulations with multiple toroidal modes, a Laplacian is constructed for each different n number. The center element of the matrix is the (i, j) component and the other eight are its neighbors $(\pm i, \pm j)$.

3.2.3 ANC field-aligned solver

In general, the Laplacian is

$$\nabla^2 f = \frac{1}{J}\frac{\partial}{\partial \xi^\alpha}\left(J \nabla \xi^\alpha \cdot \nabla \xi^\beta \frac{\partial f}{\partial \xi^\beta}\right) \tag{3.11}$$

where $\frac{1}{J} = \nabla\psi \times \nabla\zeta \cdot \nabla S$ is the Jacobian and the independent variables are $\xi = \{\psi, S, \zeta\}$. In the field-aligned version of ANC (detailed in section 3.4), instead of the perpendicular Laplacian which is the physically correct form with respect to gyrokinetics, the full Laplacian is used due to ease of implementation and numerical stability. Using the full Laplacian has the benefit of decreasing high-$k_\parallel$ components of the electrostatic potential. This can be seen by a quick check in k-space

$$\begin{aligned} -\nabla^2\phi &= \delta n \\ \rightarrow (k_\psi^2 + k_\parallel^2 + k_\zeta^2)\hat{\phi} &= \delta\hat{n} \\ \rightarrow \hat{\phi} &= \frac{\delta\hat{n}}{k_\psi^2 + k_\parallel^2 + k_\zeta^2} \end{aligned} \tag{3.12}$$

where, of course, if $k_\parallel$ is larger, then ϕ will decrease. In the field-aligned version of ANC, the independent variables have different definitions in the core, $(\psi, S, \zeta) \rightarrow$

$(\psi(R,Z), S(\psi(R,Z), \theta_{geo}(R,Z)), \zeta)$, and SOL, $(\psi, S, \zeta) \rightarrow (\psi(R,Z), S(\psi(R,Z), Z), \zeta)$ which means that the Laplacian is constructed separately for the two regions.

Using the independent variables, (ψ, S, ζ), in Eq. (3.11),

$$\begin{aligned}
\nabla^2 f = {} & g^{\psi\psi}\frac{\partial^2 f}{\partial \psi^2} + 2g^{\psi S}\frac{\partial^2 f}{\partial \psi \partial S} + g^{SS}\frac{\partial^2 f}{\partial S^2} + g^{\zeta\zeta}\frac{\partial^2 f}{\partial \zeta^2} \\
& + \frac{1}{J}\left[\frac{\partial\left(Jg^{\psi\psi}\right)}{\partial \psi} + \frac{\partial\left(Jg^{\psi S}\right)}{\partial S}\right]\frac{\partial f}{\partial \psi} + \frac{1}{J}\left[\frac{\partial\left(Jg^{\psi S}\right)}{\partial \psi} + \frac{\partial\left(Jg^{SS}\right)}{\partial S}\right]\frac{\partial f}{\partial S} \\
& \rightarrow g^{\psi\psi}\frac{\partial^2 f}{\partial \psi^2} + 2g^{\psi S}\frac{\partial^2 f}{\partial \psi \partial S} + g^{SS}\frac{\partial^2 f}{\partial S^2} + g^{\zeta\zeta}\frac{\partial^2 f}{\partial \zeta^2}
\end{aligned} \tag{3.13}$$

where the term in the blue is neglected in the code due to smallness. In the case of the separatrix line, the Laplacian is actually reduced to just

$$\nabla^2 f \rightarrow g^{\psi\psi}\frac{\partial^2 f}{\partial \psi^2} + g^{\zeta\zeta}\frac{\partial^2 f}{\partial \zeta^2} \tag{3.14}$$

because the mesh is constructed to include the perpendicular neighbors of the separatrix points so that discretization of the derivatives leaves the terms related to the parallel direction to become zero. This mesh generation is described in section 3.4.

Metric tensor elements

Unlike the original version of ANC, in the field-aligned version in ANC, the metric tensor elements must be calculated, but it turns out to be relatively simple in terms of implementation. For the SOL with independent variables $(\psi, S, \zeta) \rightarrow (\psi(R,Z), S(\psi(R,Z),Z), \zeta)$, the metric tensor elements are

$$
\begin{aligned}
g^{\psi\psi} &= \nabla\psi\cdot\nabla\psi = & \left(\frac{\partial\psi}{\partial R}\right)^2 + \left(\frac{\partial\psi}{\partial Z}\right)^2 \\
g^{SS} &= \nabla S\cdot\nabla S = & \left(\frac{\partial S}{\partial\psi}\frac{\partial\psi}{\partial R}\right)^2 + \left(\frac{\partial S}{\partial\psi}\frac{\partial\psi}{\partial Z} + \frac{\partial S}{\partial Z}\right)^2 \\
g^{\psi S} &= \nabla\psi\cdot\nabla S = & \frac{\partial S}{\partial\psi}\left[\left(\frac{\partial\psi}{\partial R}\right)^2 + \left(\frac{\partial\psi}{\partial Z}\right)^2\right] + \frac{\partial\psi}{\partial Z}\frac{\partial S}{\partial Z} \\
g^{\zeta\zeta} &= \nabla\zeta\cdot\nabla\zeta = & \frac{1}{R^2}.
\end{aligned}
\tag{3.15}
$$

For the core with independent variables $(\psi, S, \zeta) \rightarrow (\psi(R,Z), S(\psi(R,Z), \theta_{geo}(R,Z)), \zeta)$, the metric tensor elements are

$$
\begin{aligned}
g^{\psi\psi} &= \nabla\psi\cdot\nabla\psi = & \left(\frac{\partial\psi}{\partial R}\right)^2 + \left(\frac{\partial\psi}{\partial Z}\right)^2 \\
g^{SS} &= \nabla S\cdot\nabla S = & \left(\frac{\partial S}{\partial\psi}\frac{\partial\psi}{\partial R} + \frac{\partial S}{\partial\theta}\frac{\partial\theta}{\partial R}\right)^2 + \left(\frac{\partial S}{\partial\psi}\frac{\partial\psi}{\partial Z} + \frac{\partial S}{\partial\theta}\frac{\partial\theta}{\partial Z}\right)^2 \\
g^{\psi S} &= \nabla\psi\cdot\nabla S = & \frac{\partial S}{\partial\psi}\left[\left(\frac{\partial\psi}{\partial R}\right)^2 + \left(\frac{\partial\psi}{\partial Z}\right)^2\right] + \frac{\partial S}{\partial\theta}\left[\frac{\partial\psi}{\partial R}\frac{\partial\theta}{\partial R} + \frac{\partial\psi}{\partial Z}\frac{\partial\theta}{\partial R}\right] \\
g^{\zeta\zeta} &= \nabla\zeta\cdot\nabla\zeta = & \frac{1}{R^2}
\end{aligned}
\tag{3.16}
$$

where, of course, the differences between the core and SOL metric tensor elements are related to the parallel direction (S).

Jacobian

As mentioned, the Jacobian is $J = (\nabla\psi \times \nabla\zeta \cdot \nabla S)^{-1}$. For the SOL,

$$J = (\nabla\psi \times \nabla\zeta \cdot \nabla S)^{-1} = \left(-\frac{1}{R}\frac{\partial\psi}{\partial R}\frac{\partial S}{\partial Z}\right)^{-1} \tag{3.17}$$

and, for the core,

$$J = (\nabla\psi \times \nabla\zeta \cdot \nabla S)^{-1} = \left(-\frac{1}{\rho^2}\frac{\partial S}{\partial\theta}\left(\frac{Z}{R}\frac{\partial\psi}{\partial Z} + \frac{\partial\psi}{\partial R}\right)\right)^{-1} \tag{3.18}$$

where R_0 is the distance from the machine axis to the null-point and $\rho = \sqrt{(R-R_0)^2 + Z^2}$ is the radial distance from the null-point. It is also important to note that the Jacobian in the SOL does not go to infinity in the case of $R \rightarrow 0$ because $\frac{\partial\psi}{\partial R}|_{R=0} \propto aR$ which cancels out the R in the denominator. In the core, the Jacobian also does not go to infinity at the machine axis because $\frac{\partial\psi}{\partial Z}|_{R=0} = 0$ which zeroes out the term as well.

Discretization

The partial derivatives in Eq. (3.13), Eq. (3.15), and Eq. (3.16) are calculated through a mixture of analytic calculation, splines, finite difference.

$\theta(R,Z)$ is just the geometric angle about the null-point, and its value and derivatives can be calculated analytically. This is simply

$$
\begin{aligned}
\theta(R,Z) &= 2\arctan\left(\frac{Z}{\rho+(R-R_0)}\right) \\
\frac{\partial\theta(R,Z)}{\partial R} &= -Z/\rho^2 \\
\frac{\partial\theta(R,Z)}{\partial Z} &= R/\rho^2
\end{aligned}
\tag{3.19}
$$

where R_0 is the distance from the machine axis to the null-point and $\rho = \sqrt{(R-R_0)^2+Z^2}$ is the radial distance from the null-point.

Next, the poloidal flux function and arc-length functions are numerically represented by splines. The partial derivatives of ψ or S are then essentially just shifts of the coefficients (along with additional factors due to derivatives).

Finally, the perturbed field quantity, f, is numerically represented by values on the grid points. The partial derivatives of f are calculated by using central finite differencing.

In the end, the discretized Laplacian for an individual grid point (i,j) comes out to be

$$\nabla_\perp^2 \hat{f}_{i,j} = \begin{bmatrix} M_{1,3} & M_{2,3} & M_{3,3} \\ M_{1,2} & M_{2,2} & M_{3,2} \\ M_{1,1} & M_{2,1} & M_{3,1} \end{bmatrix} \hat{f}_{i,j}$$

$$\begin{aligned}
M_{1,3} &= -D(\Theta_{y,2}\Theta_{x,1}) \\
M_{2,3} &= D(\Theta_{x,1}\Delta_y) + B(2\Theta_{x,1}/x_1) + F(\Theta_{x,1}) \\
M_{3,3} &= D(\Theta_{y,1}\Theta_{x,1}) \\
M_{1,2} &= -D(\Theta_{y,2}\Delta_x) + A(2\Theta_{y,2}/y_2) - E(\Theta_{y,2}) \\
M_{2,2} &= -A(2/(y_1 y_2)) - B(2/(x_1 x_2)) + D(\Delta_x\Delta_y) + E(\Delta_y) + F(\Delta_x) - C(n^2) \\
M_{3,2} &= D(\Theta_{y,1}\Delta_x) + A(2\Theta_{y,1}/y_1) + E(\Theta_{y,1}) \\
M_{1,1} &= D(\Theta_{y,2}\Theta_{x,2}) \\
M_{2,1} &= -D(\Theta_{x,2}\Delta_y) + B(2\Theta_{x,2}/x_2) - F(\Theta_{x,2}) \\
M_{3,1} &= -D(\Theta_{y,1}\Theta_{x,2})
\end{aligned} \tag{3.20}$$

where the neglected terms are in blue and the spectral component in red. For the central point (2,2)=(i,j), the first term is related to the partial derivative in ψ, the second term is related to the partial derivative in S, and the third term is the mixed term with both ψ and S. The short-hands used above are defined as

$$\begin{aligned}
A \equiv& g^{\psi\psi}_{i,j} & B \equiv& g^{SS}_{i,j} \\
C \equiv& g^{\zeta\zeta}_{i,j} & D \equiv& 2g^{\psi S}_{i,j} \\
E \equiv& \frac{1}{J}\left[\frac{\partial\left(Jg^{\psi\psi}\right)}{\partial\psi}+\frac{\partial\left(Jg^{\psi S}\right)}{\partial S}\right]\rightarrow 0 & F \equiv& \frac{1}{J}\left[\frac{\partial\left(Jg^{\psi S}\right)}{\partial\psi}+\frac{\partial\left(Jg^{SS}\right)}{\partial S}\right]\rightarrow 0 \\
x_1 \equiv& S_{i,j}-S_{i,j-1} & y_1 \equiv& \psi_{i,j}-\psi_{i-1,j} \\
x_2 \equiv& S_{i,j+1}-S_{i,j} & y_2 \equiv& \psi_{i+1,j}-\psi_{i,j} \\
\Delta_x \equiv& \frac{x_2-x_1}{x_1x_2} & \Delta_y \equiv& \frac{y_2-y_1}{y_1y_2} \\
\Theta_{x,1} \equiv& \frac{x_1}{x_2(x_1+x_2)} & \Theta_{y,1} \equiv& \frac{y_1}{y_2(y_1+y_2)} \\
\Theta_{x,2} \equiv& \frac{x_2}{x_1(x_1+x_2)} & \Theta_{y,2} \equiv& \frac{y_2}{y_1(y_1+y_2)}
\end{aligned} \tag{3.21}$$

where the indices (i,j) correspond to the grid points belonging to (ψ, S).

3.3 Self-consistent benchmarks

The different subroutines of ANC have been independently verified, but before production simulations were initiated, self-consistent tests were performed to validate ANC against theory. To do this, I implemented an antenna into ANC, essentially to input a specified external potential, $\phi_{ext} = \hat{\phi}_A cos(\omega_A t)$, to drive waves expected to exist. A sample antenna mode structure is shown in Fig. 3.7.

When the antenna frequency and antenna mode structure match an eigenfrequency and eigenmode of the plasma, there will be a linear growth of the mode. When the antenna

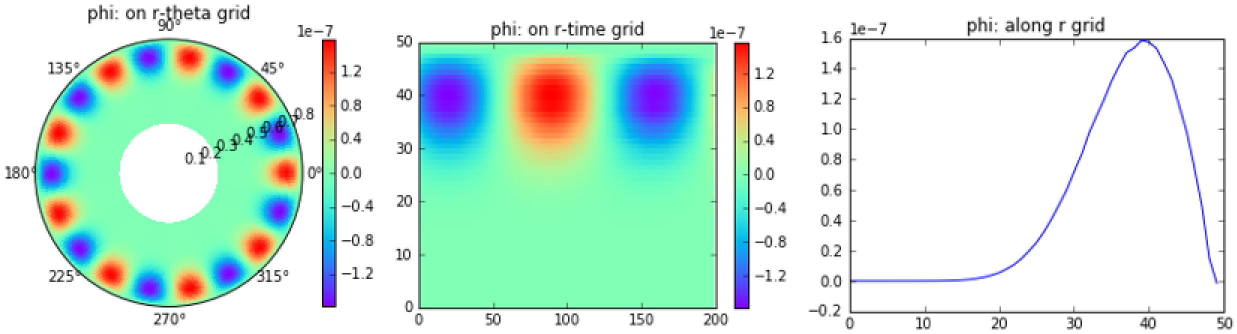

Figure 3.7: The antenna potential structure for the benchmarks is shown in three ways.

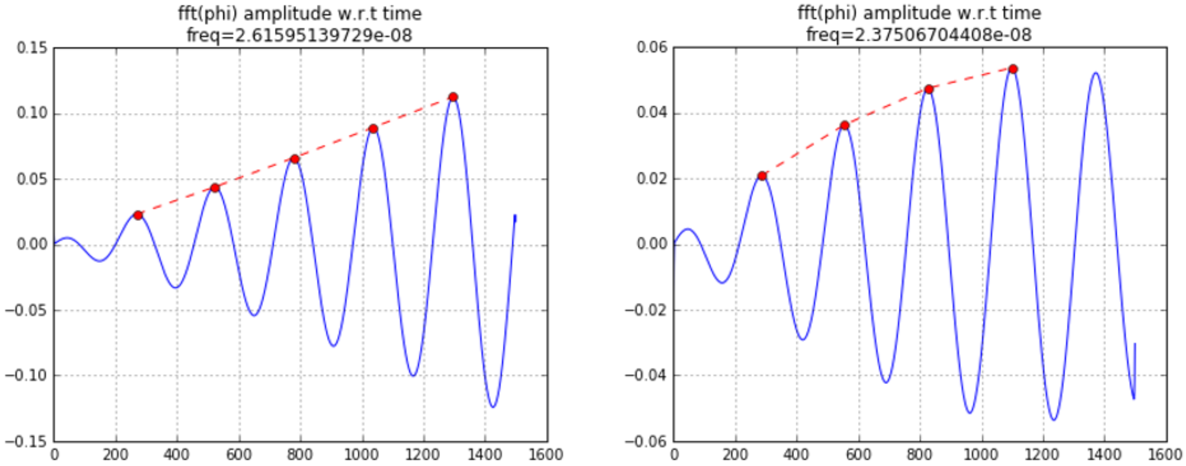

Figure 3.8: When the antenna frequency is resonant with a physical mode, the growth is linear and the maximum amplitude of potential is higher (left); when it is away from the resonant frequency, the growth is weaker and the maximum amplitude of potential is lower (right).

frequency is close to the eigenfrequency but not close enough, the growth eventually stops and a beating pattern becomes evident. The two examples of resonant and slightly-off resonant antenna frequencies are shown in Fig. 3.8. In Fig. 3.12, the maximum amplitudes excited are plotted to show a resonance peak.

Using a combination of antenna-driven waves and initialized modes, I compare dispersion from theory and from ANC simulations in both simple uniform magnetic geometry and the

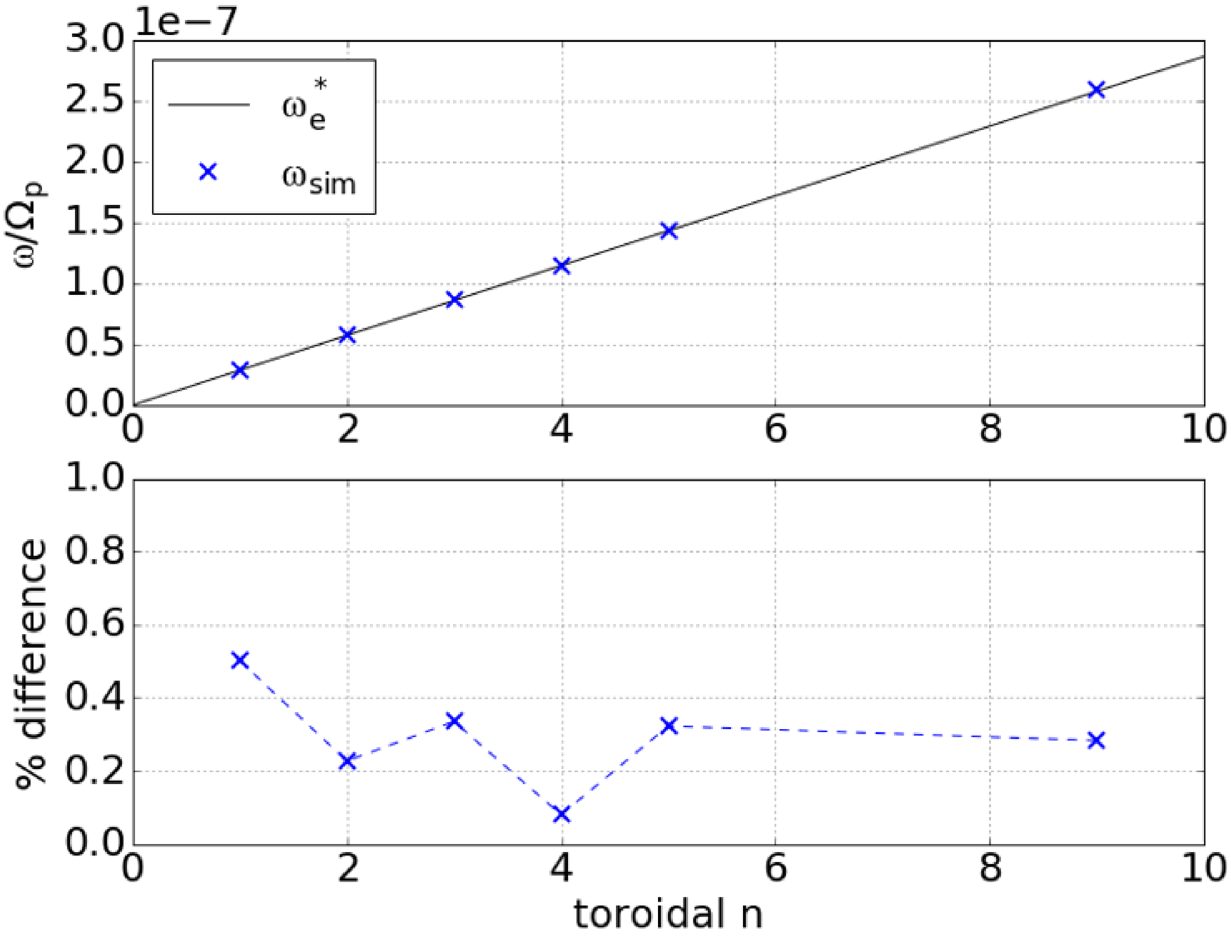

Figure 3.9: The frequency measured from simulation is plotted against the simple theory of drift-wave dispersion.

more complicated FRC geometry (although localized to be able to compare to simple theory, details in corresponding subsection).

3.3.1 Uniform straight magnetic field

In a uniform straight magnetic field ($\vec{B} = B_0\hat{z}$), it is easy to design an equilibrium profile to drive a very simple drift-wave dispersion. As shown in section A, if the wave is purely perpendicular with only a density gradient, the dispersion relation is $\omega \approx \omega_{*,e}$ from Eq. (A.4). As seen in Fig. 3.9, ANC simulations are extremely close to the theoretical dispersion.

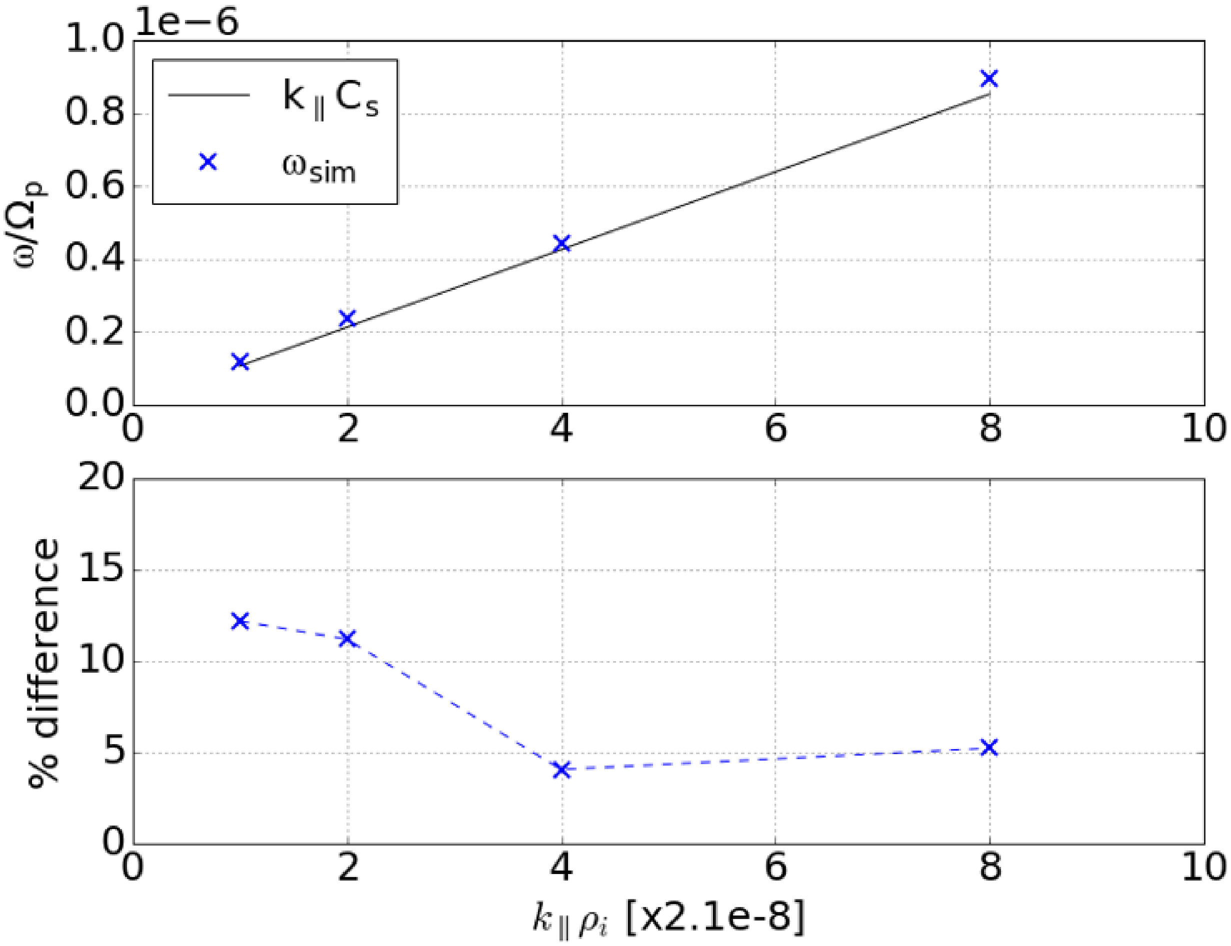

Figure 3.10: The frequency measured from simulation is plotted against the simple theory of ion-acoustic wave dispersion.

Another wave that can exist in the simple straight magnetic field geometry is the ion-acoustic wave which can be designed to be simply $\omega_{iaw} \approx k_{\|}C_s$ where $C_s = \sqrt{T_e/m_i}$. As seen in Fig. 3.10, ANC simulations are again in agreement with the theoretical dispersion.

3.3.2 Realistic magnetic field geometry

In the more complex FRC magnetic geometry, a simple theoretical dispersion cannot be as easily derived due to the curvature of the field-lines as well as the magnetic field gradient. However, a quick way to use the magnetic field geometry of the FRC while retaining the ease of simple theoretical models is to localize the simulation domain to a very small section of the FRC geometry which allows the curvature effects to be negligible and to minimize the ∇B effects. This localization is shown in Fig. 3.11.

As in the simple geometry benchmarks, there is only an equilibrium density gradient, and the expected frequency should match the simple drift-wave. In Fig. 3.12, the maximum amplitude of the electrostatic potential is plotted for different antenna frequencies used to excite the mode, and a resonance peak is traced out. The resonant frequency is found to be around $\omega_{res} \approx 0.86\omega_{*,e}$, with the 14% discrepancy likely due to the ∇B effects which oppose the diamagnetic drift and cannot be removed without reducing the equilibrium to the simple geometry case.

3.4 Field-aligned mesh

A recent feature of ANC is the field-aligned mesh. The original cylindrical regular mesh that ANC is built on is prone to aliasing effects. Most tokamak simulations, including GTC, employ a field-aligned mesh based on magnetic coordinates. A field-aligned mesh has good numerical properties due to the coarse resolution in the parallel direction which suppresses high-$k_{\|}$ noise. The good numerical properties stem from the accumulation of density onto a field-aligned mesh which effectively is equivalent to elongation of particle shape in the parallel direction, similar to past simulations with simpler geometry. In order to have cross-separatrix simulations with multiple toroidal modes, this feature is essential.

3.4.1 Field-aligned gather-scatter

This field-aligned feature of ANC was only possible after the brilliant insight by Dr. J. Bao in the method of gather-scatter in a field-aligned mesh within a cylindrical coordinate

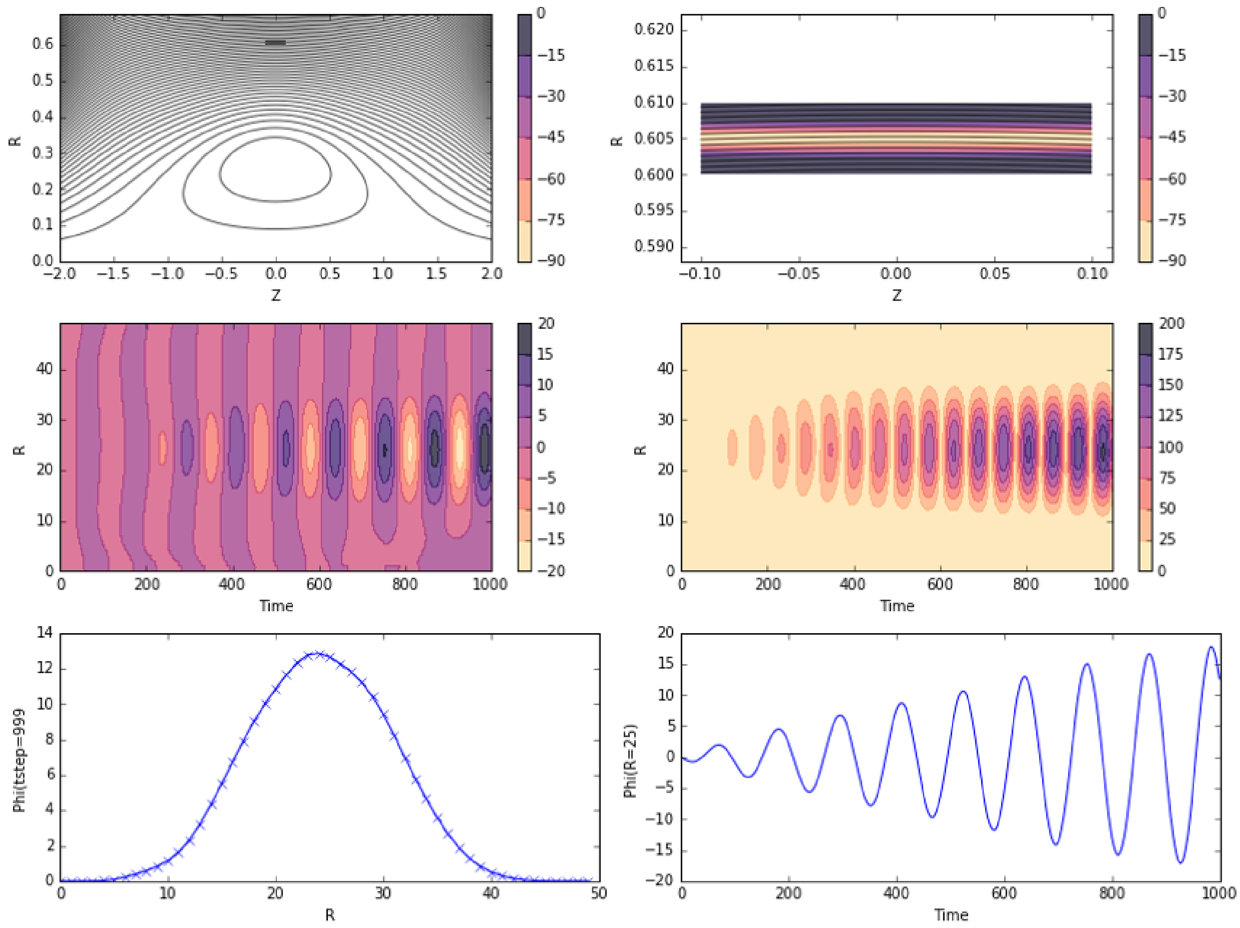

Figure 3.11: A drift-wave is excited by an antenna in a localized region (the tiny black rectangular region) of the FRC (top-left). The actual simulation domain is shown (top-right). The radial-time plots of the real and imaginary components of the potential is shown (mid-left and mid-right). The radial structure of the potential is shown (bottom-left) and the time history of the potential along the central radial line is shown (bottom-right).

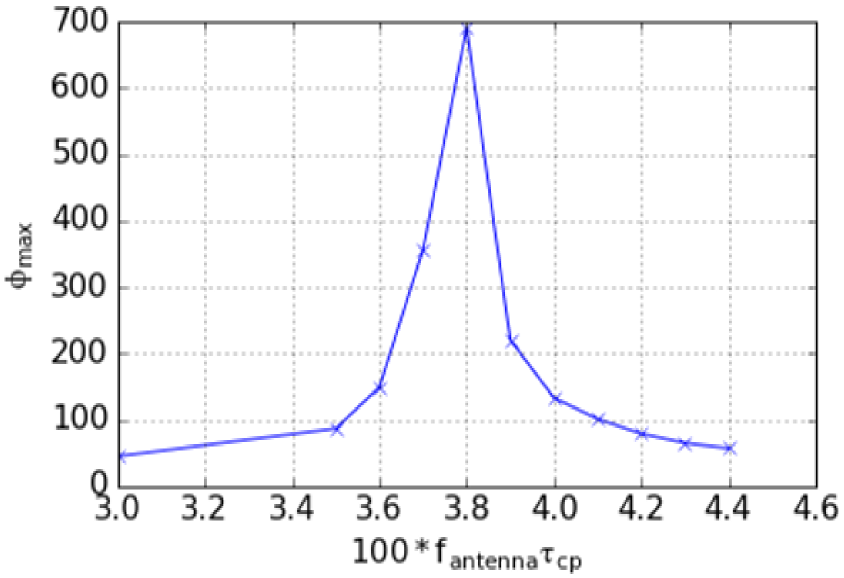

Figure 3.12: Frequency measured from simulation trace out a resonance peak around the theoretical eigenfrequency.

system, which has now been implemented in GTC. Fundamentally, the gather-scatter should occur for some coordinate system of (ψ, S, ζ); unfortunately, the arc-length, S (the parallel direction), is not well-defined, especially between the two different regions of the core and SOL.

Bao's insight was in the creation of two separate splines for the arc-lengths of the two separate regions of the core and SOL which depend on two separate sets of independent coordinates, ie. $S_{core} = S_{core}\left(\psi(R,Z), \theta_{geo}(R,Z)\right)$ and $S_{SOL} = S_{SOL}\left(\psi(R,Z), Z\right)$. The gather-scatter process was then just a simple matter of (1) finding $\psi(R,Z)$ and determining which region the particle was in, (2) finding the geometric angle about the null-point, $\theta_{geo}(R,Z)$, or the axial position, Z, (3) calculating the arc-length, S, from these variables and the corresponding spline, and finally, (4) interpolating the weight contributed to each grid point based on a simple area weighting scheme in (ψ, S). A part of the process is shown in Fig. 3.13 where the bottom right is the mesh in (ψ, S) and the bottom left is the mesh in (R, Z).

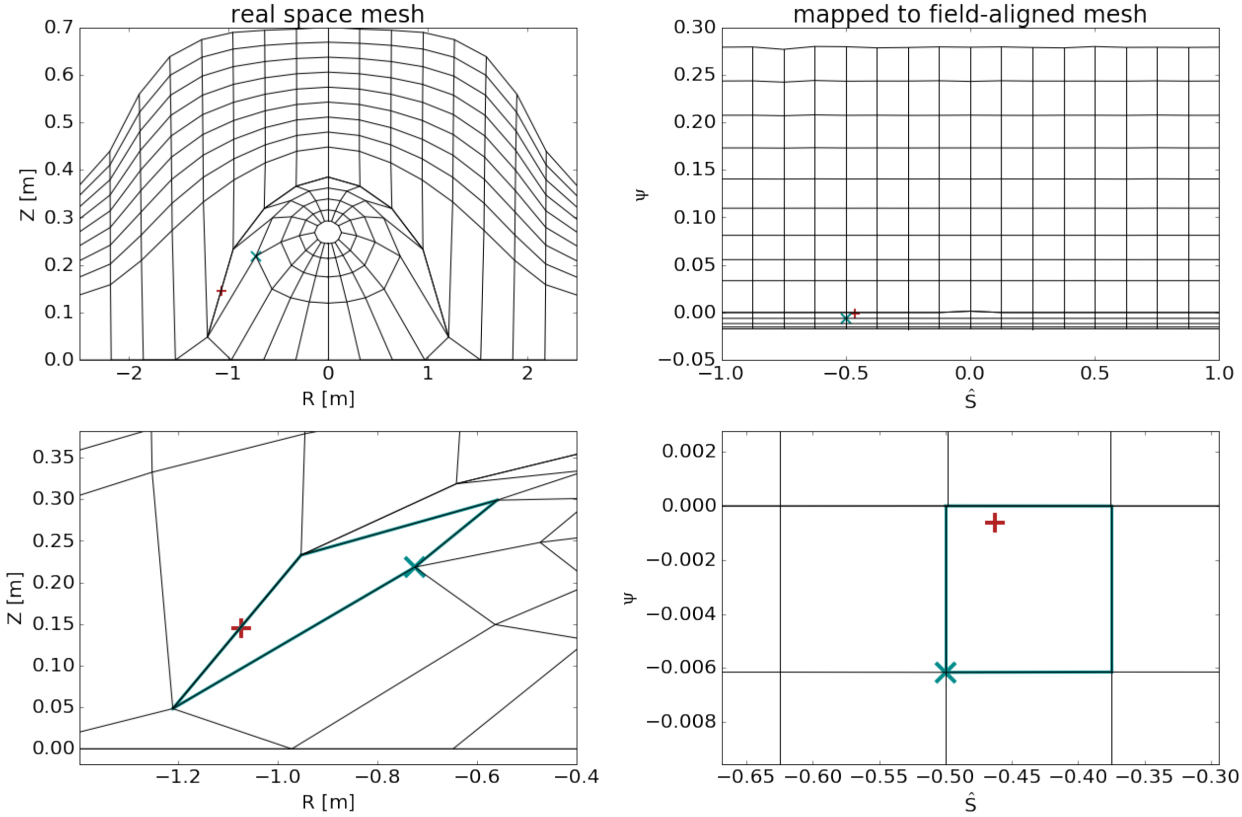

Figure 3.13: A particle is shown as the red + in the (R, Z) grid and its corresponding location in the (ψ, S) grid. The blue x represents the nearest bottom-left grid-point in the (ψ, S) mesh.

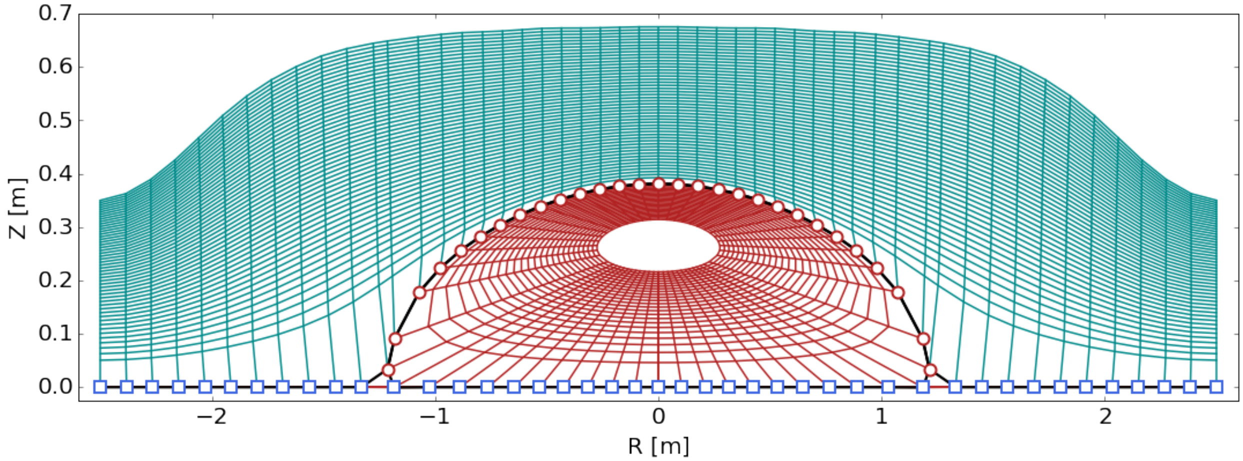

Figure 3.14: The field-aligned mesh is shown with the separatrix points marked as red circles and the axis points marked as blue squares.

3.4.2 Mesh generation

Once the gather-scatter process was realized by Bao, I was able to employ techniques to generate a field-aligned mesh from my previous experience in attempting to create a two-mesh system. First, the mesh is generated in the core using constant θ_{geo}-lines. The θ_{geo} used are based on uniform spacing in arc-length, S, with respect to the outer most closed field-line. Next, the points that lie on the separatrix and axis are then identified. Finally, the mesh is generated in the SOL using the spacing based on the separatrix such that there is a one-to-one relation between the SOL and core mesh on the separatrix points. A sample of this mesh is shown in Fig. 3.14.

One important part of the mesh generation is identifying the separatrix points and perpendicular neighboring points in the ψ-lines above and below. To find the neighboring points, ANC calculates along the line perpendicular to the local magnetic field direction until it hits one of the ψ-lines. A sample of the separatrix points and their neighboring points are shown in Fig. 3.15. These neighboring points are used for calculation in gradients of fields and also in the Poisson equation as mentioned in section 3.2. By using the local

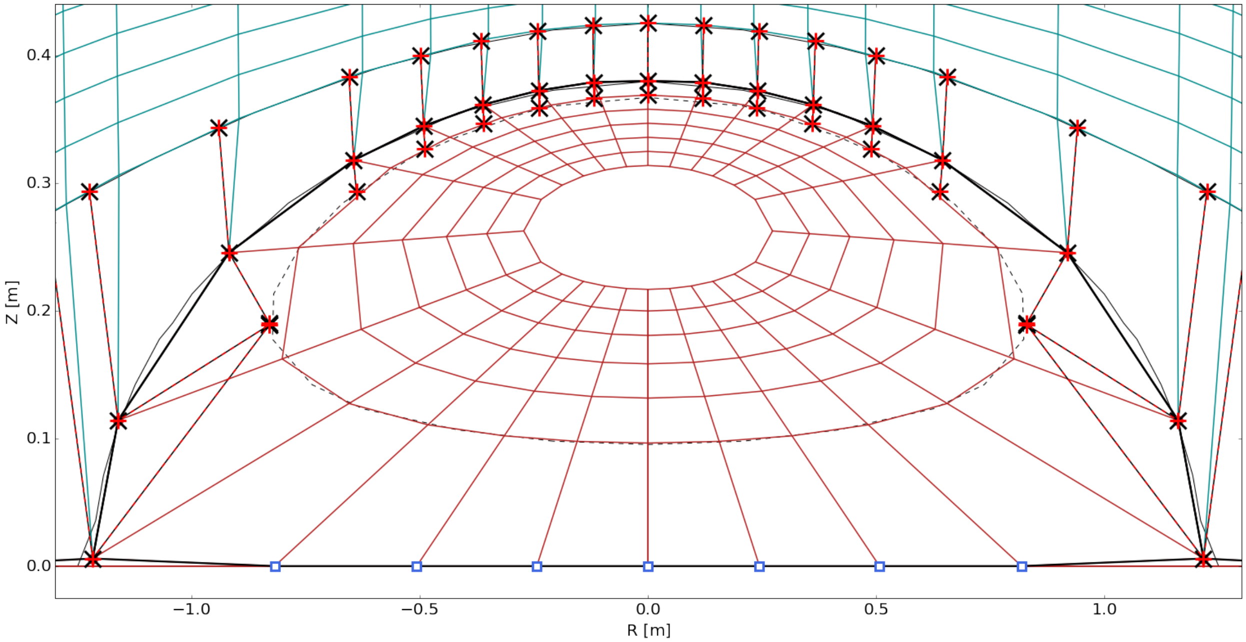

Figure 3.15: The separatrix points and their respective neighbors in $\pm\Delta\psi$.

magnetic field to find the neighboring points, this means that the neighboring points are exactly perpendicular and so the components related to S drop out (because there is no change in S!).

3.4.3 Self-consistent simulation test

The major differences between the field-aligned version and the non-field-aligned version are in the gather/scatter operations and the Poisson solver. These individual components of the field-aligned version of ANC has been tested separately, and benchmarks for the Poisson solver, the particle gather/scatter operations, and the particle trajectories are shown in the appendix section B.

A self-consistent test of the field-aligned version of ANC has been run and benchmarked against the non-field-aligned version of ANC (which itself has been validated against analytic theory of drift-waves and ion-acoustic waves as seen in section 3.3). This test simulates

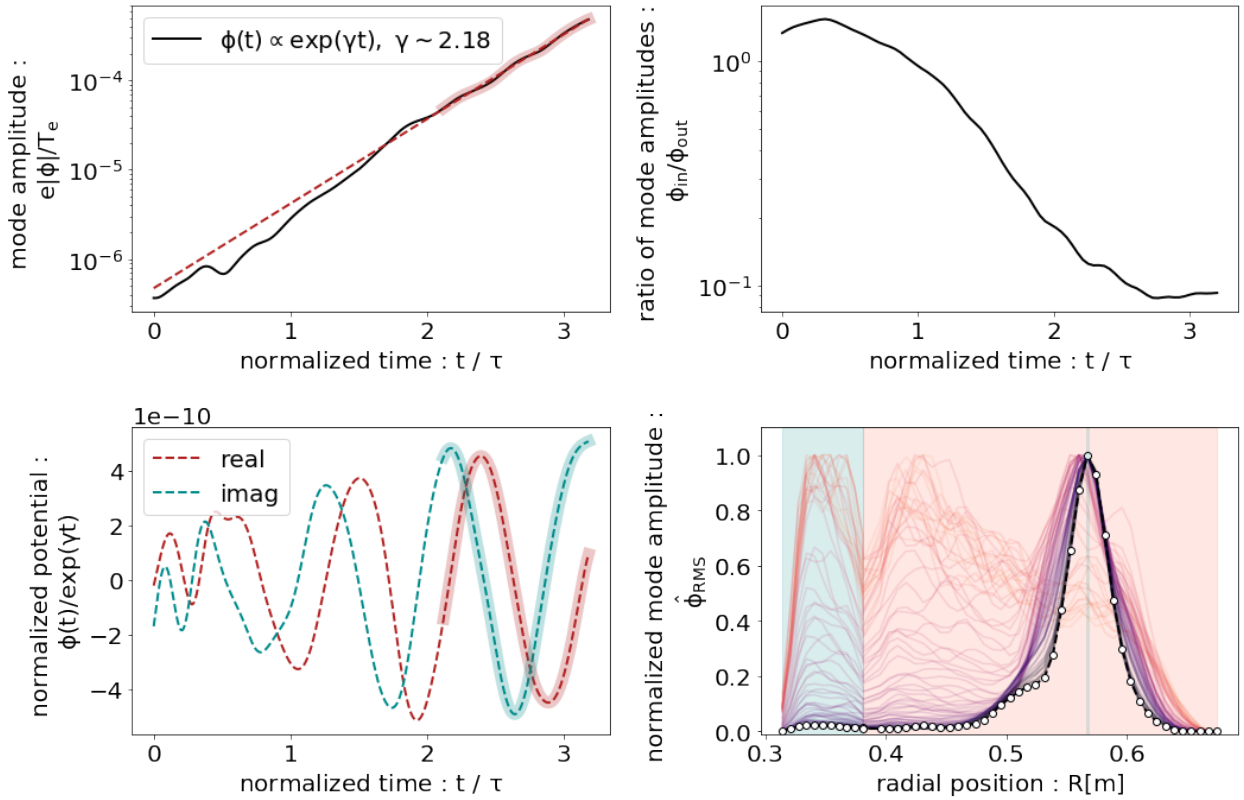

Figure 3.16: Time histories and radial profiles of the self-consistent test of the field-aligned ANC simulation of $n = 50$. Top left shows the magnitude of the potential in a semi-log plot. Bottom left shows the potential with the exponentially growing component removed. Top right shows the ratio of the mode amplitude inside to the outside of the separatrix. Bottom right shows the field-line averaged radial profile of the potential, with the blue (red) region denoting the inside (outside) region where the ratio of the top right plot is calculated from.

the $n = 50$ mode in the equilibrium used in chapter 5 and 6. In the figures, the unit of normalization for time is $T = (V_{th,i}/L)^{-1}$, same as in chapters 5 and 6.

An instability is found with frequency and growth-rate consistent with what has been simulated with the non-field-aligned version and with what has been analytically calculated for comparison (as later shown in Fig. 5.3). The time-history is shown in Fig. 3.16.

The mode structures of the field-aligned version are also seen to match the mode structures found with the non-field-aligned verison of ANC as seen in Fig. 3.17, ie. symmetric about the $Z = 0$ line and peak in the $R \sim 0.55$m region. The radial-time plot also shows outward

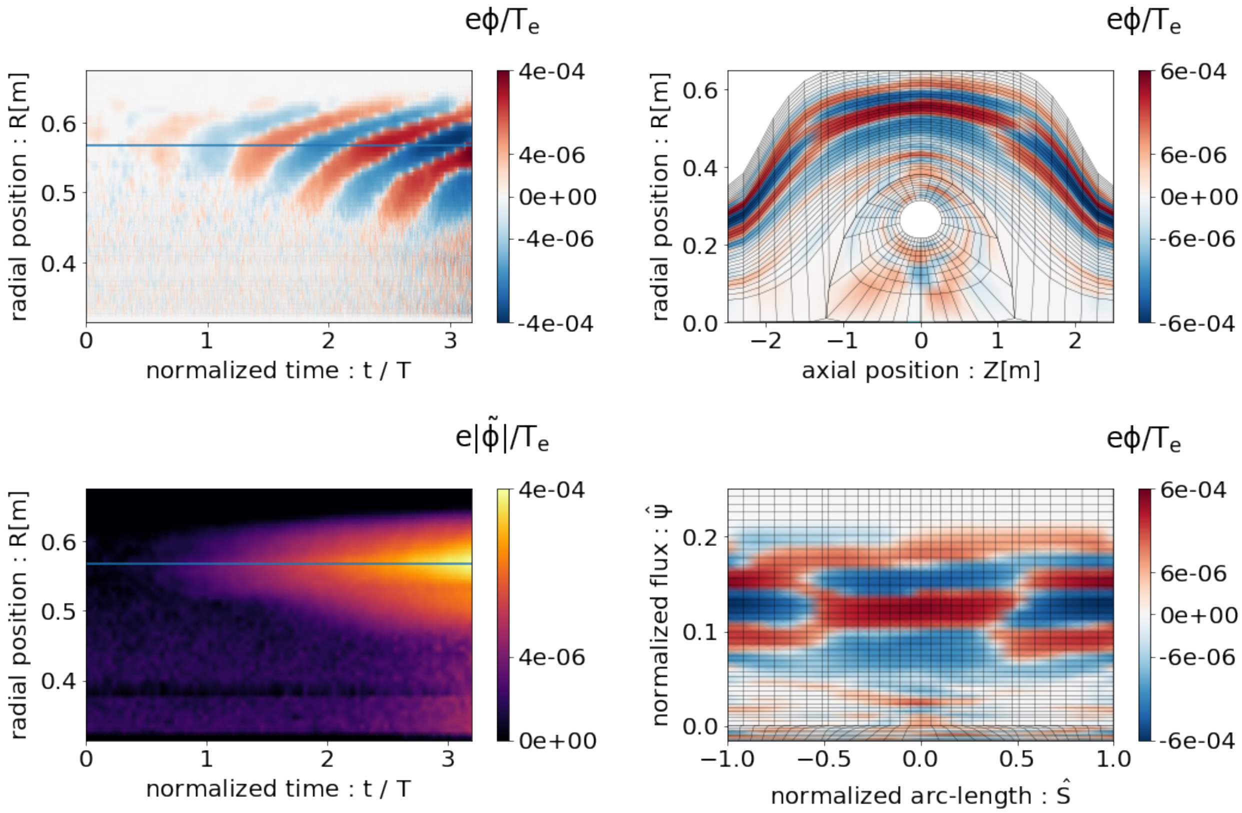

Figure 3.17: Plots of the mode structure along the outer midplane in the self-consistent test of the field-aligned ANC simulation of $n = 50$. Top left panel shows the real component of the spectrally decomposed (in the toroidal direction) potential along the outer midplane over time. Bottom left panel shows the field-line averaged magnitude of the potential along the outer midplane over time. Top right panel shows the potential in the $R - Z$ plane. Bottom right panel shows the potential in the field-aligned $\psi - S$ plane.

phase-velocity and widening of the radial profile over time, again consistent with the non-field aligned version of ANC (which can be seen in chapter 5). The mode structure is shown in both real space and in the field-aligned computational space in the figure.

Since the field-aligned version does not modify the particle dynamics within ANC, as expected from previous tests of ANC, particles in the simulation still show conservation of energy and canonical momentum as seen in Fig. 3.18.

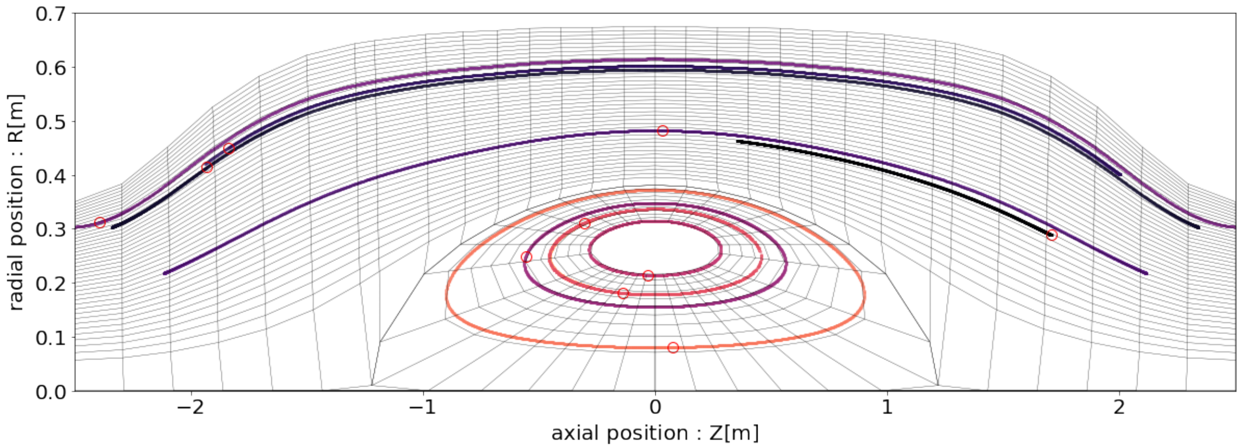

Figure 3.18: Some particle trajectories in the self-consistent test of the field-aligned ANC simulation of $n = 50$. Canonical momentum is well conserved (particles stay on their field-lines).

3.5 Summary

Because of the differences between the FRC and tokamak geometry, major modifications and feature developments were necessary for studying FRC turbulence. A lot of early development work was done by Dr. D. Fulton and Dr. I. Holod with continuing development by Dr. D. Fulton, Dr. J. Bao, and myself; in this chapter, I have focused on the more important features I have contributed the most to. My early computational work on GTC led to the ability to scan a wide range of parameters to understand local drift stabilities of the FRC. My later computational work on ANC has led to a production-ready code with the ability to simulate non-local FRC turbulence. With these tools, we have been able to investigate FRC physics as will be discussed in chapters 4 (using GTC), 5 (using ANC), and 6 (using ANC).

Chapter 4

Local drift-wave stability in the field-reversed configuration

Density fluctuation measurements by Lothar Schmitz *et al*. at the beam-driven FRC C-2 experiment at TAE[60], the density fluctuation spectra in the SOL and core were shown to be very different. The amplitudes of the SOL fluctuations follow an exponentially decreasing trend with the large amplitudes in the ion-scales. The amplitudes of the core fluctuations are weaker overall than in the SOL with the peak somewhere in the range of electron-scales. As mentioned in chapter 1, the first step of understanding microturbulence and transport is to identify the micro-instabilities which may be the cause of fluctuations, and that is the aim of this chapter, in which I use GTC to perform local linear simulations in the core and SOL separately to identify possible instabilities inherent to the different regions.

In these local linear simulations of the FRC SOL, which has mirror-like and slab-like geometry, the collisionless electrostatic drift-wave in the ion-to-electron-scale is destabilized by the electron temperature gradient due to resonance with locally barely trapped electrons. Collisions suppress this instability, but a collisional drift-wave instability can still exist at realistic pressure gradients. On the other hand, these local linear simulations (covering wavelengths up to $k_\zeta \rho_e < 0.3$) shows that drift-waves in the FRC core are robustly stable.

As mentioned in section 2.1, FRC geometry, unlike tokamak geometry, has no toroidal coupling which destabilizes the tokamak drift-waves[14, 13, 17] because the FRC lacks toroidal fields and magnetic shear. Our study in simulations of limiting cases of FRC show this stability to be due to the features of the FRC core: (1) the field-lines of the ideal FRC core geometry are not toroidally coupled, similar to the early slab geometry but with closed field-lines, leading to extremely short connection lengths to shield electronic charge separation; (2) the curvature of the field-lines is always bad, aligning with the direction of decreasing pressure, but the magnetic field is always increasing radially outward, leading to ∇B drift stabilization; and (3) the high temperature and low magnetic field lead to a large stabilizing finite Larmour radius effect[56, 58].

The characteristics of these two regions have been compared to recent TAE experiments[60] and found to be in agreement. In particular, the lack of ion-scale instability in the core is consistent with experimental measurements of a fluctuation spectrum showing a depression in the ion-scale[60]. In addition, linear pressure gradient thresholds for stability found in simulations are consistent with thresholds observed in experiments. The survey of the linear properties of these modes serves as a guide to the nonlinear turbulence simulations in chapter 5 and 6.

4.1 Simulation Model

Electrostatic simulations presented in this chapter have been conducted with the Gyrokinetic Toroidal Code (GTC) using gyro-kinetic ions and gyro-kinetic electrons. While the FRC core does contain a magnetic null-point, the simulation domains used for this chapter do not include the null-point, thus allowing gyro-kinetics to remain valid. This is discussed in section 4.1.2 and graphically shown in Fig. 4.1.2.

For these simulations, GTC has been extended to allow for the study of instabilities in the core and SOL regions of the FRC[21, 22]. In this work, electrostatic perturbative δf simulations[63, 19, 51, 45, 34] are confined either in the core or SOL region *separately* with no cross-separatrix coupling. The domain is reduced to a toroidal wedge and localized to a single flux surface as described in subsection 2.3. The equilibrium parameters of the simulations are detailed in subsection 4.1.1.

4.1.1 Equilibrium

Simulations are initialized with a FRC equilibrium which is representative of typical FRC plasmas realized in the C-2 experiment. The equilibrium is calculated using the LR_eqMI code, which is an axisymmetric force balance solver including realistic wall and coil geometry and the possibility of multiple ion species, arbitrary rotation profiles, and arbitrary temperature profiles[23]. These quantities are then transformed[18] from cylindrical coordinates $(R,\ Z,\ \phi)$ to magnetic Boozer coordinates $(\psi,\ \theta,\ \zeta)$ for use in GTC[21] as shown in Fig. 4.1. The origin of the Boozer coordinate system is located at the magnetic null-point. The magnetic field points in the poloidal direction, $\vec{\theta}$, and the guiding-center drifts are in the toroidal direction, $\vec{\zeta}$, as shown in Fig. 4.1. Here, the ion diamagnetic direction is positive $(\vec{\zeta})$, and the electron diamagnetic direction is negative $(-\vec{\zeta})$. The major radius $R_0 = 27$ cm is the distance from the machine cylindrical axis (geometry center) to the null-point (magnetic axis) as indicated by the blue dashed line. The minor radius $a = 11$ cm is the distance from the null-point to the separatrix. The separatrix radius $R_s = 38$ cm is the distance from the machine cylindrical axis to the separatrix. These are all measured along the mid-plane

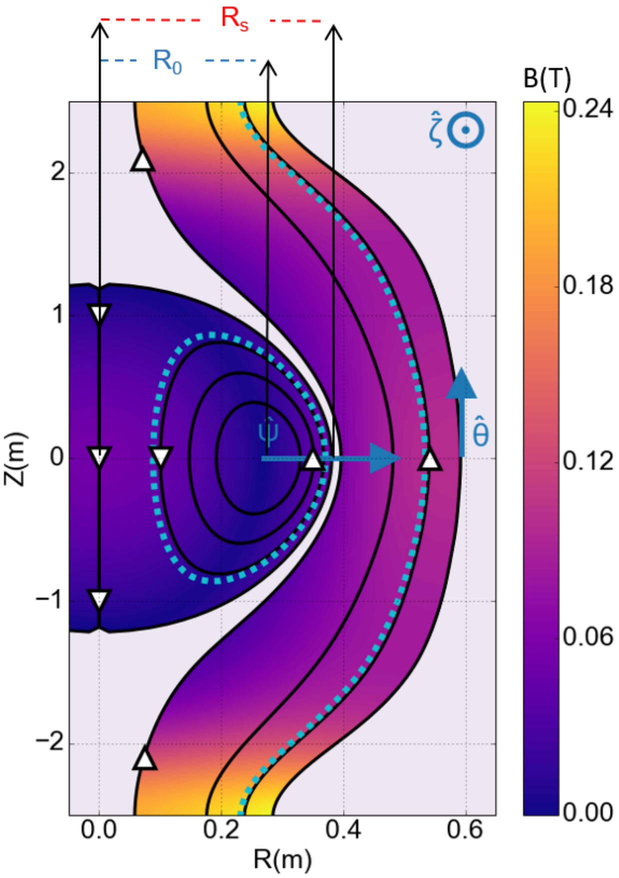

Figure 4.1: The field-aligned mesh on a poloidal plane of a typical C-2 FRC discharge is plotted along with the magnitude of the magnetic field represented by color. The flux surfaces used in simulations are represented by dashed cyan lines. Note that the axes are not proportionally scaled. Arrows denote the directions of the magnetic Boozer coordinate system.

Table 4.1: Parameters used in simulations of core and SOL.

Quantities	Core	SOL
n_e (cm^{-3})	4.0×10^{13}	2.0×10^{13}
T_e (eV)	80	40
T_i (eV)	400	200
ρ_i (cm)	6.0	2.2
ρ_e (cm)	0.044	0.016
$\frac{R_0}{C_s}$ (µs)	1.8	2.5
ν^*_{e-i}	2.1	5.7
ν^*_{i-i}	0.10	0.27

($\theta = 0$ or $Z = 0$).

The equilibrium used corresponds to an early time in a C-2 discharge, just after the CTs merge to form a single FRC before a significant fast ion population has built up. At this stage, the size of the plasma is large and diagnostics are more robust. In the simulations, temperature and density gradients are input to drive instabilities in plasma composed of deuterons and electrons. Parameters are chosen to resemble the conditions of recent experiments at TAE[60] and are summarized in table 4.1. The calculated quantities are the ion gyro-radius $\rho_i = \sqrt{m_i T_i}/(eB)$, electron gyro-radius $\rho_e = \sqrt{m_e T_e}/(eB)$, and ion acoustic speed $C_s = \sqrt{(T_i + T_e)/m_i}$.

Temperature and density gradients drive the instabilities. The strengths of these drives are defined by their scale lengths normalized by the machine scale length (where the local minor radius r is the distance measured from the null-point along $\theta = 0$),

$$\kappa_f = \frac{R_0}{L_f} = \frac{R_0}{f}\frac{\partial}{\partial r} f \tag{4.1}$$

The drives used are the density gradient $\kappa_n = R_0/L_n$, ion temperature gradient $\kappa_{T_i} = R_0/L_{T_i}$, and electron temperature gradient $\kappa_{T_e} = R_0/L_{T_e}$. In addition, the importance of the drives can be defined by the ratios between the scale lengths of the temperature gradients and the density gradient, $\eta_i = \kappa_{T_i}/\kappa_n$ and $\eta_e = \kappa_{T_e}/\kappa_n$. In most of the simulations presented, the strengths of the three drives are equal, ie. $\eta_i = \eta_e = \eta = 1$, and the magnitude of the drive strength would then be referred to as $\kappa (= \kappa_n = \kappa_{T_i} = \kappa_{T_e})$.

Simulations were run both with and without collisions based on the Fokker-Planck model[46] to understand the effects of collisions. The collisional frequencies are based on the NRL Plasma Formulary[37] and are calculated by $\nu_{e-e} = \left(3.44 \times 10^5 \frac{T_e^{3/2}}{n\lambda_{e-e}}\right)^{-1}$, $\nu_{e-i} = \left(3.44 \times 10^5 \frac{T_e^{3/2}}{n\lambda_{e-i}}\right)^{-1}$, and $\nu_{i-i} = \left(2.09 \times 10^7 \frac{T_i^{3/2}}{n\lambda_{i-i}} (\frac{m_i}{m_p})^{1/2}\right)^{-1}$ (where the Coulomb logarithms λ can also be found in the NRL Plasma Formulary).The effective collisionality is the collisional frequency normalized by the transit frequency and is calculated by $\nu^*_{e-e} = \nu_{e-e}/\omega_{tr,e}$, $\nu^*_{e-i} = \nu_{e-i}/\omega_{tr,e}$, $\nu^*_{i-i} = \nu_{i-i}/\omega_{tr,i}$. The transit frequency of an electron and ion passing along a field-line is $\omega_{tr,e} = V_{th,e}/L$ and $\omega_{tr,i} = V_{th,i}/L$, respectively. Here, $V_{th-i} = \sqrt{T_i/m_i}$ is the ion thermal velocity, and $V_{th-e} = \sqrt{T_e/m_e}$ is the electron thermal velocity. In our simulation domain, the field-line length of the core is $L \approx 3.6$ m, while the field-line length of the SOL is $L \approx 5.0$ m. The effective collisionality is high in both regions for the colder electrons, but low for the hotter ions with a low ion impurity modeled by $Z_{eff} = 1.5$ in both regions.

4.1.2 Flux-tube domain

The focus of this study is to characterize the local linear properties of the FRC instabilities in the core and SOL *separately*. The large number of simulations is enabled by the reduction of the simulation domain from a full torus $[0,\ 2\pi]$ to a partial torus $[0,\ 2\pi/n]$ where n is the particular toroidal mode number of interest. In these simulations, the toroidal wavelength is assumed to be much shorter than the radial wavelength of the instabilities, ie. $k_r \ll k_\zeta$.

The radial domain is thus localized to a single flux surface where $R_0 + r = 37$ cm in the core and $R_0 + r = 52$ cm in the scrape-off layer as shown in Fig. 4.1. These flux surfaces *do not* include the magnetic null-point, allowing the guiding-center approximation to remain valid[10]. The average gyro-kinetic parameter is $\rho_i/L_B \simeq 0.2$ in the core and $\rho_i/L_B \simeq 0.006$ in the SOL which are gyro-kinetically valid (about 1.3% difference between the guiding-center and orbit-averaged positions in the case of $\rho_i/L_B \simeq 0.2$ as shown by Brizard[10]).

In this gyro-kinetic simulation[42], dynamics faster than ion gyro-period are removed while ion and electron finite Larmour radius (FLR) effects are retained through accurate representation of gyro-averaging on particles via direct calculations of Bessel functions for the scattering of charge onto the grid and in the gathering of fields onto the charge. Due to the neglect of radial gyro-averaging, the growth-rate of instability is expected to be higher when compared to non-local simulations. Previous work by Naitou *et al*[49] with fully kinetic particle dynamics also support the expectation of strongly stabilizing FLR effects. This assumption was found to be consistent based on simulation results presented in section 5.3.

4.2 Stable drift-waves in the FRC core

Within gyro-kinetically valid regimes

$$\frac{\omega}{\Omega_i} \sim \frac{\rho_i}{L_B} \sim \frac{e\phi}{T} < 1, \ \frac{k_\parallel}{k_\perp} \ll 1 \tag{4.2}$$

(where ρ_i is the ion gyro-radius, $L_B = \frac{1}{B}\frac{\partial B}{\partial r}$ is the magnetic field scale length, and ϕ is the perturbed electrostatic potential) the electrostatic drift-wave is found to be stable in the FRC core when driven by pressure gradients relevant to the C-2 advanced beam driven FRC experiment. Simulations with equal temperature and density gradients ($\eta_i = \eta_e = \eta = 1$) and with drive strengths up to $\frac{R_0}{L_n} = \kappa_n < 5$ were performed. Toroidal wavelengths were scanned from ion scale to electron scale up to $k_\zeta \rho_e < 0.3$. From these GTC simulations, the FRC core is found to be stable within this regime.

4.2.1 Mechanisms for core stability

To understand this surprising stability, further simulations based on limiting cases were studied.

From magnetohydrodynamics, the radially increasing quantity $\oint \frac{dl}{B}$ suggests the existence of a flute instability in the core. An instability can be found by suppressing particle motion in the simulation by evolving only particle weight (δf) and holding particle positions and velocities fixed (ie. initial phase space coordinates of particles are fixed). This indicates the importance of electron kinetics for stability. Work based on this instability also finds both the finite Larmour radius[58] (FLR) and the ∇B effects to be additional stabilization effects as expected. Similar simulations turning on and off FLR and ∇B effects were also performed in the SOL and are detailed in the next section. Simulations also find that only the electron kinetic effects need to be suppressed for the core to exhibit this instability.

In simulations of purely $k_\parallel = 0$ but with evolution of both particle weight and phase space positions, in the limit of far-from-experimental conditions (for example, temperature 100x lower), stability persists when FLR effects are kept; however, when FLR effects are turned off at these limiting case conditions conditions, the $k_\parallel = 0$ mode can become unstable.

Additional limiting conditions further show the importance of electron kinetic effects. In the limit of artificially heavy electrons ($m_e/m_p > 0.25 \sim 0.5$), an unstable mode peaking in the outer mid-plane can exist. In the limit of artificially elongated geometry approaching a theta-pinch-like geometry ($Z_{lim}/Z_0 < 5 \sim 7$, where Z_{lim} is the artificially elongated length and Z_0 is the original C-2-like length), a similar unstable mode can also form in the outer mid-plane. These limiting cases suggest the electron kinetic effects, especially, the short electron transit time to be important FRC features which contribute to the core stability.

The broad stability of the core within the C-2-like parameters may provide the basis for understanding some of the experimentally observed phenomena. Experiments observe robust fluctuations in the SOL and fluctuations of an order of magnitude smaller in the core[60]. Furthermore, in the same experiments, the core spectrum exhibits a depression in the ion range ($k_\zeta \rho_s < 15$) unlike the SOL spectrum.

Because our linear, local simulations do not include the stabilizing influences of fast ions and non-local effects which exist in the experiments, instabilities should be enhanced within these simulations. However, the results of the simulations show the core stability to be extremely robust.

It should be noted that one element missing from these simulations may explain fluctuations in the core: the coupling of the SOL and core. Cross-separatrix coupling between the two regions may introduce fluctuations originating from the SOL (detailed in the next section) into the core which, by itself, is found to be inherently stable.

4.3 Drift-wave instabilities in the SOL

4.3.1 Collisionless $\eta = 1$ instability

GTC simulations were also performed for the SOL, using C-2-like parameters detailed in table 4.1 with $\eta = 1$. Relative to the core, the temperatures and densities of both species are lower by a factor of 2 while the magnitude of the background magnetic field is roughly stronger by a factor of 2. Under these conditions, simulations show the existence of unstable modes ranging from ion-scale to electron-scale wavelengths. This is consistent with SOL experimental measurements of density fluctuations which exhibit an exponential spectrum ranging from the ion-scale to electron-scale[60].

Fig. 4.2 shows the instability frequency (ω_r) and growth-rate (γ) over a range of $k_\zeta \rho_s$ for various drive strengths. ω_r is in the electron diamagnetic direction and the electron curvature drift direction, but opposite to the electron ∇B drift direction. As $k_\zeta \rho_s$ increases, the magnitude of ω_r decreases until a jump up to a similar frequency which trends downward again. This jump is associated with a change in the poloidal mode structure from odd parity about the midplane to even parity.

A stability threshold is found at drive strength around $\kappa_{sim} \approx 3 \sim 5$ for longer wavelengths as seen in Fig. 4.3, which is comparable to $\kappa_{exp} \approx 3.9$ as measured in experiments. Shorter wavelengths are found to have lower stability thresholds.

As seen in the mid-panel of Fig. 4.4, the mode structure in the SOL is dominated by poloidal mode number $m = 1$ with smaller components of $m = 0$ and $m = 2$ (where the poloidal direction is the horizontal axis). The central location of the mode can be explained by the effects of gyro-averaging and by the behavior of the resonant particles. As seen in Fig. 2.1, k_ζ is lower at the mid-plane ($Z \sim 0$) and higher at the axial ends ($Z \sim \pm 2$) by more than a factor of two, leading to a weaker gyro-averaging effect in the central location. The dominant

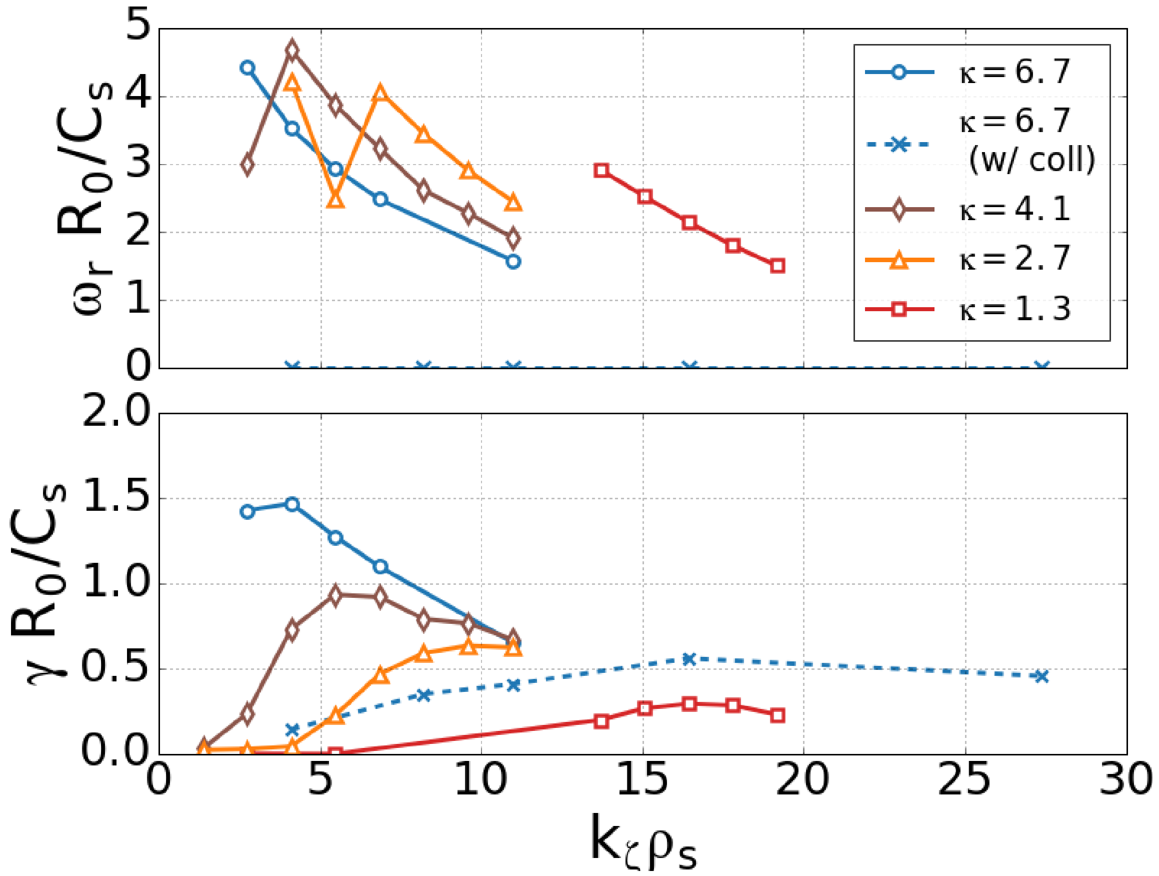

Figure 4.2: Real frequency (ω_r) and growth-rate (γ) for different drive strengths (κ) of the collisionless (collisional) $\eta = 1$ SOL instability is shown as solid (dashed) lines. As the drive decreases, the instability shifts toward the shorter wavelength (k_ζ).

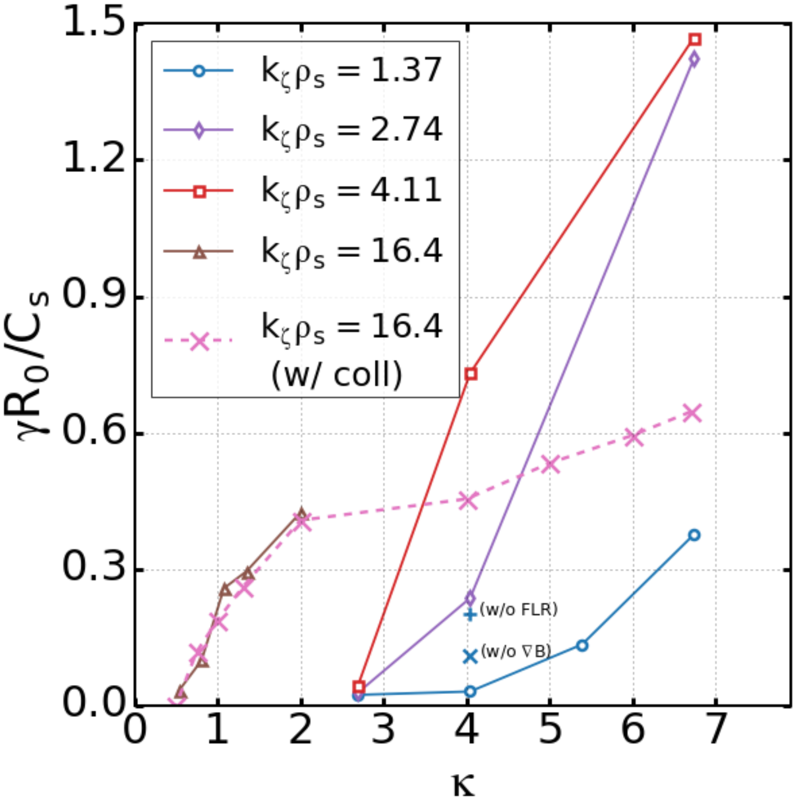

Figure 4.3: Growth-rates (γ) vs drives (κ) for unstable collisionless $\eta = 1$ SOL modes at various length-scales are plotted as solid lines. The unstable collisional $k_\zeta \rho_s = 16.4$ mode for $\eta = 1$ is also plotted as the dashed line. The threshold is found to be lower for shorter wavelengths.[60] The growth rates for $k_\zeta \rho_s = 1.37$ (blue) without FLR effects (+) and without ∇B effects (x) are also plotted for comparison.

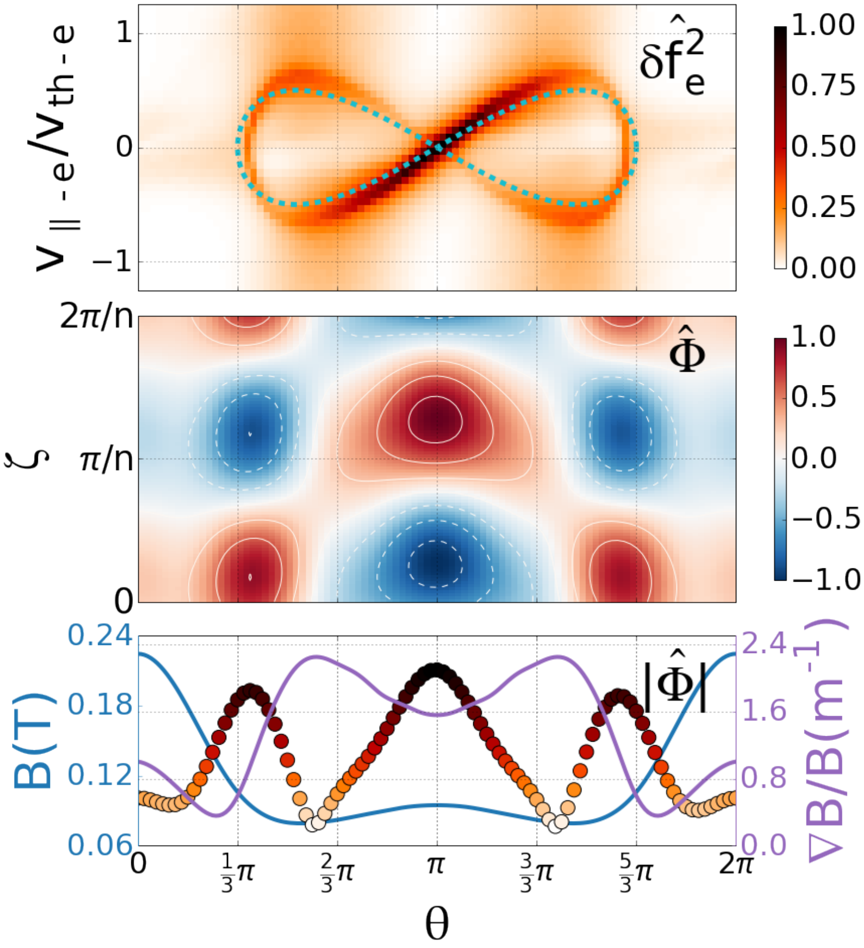

Figure 4.4: The top panel shows the $v_\parallel - \theta$ phase-space of the electrons with the color representing δf_e^2. The middle panel shows the electrostatic potential in the $\zeta - \theta$ plane for the case of $k_\zeta \rho_s = 4.1$ ($n = 75$, $\eta = 1$, $\kappa = 6.7$). The bottom panel shows the potential along the poloidal direction for $\zeta = 0$. In addition, the magnitude and the radial gradient of the magnetic field are shown as the blue and purple curves corresponding to the left and right axes, respectively.

particle resonance is due to *barely trapped electrons* in the central location, as seen in the figure-8 structure in the $v_\parallel - \theta$ phase-space plot in Fig. 4.4 (detailed in the next subsection).

4.3.2 Wave-particle resonances

The square of the perturbed distribution functions δf^2 is plotted in the plane of energy (E/T) vs pitch angle ($\mu B_0/E$) for both species in Fig. 4.5 for the $k_\zeta \rho_s = 4.1$ ($n = 75$, $\eta = 1$, $\kappa = 6.7$). For this instability, electron resonance is more important than ion resonance ($\delta f_e^2 > \delta f_i^2$). The resonant ion motion is the drift due to ∇B and curvature, as shown by the curves in the upper panel of Fig. 4.5. More importantly, the resonant electron motion which drives this instability is shown to be the bounce motion of *barely trapped electrons*, as shown in the lower panel of Fig. 4.5.

The electrons can be separated into three groups: locally trapped electrons, globally trapped electrons, and passing electrons. In the SOL, the geometry is such that there are two small magnetic wells and an overall large magnetic well as seen in the blue curve of the bottom panel of Fig. 4.4. *Locally trapped electrons* are bound within the two smaller magnetic wells. *Globally trapped electrons* are bound within the overall larger magnetic well. *Passing electrons* are able to freely stream through the magnetic well in the periodic domain. The boundaries of these trapped-passing regimes is denoted by arrows in Fig. 4.5. From the perturbed distributions of the electrons in Fig. 4.5, it can be clearly seen that the mode frequency is aligned with the bounce frequency of the locally barely trapped electrons at $\mu B_0/E = 1$. This resonant motion can also been seen when the perturbed electron distribution function is plotted in phase space ($v_\parallel$ vs θ) as in the top panel of Fig. 4.4. The figure-8 shape highlights the motion of the barely trapped electrons moving back and forth within the magnetic well.

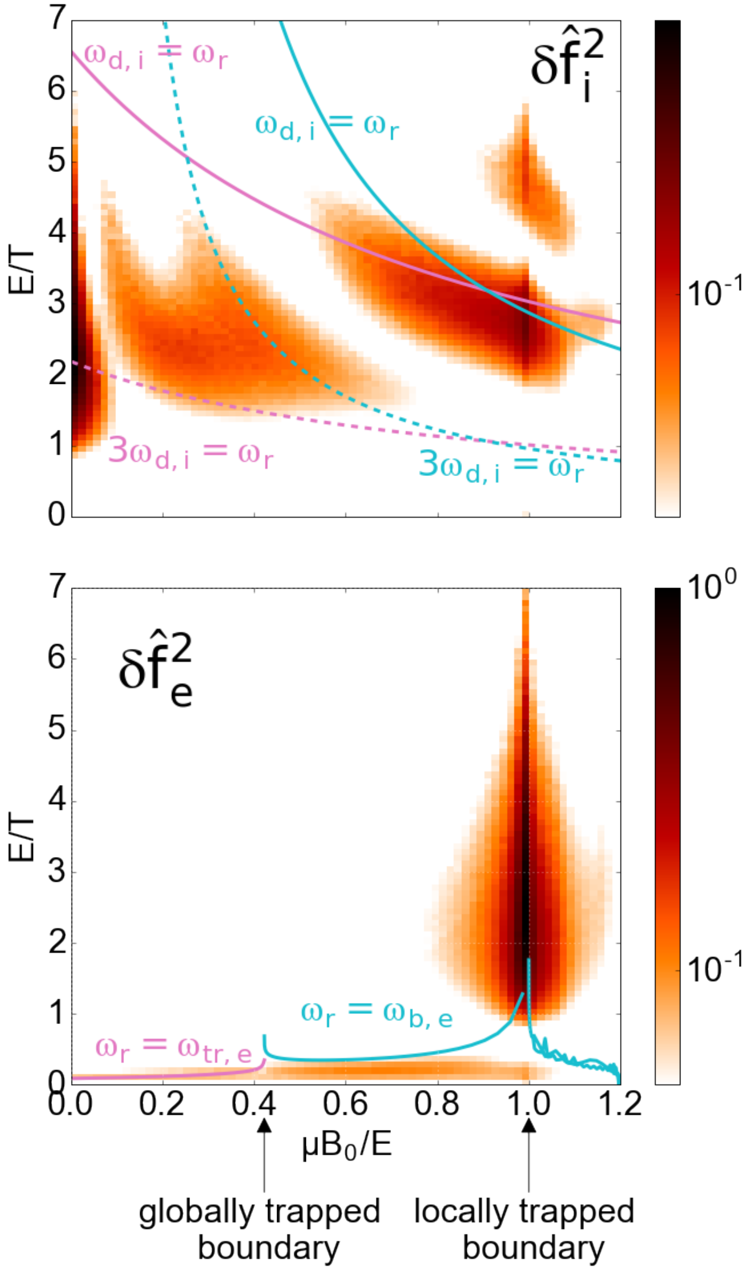

Figure 4.5: δf^2 (normalized by the maximum δf_e^2) is plotted for the ions (upper panel) and electrons (lower panel) with respect to energy and pitch angle. For ions, curves represent the ion drift frequency; pink (cyan) corresponds to values calculated at $\theta = \pi$ ($\theta = \pi/3$). For electrons, the pink (cyan) corresponds to the electron transit frequency (electron bounce frequency).

Further evidence of the importance of this bounce motion of the electrons in driving this instability is seen from the case of purely density gradient driven instability ($\eta = 0$) and the case of ion-temperature and density gradient driven instability ($\eta_i = 1$) (detailed in the next section).

4.3.3 Stabilizing mechanisms

As in the core, the stabilizing influences of the finite Larmour radius (FLR) and magnetic well (negative ∇B) are explored in the SOL by turning on and off these effects in simulations. This is shown for the $k_\zeta \rho_s = 1.37$ case for $\kappa \sim 4$ in Fig. 4.3. Like the core, it is found that the FLR effect is more strongly stabilizing than the ∇B effect when the drive is strong. However, in realistic plasmas, nonlinear effects (such as energy and particle transport) tend to reduce the pressure profile toward marginal stability, ie. flattening, and when the pressure drive is marginal, both FLR and grad-B are important in the complete suppression of instability.

In the experiments, the temperature gradients can actually be stronger than the density gradients. In the simulations presented in the previous subsections, the gradients of the density, ion temperature, and electron temperature are equal. In order to better understand the drive of the instability for $\eta = 1$, simulations of the $k_\zeta \rho_s = 4.1$ instability was repeated with the density gradient unchanged at $\kappa_n = 6.7$ while *separately* varying the ion temperature gradient κ_{T_i} and electron temperature gradient κ_{T_e}. As shown in Fig. 4.6, the electron temperature gradient is destabilizing while the ion temperature gradient is stabilizing. In addition, this instability exists even when there is only a density gradient ($\eta_e = \eta_i = 0,\ \kappa_n \neq 0$).

These results can be understood by looking at the electron perturbed distribution functions. In the $\eta = 0$ case as shown in the top panel of Fig. 4.7, the resonant electrons are at lower energy in contrast to the $\eta = 1$ case. The electron resonance is also no longer dominated

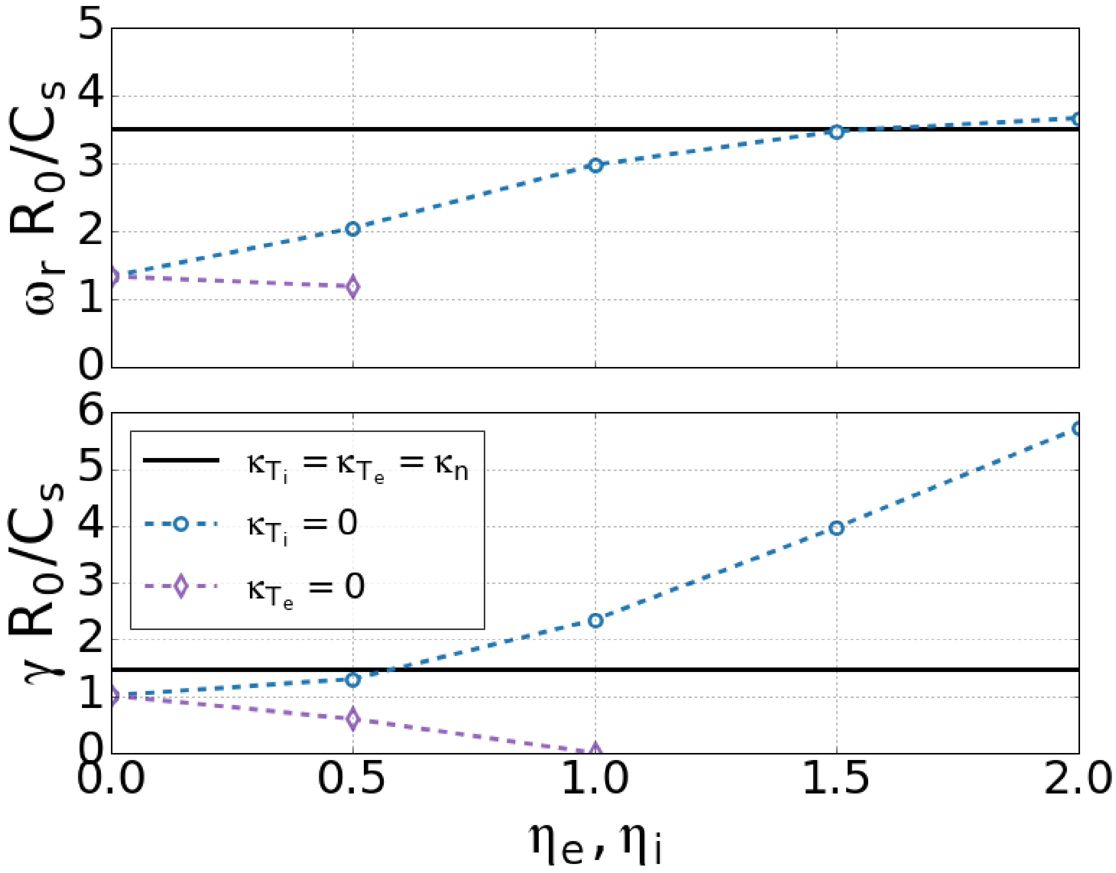

Figure 4.6: Dispersion relation with respect to η_e (η_i) is plotted as the blue (purple) dashed lines. The frequency and growth-rate for the $\eta = 1$ (black) case is plotted as the solid line for comparison. The density gradient drive κ_n is kept constant while κ_{T_e} (κ_{T_i}) is varied for the η_e (η_i) scan. Note that the mode is unstable even with only κ_n.

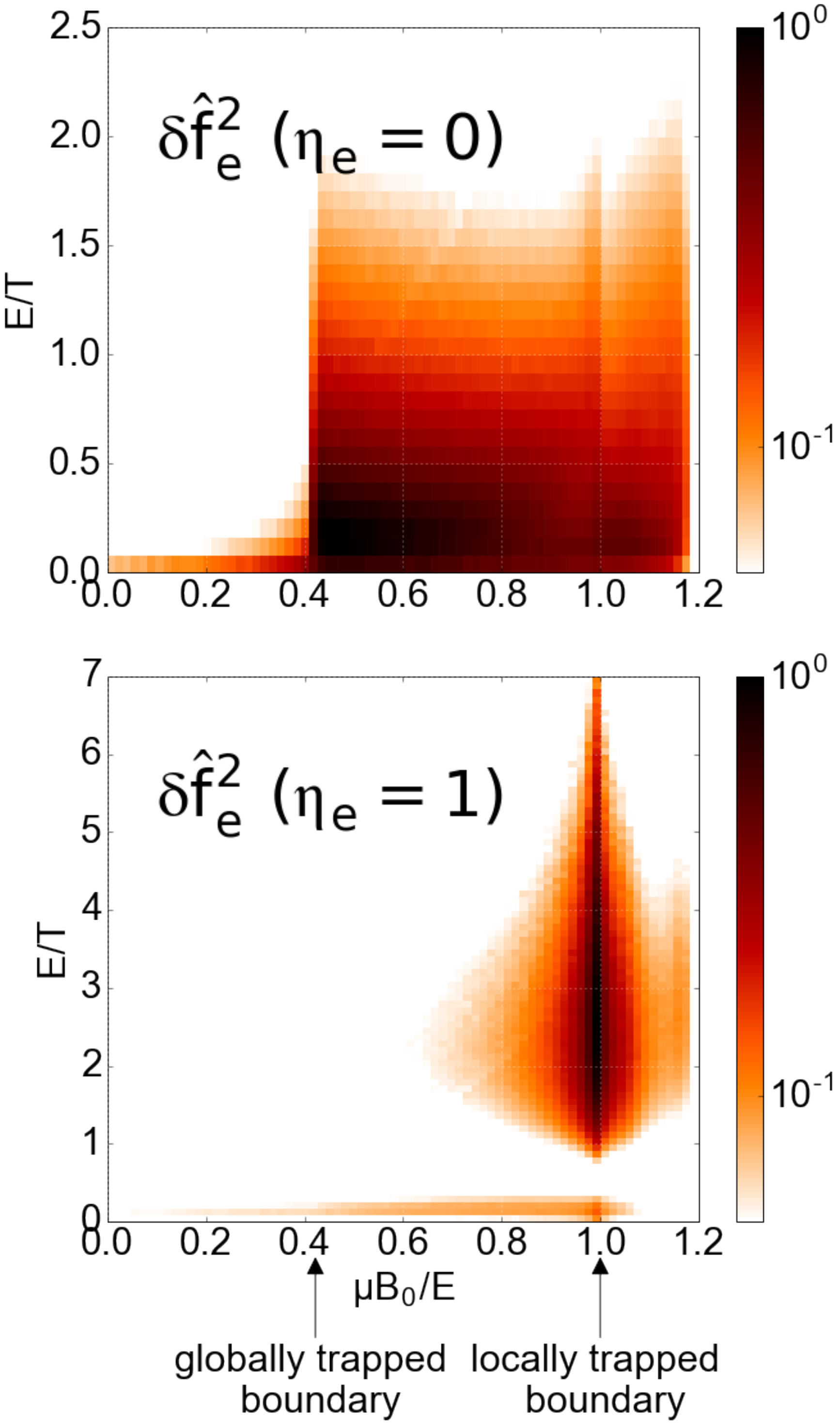

Figure 4.7: The δf_e^2 (normalized by the maximum δf_e^2) is plotted for $\eta_e = 0$ and $\eta_e = 1$ with respect to energy and pitch angle. When the electron temperature gradient (κ_{T_e}) is decreased ($\eta_e = 1 \rightarrow \eta_e = 0$), the electron resonance shifts from locally trapped to globally trapped.

by the locally barely trapped electrons but still by trapped electrons. In the $\eta_e = 1,\ \eta_i = 0$ case, the frequency is comparable to the $\eta = 1$ case but with even faster growth. The resonant ions are at lower energy while the resonant electrons are, as in the $\eta = 1$ case, the high energy locally barely trapped electrons, as seen in the bottom panel of Fig. 4.7. From the comparison of the three cases, it is clear that the motion of the locally barely trapped electrons is the resonance that drives the collisionless SOL instability.

4.3.4 Collisional effects

Using the Fokker-Planck model, the SOL instability for $\eta = 1$ was simulated with pitch-angle scattering through electron-ion collisions over a range of collisionality, from collisionless to the collision frequency defined for Z_{eff}=1.5 using equilibrium densities and temperatures detailed in table 4.1. With collisions, both frequency and growth-rate decrease, but as the collisionality is lowered, the collisionless frequency and growth-rate are recovered. While collisions are strongly stabilizing in the long wavelength case, there is negligible effect to the mode structure which is strongly dominated by the $m = 0$ and $m = 1$ harmonics.

The effect of collisions on this instability can be understood from the locally trapped electron resonance. Pitch-angle scattering frequently moves electrons in and out of that particular energy-pitch position, essentially removing the drive of this instability. However, as seen in Fig. 4.2 and Fig. 4.3, there is still a significant instability which can exist at shorter wavelengths even when the collisionless mode is suppressed by collisions.

4.4 Discussion

Local gyrokinetic simulations have been used to investigate electrostatic pressure gradient-driven drift-waves in the FRC. While the FRC core was expected to be less unstable[59] due to the large ion gyro-radius, simulations found drift-waves in the core to be stable with C-2-like parameters for pressure gradient drives up to $\rho_i/L_P \leq \mathcal{O}(1)$ with equal temperature and density gradients ($\eta = 1$) for ion-to-electron scale wavelengths ($k_\zeta\rho_e < 0.3$). Our studies of limiting cases in the FRC strongly suggest that this stability is due to the short electron connection length with further stabilizing contribution from FLR[56] and ∇B effects. Only when the FRC geometry is artificially elongated from the typical C-2-like FRC toward the field-reversed theta pinch (by Z_{lim}/Z_0 exceeding $5 \sim 7$) does the known drift-wave instability appear, consistent with the importance of electron parallel dynamics. It should also be noted that the electron connection length along the field-lines in the FRC core is much shorter than those in tokamaks.

In the SOL, a pressure gradient driven mode with wavelengths ranging from ion-scale to electron-scale has been found. This collisionless instability is driven by magnetically trapped electrons. The unstable mode peaks are correlated with the regions with weakest magnetic fields, strongest curvature, and local minima of ∇B. Collisions suppress this instability but allow a different lower frequency collisional instability at shorter wavelengths.

In experiments conducted by Schmitz *et al*[60], density fluctuations measured in the core display a "depressed" wavenumber spectrum in which fluctuation amplitudes are low at ion-scale wavelengths but peak at electron-scale wavelengths (in the range around $k_\zeta\rho_e \approx 0.15 \sim 0.45$). The fluctuations measured in the SOL have a more typical wavenumber spectrum with higher amplitudes at ion-scale and exponentially decreasing amplitudes toward shorter wavelengths. The stability exhibited in the simulations of the core is consistent with the experimental core fluctuation spectrum; however, simulations using Vlasov ions is necessary to explore the possibility of higher frequency instabilities. The ion-to-electron-scale nature of the instability of the SOL displayed in simulations is consistent with the experimentally measured SOL fluctuation spectrum. In addition, experimental data show the existence of fluctuation thresholds[60] at normalized drive strengths of $\kappa_{exp} \approx 3.9$. In simulations, collisionless linear thresholds are found at $\kappa_{sim} \approx 3 \sim 5$ in the SOL for the longer wavelength modes.

Based on the fastest growth rates of the collisionless SOL instability driven by the largest and smallest simulated drive strengths $\kappa \approx 8.1 \sim 1.3$, the characteristic growth times are $\gamma \approx 1.75 \sim 0.25 C_s/R_0 \rightarrow \tau_{SOL} = 1.4 \sim 10\,\mu\text{s}$. The fastest growing collisional SOL mode, driven by $\kappa = 6.7$, has a comparable growth time of $\gamma \approx 0.65 C_s/R_0 \rightarrow \tau_{SOL} = 3.9\,\mu\text{s}$. In the C-2 experiments, the FRC plasma lifetimes are on the order of milliseconds, and so both the collisionless and collisional SOL modes have enough time to grow to a substantial amplitude to explain the fluctuation spectrum observed.

In experimental measurements of density fluctuations[60], the FRC core and SOL show distinct behaviors. The SOL displays strong density fluctuations which follow an exponential scaling while the quiescent core density fluctuations are lower in amplitude by an order of magnitude. In agreement with these experimental results, our simulations find drift-waves to be robustly stable in the core and unstable in the SOL.

The surprising stability of electrostatic drift-waves in the core requires further studies to isolate the origin of the fluctuations observed in experiments. Higher frequency instabilities may exist in the core, but the origin of the fluctuations may also lie in the interaction of the SOL and core. Chapter 5 focuses on the physics of cross-separatrix interactions and the propagation of fluctuations from SOL to core.

Chapter 5

Origins of core fluctuations through cross-separatrix coupling

In the comprehensive set of local, linear simulations[40] of chapter 4, the electrostatic drift-wave is found to be stable in the core and unstable in the scrape-off layer. However, experimental observations show that density fluctuations exist in both the core and scrape-off layer[60]. Since the core is not inherently unstable, how can the results of linear stability in the core and the existence of core fluctuations be reconciled?

In the local linear simulations, the core and SOL were simulated separately; in reality, the core and SOL exist next to each other and are coupled through the separatrix. Although there are a variety of other possibilities, a likely source of fluctuations in the linearly stable core is a spread of fluctuations from the linearly unstable SOL. In this chapter, I explore this hypothesis through global gyro-kinetic ANC simulations of C-2-like FRC geometry.

An ion temperature gradient driven drift-wave instability first grows in the SOL and is found to linearly propagate into the core in linear regimes. Simulation results of the ITG are found to be in agreement with analytically derived local dispersion relations. Nonlinear single-mode simulations also show turbulence spreading, leading to increased fluctuation amplitude in the core just before saturation and afterwards.

5.1 Simulation model

Simulations presented in this chapter have been performed with A New Code (ANC), a first principles code developed by some of the developers of the Gyrokinetic Toroidal Code (GTC). The version of ANC used is the cylindrical non-field-aligned version as detailed in chapter 3. Ions are gyrokinetic with FLR effects calculated by 4-point sampling of the gyro-orbit. While local simulations used gyro-kinetic electrons, in the simulations of this chapter, electrons are represented by the adiabatic response in the Poisson equation. This is a first step due to numerical difficulties in time-resolution (faster electron motion along the parallel direction causes stricter constraint) and grid-resolution (shorter wavelength structures may need to be resolved). Future simulations will use drift-kinetic electrons as the recent field-aligned features of ANC (described in chapter section 3.4) will help mitigate some of the numerical difficulties.

5.1.1 Simulation domain

Single toroidal mode

In the simulations of this chapter, only a single toroidal mode (with toroidal mode number denoted by n) is kept while all other toroidal modes are filtered out. This allows simulations to be more cost-effective through the use of a toroidal wedge domain as described in section 2.3.

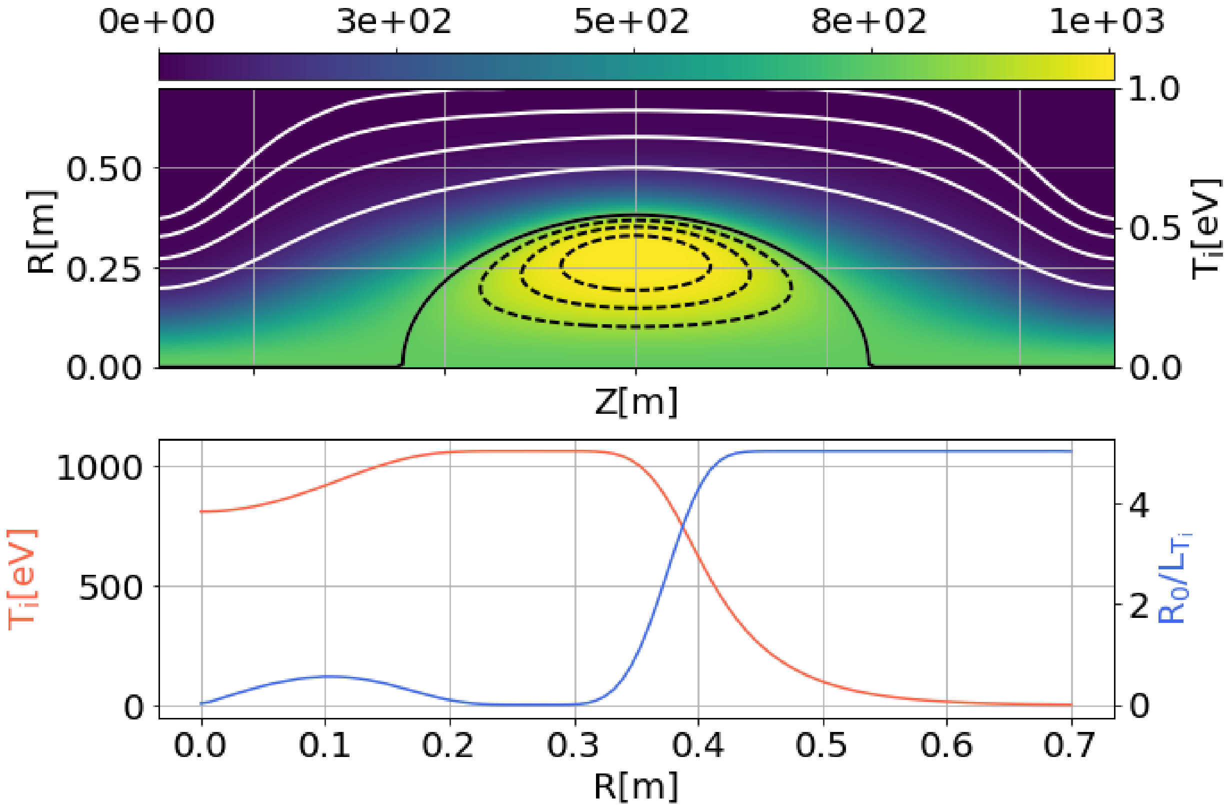

Figure 5.1: The equilibrium ion temperature is plotted on the R-Z plane in the top panel. Contour lines of constant flux are drawn with white (SOL) and black (core). The equilibrium ion temperature and scale length are plotted in the bottom panel for $Z = 0$.

Full geometry

The simulation domain of the simulations of this chapter contain both the core and SOL. The SOL is cut off at $Z = \pm 5$[m] right before the formation section of the FRC and uses a periodic axial boundary. The radial boundaries are such that fluctuations within a distance near the outer boundary are zeroed. These simulations use the second Poisson solver described in section 3.2.

Table 5.1: Simulation parameters at R=0.55[m]

$R_0/L_{T,i}$	$R_0/L_{T,e}$	R_0/L_n	ρ_i (cm)	ρ_e (cm)
5	0	5	0.6	0.015

5.1.2 Equilibrium

Simulations are initialized with a FRC equilibrium magnetic geometry which is representative of typical FRC plasmas realized in the C-2 experiment calculated using the LR_eqMI code[23]. The equilibrium pressure is designed to drive instability in the SOL with ion temperature and density gradients. Electron temperature is flat at $T_e = 80$[eV].

5.2 Linear ITG instability

5.2.1 Mode structure

With this equilibrium, an instability is found to start in the SOL. Figure 5.2 shows the mode structure, time history, and radial profiles of the instability for $n = 20$ (where n is the toroidal mode number). In the figure, *real* and *imag* refer to the real and imaginary components of the electrostatic potential which is spectrally decomposed in the toroidal direction.

The electrostatic potential is displayed with a logarithmic colorbar due to the much lower amplitude of potential in the core. The mode structure is elongated along the field-line direction with an even parity about $Z = 0$ and a parallel wavelength roughly about 5[m]. The radial wavelength can be seen to be roughly about 0.1[m] from the bottom left panel with the solid and dashed lines representing the real and imaginary components of the spectrally decomposed potential. From the radial-time plot of the potential, it can be seen that the

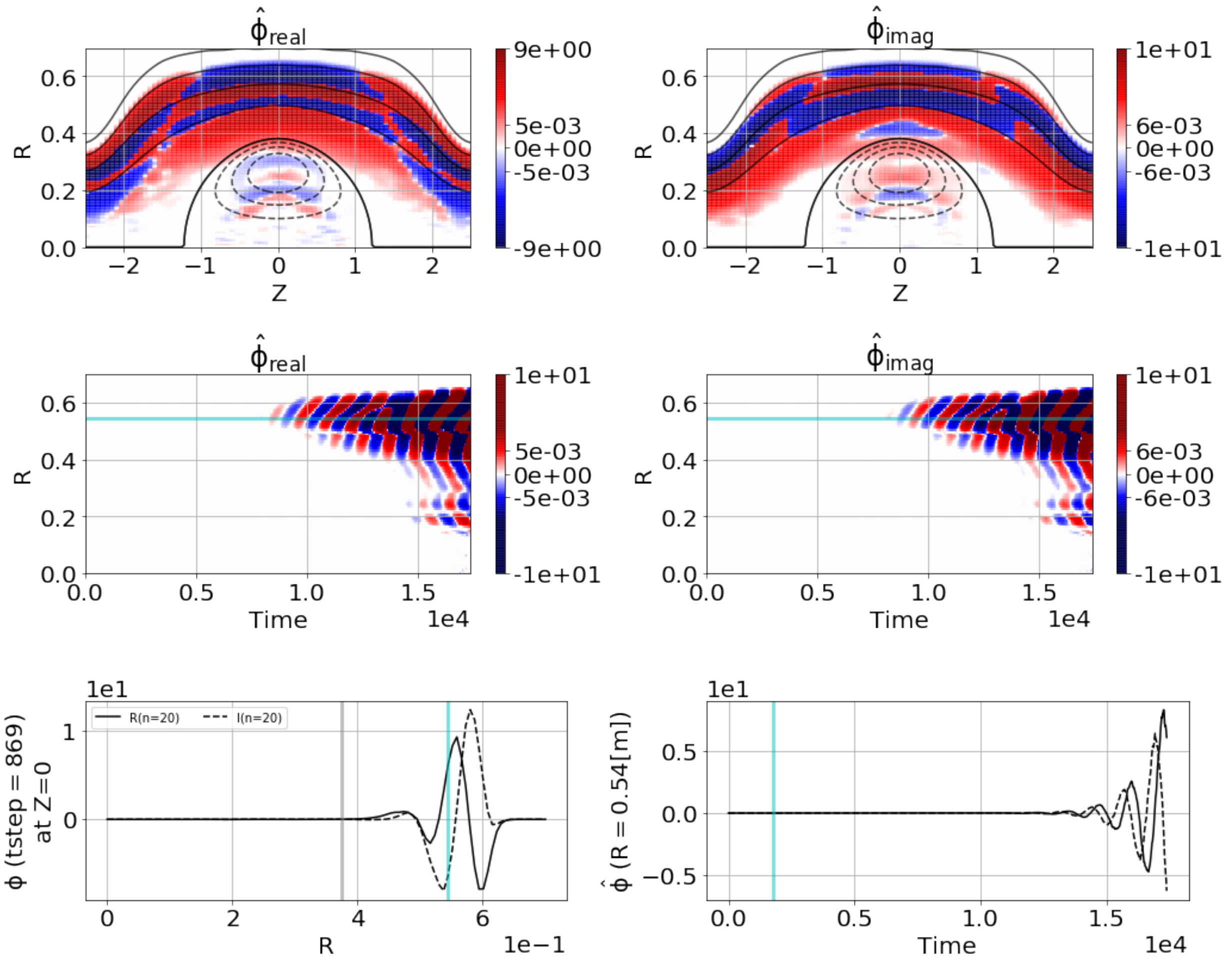

Figure 5.2: A summary of one ANC simulation. The top panels show the real and imaginary components of the electrostatic potential $\phi(R, Z)$ after toroidal decomposition. The middle panels show the potential along $Z = 0$ against the radial position and time. The bottom left panel shows the potential against the radial position at the last time step, and the bottom right panel shows the mode history at the particular radial position of $R = 0.54$.

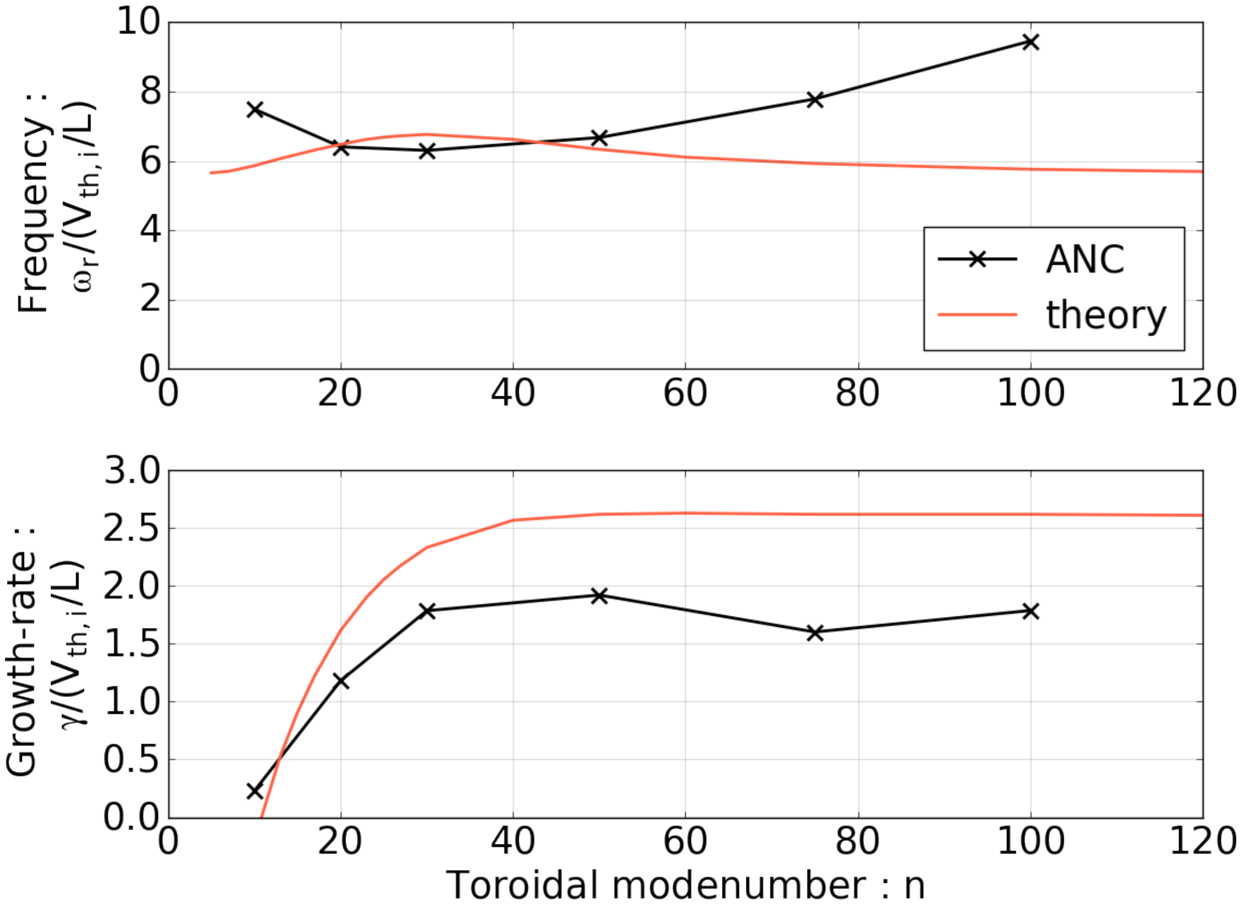

Figure 5.3: The dispersion from simulation and from simple local theory are plotted for comparison. The frequencies are consistent in the relative magnitude and in the direction (both are ion diamagnetic direction) while the growth rates are consistent in trend (threshold around $n \sim 10$ and flattening towards higher n). The discrepancy in growth rates are likely due to the extremely simplified model used for the analytic dispersion.

instability starts in the SOL and eventually moves past the separatrix ($R_s = 0.38$[cm] at $Z = 0$). This will be further examined in section 5.3.

5.2.2 Linear dispersion

The exponential growth of the instability is clear from the bottom right panel which also shows the real component leading the imaginary component, meaning that the propagation is in the positive toroidal direction. Within ANC, the coordinate system is such that $\hat{R} \times \hat{Z} =$

$\hat{\zeta}$ while the ion diamagnetic direction is $v_* \equiv \frac{-\nabla P_i \times B}{enB^2} \parallel \hat{R} \times \hat{Z} = \hat{\zeta}$, meaning that the propagation of this instability is in the ion diamagnetic direction.

Six different mode numbers were surveyed, and the results are plotted in black in Fig. 5.3. This instability was found to have frequencies in the ion diamagnetic direction with frequencies near the ion acoustic frequency ($\omega_r/2\pi \sim V_{th}/L$ where $L \approx 5$m is the field-line length). This mode was found to have a threshold near $n = 10$ ($k_\zeta \rho_s \sim 0.15$) with growth rates remaining relatively similar for mode numbers greater than $n = 30$ ($k_\zeta \rho_s \sim 0.5$).

An analytic dispersion relation can be derived for this unstable mode due to the simplicity of the adiabatic electron model. Since the frequencies found from ANC simulations are in the range of $\omega_* > \omega_{sim} \sim k_\parallel v_{th} \gg k_\zeta v_d \equiv |\omega_{\nabla_\perp B}|, |\omega_{curv}|$ (where $\omega_{\nabla_\perp B}$ and ω_{curv} are the drift-frequencies due to non-uniformities in the magnetic field), the toroidal drifts can be safely ignored such that this becomes a slab-like ITG dispersion relation,

$$0 = (\tau + 1)\hat{\omega} + (\hat{\omega} - \hat{\omega}^* + \frac{1}{2}\hat{\omega}_T^*)(W - 1)\Lambda_0 - \hat{\omega}_T^* \left(\frac{1}{2}\hat{\omega}^2 W \Lambda_0 + (W - 1)(\Lambda_1 - \Lambda_0)b \right) \quad (5.1)$$

where $W(x) = \frac{1}{\sqrt{2\pi}} \int \frac{y}{y-x} e^{-\frac{y^2}{2}} dy$ is the derivative of the plasma dispersion function, $\omega_* = k_y v_{th} \rho_i / L_n$ and $\omega_T^* k_y v_{th} \rho_i / L_{T_i}$ are the drift frequencies due to density and temperature gradients, $b = k_\perp^2 \rho_i^2$ is a measure of the mode wavelength relative to ion gyroradius, and $\Lambda_0 = e^{-b} I_0(b)$ and $\Lambda_1 = e^{-b} I_1(b)$ are the FLR effects represented by exponentially scaled modified Bessel functions.

In Fig. 5.3, frequencies and growth rates numerically calculated from this analytic dispersion is plotted in red. Deviations between the local theoretical dispersion relation and the dispersion relation found from simulation may be due to the local approximation; $k_\parallel$ and k_r are not good quantum numbers but are merely convenient approximations. Despite the approximations made, this local dispersion relation captures many of the important trends seen in the simulation. The analytic frequency is in the ion diamagnetic direction and is also near the ion acoustic frequency in magnitude, consistent with the frequencies found from simulation.

The analytic dispersion also displays a threshold near $n = 10$. While the local dispersion has higher growth rates, a similar flattening of the growth rates for higher toroidal mode numbers. This flattening, finite growth-rate may be surprising because of the common assumption for short wavelength limit of $b \gg 1$ in which ions are treated as adiabatic (thus, resulting in removing this kind of instability); however, a rigorous treatment of the FLR effect represented by the exponentially scaled modified Bessel functions would show that the functions do not decay to zero quickly enough in the short wavelength limit

$$\begin{aligned}
\Lambda_0(b) &\to \frac{b^{-1/2}}{\sqrt{2\pi}} + i\frac{Exp(-2b)}{\sqrt{2\pi b}} + \mathcal{O}(b^{3/2}) \approx \frac{1}{\sqrt{2\pi b}} \\
\Lambda_1(b) &\to \frac{1}{\sqrt{2\pi b}} - i\frac{Exp(-2b)}{\sqrt{2\pi b}} + \mathcal{O}(b^{3/2}) \approx \frac{1}{\sqrt{2\pi b}} \\
\Lambda_0(b) - \Lambda_1(b) &\to \frac{b^{-3/2}}{2\sqrt{2\pi}} + i\frac{2Exp(-2b)}{\sqrt{2\pi b}} \approx \frac{b^{3/2}}{2\sqrt{2\pi}}.
\end{aligned} \tag{5.2}$$

Because of the drift frequencies ($\omega^*, \omega_T^* \propto \sqrt{b}$) in the dispersion, a finite growth-rate for this mode can exist even in the short wavelength limit.

In Fig. 5.3, only the unstable mode from the analytic dispersion was displayed. Numerical solutions of the dispersion relation show many damped modes at higher frequencies and oppositely signed frequencies. The full results of the analytic dispersion are shown in Fig. 5.4, with the unstable branch plotted in orange and the stable or damped branches plotted in gray with arbitrary units for the frequencies and growth rates.

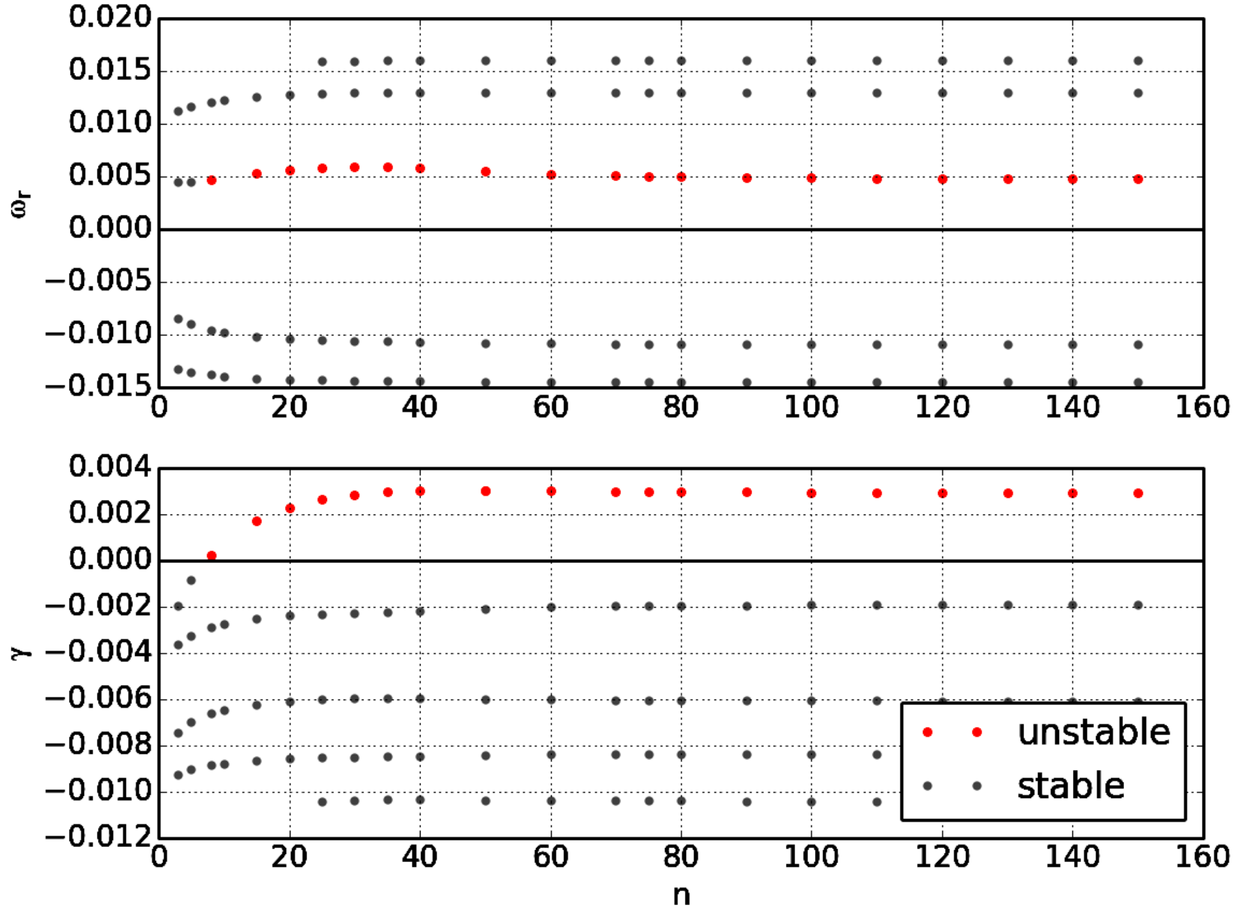

Figure 5.4: Numerical solutions of Eq. (5.1) are shown with stable branches plotted in gray and the unstable branch in orange. Frequencies and growth rates are plotted in units of ion gyrofrequency.

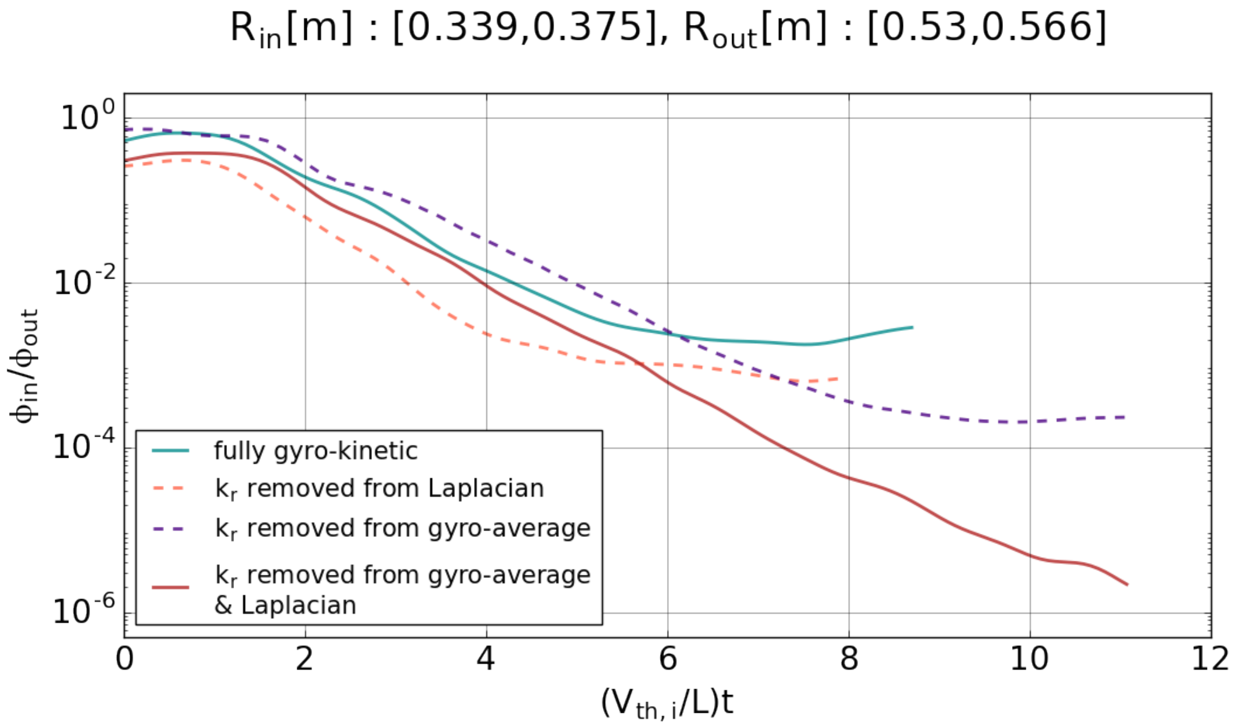

Figure 5.5: Comparison of the ratio of the potential inside and outside of the separatrix with radial effects numerically turned on and off. Initially, there is noise of equal amplitude in both the core and SOL so that the ratio is $\mathcal{O}(1)$. As the instability in the SOL grows, the denominator grows such that the ratio decreases. If radial effects are included, then instability will propagate into the core region allowing for the ratio to flatten out. In the red line, the simulation is radially localized (all radially non-local effects numerically removed) so that instability never reaches the core leaving the red line to continue to decrease without flattening.

5.3 Linear propagations

5.3.1 Radial coupling

One major difference between the simulations of this chapter and chapter 4 is radial gyro-averaging. These radial effects arise through the particle side which interpolates a gyro-averaged field onto the particle or through the field side which solves for the field with a radially non-local Laplacian as described in section 3.2. These can be numerically turned off and on to understand their effect on the instability in the FRC.

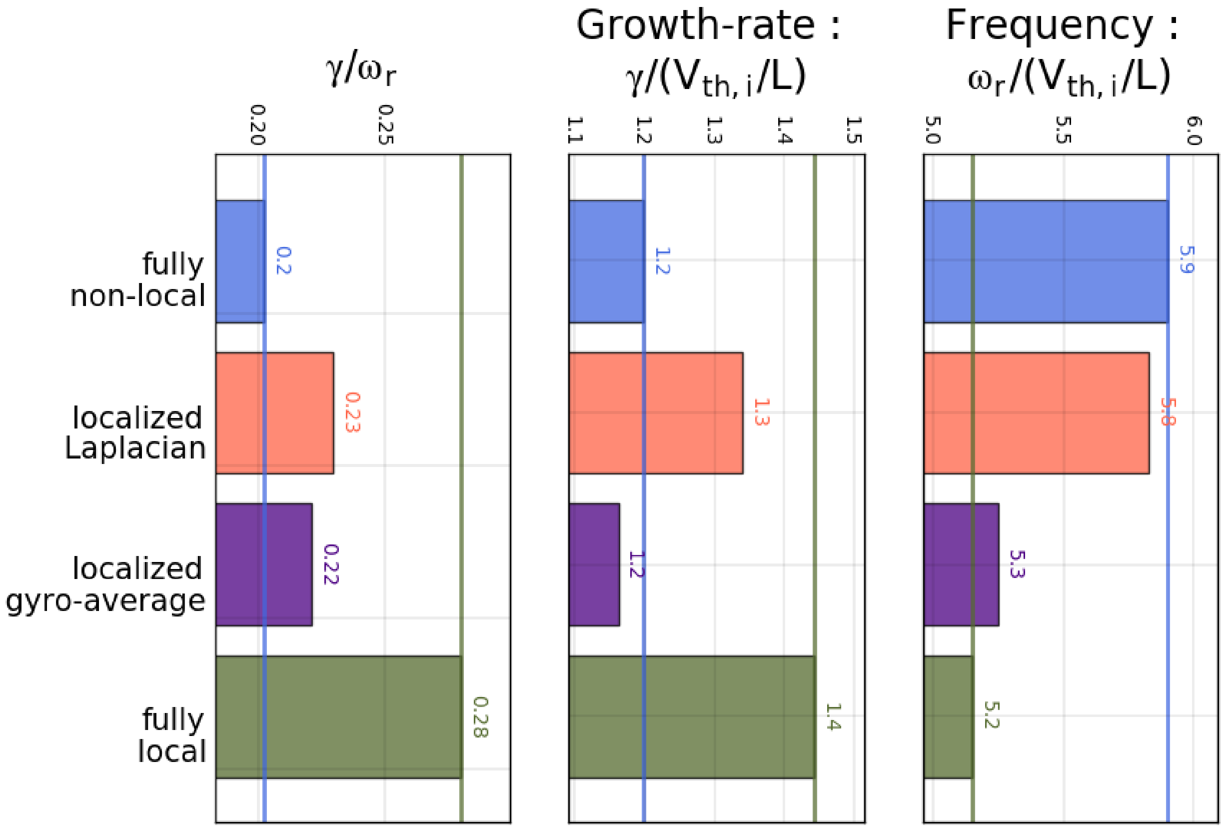

Figure 5.6: growth rates and frequencies of the four cases comparing radial effects are shown. Between the radially local and radially non-local cases, the growth-rate is lower in the non-local case (85% of local case) with a higher frequency (113% of local case).

The most important effect of the radial gyro-averaging is in the formation of a radial eigenmode structure. In Fig. 5.5, the ratio of average electrostatic potential inside to outside is plotted against time for $n = 20$. As the instability begins to grow outside in the SOL, the denominator grows so that the ratio decreases. If the potential inside begins to grow at the same rate (and thus, the eigenmode has extended into the core), then the ratio begins to flatten out. Without radial effects (ie. radially localized), the ratio decreases indefinitely because there is no instability in the core, and the eigenmode does not extend into the core. With both or either of the radially non-local effects, the eigenmode extends into the core. These results are understandable since radially non-local effects introduce k_r into the dispersion, allowing for a possible radial group velocity.

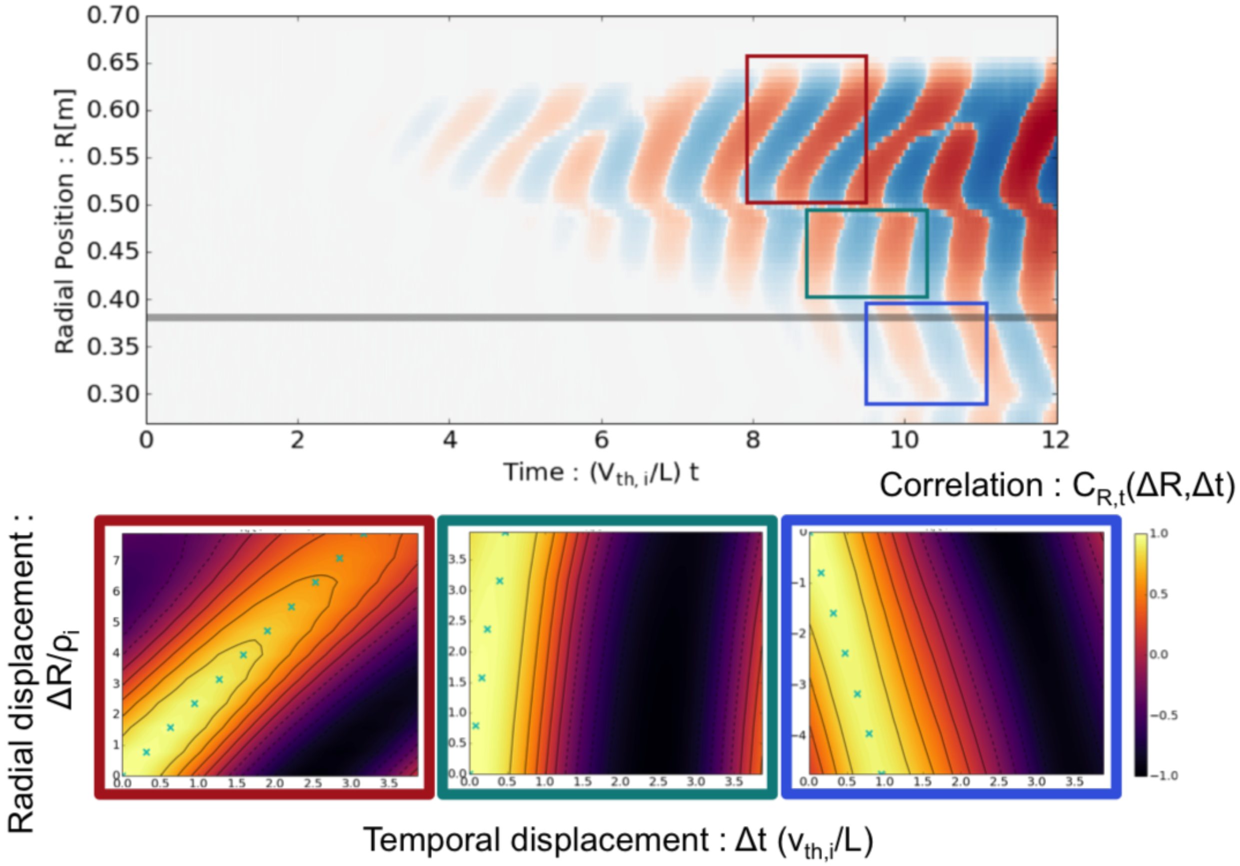

Figure 5.7: The phase velocity is found at three separate regions by calculating two-point two-time correlation functions. Outside of the separatrix, there is a radially outward phase velocity while, inside of the separatrix, there is a radially inward phase velocity.

Additionally, the two radial effects modify the growth-rate and frequency differently. Radial localization of the ion polarization in the Poisson equation causes the growth-rate to increase while removal of radial gyro-averaging of the field causes the frequency to drop. However, aside from the radial direction, the overall mode structures are pretty similar in all four of these cases. These results indicate that the assumption of chapter 4 (ie. localized simulations being similar but more pessimistic relative to instability) was justified.

Table 5.2: Comparison of phase velocities and measured propagation of turbulent structures (velocities in units of [m/s]).

	core	SOL
experiment	-2.6×10^4	1.55×10^4
simulation	-4.2×10^3	$2.0 \sim 5.5 \times 10^3$

5.3.2 Phase velocities

The phase velocity of the unstable mode can be found by calculating the two-point two-time correlation function,

$$C\left(\Delta t, \Delta R\right) = \frac{\langle \phi(t+\Delta t, R+\Delta R)\phi(t,R)\rangle}{\sqrt{\langle \phi^2(t+\Delta t, R+\Delta R)\rangle \langle \phi^2(t,R)\rangle}} \tag{5.3}$$

which is a measure of the correlation of two different points separated in space-time, ranging from 1 (correlated) to -1 (anti-correlated). The slope of the correlation function then gives the phase velocity, which are listed in table 5.2. In Fig. 5.7, the correlation functions for three separate regions are plotted in the top three panels. The locations used for the correlation functions are shown in the bottom panel of the figure which plots the potential at $Z = 0$ with respect to the radial position and time: the red square is far out in the SOL, the green square is just outside of the separatrix, and the blue square is just inside of the separatix.

From the slopes of the correlation functions, it can be seen that there is an outward phase velocity outside of the separatrix and an inward phase velocity inside of the separatrix which are shown in table 5.2. The slower velocity in the SOL corresponds to more radially outward region in the red box (in Fig. 5.7) while the faster velocity corresponds to the region just outside of the separatrix in the green box (in Fig. 5.7).

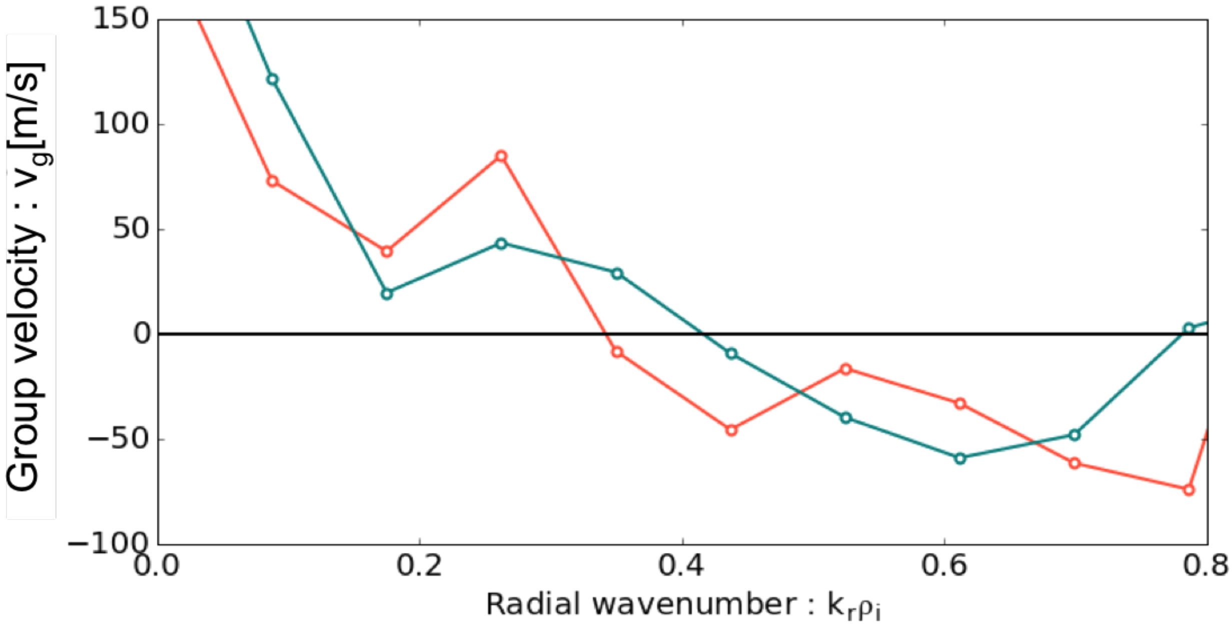

Figure 5.8: The group velocity can be estimated by calculating the dispersion $\omega_r(k_r)$ and differentiating. The red and blue lines are the group velocities calculated through the real and imaginary components of toroidally spectral-decomposed potential.

It can be seen that the simulation phase velocity is only 16% and 37% of the experimental values in the core and SOL which is a large difference. This difference is likely due to the simplified model of the simulations. The experimental values come from radial propagation delay extracted from cross-correlations of two adjacent Doppler Backscattering channels and contain all physics within the FRC. The simulation values here are based on linear physics, an adiabatic electron model, and no shear flows, all three of which may affect direct quantitative comparisons between the experiment and simulation here. Despite these differences, it should be noted that the comparison does show consistency between simulation and experiment in the inward propagation inside of the separatrix and outward propagation outside of the separatrix.

5.3.3 Group velocity

The group velocity of the unstable mode can be estimated in different ways. The first way is to use the definition of group velocity $v_g \equiv \frac{\partial \omega_r}{\partial k_r}$. The potential at $Z = 0$ can be spectrally decomposed from R to k_r using a Fourier transform (this Fourier transform is localized in a window outside of the separatrix). The frequency can then be calculated for different k_r to obtain $\omega_r(k_r)$ and its derivative. The results of this process is shown in Fig. 5.8 where the red and blue line are the group velocities based on the real and imaginary components of the toroidally spectral decomposed potential.

The actual mode structure exists in the range of $k_r < 0.8$, and it can be seen that the longer wavelengths move outward while shorter wavelengths move inward. It should be noted that the radial wavelength should rigorously use Fourier-Bessel decomposition so quantitative discrepancies may arise from the use of just Fourier decomposition.

Another way that group velocity can be estimated is by using the ratio of potential similar to Fig. 5.5. However, instead of the ratio of the average potential in different regions, I use the ratio of potential at different radial positions to the potential at a position of the peak mode amplitude which I term the source radial position, ie. $\phi(R)/\phi(R_{source})$. The time at which the ratio flattens can be found by searching for the first moment the derivative of the ratio goes to zero as seen in Fig. 5.9.

Using this method, I find the time at which the ratio flattens for each different radial position, and these are plotted as the white circles on the right panel of Fig. 5.10. On the left panel, the group velocities, estimated by the slope calculated from the time and radial positions, are displayed. The inward velocities are plotted in red with the vertical red line indicating an average of $< v_g > \approx -180$[m/s]. The outward velocities are plotted in blue with the vertical blue indicating an average of $< v_g > \approx 370$[m/s]. This is consistent with the group velocities

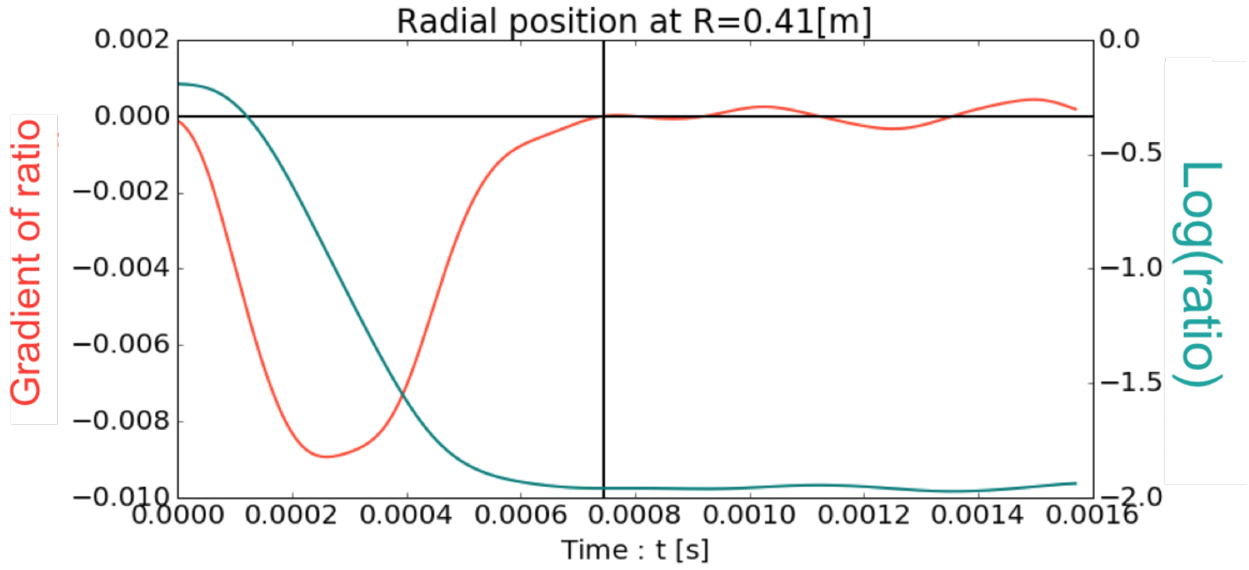

Figure 5.9: A sample of how to find the estimated time of eigenfunction formation. The ratio of potential at some radial location $\phi(R)$ to the potential at the location of the peak amplitude will initially decrease before flattening out. The estimated time can be found by finding the location of the initial flattening.

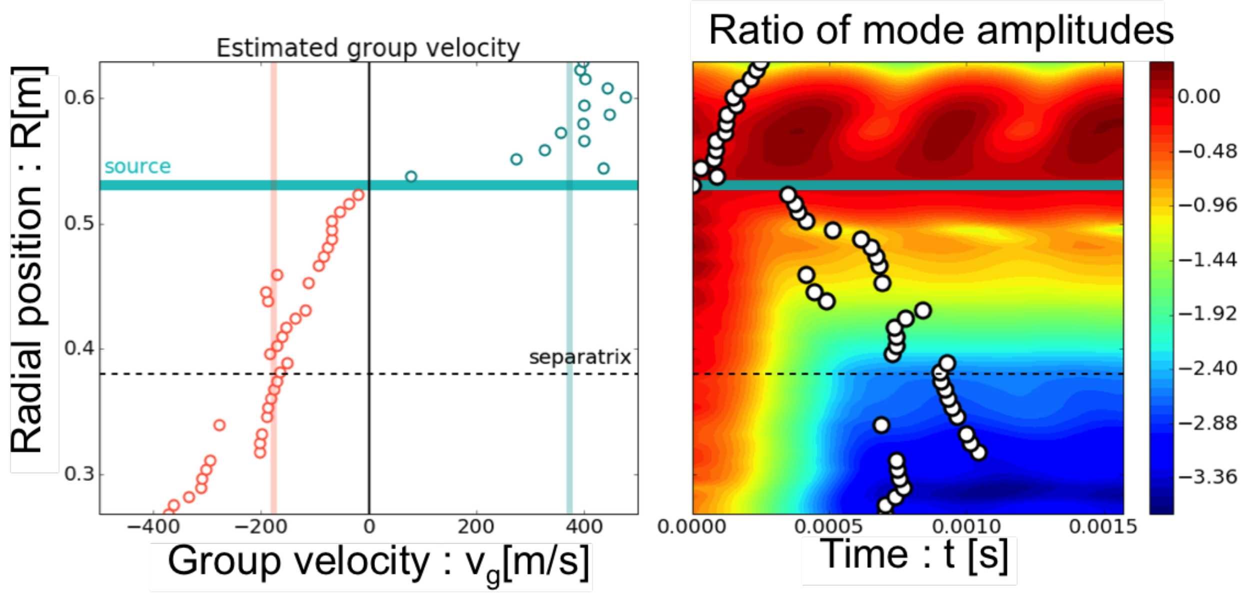

Figure 5.10: Using the estimated time from the method seen in Fig. 5.9, estimates for the group velocities can be calculated for the different radial positions and are plotted on the left panel. The right panel shows the estimated points where the ratios of potential begin to flatten.

found from the dispersion relation where the inward velocities are lower than the outward velocities as well.

An important feature from this analysis is the time required for the instability to propagate into the core and form an eigenmode. Seen in the right panel of Fig. 5.10, it takes about 1[ms] before the eigenmode forms which is on the order of the FRC experiments and, therefore, able to be the mechanism in which the core fluctuations arrive.

5.4 Nonlinear spreading

5.4.1 Ratio of core to SOL mode amplitude

With nonlinear effects included in the simulation, the unstable mode saturates due to the nonlinear feedback to the particles in the form of the $E \times B$ drift where the electric field comes from the self-consistent potential found from the Poisson equation.

In the top panel of Fig. 5.11, the magnitude of the potential at $Z = 0$ for $n = 30$ is plotted against radial position and time with a logarithmic colorbar. Just as in the linear simulation, the unstable mode grows first in the SOL and the full eigenmode is formed around $(V_{th,i}/L)t = 7 \sim 10$ (about 1[ms] or less). After $(V_{th,i}/L)t \approx 10$, there is a clear saturation at mode amplitude about $\frac{e|\phi|}{T_e} \sim 0.05$ in the SOL region.

In the bottom panel of Fig. 5.11, the ratio of the potential inside and outside of the separatrix (just as in section 5.3) is plotted in red and blue for the nonlinear and linear simulations of $n = 30$. Just as in section 5.3, the linear ratio initially decreases as the instability grows in the SOL and flattens when the eigenmode is formed in both the SOL and core. The nonlinear ratio, however, rises up as the mode begins to saturate (II). After saturation $(III \sim V)$, the ratio has risen from $\mathcal{O}(10^{-3})$ to $\mathcal{O}(10^{-1})$.

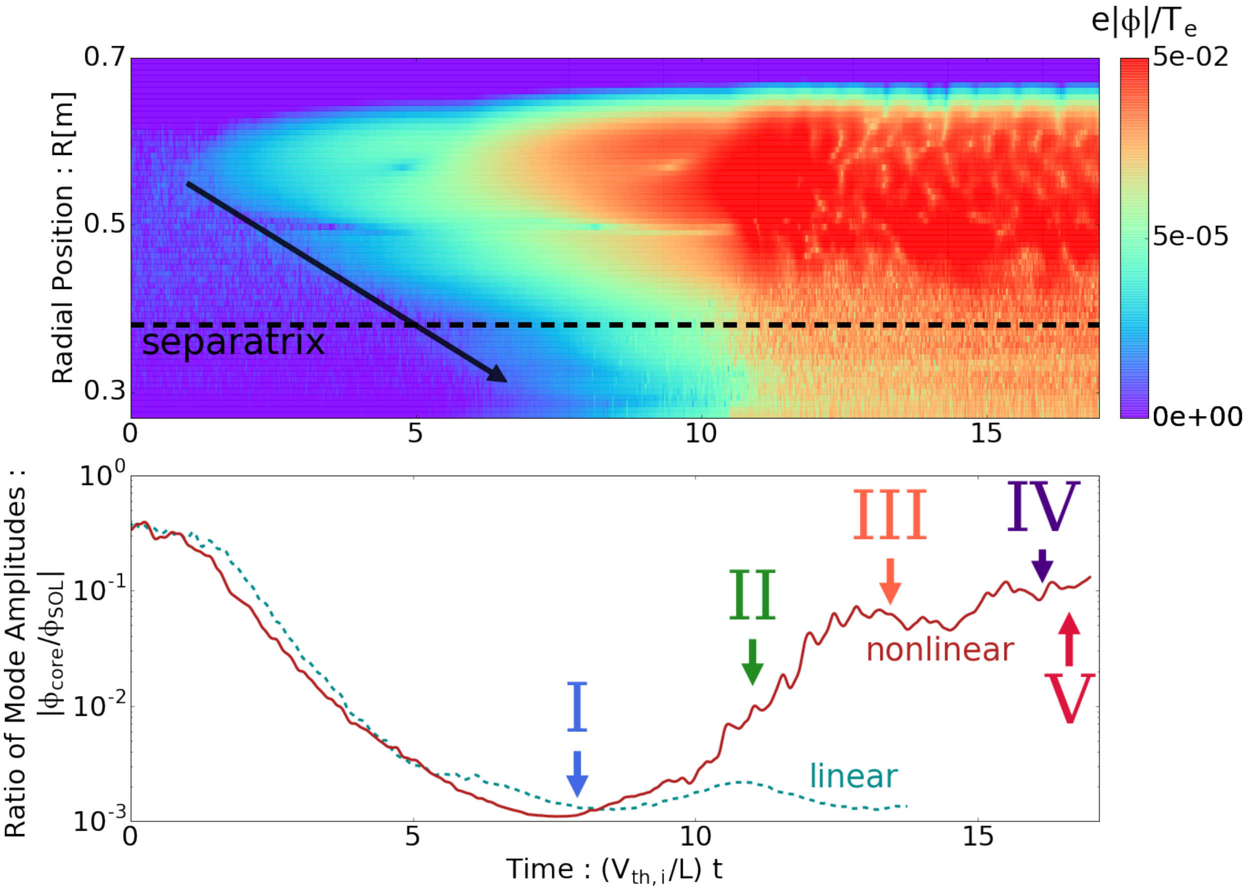

Figure 5.11: The top panel shows the electrostatic potential at $Z = 0$. The mode can be seen to start in the SOL before spreading past the separatrix. The bottom panel shows the time-history of the ratio of electrostatic potential inside and outside of the separatrix with the dashed blue line having non-linear effects turned off and the solid red line having non-linear effects turned on. In both cases, initially, there is noise of equal amplitude in both the core and SOL so that the ratio is $\mathcal{O}(1)$. As the instability in the SOL grows, the denominator grows such that the ratio decreases. With non-linear effects included, mode saturation occurs and the ratio of core to SOL potential increases from $\mathcal{O}(10^{-3})$ to $\mathcal{O}(10^{-1})$.

This behavior is due to the saturation of the mode which halts the increase of the potential outside of the separatrix (denominator of the ratio), but the potential inside of the separatrix (numerator) still increases due to nonlinear spreading from the outside. This increase in the inside potential is due to nonlinear spreading because, as shown in section 5.3 and in chapter 4, the core is stable. At some point, there is a balance between the spreading from the SOL to the core and local damping in the core such that the ratio holds at about $\phi_{core}/\phi_{SOL} \sim 10^{-1}$.

Although this simulation contains only a single toroidal mode, this saturated ratio of mode amplitude between the core and SOL is consistent with the experimental measurements of density fluctuations in which the ratio of core to SOL fluctuations ranges from $\mathcal{O}(10^{-2})$ to $\mathcal{O}(10^{-1})$ as shown in Fig. 1.2.

5.4.2 Nonlinear spreading

In addition to saturation, there is modification of the mode structure. In Fig. 5.12, the mode structure is plotted for the linearly growing phase (I) and for the time of saturation (III) for comparison. (Note that the logarithmic colorbar scale is different between this figure and the previously shown in Fig. 5.2 which accounts for the differences in the linear figures. However, the colorbars for this comparison are using logarithmic scale of the same ratio.)

From the R-Z plot, it can be seen that the mode broadens from a shorter radial width to a longer radial width. In addition, the mode clearly shifts a bit closer to the separatrix, with small scale structures in the core and just outside of the separatrix.

This broadening and inward shift can be more easily seen in the radial envelope of the instability. In Fig. 5.13, the normalized field-line-averaged magnitude of the potential is plotted against the poloidal flux function (ie. radial position) for different times corresponding to the times marked in Fig. 5.11. Here, it can be clearly seen that the linear

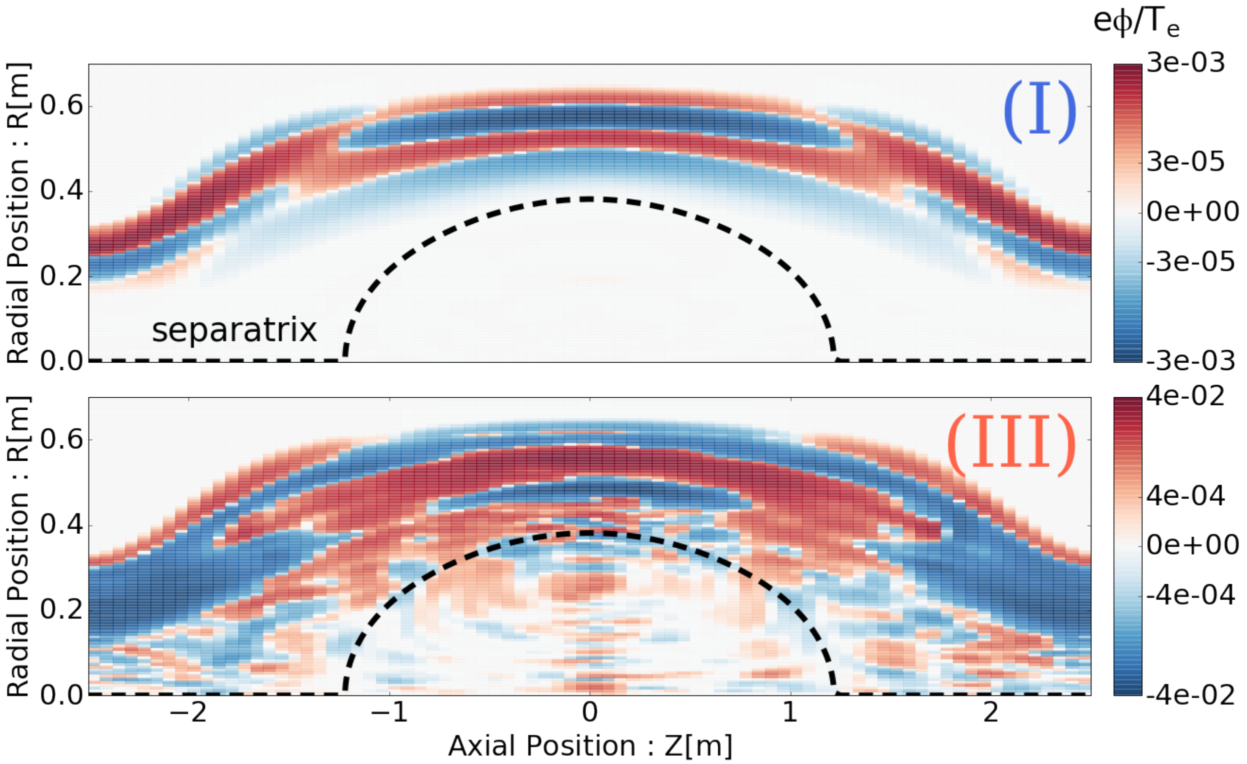

Figure 5.12: The two panels show the mode structures at different times marked within the time-history in Fig. 5.11. At (I), the linear eigenmode has formed. At (III), the mode has saturated and the original mode structure has broadened and shifted more inward.

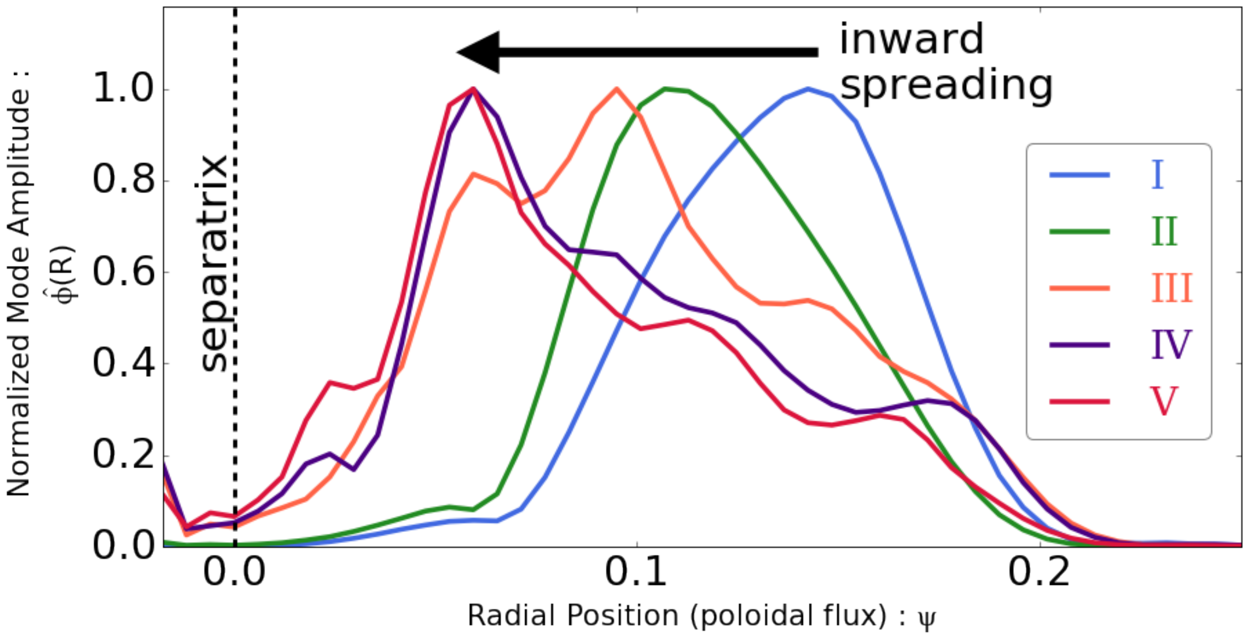

Figure 5.13: Normalized field-line averaged electrostatic potential is plotted for the different times marked within the time-history in Fig. 5.11. It can be clearly seen that radial envelope shifts inward and broadens during (I)-(III). The broadened structure does not change much between (IV)-(V) after mode saturation.

mode forms in the SOL with very low amplitude in the core (I). There is turbulence spreading inward as the mode is saturating (II). The fluctuation profile is broadened after saturation with slightly higher amplitude in the core (III). The broadened fluctuation profile shifts a bit more inward but remains mostly outside of the separatrix ($IV - V$).

5.5 Discussion

Previous local linear simulations studied the properties of pressure gradient driven drift-waves in the FRC and found the core to be robustly stable and the SOL to be unstable[40]. However, in experiments conducted by Schmitz *et al*[60], fluctuations exist in both the core and SOL. A possible candidate suggested for the origin of the core fluctuations is turbulence spreading from the SOL. In this chapter, nonlocal gyrokinetic simulations have been used to investigate the origins of fluctuations in the FRC core.

Using gyrokinetic ions and adiabatic electrons, nonlocal simulations find that a slab-like ITG instability develops in the SOL. It is shown that this instability can propagate from outside of the separatrix to inside of the separatrix. Numerical scans reducing the simulations to the local approximation show that the extension of the radial eigenmode into the core is due to radially nonlocal FLR effects. When radially nonlocal FLR effects are completely dropped (ie. fully local approximation), the instability grows only in the SOL while the core remains stable as expected from the previous local linear simulations.

This linear extension of the instability into the core is due to the modification of the dispersion relation. With a finite k_r, both phase and group velocities in the radial direction become possible. The phase velocity is calculated in separate regions from the simulation results. Just inside the separatrix, a radially inward phase velocity of $v_{ph,in} \sim -4.2 \times 10^3$[m/s] is found while, just outside of the separatrix, a radially outward phase velocity of $v_{ph,out} \sim 5.5 \times 10^3$[m/s] is found. In comparison, radial propagation velocities of turbulent structures, extracted from experimental DBS measurements, show faster velocities ($v_{ph,in} \sim -2.6 \times 10^4$[m/s], $v_{ph,out} \sim 1.55 \times 10^4$[m/s]) but are also consistent in the directions of propagation.

From the simulations, group velocities can also be estimated from two methods described in section 5.3. Using the mean radially inward group velocity found ($v_g \sim -180$[m/s]), the estimated time for the instability to propagate into the core and establish the eigenmode is on the order of ~ 1[ms] which is within the millisecond FRC lifetimes. Interestingly, the second method of calculating radial group velocity also indicates that shorter wavelengths move inward while longer wavelengths move outward which is also consistent with the core fluctuation spectrum which peaks at shorter wavelengths.

In these nonlocal simulations, the inclusion of nonlinear effects has also been studied. Despite lacking zonal flows in these simulations, nonlinear saturation occurs around $\frac{e|\phi|}{T_e} \sim 0.05$ in the SOL region. The radial envelope of the electrostatic potential both widens and moves inward during the nonlinear phase. Moreover, the ratio of the saturated amplitude in the core to the SOL is about $\mathcal{O}(10^{-1})$ which is consistent with the lower amplitude fluctuations ($\mathcal{O}(10^{-1}) \sim \mathcal{O}(10^{-2})$) measured by Schmitz *et al*[60].

The spread of fluctuations from the SOL to the core has been studied with single-mode simulations and shown to be consistent with various aspects of experimental measurements. Since the origin of fluctuations is shown to be from the SOL, chapter 6 focuses on the physics of turbulence and transport in just the SOL using multiple-mode simulations.

Chapter 6

Turbulent transport in the scrape-off layer

In the comprehensive set of local, linear simulations of chapter 4, the electrostatic drift-wave is found to be stable in the core and unstable in the SOL. With the cross-separatrix, non-local simulations of a single toroidal mode of chapter 5, fluctuations are shown to radially spread from the SOL to the linearly stable core. The instability is also shown to saturate with the saturated amplitude being larger in the SOL by an order of magnitude, again affirming the turbulent property of the SOL.

To study turbulence, containing multiple toroidal modes for the mixing and overlapping of different modes can generate more realistic eddies during the nonlinear phase. In this chapter, turbulent transport in the SOL is investigated through non-local simulations of multiple toroidal modes using the same equilibrium as in chapter 5. These simulations are confined to the SOL as a first step due to the importance of the SOL as a source of instability and turbulence.

As in chapter 5, an ion temperature gradient driven drift-wave instability grows. Saturation occurs at similar levels as before, and profile relaxation is observed after saturation (but is not the mechanism of saturation). Due to the multiple toroidal modes allowed in the simulation, mode-mode coupling occurs, and previously damped or near-stable modes are able to grow through nonlinear wave-wave interactions. By the end of simulation, a previously hypothesized inverse toroidal spectral cascade is observed and confirmed. Finally, self-consistent ion heat flux is calculated, and an upper bound for the electron heat flux is also calculated through the use of test particles.

6.1 Simulation model

Simulations presented in this chapter have been performed with A New Code (ANC), using the cylindrical non-field-aligned version as detailed in chapter 3. The equilibrium and set-up are almost the same as in chapter 5, with the exception of multiple toroidal modes and reduction of the simulation domain to just the SOL.

Ions are gyrokinetic with FLR effects calculated by 4-point sampling of the gyro-orbit while electrons are represented by the adiabatic response in the Poisson equation. This is a first step due to numerical difficulties in time-resolution (faster electron motion along the parallel direction creates stricter constraint due to CFL conditions) and grid-resolution (shorter wavelength structures may need to be resolved). Future simulations will use drift-kinetic electrons as the recent field-aligned features of ANC (described in chapter section 3.4) will help mitigate some of the numerical difficulties.

6.1.1 Simulation domain

Multiple toroidal modes

In the simulations of this chapter, multiple toroidal modes (with toroidal mode number denoted by n) are kept. Here, a toroidal wedge domain of $[0, \frac{2}{5}\pi]$ is used, as described in section 2.3. Sixteen toroidal modes (multiples of 5, ie. $n = \{5, 10, ..., 75, 80\}$) are kept with the zonal mode and other toroidal modes filtered out. (The zonal mode is filtered out of these simulations due to the numerical difficulty of correcting resolving it within the non-field-aligned version of ANC.)

In the solution for the electrostatic potential, a Laplacian for each different toroidally decomposed component is used, as described in section 3.2. However, the self-consistent electric field is found by differentiating the potential in real space so different toroidal mode numbers can couple through the particle equations of motion when nonlinear effects are included.

SOL geometry

Chapters 4 and 5 have shown the importance of the SOL in driving turbulence in the FRC. For the simulations of this chapter, the simulation domain contains only the SOL as shown by Fig. 6.1. The SOL is cut off at $Z = \pm 5$[m] right before the formation section of the FRC and uses a periodic axial boundary. The radial boundaries are such that the fluctuations and particle weight ($\delta f/f$) of particles within a distance near the outer boundary are zeroed. These simulations use the second Poisson solver described in section 3.2.

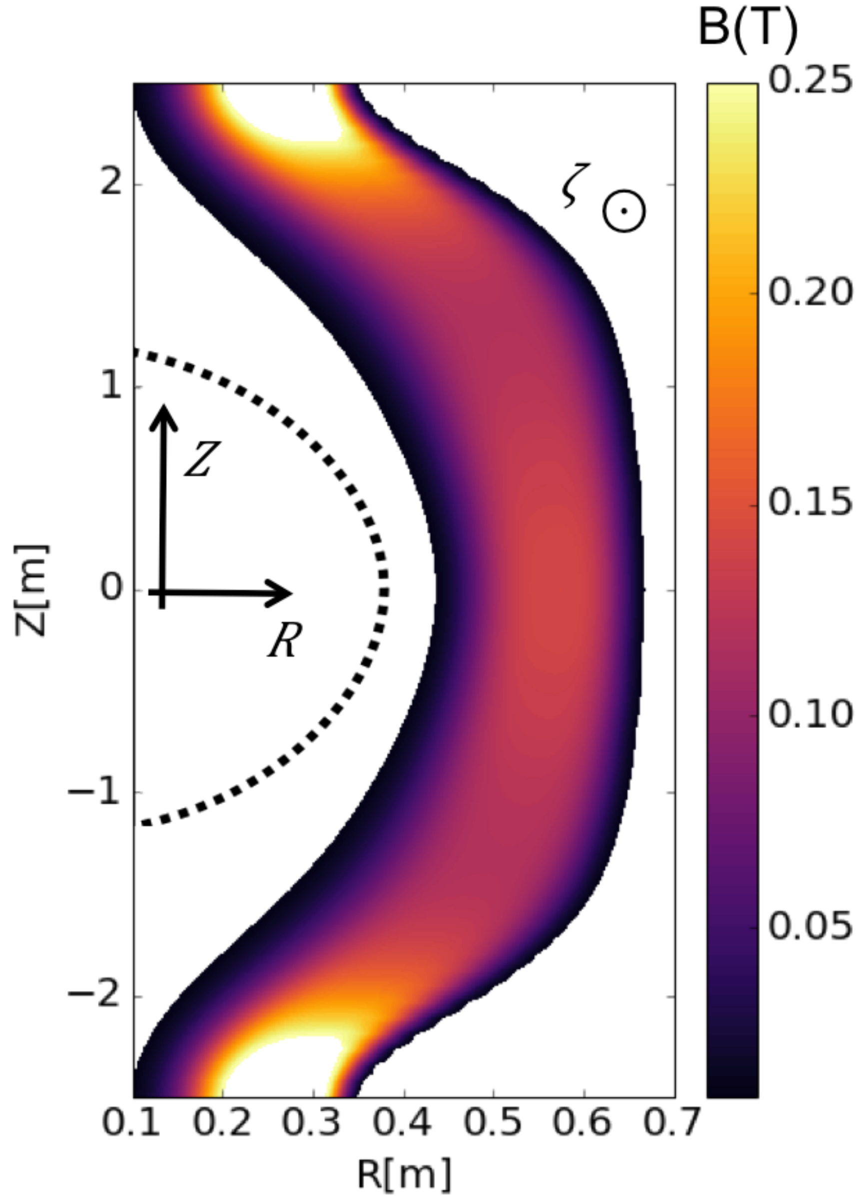

Figure 6.1: The equilibrium magnetic field strength is plotted on the R-Z plane with the directions shown. The dashed line represents where the separatrix is located. The simulation domain is restricted to just the SOL by smoothly zeroing particle weights outside of the radial boundaries shown.

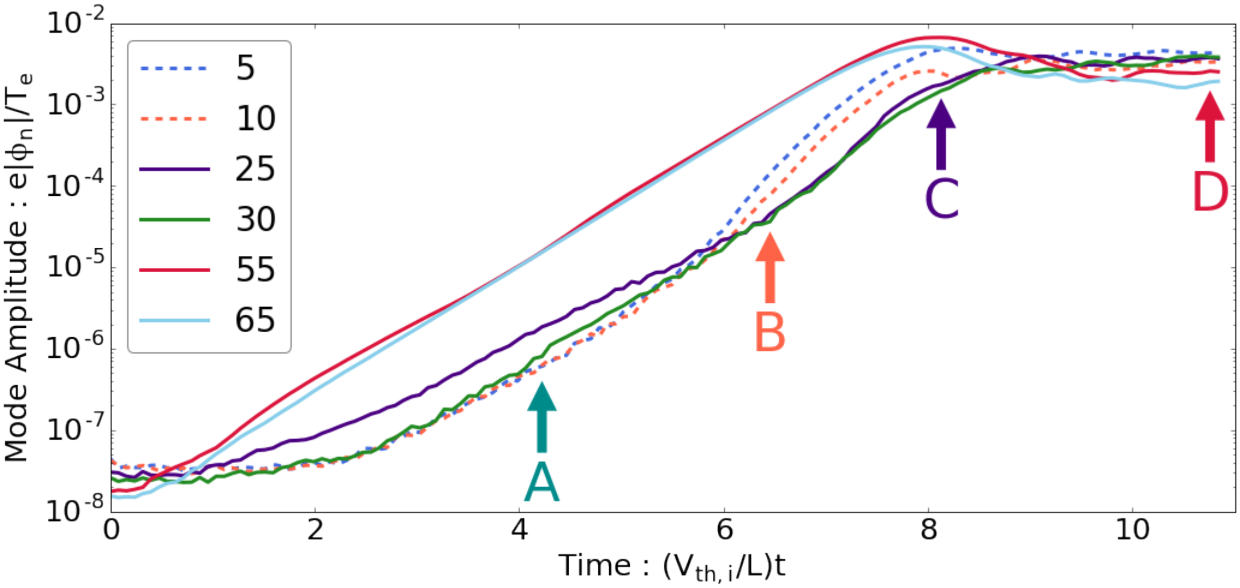

Figure 6.2: The time history of RMS potential of selected toroidal modes is plotted. (A) and (B) denote linearly growing times, (C) denotes the moment of saturation, and (D) denotes time after saturation. Note that the earliest growing modes are shorter wavelength modes before the longer wavelength modes catch up and overtake in amplitude.

Equilibrium

As in chapter 5, simulations are initialized with a FRC equilibrium magnetic geometry which is representative of typical FRC plasmas realized in the C-2 experiment calculated using the LR_eqMI code[23]. The equilibrium pressure is designed to drive instability in the SOL with ion temperature and density gradients. Electron temperature is flat at $T_e = 80$[eV].

Within this chapter, the unit of time is defined as $\tau \equiv (V_{th,i}/L)$.

6.2 Turbulent structure

6.2.1 Saturated electrostatic potential

In chapter 5, an instability was found to grow in the SOL and spread into the core. Using the same equilibrium, an instability is found as expected, and its nonlinear saturation and evolution with multiple toroidal modes is studied.

The time history of the electrostic potential is plotted for a selected number of toroidal modes in Fig. 6.2. The fastest growing modes are the shorter wavelength modes while the initially damped or stable modes are the longest wavelength modes. Four different times are marked and referred to in later sections: (A) the initial linear growth phase, (B) the later linear growth phase in which shorter wavelength modes have overtaken the intermediate wavelength modes, (C) the moment of nonlinear saturation, and (D) about two linear wave periods after saturation.

6.2.2 3-D turbulence structure

The mode structure in the R-Z plane is quite similar to chapter 5, but since this set of simulations contains multiple toroidal modes, it is instructive to see the 3-dimensional turbulence structure. In Fig. 6.3 and Fig. 6.4, the mode structures of a linearly growing time-step near (B) and the nonlinearly saturated time-step near (D) are shown. The separatrix drift-surface is represented by the purple, and a SOL drift-surface is represented by the transparent blue.

The $R - Z$ structure (seen by the slice along the axial direction) shows a long parallel wavelength which remains from the linearly growing time-step to the nonlinearly saturated time-step. However, the $R - \zeta$ structure (seen by the slices perpendicular to the axial

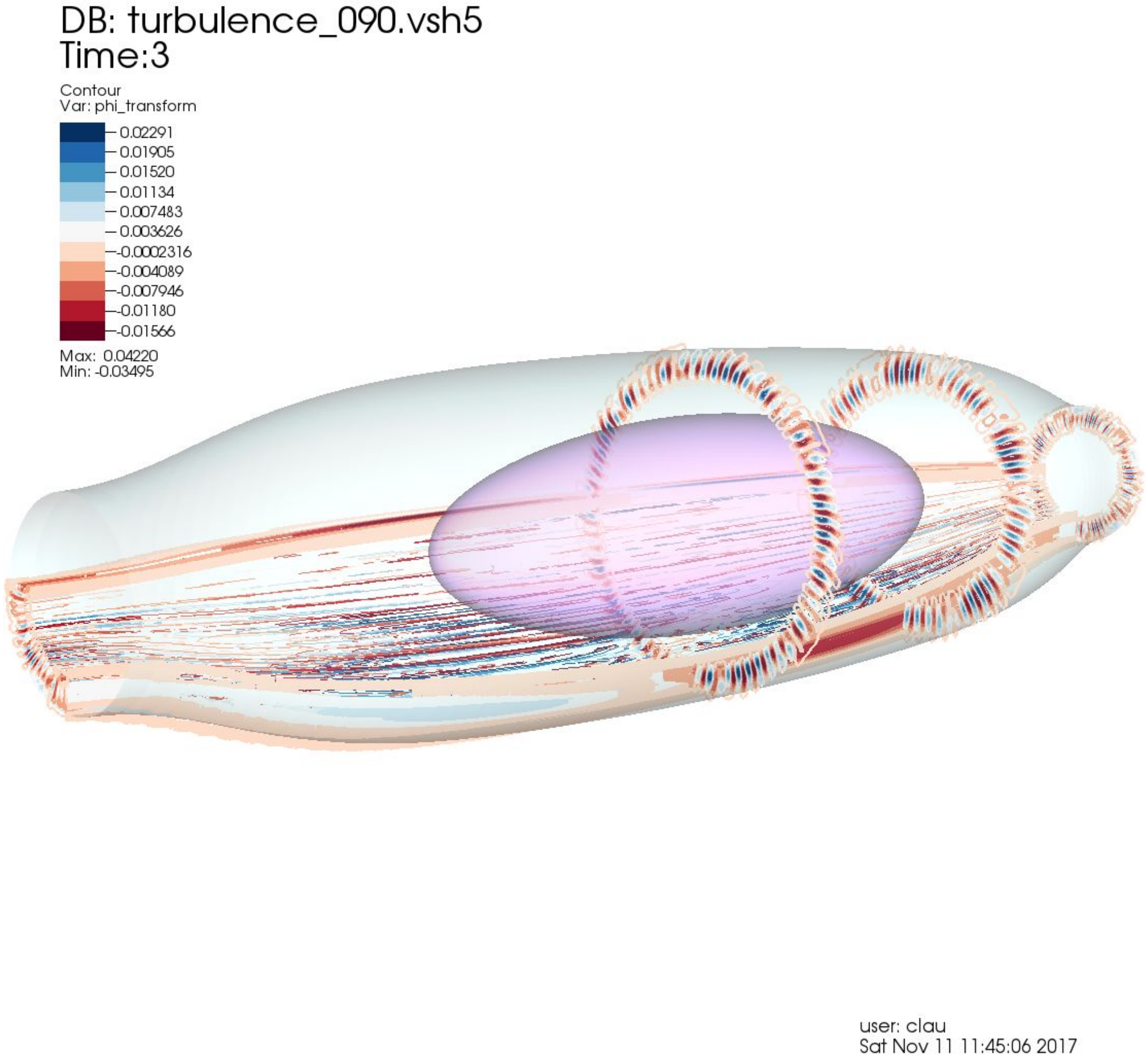

Figure 6.3: The 3D linear eigenmode structure from ANC simulations is shown. 2D planes are cut to show structures at ($Z = 0$[m],$Z = -1.25$[m],$Z = -2.5$[m]). The transparent purple oval shape shows the location of the separatrix while the transparent blue bottle shape shows the location of a drift-surface in the SOL.

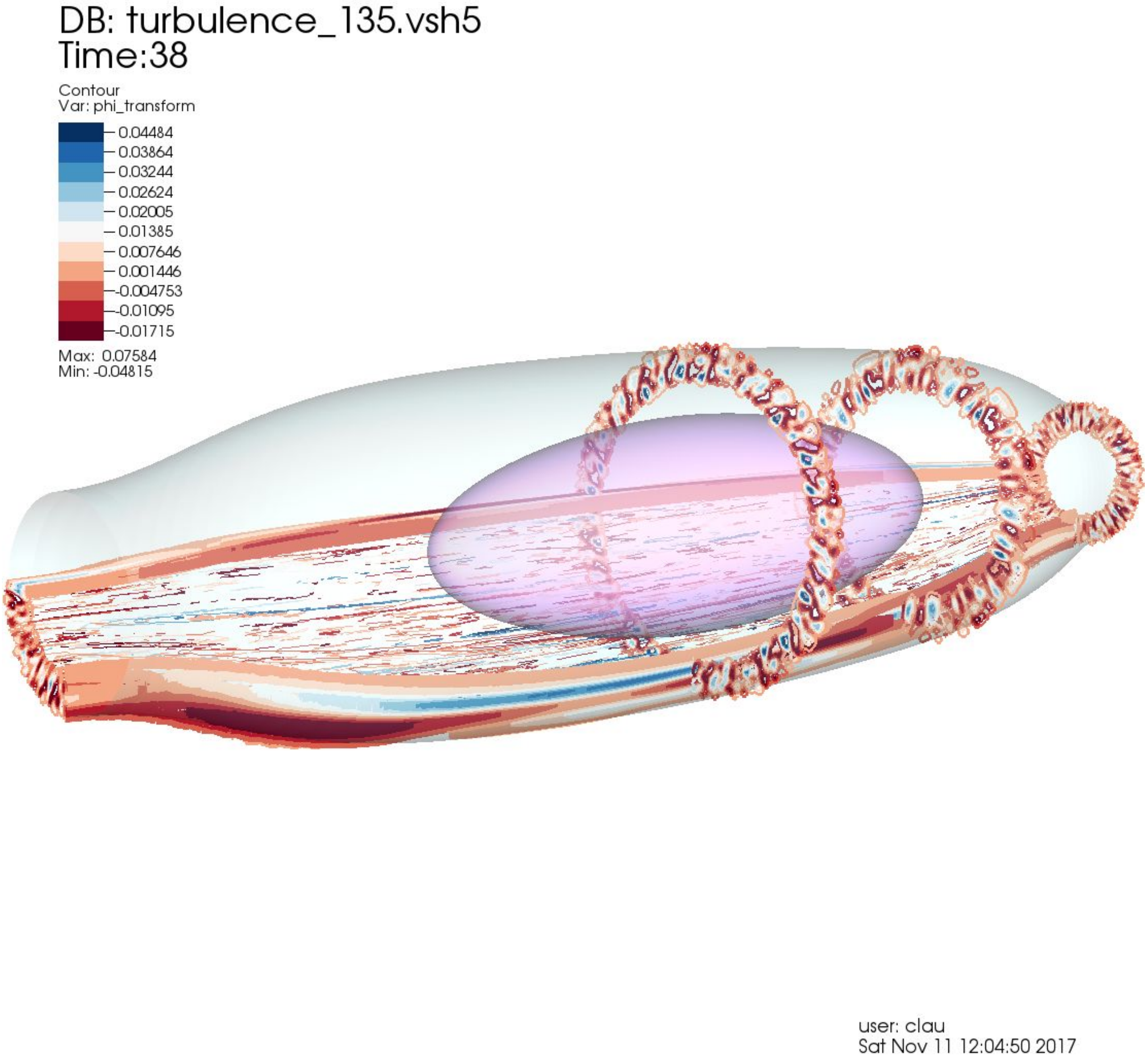

Figure 6.4: The 3D turbulence structure from ANC simulations is shown. 2D planes are cut to show turbulence structures at ($Z = 0$[m],$Z = -1.25$[m],$Z = -2.5$[m]). The transparent purple oval shape shows the location of the separatrix while the transparent blue bottle shape shows the location of a drift-surface in the SOL.

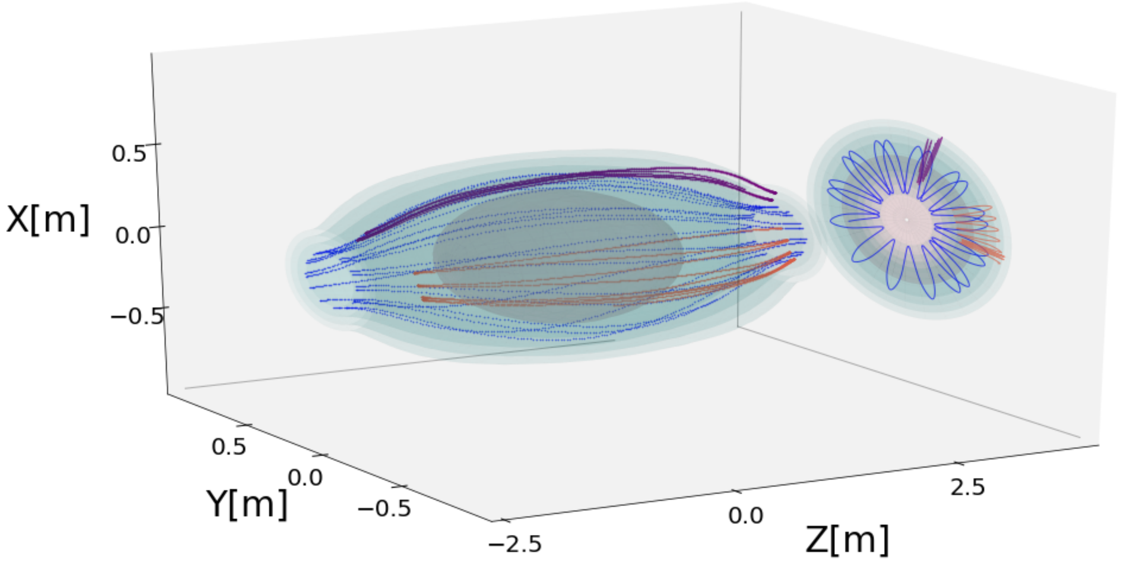

Figure 6.5: Several trajectories of ion gyrocenters are plotted in 3D space. The trajectories are also projected onto the X-Z plane and X-Y plane. (Since the simulation domain is a toroidal wedge, the toroidal motion should be viewed with the understanding that there is a periodic boundary explaining the well-confined toroidal position. Different particles are plotted with a toroidal offset to maintain ease of view.)

direction) is modified from a very short wavelength pattern in the linearly growing stage to the much larger structure eddies in the saturated turbulent stage. The radial wavelength can also be seen to decrease in the $R - Z$ structure, which will be discussed in section 6.4.

6.2.3 Gyrocenter trajectories

The full 3-dimensional trajectories and their 2-dimensional projections along the axial direction for several tracked ion gyrocenters are shown in Fig. 6.5 to give a sense of the motions of particles in the simulations. From the full trajectories, it can be seen that there are both ions trapped within the larger magnetic mirror of the SOL (purple and orange) and ions that are not trapped (blue) (and are treated by a periodic axial boundary condition).

The toroidal drifts of the ions are more easily seen in the 2-dimensional projection. These drifts are made up of the curvature and ∇B drifts (linear) and the $E \times B$ drift (nonlinear). The toroidal drift of the passing ion (blue) is large because the component of the curvature drift is large due to the larger parallel velocity relative to its perpendicular velocity. The toroidal drifts of the trapped ions (purple and orange) are smaller because the component of curvature and ∇B drifts are more comparable. The change in pattern of the trajectories is due to the toroidal component of the $E \times B$ drift.

The gyrocenters stay on their initial drift-surface until the radial component of the nonlinear $E \times B$ drift moves them outward. This can be seen in the trapped ions which move radially outward from their initial orbits. (This should not be confused with the radial part of the 2-dimensional projection which is due to the particles staying on their drift-surfaces.)

6.3 Mode-mode coupling

6.3.1 Growth-rates

As seen in the time-history plot of Fig. 6.2, there is a change in the growth rates of different toroidal modes. In Fig. 6.6, the growth-rate is calculated for the different toroidal modes using a least-squares fit with time segments of roughly about 0.8τ. It can be seen that the longer wavelength modes are stable before $t/\tau \sim 2$ and are almost double the growth rates of the other modes from about $t/\tau \sim 6$ until saturation.

Taking a little more care to calculate the growth rates with larger time segments, the linearly growth phase can be roughly separated into three segments. The exponential fits based on these three segments are shown in Fig. 6.7 for each toroidal mode in the simulation.

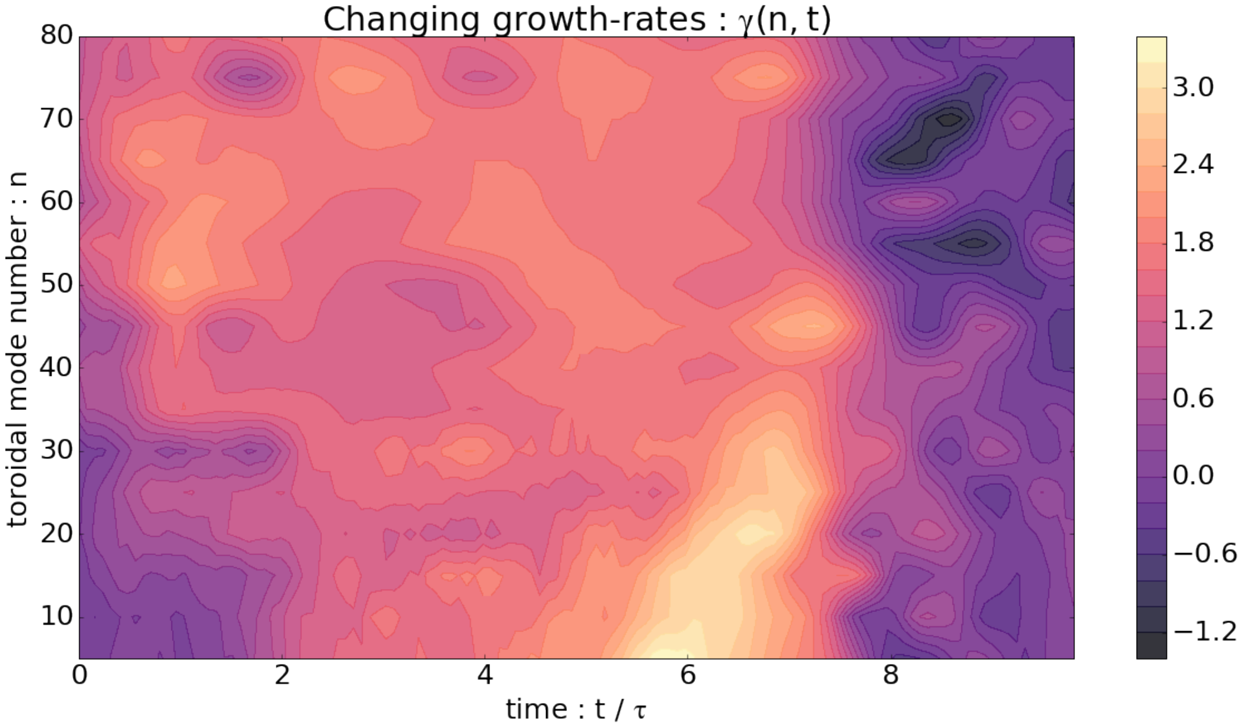

Figure 6.6: The time history of growth rates calculated for different toroidal modes is plotted. The originally damped or stable longer wavelength modes begin to grow at the same rates before roughly doubling in growth rates.

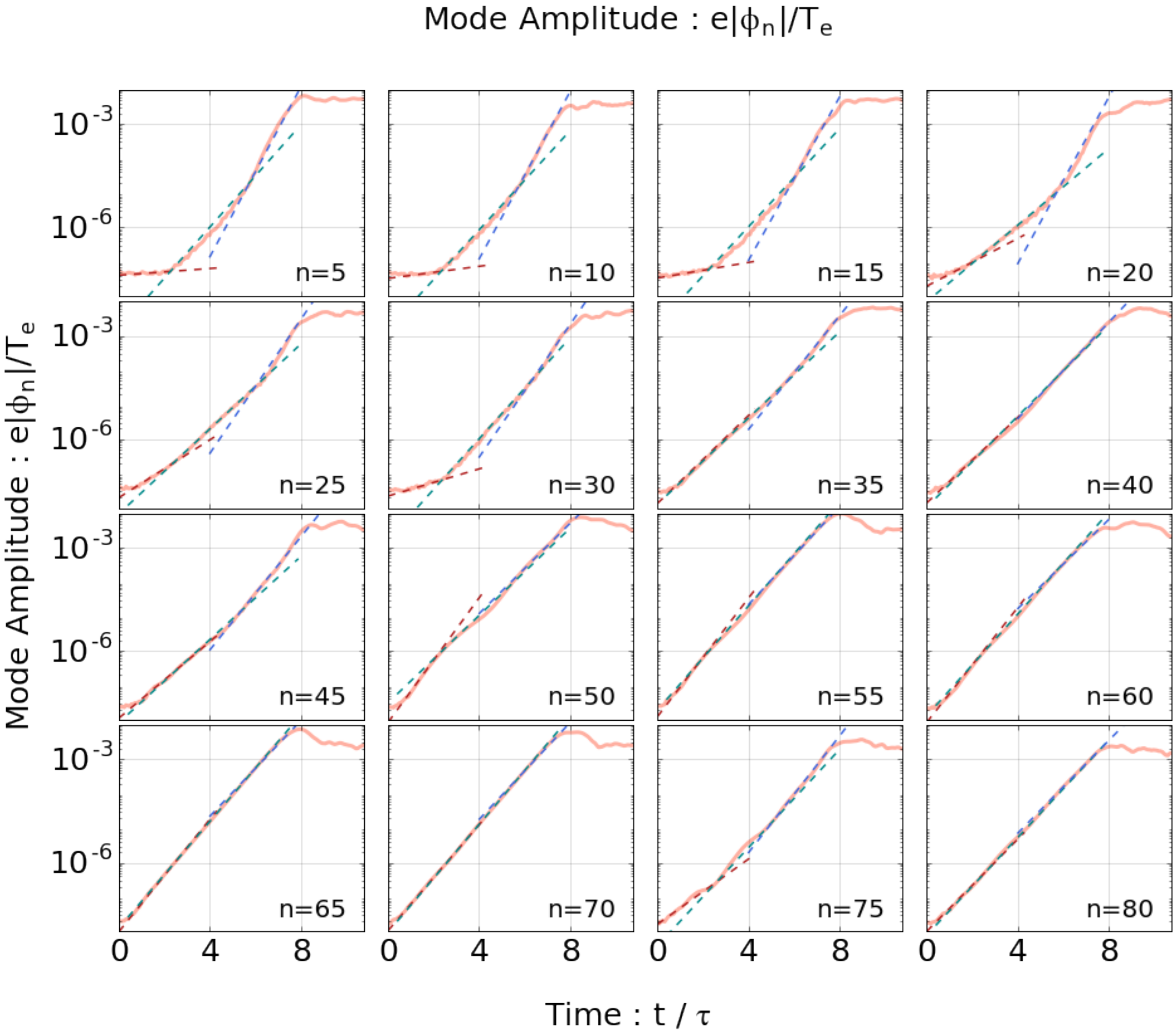

Figure 6.7: The growth-rate calculation (through linear fitting of $\log \phi(t)$) is shown for all different toroidal modes in the simulation. For the longest wavelengths ($n = 5 \sim 15$), the growth-rate clearly changes from stable to unstable with increasing growth-rate.

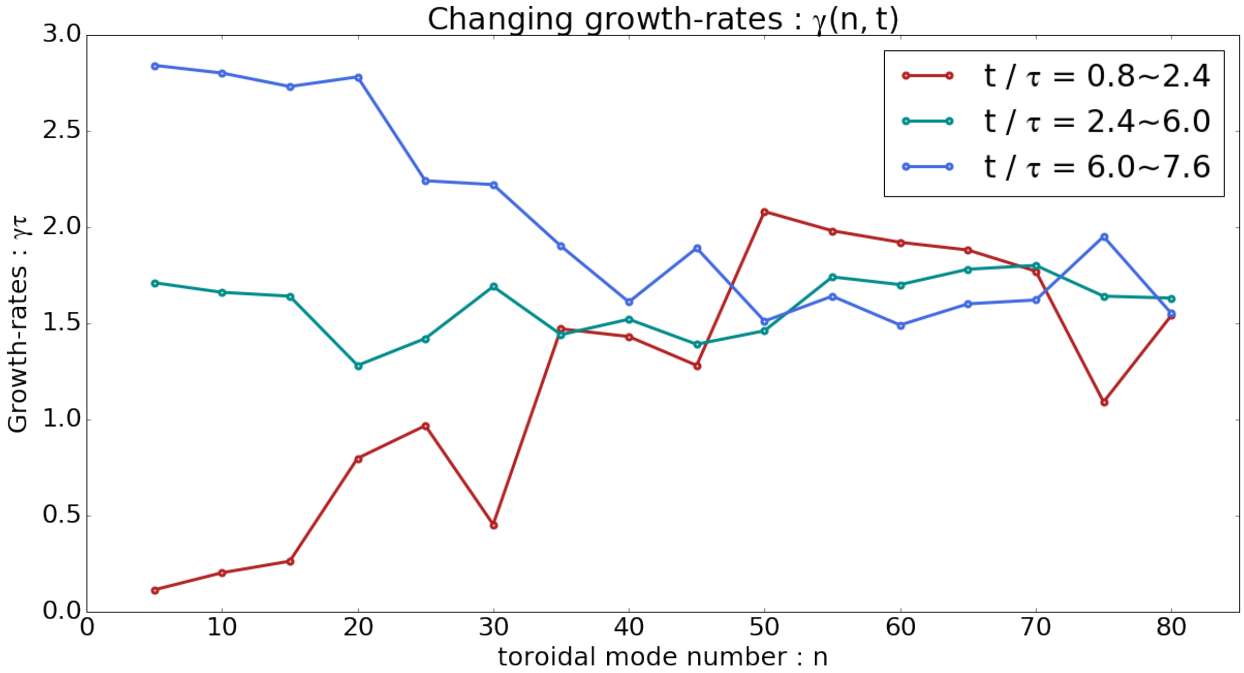

Figure 6.8: The growth-rate has roughly three phases as seen in Fig. 6.7. Here, the growth rates for each of those three phases is plotted against the toroidal mode number. The originally damped or stable longer wavelength modes are numerically coupled to the other modes before the nonlinear coupling leads to almost double the growth-rate of the unstable modes.

The growth rates calculated from the least-square fits for these three segments are shown in Fig. 6.8. It can be seen that the growth rates of the middling to short wavelengths ($n \geq 40$) mostly remain about the same growth-rate through the evolution of the instability. The longer wavelengths, especially $n = 5 \sim 15$ jump to almost double the growth rates of the shorter wavelengths. This change in growth rates is due to the mode-mode coupling, detailed in the next subsection.

6.3.2 Three-wave interactions

Spectral density calculation

The spectral density can be calculated to illustrate the changes in energy among the different toroidal modes in the simulation. To calculate the spectral density, the autocorrelation[38, 53] is first calculated

$$\begin{aligned} C_k(\tau) &= \lim_{T\to\infty} \int_{-T/2}^{T/2} dt \Phi_k(t)\Phi_k^*(t+\tau) \\ \to &= \frac{1}{N-m} \sum_{n=1}^{N-m} \Phi_k(n\Delta t)\Phi_k^*((n+m)\Delta t) \end{aligned} \tag{6.1}$$

which gives a sense of how quickly the signal decays with respect to time. The autocorrelations calculated for the nonlinearly saturated phase are shown in Fig. 6.9 as

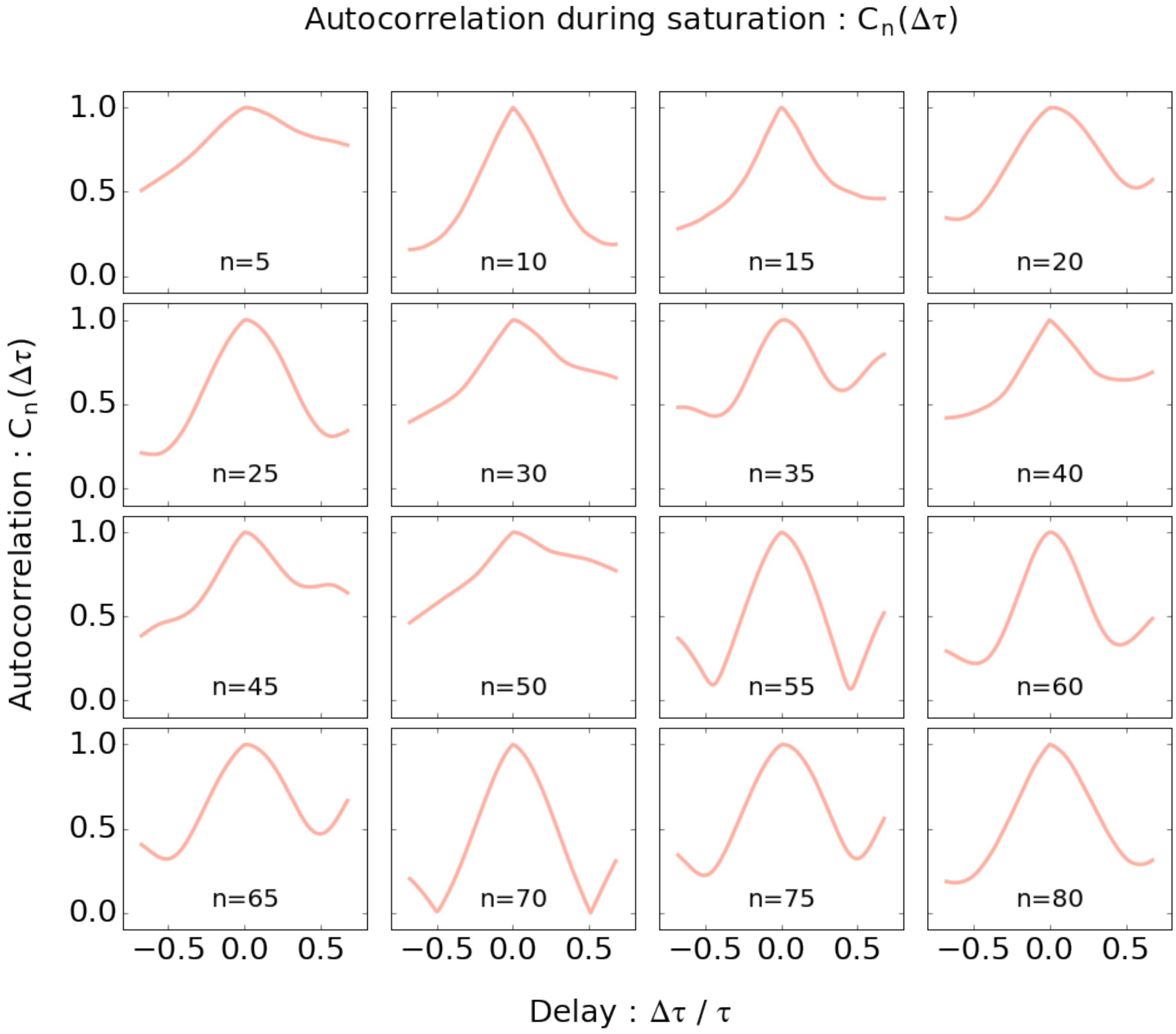

Figure 6.9: The autocorrelations for all of the toroidal modes are calculated for the nonlinearly saturated phase. By itself, the autocorrelations are not easy to understand, but the spectral density can be calculated from these to yield more familiar dispersions as seen in Fig. 6.10.

an example. By itself, however, the autocorrelations are not easy to interpret. Using the autocorrelation, the spectral density[38, 53] can be calculated by

$$
\begin{aligned}
S_k(\omega) &= \sum_{m=-M}^{M} \lambda(m\Delta t) C_k(m\Delta t) e^{i\omega(m\Delta t)} \\
&= \sum_{m=-M}^{M} sin^2(\pi \frac{m}{M-1}) C_k(m\Delta t) e^{i\omega(m\Delta t)}
\end{aligned}
\tag{6.2}
$$

which selects out different frequencies (where the Hanning window function was inserted for the window function $\lambda(\tau)$ to ensure a correct frequency response) and yields a more familiar visualization of the data for physicists.

Linear spectral analysis

Using electrostatic potential data located at the outer midplane around the location of the peak of the mode ($R = 0.53$[m],$Z = 0$[m]), the spectral density is calculated for the duration of the linearly growing phase and shown in Fig. 6.10. For convenience, the conventional directions are used for the frequencies such that the ion direction is negative. The top panel shows the spectral density normalized to the maximum value per toroidal wavelength while the bottom panel has no such normalization. The cyan circles (cross) are the unstable (stable) frequencies found from the simulations of chapter 5 and match relatively well as expected for the linearly growing phase.

Interestingly, the bottom plot shows that much of the energy is located in $n = 70$ which seems to contradict the toroidal spectrum as seen in Fig. 6.22. However, this is because this spectral density is calculated from a single point in the R-Z plane while the toroidal spectrum in Fig. 6.22 is based on the whole simulation domain.

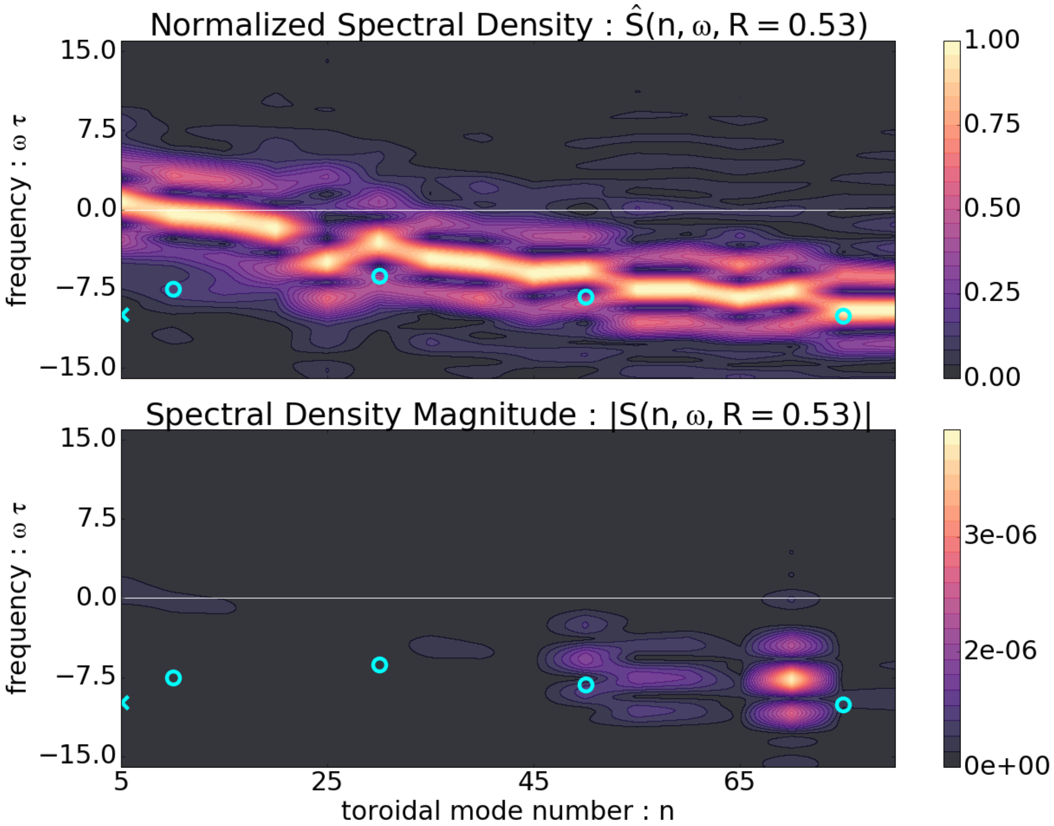

Figure 6.10: The spectral density (normalized per toroidal mode number and absolute), calculated from the linearly growing phase at (R = 0.53[m], Z = 0[m]), is plotted. It can be seen that much of the energy is residing in the short wavelength modes. The cyan circles (cross) are the frequencies of instabilities (stable modes) found from previous single toroidal mode simulations of chapter 5. Despite being confined in the SOL, the dispersion is essentially the same.

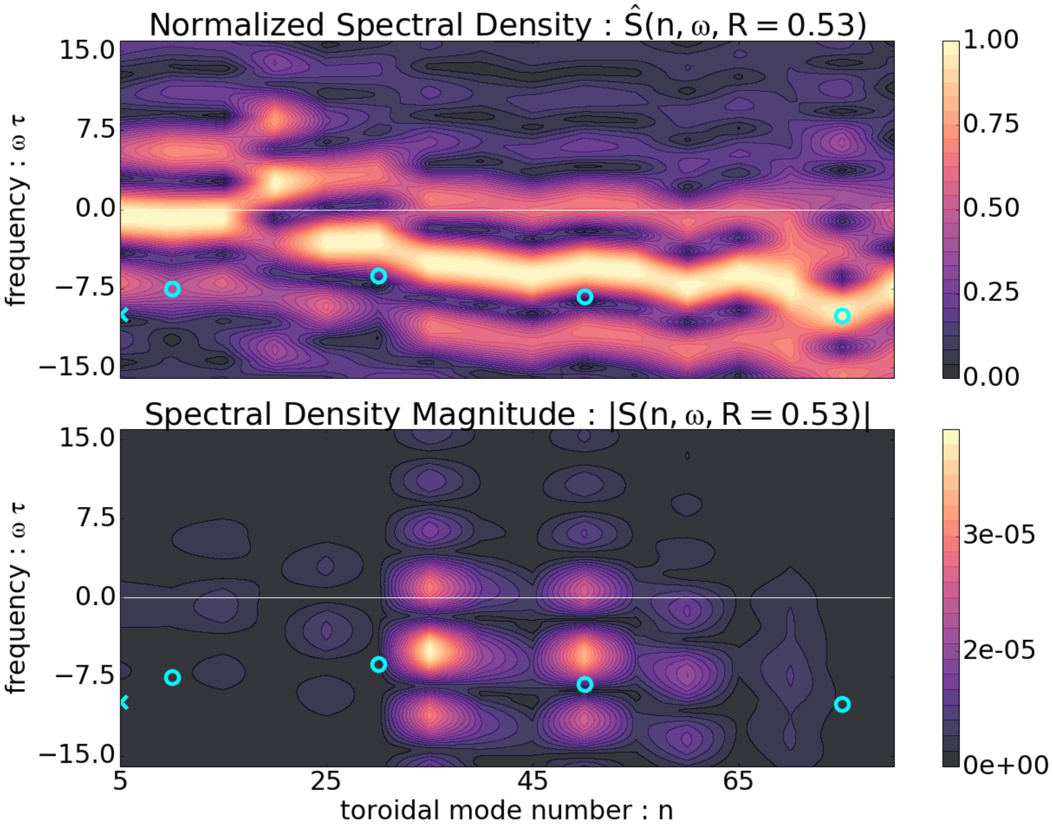

Figure 6.11: The spectral density (normalized per toroidal mode number and absolute), calculated from the nonlinearly saturated phase at ($R = 0.53$[m], $Z = 0$[m]), is plotted. There is a spectral broadening as well as a slight frequency shift. In addition, the peaks have moved from the shorter wavelengths to the slightly longer wavelengths at this location.

Nonlinear spectral analysis

From the same location, the spectral density is calculated for the duration of the nonlinearly saturated phase and shown in Fig. 6.11. There is a slight frequency shift and a spectral broadening that is evident from the normalized spectral density. Even more clearly, in the bottom panel, the energy has shifted from the short wavelength $n = 75$ mode to the longer wavelength modes. Because this spectral density is calculated only from the outer midplane location, it does not show the cascade to the longest wavelengths as shown in Fig. 6.22.

Three-wave coupling

Using the normalized spectral density of the linearly growing phase, the three-wave coupling is shown in Fig. 6.12 which matches the top panel of Fig. 6.10. In the figure, the wave matching conditions ($\vec{k}_1 + \vec{k}_2 = \vec{k}_3$ and $\omega_1 + \omega_2 = \omega_3$) can be seen to be satisfied by $n_1 = 70$, $n_2 = 65$, $n_3 = 5$. Physically, this is the beating of the two waves leading to the excitation of the third wave. It turns out that $n = 5$, the lowest toroidal mode number kept in the simulation, is quite easy to excite because of the easily satisfied matching conditions, and, indeed, this is seen in the inverse cascade where $n = 5$ rises first before other short wavelength modes grow. This longest wavelength mode acts as a quasi-particle for the unstable, shorter wavelength modes to scatter off. This leads to a successive cascade to longer wavelengths[43].

6.4 Nonlinear evolution

During the nonlinear saturation of the instability, there are a number of changes that the plasma goes through. Some have been mentioned or alluded to in previous sections, such as the spectral broadening and inverse toroidal cascade.

6.4.1 Profile relaxation

The simulations of this chapter do not have sources. As expected from having non-zero flux, the pressure profiles are seen to flatten and relax during the nonlinearly saturated times. In Fig. 6.13, the ion temperature profile is shown for the different times marked from the time-history plot, Fig. 6.2. It can be seen that, before saturation at (A) and (B), the ion temperature profile is essentially unchanged from the equilibrium ion temperature profile. At the point of saturation at (C), the ion temperature has begun to relax a small amount

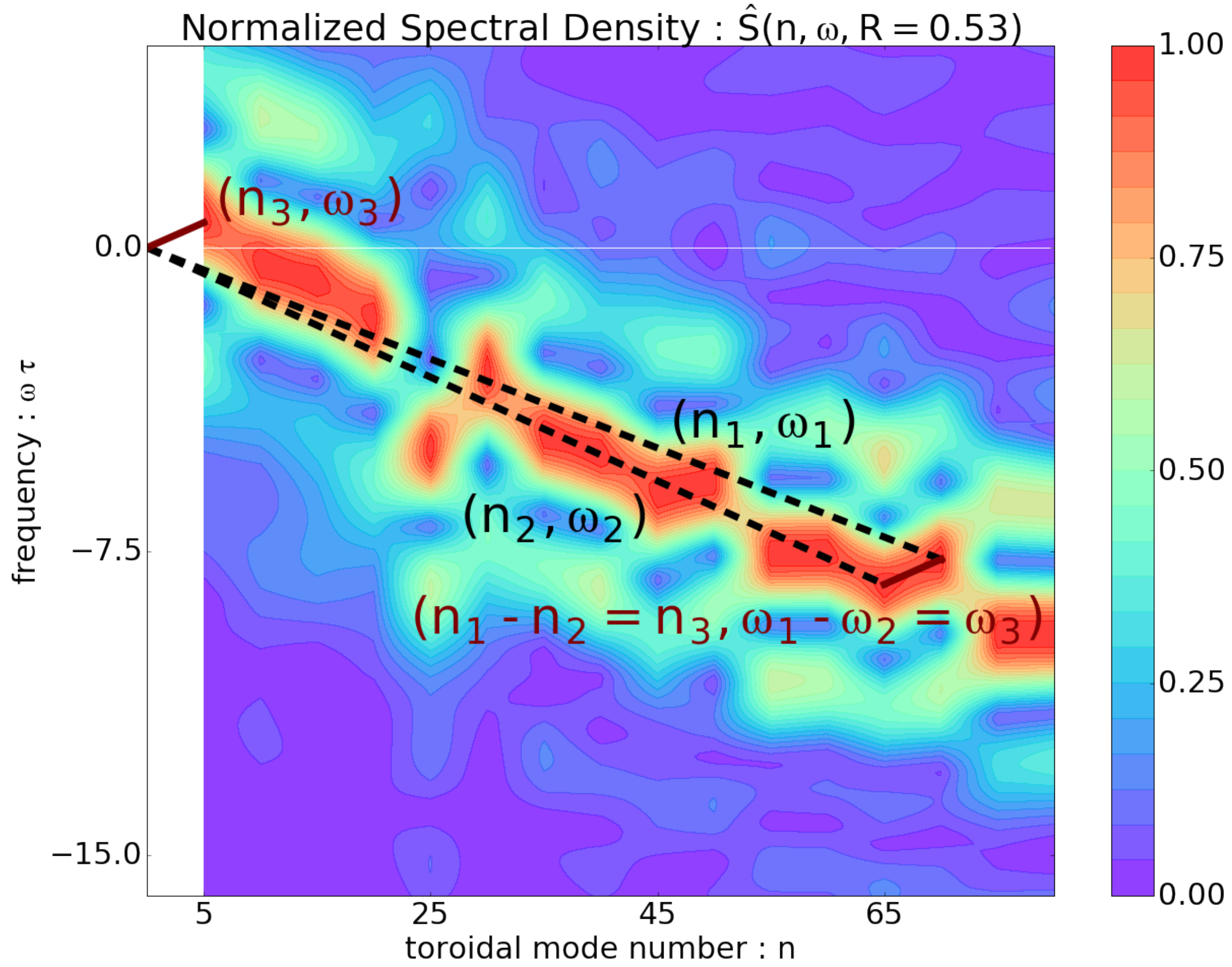

Figure 6.12: The normalized (per toroidal mode number) spectral density, calculated from the linear growing phase at ($R = 0.53$[m], $Z = 0$[m]), is plotted to illustrate the wave matching conditions. Black lines represent the wavenumber vectors to ($n_1 = 70, \omega_1$) and ($n_2 = 65, \omega_2$). The red lines represent the result of vector subtraction ($n_3 = n_1 - n_2 = 5, \omega_3 = \omega_1 - \omega_2$).

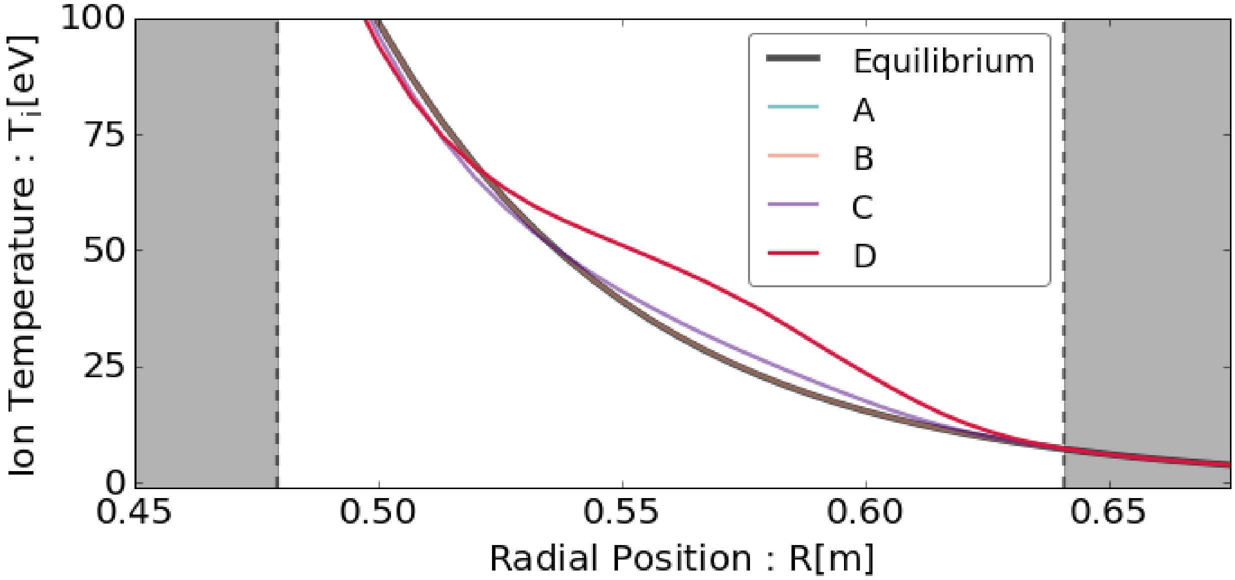

Figure 6.13: The ion temperature profile is plotted for the different times marked on Fig. 6.2. The grey shaded regions denote the regions where the radial boundary begins. The temperature profile does not change much at the moment of saturation (C), but relaxation is more pronounced after saturation (D).

but remains close to the equilibrium profile so that it is clear that the saturation mechanism is not due to profile flattening. Finally, at the end of simulation at (D), the ion temperature profile has been modified such that the inner region is cooler and the outer region is hotter (remembering that density is lower towards the outer region such that energy conservation is fine). This behavior is consistent with the outward ion heat flux which is shown in section 6.5.

6.4.2 Turbulent structure

Radial envelope spreading

As in the cross-separatrix simulations of chapter 5, the radial envelope of the mode broadens. In Fig. 6.14, there is a clear linear eigenmode structure seen at the linearly growing times of (A) and (B). By the point of saturation (C), the envelope has begun to spread inward and

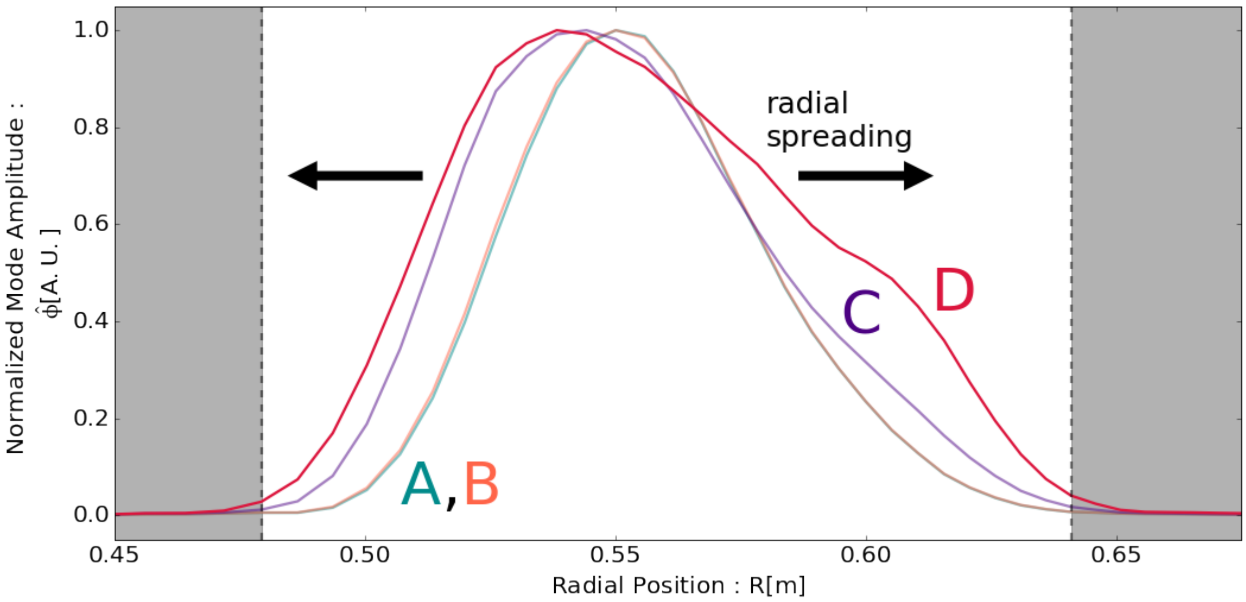

Figure 6.14: The normalized radial envelope of the electrostatic potential is plotted for the different times marked on Fig. 6.2. The grey shaded regions denote the regions where the radial boundary begins. The radial envelope widens and spreads during nonlinear saturation.

outward. Near the end of simulation (D), the broadening has pushed to where the simulation boundaries exist.

This radial spreading also is seen by calculating the mean parallel wavelength. As seen in Fig. 6.15, as the radial envelope spreads, the mean parallel wavelength decreases. This is facilitated by the coupling to the longest toroidal wavelength modes ($n = 5$) which have the largest gains in the regions where the envelope has spread.

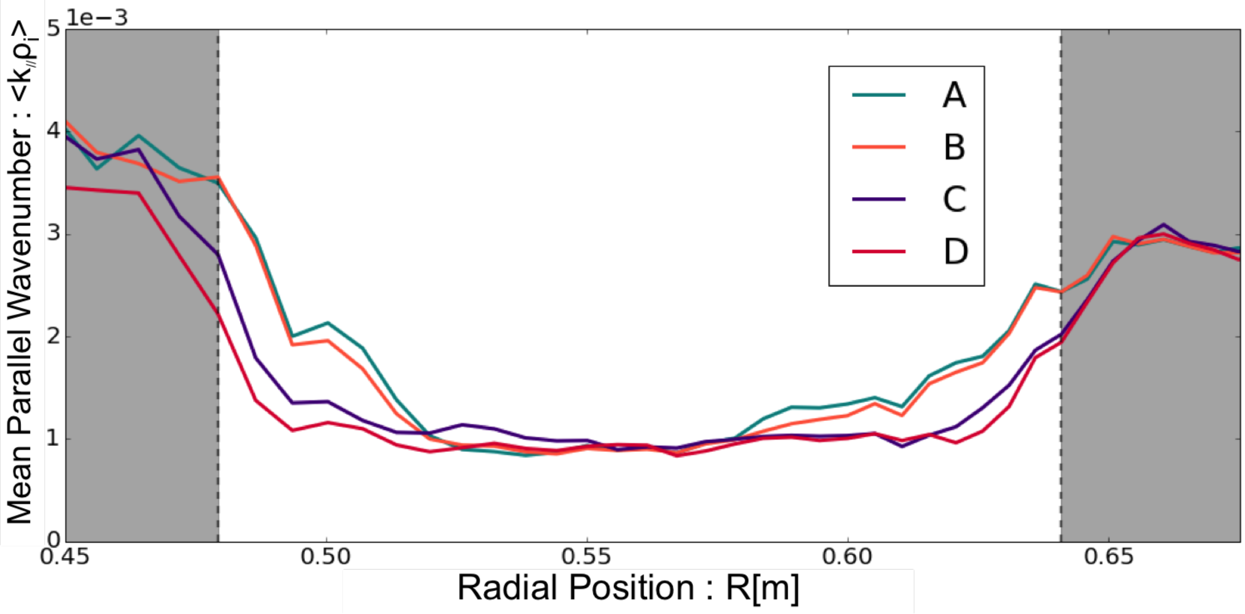

Figure 6.15: The mean parallel wavelength normalized by ion gyro-radius is plotted for the different times marked on Fig. 6.2. The grey shaded regions denote the regions where the radial boundary begins. The changes in the parallel wavelength corresponds to the radial broadening of the mode structure.

Radial correlation length

In addition to the radial envelope, the radial correlation length has also changed during nonlinear saturation. To calculate the radial correlation, $C_R(\Delta R)$, first, the two point correlation $C_{R,\zeta}(\Delta R, \Delta\zeta)$ is calculated

$$C_{R,\zeta}(\Delta R, \Delta\zeta) = \frac{\langle \phi(R+\Delta R, \zeta+\Delta\zeta) \cdot \phi(R,\zeta) \rangle}{\sqrt{\langle \phi^2(R+\Delta R, \zeta+\Delta\zeta) \rangle \cdot \langle \phi^2(R,\zeta) \rangle}} \tag{6.3}$$

from which the maximum correlation per radial delay is kept (so that the correlation is not affected by the angle). This is calculated for the time-steps of the two ranges of the linearly growing phase (A∼B) and nonlinearly saturated phase (C∼D). The ensembles are

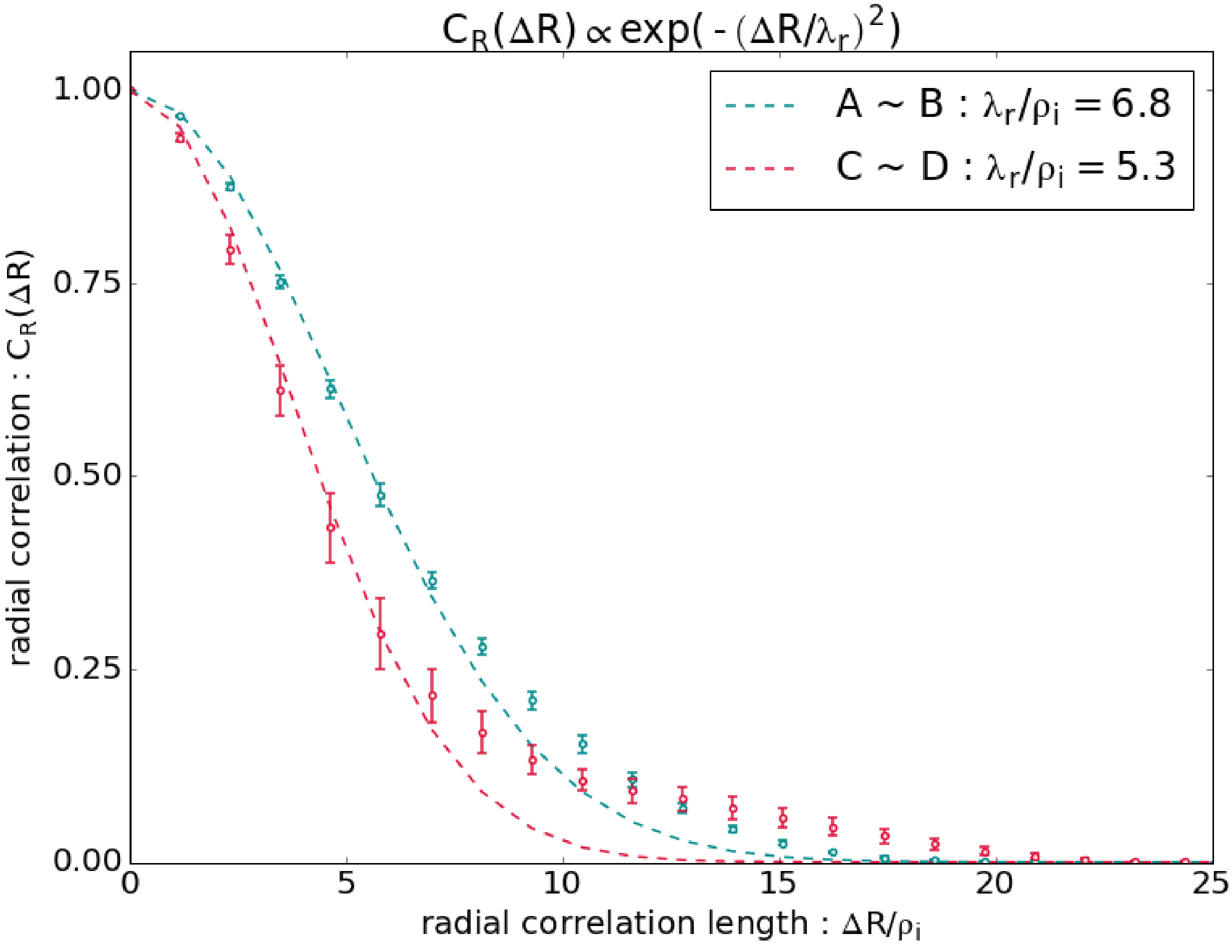

Figure 6.16: The radial correlation function is calculated for the time ranges of the linearly growing phase ($A \sim B$) in blue and the nonlinearly saturated phase ($C \sim D$) in red for $Z = 0$[m]. The error bars are standard deviations from the different time steps of the time ranges. The mean microscopic eddy size (correlation length) decreases by about $\sim 1.5\rho_i$ in the saturated phase but a significant tail persists in the saturated phase (representing eddy sizes of $10 \sim 15\rho_i$).

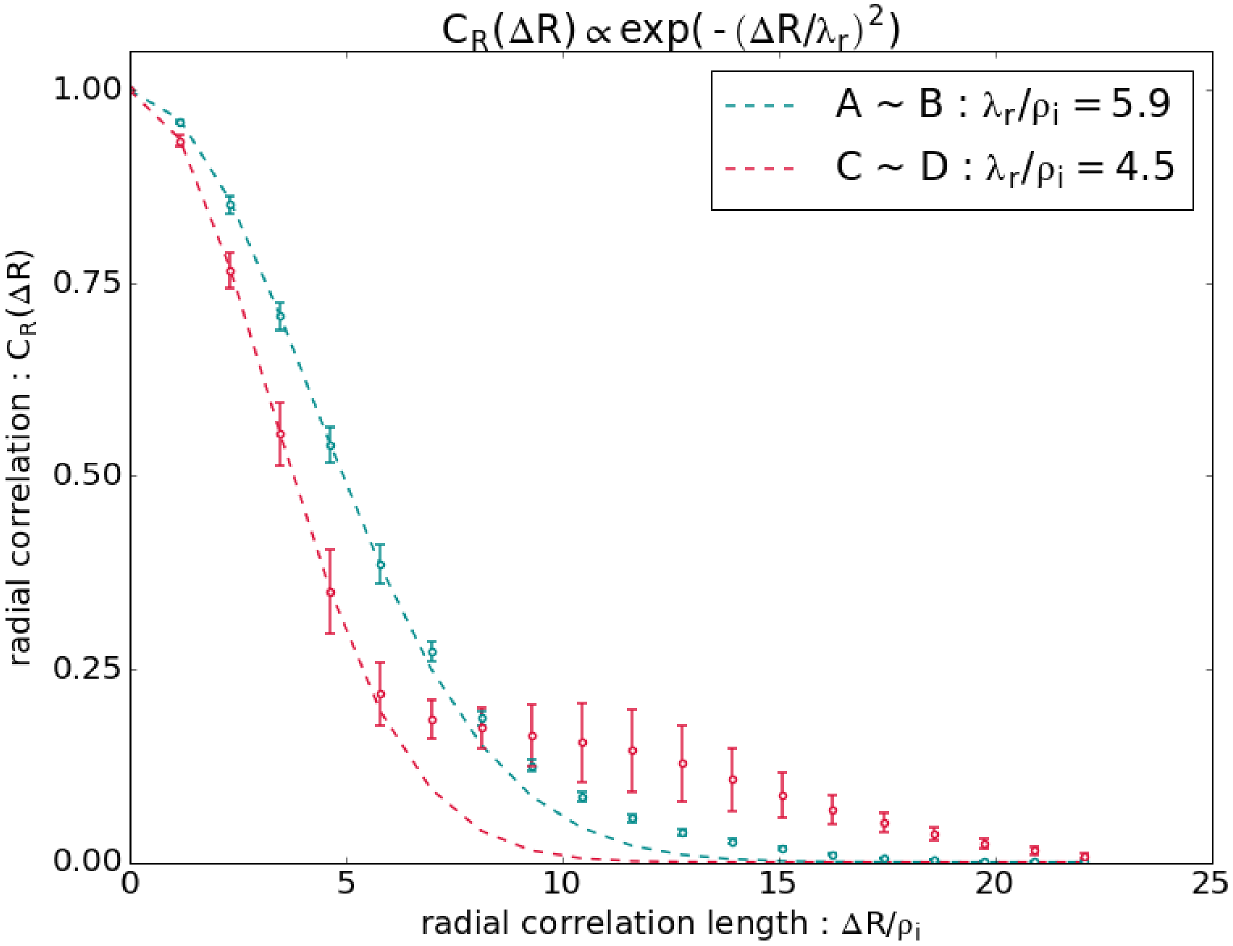

Figure 6.17: The radial correlation function is calculated for the time ranges of the linearly growing phase ($A \sim B$) in blue and the nonlinearly saturated phase ($C \sim D$) in red for $Z = -2.5$[m]. The error bars are standard deviations from the different time steps of the time ranges. The mean microscopic eddy size (correlation length) decreases by about $\sim 1.5\rho_i$ in the saturated phase but a significant tail persists in the saturated phase (representing eddy sizes of $10 \sim 15\rho_i$).

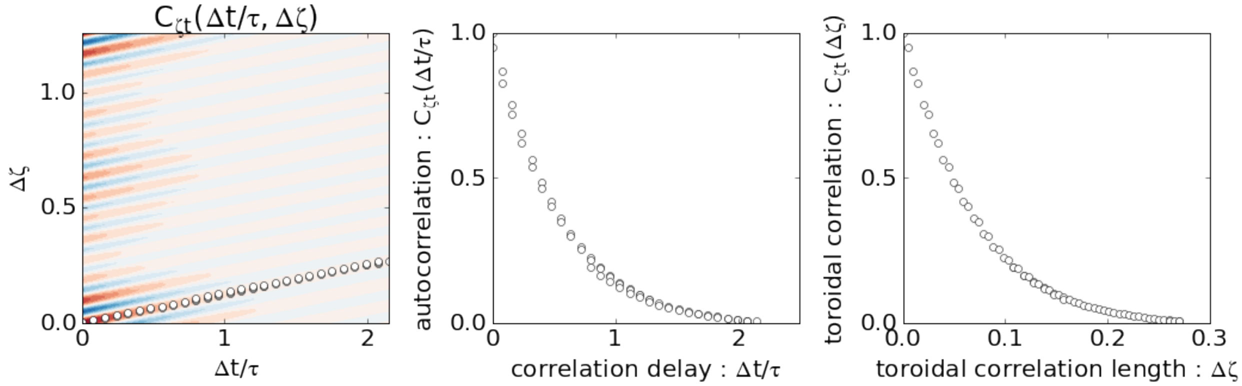

Figure 6.18: The toroidal-time correlation function is calculated for the time ranges of the linearly growing phase ($A \sim B$). The toroidal angle and temporal delay correlation of the toroidal structure can be found by following along the maximum ridge as shown in the 2-D plot on the left. The resulting points are shown on the two 1-D plots on the right.

averaged with the standard deviations shown as error bars in Fig. 6.16 for the axial midplane ($Z = 0[m]$) and in Fig. 6.17 for the axial end ($Z = -2.5[m]$).

Although the radial envelope has broadened, the radial correlation length of the turbulence is found to be actually shorter than the radial correlation length of the linear mode structure by about $\sim 1.5\rho_i$. There is also a minor tail which represents radial streamers of about $10 \sim 15\rho_i$ in length.

Toroidal correlation length

As in section 5.3, a two-point-two-time correlation can be calculated, but for the toroidal direction instead of the radial direction

$$C_{\zeta,t}(\Delta\zeta, \Delta t) = \frac{\langle \phi(\zeta + \Delta\zeta, t + \Delta t) \cdot \phi(\zeta, t) \rangle}{\sqrt{\langle \phi^2(\zeta + \Delta\zeta, t + \Delta t) \rangle \cdot \langle \phi^2(\zeta, t) \rangle}}. \tag{6.4}$$

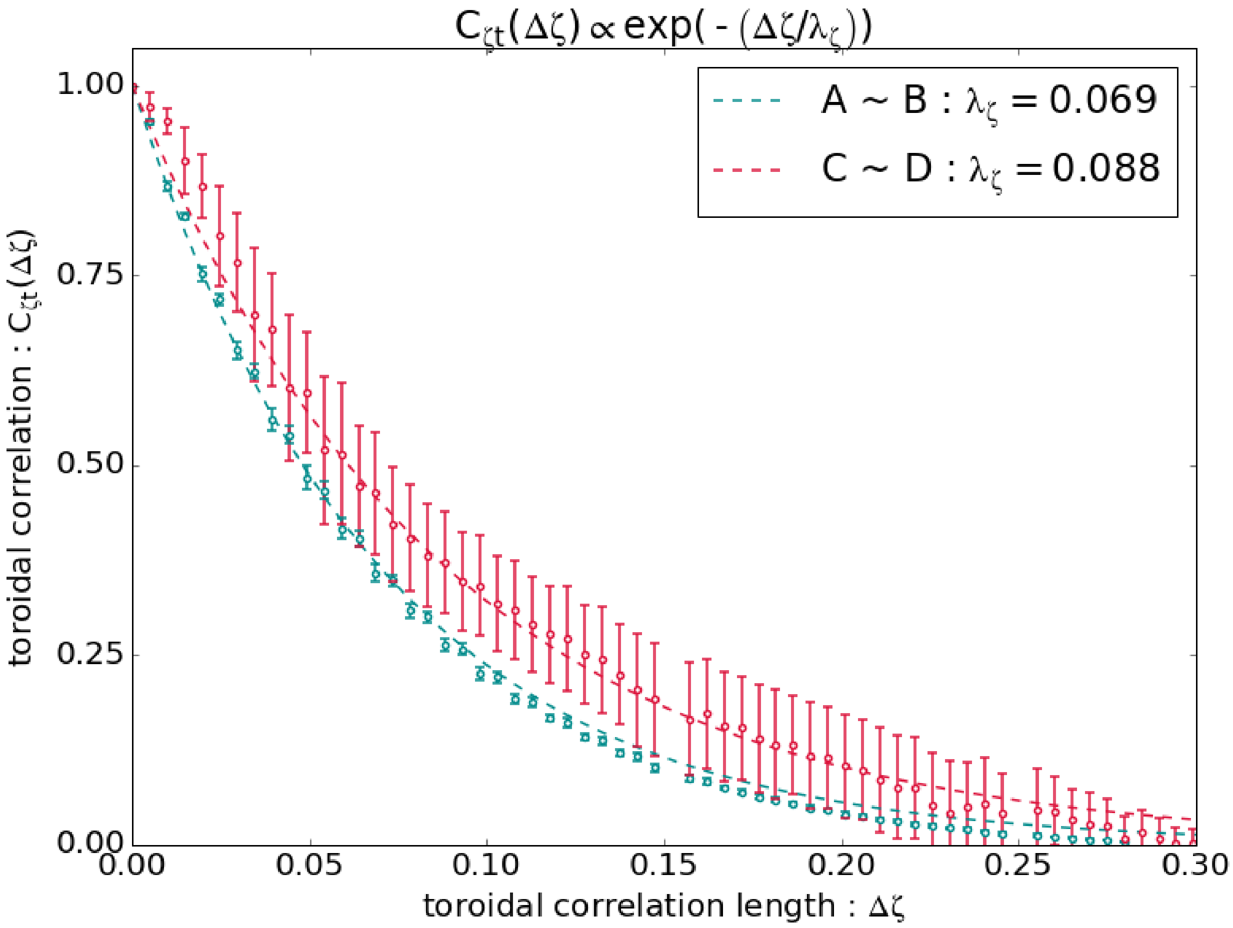

Figure 6.19: The toroidal correlation function is calculated for the time ranges of the linearly growing phase ($A \sim B$) in blue and the nonlinearly saturated phase ($C \sim D$) in red. The error bars are standard deviations from the different radial positions.

This correlation describes the structures of the self-consistent electric fields that drive the turbulent transport (via $V_{E\times B}$). By following along the maximum ridge as in the example shown Fig. 6.18, the correlation of these toroidal structures can be understood in terms of characteristic toroidal angle and characteristic times which essentially describe how far (spatially) and long (temporally) these structures last.

A characteristic length and time can be calculated from these 1-D correlations through fitting with an exponential decay function. Using multiple radial positions where the mode exists, along the midplane ($Z = 0$[m]), an exponential decay fit over the mean values is shown in

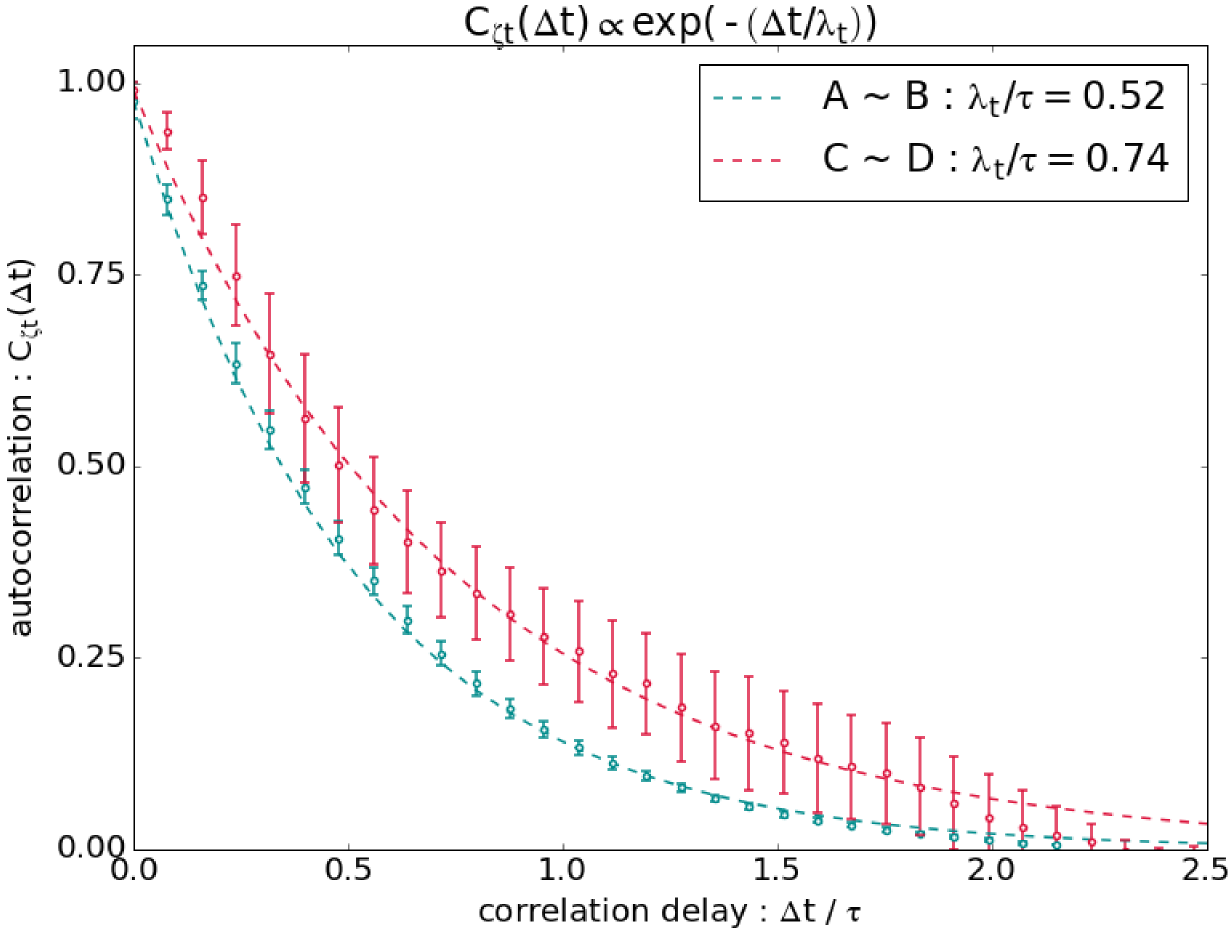

Figure 6.20: The autocorrelation function is calculated for the time ranges of the linearly growing phase ($A \sim B$) in blue and the nonlinearly saturated phase ($C \sim D$) in red. The error bars are standard deviations from the different radial positions.

Fig. 6.19 and in Fig. 6.20 where the error bars represent the standard deviation of those different radial positions.

As seen in the figures, the characteristic correlation length of these toroidal structures increases in the nonlinearly saturated phase compared to the linearly growing phase. This is consistent with the inverse spectral cascade where the spectrum shifts from being dominated by shorter wavelength modes to being dominated by longer wavelength modes. Correspondingly, the characteristic time of these toroidal structures is longer than in the linear phase.

6.4.3 Inverse spectral cascade

In the time-history plot of the amplitudes of different modes in Fig. 6.2, the shortest wavelength modes were seen to grow first with the longer wavelength modes starting damped or stable but overtaking the other modes by the end of the simulation. This corresponds to the change in the mean toroidal wavelength from shorter wavelength ($\langle k_\zeta \rho_i \rangle \sim 1$) to a longer wavelength ($\langle k_\zeta \rho_i \rangle \sim 0.5$), as seen in Fig. 6.21. The transition occurs around $t/\tau \approx 7 \sim 8$, ie. around the time of saturation (C).

This transition in toroidal wavelength can also seen in the normalized toroidal spectrum, shown Fig. 6.22. The largest modes for the linearly growing times (A) and (B) are the short wavelength modes of ($n = 55, n = 65$). During the point of saturation (C), the other modes have grown to a comparable amplitude with the longest wavelength ($n = 5$) being almost equal to ($n = 65$). By the end of simulation (D), the inverse cascade has finished, leaving the shape of the toroidal spectrum to be consistent with the experimental observations by Schmitz *et al*[60] (as shown in Fig. 1.2).

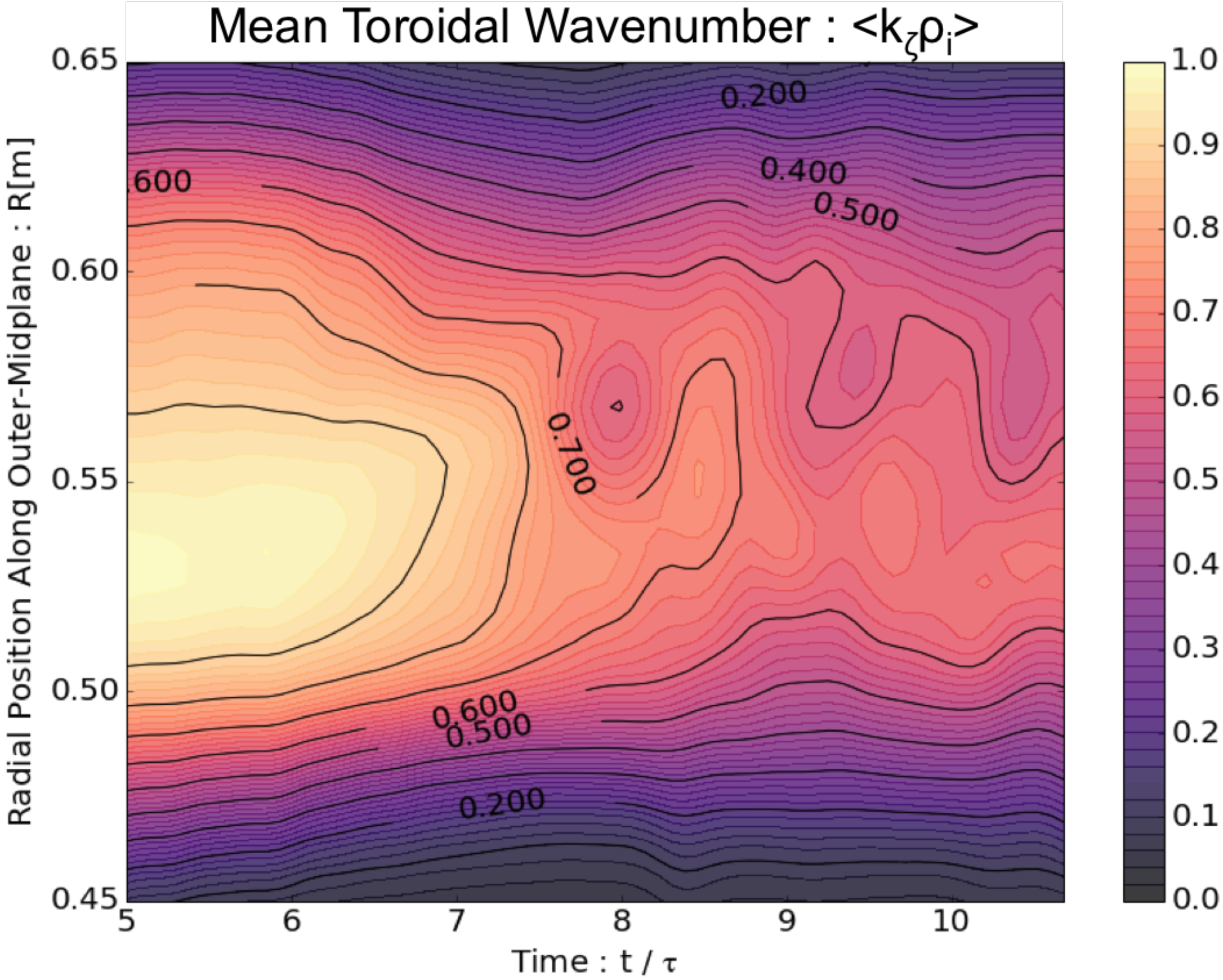

Figure 6.21: The average toroidal wavenumber normalized by the ion gyro-radius is plotted against radial position and time. The average wavenumber is initially shorter ($\langle k_\zeta \rho_i \rangle \sim 1$) and the transition to a longer average wavenumber ($\langle k_\zeta \rho_i \rangle \sim 0.5$) occurs near saturation.

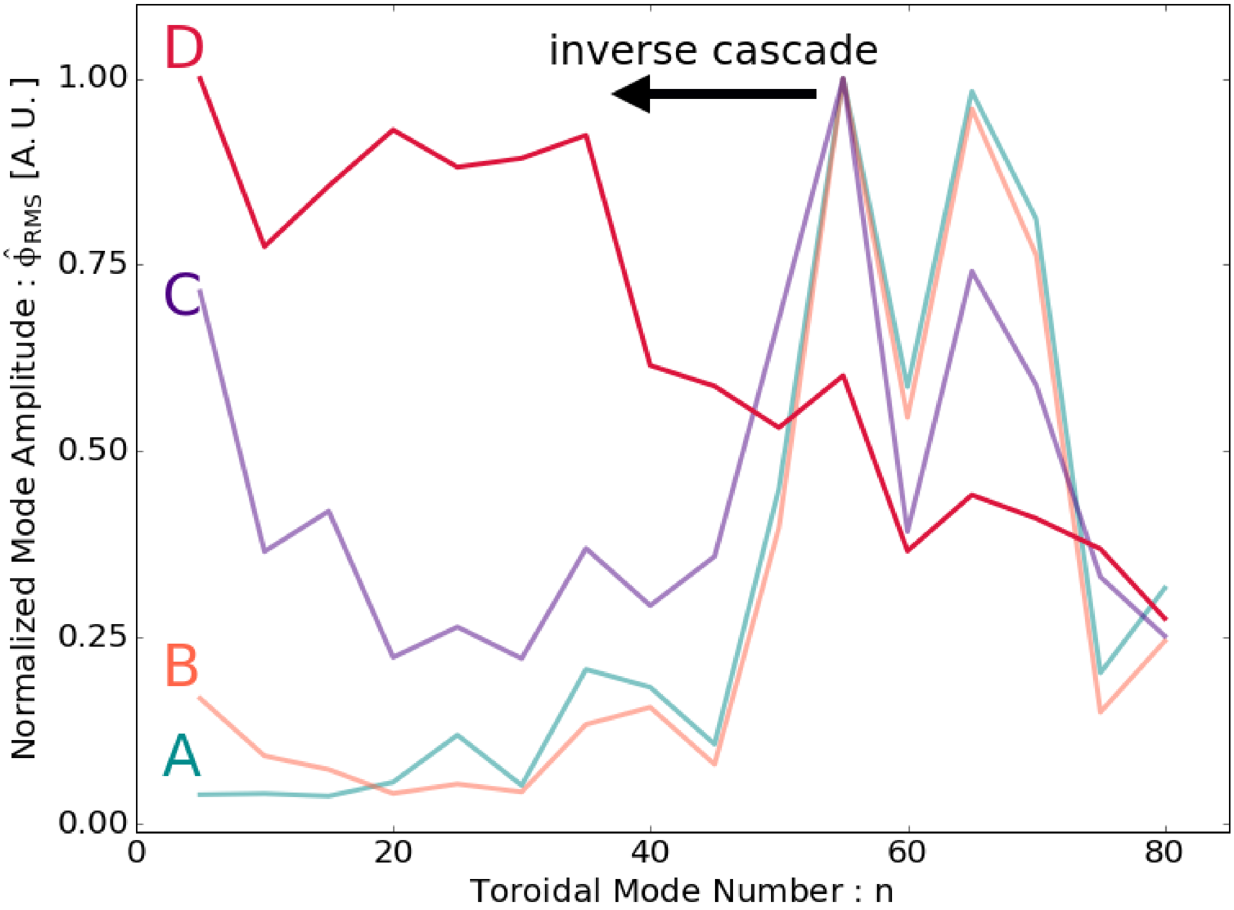

Figure 6.22: The normalized toroidal spectrum is plotted for the different times marked on Fig. 6.2. The largest amplitudes are in the short wavelength modes in the beginning before an inverse cascade to the longer wavelength modes.

During this inverse cascade, the longest wavelength mode ($n = 5$) grows first. As mentioned in section 6.3, the $n = 5$ is the lowest toroidal mode number available with the most number of three-wave coupling combinations (thirty combinations when including combinations such as $(70 - 65 = 5)$ and $(65 - 70 = -5)$ as distinct combinations to obtain an $(n = 5)$ mode within the simulation) within the set of toroidal mode numbers without even considering the frequency matching aspect which has already been shown in section 6.3.

6.5 Transport

Because these simulations use an adiabatic electron model, particle diffusivity is not calculated since the particle flux is $\Gamma \propto \int d^3\vec{v}\ (i\vec{k}\phi \times \vec{B})\delta f \propto i\ \delta n_e^2$, where the self-consistent potential comes from the $\vec{E} \times \vec{B}$ drift which is directly related to the density due to the adiabatic model. This results in a purely imaginary particle flux which means that, theoretically, the adiabatic model produces no particle diffusivity.

6.5.1 Heat flux

However, the self-consistent ion energy flux due to the electrostatic turbulence can be calculated from all of ions in the simulation via $q_i = \int d^3\vec{v}\ (\frac{1}{2}m_i v_i^2 - \frac{3}{2}T_i)(\vec{v}_E \cdot \hat{\psi})\delta f_i$. Here, the interest is in the transport due to turbulence so that the velocity used is the radial component of the $\vec{E} \times \vec{B}$ drift, where the electric field $\vec{E}$ is from the self-consistent electric fields.

As seen in the upper panel of Fig. 6.23, the simulations show that most of the ion energy flux at the point of saturation (C) is radially outward. This is in agreement with the profile relaxation seen in Fig. 6.13 as heat is moving radially outward, causing the flattening of the ion temperature profile.

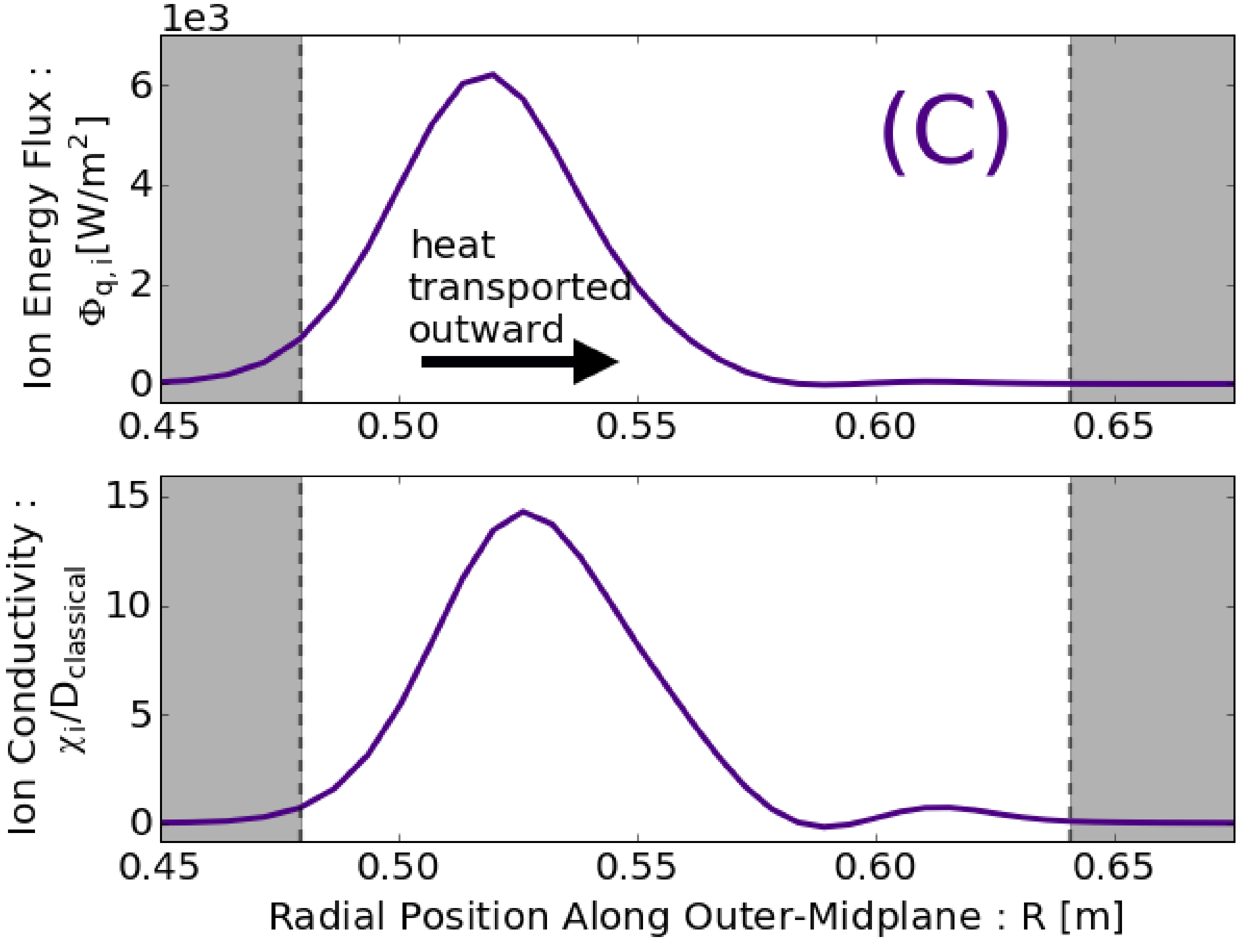

Figure 6.23: The ion heat flux and ion conductivity are plotted for the moment of saturation. The grey shaded regions denote the regions where the radial boundary begins. The radially outward heat flux is consistent with the ion temperature profile change seen in Fig. 6.13.

Ion conductivity can also be calculated from Fick's law $q_i = \chi_i n_i \nabla T_i$. From these simulations, it is found that the peak ion conductivity is about $\chi_i \sim 2.5[\mathrm{m}^2/\mathrm{s}]$. Although these simulations are collisionless, this ion conductivity due to turbulence can still be compared to the classical collisional diffusivity (ρ_i^2/τ_{ii}) for reference. In the bottom panel of Fig. 6.23, the conductivity normalized by the local ion conductivity is plotted with a clearly anomalous ion conductivity.

Although the current simulations model the electron species as adiabatic, an upper limit for the electron heat transport can be calculated through test electron particles. That is, electron simulation particles, which do not contribute to the ion turbulence, can be used to calculate an upper bound on the electron energy flux in the same approach as in the case of the ions. With these test particles, an electron energy flux with a maximum about $q_e \sim 4\mathrm{MW}/\mathrm{m}^2$ is found, comparable to what is measured at the C-2/C-2U experiments. Due to the flat electron temperature profile, this energy flux yields only a convective component rather than a combination of convective and conductive heat flow.

6.6 Discussion

Previous local linear simulations studied the properties of pressure gradient driven drift-waves in the FRC and found the core to be robustly stable and the SOL to be unstable[40]. Later nonlocal single-mode gyrokinetic simulations showed fluctuations originating from the SOL spread into the FRC core. In this chapter, nonlocal multiple-mode gyrokinetic simulations have been used to study turbulence in just the SOL.

Using gyrokinetic ions and adiabatic electrons, nonlocal simulations containing multiple toroidal modes find that a slab-like ITG instability develops and saturates in a similar fashion as in chapter 5. With multiple toroidal modes allowed in the simulation, it is shown that linearly stable or damped modes are able to grow to significant amplitudes through mode-mode coupling.

The experimentally measured SOL density fluctuation spectrum is an exponentially decreasing function as shown in Fig. 1.2[60]. In Lau *et al*[40], a toroidal inverse cascade was proposed to be the mechanism, or one of the mechanisms, from which the spectrum can be formed from linear instabilities with length scales in the intermediate range between ion and electron scales. By the end of simulation, about two linear wave periods after saturation, the toroidal spectrum, originally dominated by shorter wavelength modes, confirms this inverse cascade with the largest amplitudes in the longer wavelength end of the toroidal spectrum.

With multiple toroidal modes, the turbulent eddies are shown to be shorter in radial correlation length than in the linearly growing stage but with a population of longer radial streamers. Consistent with the inverse cascade, the characteristic size of the toroidal structures increases. Concurrently, the characteristic duration of the toroidal structures also increases. These eddy characteristics determine the electric fields which cause transport.

For this ion-scale turbulence, transport quantities have been calculated from self-consistent particle simulations for the first time. At the point of saturation, a radially outward ion energy flux with a maximum of $\Phi_{q,i} \sim 6[\mathrm{W/m^2}]$ is found, consistent with the ion temperature relaxation found from simulations. With test electrons, an upper bound for the electron energy flux has also been calculated to around a maximum of $\Phi_{q,e} \sim 4[\mathrm{MW/m^2}]$.

Ion-scale turbulence in the SOL has been studied with multiple-mode simulations and shown to be consistent with various aspects of experimental measurements. These are the first self-consistent particle-in-cell simulations of turbulence and transport in the FRC. However, this is just the beginning of the turbulence simulations. Future work will include a variety of additional physics, especially cross-separatrix turbulence.

Chapter 7

Conclusion

7.1 Highlights of the thesis

A New Code (ANC) has been developed for use in global simulations in chapter 3. Specific formulations and implementations of the Poisson equation are detailed for future development and usage.

In the comprehensive set of local, linear simulations of chapter 4, the electrostatic drift-wave is found to be stable in the core and unstable in the SOL. Because the core was expected to be *less unstable*, the result of stability in the core was a surprise, prompting the question of "where do the fluctuations in the SOL originate?"

With the cross-separatrix, non-local simulations of a single toroidal mode of chapter 5, instability is shown to radially spread from the SOL to the linearly stable core, answering the previous question. The instability is also shown to saturate with the saturated amplitude being larger in the SOL by an order of magnitude, again affirming the turbulent property of the SOL. Due to lower numerical restrictions and the observed importance of the SOL, simulations were then refocused on just the SOL.

Finally, in chapter 6, focusing on non-local simulations of multiple toroidal modes in just the SOL, a previously hypothesized inverse toroidal spectral cascade is observed and confirmed. Self-consistent ion heat flux is calculated for the first time, and an upper bound for the electron heat flux is also calculated through the use of test particles.

7.2 Future work

Understanding turbulence and transport in the FRC is not an easy task. While tokamak turbulence has had decades of theoretical and computational research, FRC turbulence is relatively young because the ability to conquer the MHD instabilities has only been demonstrated by TAE in the recent years.

Because of the freshness of this field, the work shown in this thesis does not contain all the possible physics that may exist in realistic FRCs. To understand all the possible physics that exist in realistic FRCs would span several careers; however, several physical features which should be understood in the near future are outlined below, somewhat in order of ease and feasibility.

Multiple-mode coupled-core-SOL turbulence

The natural next step from this thesis is to simulate multiple toroidal modes with a global cross-separatrix domain. This would be a more complete simulation which would possibly lead to an understanding of how the distinct density fluctuation spectra arise.

Equilibrium rotation and shear flow

In the experiments, a background rotation is established through a background electric field to control for the rotational MHD instability. Undoubtedly, the shearing modifies the mode structures, typical eddy structures, and possibly, even saturation levels.

Self-consistent zonal flow

With the field-aligned version of ANC, inclusion of zonal flow is possible. Although simulations have shown zonal-flow-free saturation, it is known that zonal flow regulates plasma turbulence. Its inclusion opens another channel of mode-mode coupling and will likely quantitatively modify the saturation levels.

Fully kinetic ions

As mentioned within this thesis, there are regions of the FRC in which gyrokinetics is not applicable. In addition, there are larger gyroradius orbits beyond the usual cyclotron orbit which may not be captured by the gyrokinetic model of this thesis. By changing our model from gyrokinetic ions to fully kinetic ions, we would be able to next explore the effects of the magnetic null regions, betatron and figure-8 orbits, and possibly higher frequency instabilities.

Electron temperature gradient (ETG)

W. Horton suggests that a possible origin of core fluctuations may also be very short-scale ETG modes. A variety of parameter scans to find a possible ETG instability can be a good starting project for a future graduate student.

Equilibrium toroidal magnetic field

An ideal FRC has only a poloidal magnetic field. However, L. Schmitz and other FRC experimentalists suggest that it is possible for a toroidal magnetic field component to exist. A small, finite, toroidal magnetic field would significantly modify the field-line length which modify the short-field line stabilization. Understanding the effects of a non-ideal FRC geometry would be important and would also coincide with the upgraded FRC experiments at TAE which will include better diagnostics of the magnetic fields.

Electromagnetic perturbations

The work of this thesis was focused only on electrostatic modes which are historically understood to be the most dangerous for confinement. However, the FRC is high-β and so electromagnetic effects should be included. For electrostatic modes, finite β effects are known to be stabilizing, but other modes, electromagnetic in nature, may also exist. A possible candidate for core transport, for example, is electromagnetic fluttering.

Parallel transport

In this thesis, only perpendicular transport is studied. Due to the close interaction between the core and SOL, parallel confinement time is also a significant factor of the confinement of the FRC as a whole. Realistic transport scalings for guiding designs towards future fusion reactors will necessarily require simulations to contain both parallel and perpendicular transport.

Bibliography

[1] Y. Aso, S. Himeno, and K. Hirano. Experimental studies on energy transport in a reversed-field theta pinch. *Nucl. Fusion*, 23(6):751, 1983.

[2] S. P. Auerbach and W. C. Condit. Classical diffusion in a field-reversed mirror. *Nucl. Fusion*, 21(8):927, 1981.

[3] J. Bao and Z. Lin. A conservative scheme for electromagnetic simulation of magnetized plasmas with kinetic electrons. *arXiv preprint arXiv:1702.01406*, 2017.

[4] D. C. Barnes, J. L. Schwarzmeier, H. R. Lewis, and C. E. Seyler. Kinetic tilting stability of fieldreversed configurations. *Phys. Fluids*, 29(8):2616–2629, 1986.

[5] M. Binderbauer, T. Tajima, M. Tuszewski, L. Schmitz, A. Smirnov, H. Gota, E. Garate, D. Barnes, B. Deng, E. Trask, et al. Recent breakthroughs on c-2u: Norman's legacy. In T. Tajima and M. Binderbauer, editors, *The Physics of Plasma-Driven Accelerators and Accelerator-Driven Fusion: The Proceedings of Norman Rostoker Memorial Symposium*, page 030003. AIP Publishing, Melville, NY, 2016.

[6] M. W. Binderbauer, H. Y. Guo, M. Tuszewski, S. Putvinski, L. Sevier, D. Barnes, N. Rostoker, M. G. Anderson, R. Andow, L. Bonelli, et al. Dynamic formation of a hot field reversed configuration with improved confinement by supersonic merging of two colliding high-β compact toroids. *Phys. Rev. Lett.*, 105:045003, 2010.

[7] M. W. Binderbauer and N. Rostoker. Turbulent transport in magnetic confinement: how to avoid it. *J. Plasma Phys.*, 56:451–465, 1996.

[8] M. W. Binderbauer, T. Tajima, L. C. Steinhauer, E. Garate, M. Tuszewski, L. Schmitz, H. Y. Guo, A. Smirnov, H. Gota, D. Barnes, et al. A high performance field-reversed configuration. *Phys. Plasmas*, 22(5), 2015.

[9] J. U. Brackbill, D. W. Forslund, K. B. Quest, and D. Winske. Nonlinear evolution of the lower-hybrid drift instability. *Phys. Fluids*, 27(11):2682–2693, 1984.

[10] A. J. Brizard. On the validity of the guiding-center approximation in the presence of strong magnetic gradients. *Phys. Plasmas*, 24(4):042115, 2017.

[11] E. J. Caramana. The long-time evolution approximation for a quasi-one-dimensional plasma system. *Phys. Fluids*, 28(12):3557–3566, 1985.

[12] A. W. Carlson. A search for lower-hybrid-drift fluctuations in a field-reversed configuration using co2 heterodyne scattering. *Phys. Fluids*, 30(5):1497–1509, 1987.

[13] L. Chen, M. Chance, and C. Cheng. Absolute dissipative drift-wave instabilities in tokamaks. *Nucl. Fusion*, 20(7):901, 1980.

[14] C. Cheng and L. Chen. Unstable universal drift eigenmodes in toroidal plasmas. *Phys. Fluids*, 23(9):1770–1773, 1980.

[15] R. A. Clemente and E. M. Freire. Classical particle-diffusion time for analytical compact tori equilibria. *Plasma Phys. Control. Fusion*, 28(7):951, 1986.

[16] R. A. Clemente and C. E. Grillo. Internal tilting and classical transport for field-reversed configurations based on the Maschke-Hernegger solution. *Phys. Fluids*, 27(3):658–660, 1984.

[17] J. Connor, R. Hastie, and J. Taylor. Stability of general plasma equilibria. iii. *Plasma Phys.*, 22(7):757, 1980.

[18] W. D. D'haeseleer, W. N. G. Hitchon, J. D. Callen, and J. L. Shohet. The clebsch-type coordinate systems. In R. Glowinski, M. Holt, P. Hut, H. B. Keller, J. Killeen, S. A. Orszag, and V. V. Rusanov, editors, *Flux Coordinates and Magnetic Field Structure: a Guide to a Fundamental Tool of Plasma Theory.* Springer-Verlag, Berlin, Germany, 1991.

[19] A. Dimits and W. W. Lee. Partially linearized algorithms in gyrokinetic particle simulation. *J. Comput. Phys.*, 107(2):309–323, 1993.

[20] D. Fulton and C. Lau. A new code (anc) : global, cross-separatrix turbulent transport particle-in-cell code.

[21] D. Fulton, C. Lau, I. Holod, Z. Lin, and S. Dettrick. Gyrokinetic particle simulation of a field reversed configuration. *Phys. Plasmas*, 23(1):012509, 2016.

[22] D. Fulton, C. Lau, L. Schmitz, I. Holod, Z. Lin, T. Tajima, M. Binderbauer, and the TAE Team. Gyrokinetic simulation of driftwave instability in field-reversed configuration. *Phys. Plasmas*, 2016.

[23] L. Galeotti, D. C. Barnes, F. Ceccherini, and F. Pegoraro. Plasma equilibria with multiple ion species: Equations and algorithm. *Phys. Plasmas*, 18(8):082509, 2011.

[24] N. T. Gladd, J. F. Drake, C. L. Chang, and C. S. Liu. Electron temperature gradient driven microtearing mode. *Phys. Fluids*, 23(6):1182–1192, 1980.

[25] N. T. Gladd, A. G. Sgro, and D. W. Hewett. Microstability properties of the sheath region of a field-reversed configuration. *Phys. Fluids*, 28(7):2222–2234, 1985.

[26] H. Guo, M. Binderbauer, T. Tajima, R. Milroy, L. Steinhauer, X. Yang, E. Garate, H. Gota, S. Korepanov, A. Necas, et al. Achieving a long-lived high-beta plasma state by energetic beam injection. *Nature Commun.*, 6, 2015.

[27] S. Gupta, D. Barnes, S. Dettrick, E. Trask, M. Tuszewski, B. Deng, H. Gota, D. Gupta, K. Hubbard, S. Korepanov, et al. Transport studies in high-performance field reversed configuration plasmas. *Phys. Plasmas*, 23(5):052307, 2016.

[28] S. Hamada. A model of equilibrium transport and evolution of field reversed configurations. *Nucl. Fusion*, 26(6):729, 1986.

[29] S. Hamasaki and D. Book. Numerical simulation of the anomalous transport process in radially compressed reversed-field configurations. *Nucl. Fusion*, 20(3):289, 1980.

[30] W. W. Heidbrink and G. J. Sadler. The behaviour of fast ions in tokamak experiments. *Nucl. Fusion*, 34(4):535, 1994.

[31] S. Hirshman and K. Molvig. Turbulent destabilization and saturation of the universal drift mode in a sheared magnetic field. *Phys. Rev. Lett.*, 42(10):648, 1979.

[32] A. L. Hoffman and R. D. Milroy. Particle lifetime scaling in field-reversed configurations based on lower-hybrid-drift resistivity. *Phys. Fluids*, 26(11):3170–3172, 1983.

[33] A. L. Hoffman, R. D. Milroy, and L. C. Steinhauer. Poloidal flux loss in a field-reversed theta pinch. *Appl. Phys. Lett.*, 41:31–33, 1982.

[34] I. Holod, W. L. Zhang, Y. Xiao, and Z. Lin. Electromagnetic formulation of global gyrokinetic particle simulation in toroidal geometry. *Phys. Plasmas*, 16(12):122307, 2009.

[35] R. Horiuchi and T. Sato. Full magnetohydrodynamic simulation of the tilting instability in a field reversed configuration. *Phys. Fluids B*, 1(3):581–590, 1989.

[36] M. Y. Hsiao, K. A. Werley, and K. M. Ling. Cfrx, a one-and-a-quarter-dimensional transport code for field-reversed configuration studies. *Comput. Phys. Commun.*, 54(2):329–352, 1989.

[37] J. D. Huba. Nrl: Plasma formulary. Technical report, NAVAL RESEARCH LAB WASHINGTON DC BEAM PHYSICS BRANCH, 2004.

[38] T. Kamimura, T. Wagner, and J. Dawson. Simulation study of bernstein modes. *The Physics of Fluids*, 21(7):1151–1167, 1978.

[39] Y. Kishimoto, T. Tajima, W. Horton, M. LeBrun, and J. Kim. Theory of self-organized critical transport in tokamak plasmas. *Phys. Plasmas*, 3(4):1289–1307, 1996.

[40] C. Lau, D. Fulton, I. Holod, Z. Lin, M. Binderbauer, T. Tajima, and L. Schmitz. Drift-wave stability in the field-reversed configuration. *Physics of Plasmas*, 24(8):082512, 2017.

[41] M. LeBrun, T. Tajima, M. Gray, G. Furnish, and W. Horton. Toroidal effects on drift wave turbulence. *Phys. Fluids B*, 5(3):752–773, 1993.

[42] W. W. Lee. Gyrokinetic approach in particle simulation. *Phys. Fluids*, 26(2):556–562, 1983.

[43] Z. Lin, L. Chen, and F. Zonca. Role of nonlinear toroidal coupling in electron temperature gradient turbulence a. *Physics of plasmas*, 12(5):056125, 2005.

[44] Z. Lin, T. S. Hahm, W. W. Lee, W. M. Tang, and R. B. White. Turbulent Transport Reduction by Zonal Flows: Massively Parallel Simulations. *Science*, 281:1835, 1998.

[45] Z. Lin, Y. Nishimura, Y. Xiao, I. Holod, W. L. Zhang, and L. Chen. Global gyrokinetic particle simulations with kinetic electrons. *Plasma Phys. and Control. Fusion*, 49:163, 2007.

[46] Z. Lin, W. M. Tang, and W. W. Lee. Gyrokinetic particle simulation of neoclassical transport. *Phys. Plasmas*, 2(8):2975–2988, 1995.

[47] R. K. Linford. Los alamos compact toroid, fast liner, and high-density z-pinch programs. In B. Brunelli and G. G. Leotta, editors, *Unconventional Approaches to Fusion*, volume 13, page 463. Plenum Press, New York and London, 1982.

[48] A. B. Mikhailovskii. Weakly inhomogeneous collisionless plasma. In *The Theory of Plasma Instabilities, Volume 2: Instabilities of an Inhomogeneous Plasma*, page 49. Springer US, New York, 1974.

[49] H. Naitou, T. Kamimura, and J. M. Dawson. Kinetic effects on the convective plasma diffusion and the heat transport. *J. Phys. Soc. Jpn.*, 46(1):258–265, 1979.

[50] K. Nguyen and T. Kammash. Classical transport coefficients in a field-reversed configuration. *Plasma Phys.*, 24(2):177, 1982.

[51] S. E. Parker and W. W. Lee. A fully nonlinear characteristic method for gyrokinetic simulation. *Phys. Fluids B: Plasma Phys.*, 5(1):77–86, 1993.

[52] L. Pearlstein and H. Berk. Universal eigenmode in a strongly sheared magnetic field. *Phys. Rev. Lett.*, 23(5):220, 1969.

[53] M. B. Priestley. Spectral analysis and time series. 1981.

[54] D. C. Quimby, A. L. Hoffman, and G. C. Vlases. Linus cycle calculations including plasma transport and resistive flux loss. *Nucl. Fusion*, 21(5):553, 1981.

[55] D. J. Rej and M. Tuszewski. A zero-dimensional transport model for field-reversed configurations. *Phys. Fluids*, 27(6):1514–1520, 1984.

[56] M. Rosenbluth, N. Krall, and N. Rostoker. Finite larmour radius stabilization of "weakly" unstable confined plasmas. *Nucl. Fusion, Suppl.*, 1:143, 1962.

[57] D. W. Ross and S. M. Mahajan. Are drift-wave eigenmodes unstable? *Phys. Rev. Lett.*, 40(5):324, 1978.

[58] N. Rostoker. Closing remarks. In T. Tajima and M. Okamoto, editors, *Physics of high energy particles in toroidal systems*, volume 1. AIP Publishing, 1994.

[59] N. Rostoker, F. Wessel, H. Rahman, B. C. Maglich, B. Spivey, and A. Fisher. Magnetic fusion with high energy self-colliding ion beams. *Phys. Rev. Lett.*, 70:1818–1821, 1993.

[60] L. Schmitz, D. Fulton, E. Ruskov, C. Lau, B. Deng, T. Tajima, M. Binderbauer, I. Holod, Z. Lin, H. Gota, et al. Suppressed ion-scale turbulence in a hot high-β plasma. *Nature Commun.*, 7, 2016.

[61] D. E. Shumaker. Transport simulation of a field-reversed configuration plasma. *Fusion Technol.*, 13:555, 1988.

[62] R. Sydora, J. Leboeuf, and T. Tajima. Particle simulation of drift waves in a sheared magnetic field. *Phys. Fluids*, 28(2):528–537, 1985.

[63] T. Tajima. Guiding-center method. In *Computational Plasma Physics: With Applications to Fusion and Astrophysics*, volume 1, page 189. Addison-Wesley, Redwood City, CA, 1989.

[64] K. Tsang, J. Whitson, J. Callen, P. Catto, and J. Smith. Drift alfven waves in tokamaks. *Phys. Rev. Lett.*, 41(8):557, 1978.

[65] M. Tuszewski and R. K. Linford. Particle transport in field-reversed configurations. *Phys. Fluids*, 25(5):765–774, 1982.

[66] M. Tuszewski, A. Smirnov, M. C. Thompson, T. Akhmetov, A. Ivanov, R. Voskoboynikov, D. C. Barnes, M. W. Binderbauer, R. Brown, D. Q. Bui, et al. A new high performance field reversed configuration operating regime in the c-2 device. *Phys. Plasmas*, 19(5):056108, 2012.

[67] K. A. Werley. One-and-a-quarter-dimensional transport modeling of the field-reversed configuration. *Phys. Fluids*, 30(7):2129–2138, 1987.

[68] D. Winske and P. C. Liewer. Particle simulation studies of the lower hybrid drift instability. *Phys. Fluids*, 21(6):1017–1025, 1978.

[69] H. Yumi, T. Toshiki, and K. Yoshiomi. Classification of particle orbits and related stochasticity of plasma ion motion in a field-reversed configuration with d-3he advanced fuel. *Nuclear fusion*, 42(9):1075, 2002.

Appendix A

Basics of drift-waves

Drift-waves are low-frequency perturbations which exist in plasmas with pressure gradients. Because all confined plasmas necessarily contain pressure gradients, drift-waves are ubiquitous to all fusion reactors. (Whether drift-waves are important within the reactors' operational time-scale is a different issue, ie. magnetized target fusion (MTF) or inertial confinement fusion (ICF) devices operate at much shorter time-scales such that Rayleigh-Taylor instabilities are much more important to consider than drift-wave instabilities.) Here, I present some of the basics of drift-waves in slab geometry which is actually more relevant for ideal FRC drift-waves due to the lack of toroidal coupling.

A.1 Simple fluid description of drift-waves

In the simplest case, the perturbation moves in the direction perpendicular to the pressure gradient and magnetic field direction. This simple picture of drift-waves can be drawn with a fluid model. First, assume an equilibrium with a density gradient in the $\hat{x}$ direction and a uniform magnetic field pointing in the $\hat{z}$ direction. The electrons can be modeled with an adiabatic response

$$\delta n_e = n_0 \frac{e\phi}{T_e}. \tag{A.1}$$

This relation arises from an expansion ($\frac{e\phi}{T_e} \ll 1$ and $n_e = n_0 + \delta n_e$) from the result of force balance in the parallel direction

$$\frac{\partial \phi}{\partial z} - \frac{T_e}{n_e}\frac{\partial n_e}{\partial z} = 0 \rightarrow \frac{n_e}{n_0} \quad = e^{\frac{e\phi}{T_e}} \tag{A.2}$$

and is only valid if $k_\parallel = k_z \neq 0$. On the other hand, the ions can be modeled from the continuity equation (ignoring the parallel direction for this simple case, which corresponds to a regime where $k_\parallel$ is small but non-zero)

$$\begin{aligned} \frac{\partial n_i}{\partial t} + v_{E_x}\frac{dn_0}{dx} &= 0 \\ \frac{\partial n_i}{\partial t} - \frac{1}{B_0}\frac{\partial \phi}{\partial y}\frac{dn_0}{dx} &= 0 \\ -i\omega\delta n_i - \frac{1}{B_0}(ik_y\phi)\frac{dn_0}{dx} &= 0 \\ \rightarrow \delta n_i &= -\frac{1}{\omega}\frac{k_y\phi}{B_0}\frac{dn_0}{dx} \end{aligned} \tag{A.3}$$

where the equation has been linearized so that we only look at the linear response of the ions. The dispersion for this simple picture of the drift-wave then pops out from the quasi-neutrality condition

$$\begin{aligned}
\delta n_i &= \delta n_e \\
-\frac{1}{\omega}\frac{k_y\phi}{B_0}\frac{dn_0}{dx} &= n_0\frac{e\phi}{T_e} \\
\omega &= -\frac{\frac{k_y}{B_0}\frac{dn_0}{dx}}{n_0\frac{e}{T_e}} \\
\rightarrow \omega &= -k_y\frac{T_e}{eB_0}\frac{dln(n_0)}{dx} \\
\rightarrow \omega &= k_y v_{*,e}
\end{aligned} \tag{A.4}$$

where the so-called diamagnetic drift velocity $v_{*,e} = -\frac{T_e}{eB_0}\frac{dln(n_0)}{dx}$ has been used (and is equivalently defined for the ions but with the opposite sign, ie. opposite drift direction). Note that this simple dispersion has no unstable roots because the electron response is free to cancel out space charge such that there is no positive feedback to cause instability. To destabilize the drift-wave, at least for the model of $k_\parallel \neq 0$, the model must allow electrons to be impeded by collisions, kinetic effects, and so on.

One important aspect of drift-wave physics is understand the stability of these perturbations since unstable drift-waves grow to become large enough to cause transport of particles, energy, momentum, and so on. In chapter 1, the historical research path of drift stabilities has been lightly summarized. In the following text, some mathematics and physics are outlined and derived for understanding the basics of drift-wave instabilities. At its heart, these instabilities occur when there is a phase shift due to some effects.

A.1.1 Destabilization due phase-shift

To destabilize the drift-wave within our fluid model, a simple change is to add a delay, ie. phase shift, to represent some limitation of electrons to shield out the space charge. This delay can be caused by different effects, but an easy one to imagine is the delay caused by electron-ion collisions. This can be shown easily by modifying Eq. (A.1) to include a phase shift

$$\delta n_e = n_0 \frac{e\phi}{T_e}(1 - i\delta) \tag{A.5}$$

which would modify the dispersion Eq. (A.4) to be

$$\begin{aligned} \omega &= \frac{k_y v_{*,e}}{1 - i\delta} \\ \rightarrow \omega &\approx k_y v_{*,e}(1 - i\delta) \end{aligned} \tag{A.6}$$

for $\delta \ll 1$. The dispersion now allows for the frequency to have an imaginary component which, depending on the sign of δ, can be unstable or damped.

A.2 Kinetic description of drift-waves

A more complicated realistic picture of the drift-wave can be developed from a kinetic perspective by integrating along unperturbed orbits to calculate the perturbed density (which is then used with the quasi-neutrality condition as in the fluid derivation).

Again, we assume an equilibrium with a density gradient in the $\hat{x}$ direction and a uniform magnetic field pointing in the $\hat{z}$ direction. We start with the fully-kinetic Vlasov equation

$$\frac{D}{Dt}f = \left[\frac{\partial}{\partial t} + \vec{v}\cdot\frac{\partial}{\partial \vec{x}} + \vec{a}\cdot\frac{\partial}{\partial \vec{v}}\right] f = 0 \tag{A.7}$$

(from which the fluid equations can be derived by finding the moments of the Vlasov equation). The unperturbed distribution, with respect to constants of motion, $f_0(\vec{X}, H)$ is

$$f_0(\vec{X}, H) = \frac{n_0(\vec{X})}{\left(\frac{2\pi T(\vec{X})}{m}\right)^{3/2}} \exp\left[-\frac{H}{T(\vec{X})}\right] \tag{A.8}$$

where the constants of motion are

$$\begin{aligned} \vec{X} &= \vec{x} + \frac{v_y}{\Omega_c} \\ H &= \frac{1}{2}mv^2 - Fx \end{aligned} \tag{A.9}$$

where H is just the energy (with some possible force such as curvature) and $\vec{X}$ comes from the conjugate momentum which is conserved ($p_y = mv_y + qxB$). For weakly inhomogeneous plasmas ($\frac{v_y}{\Omega_c} \ll L_p$), we can Taylor expand the unperturbed distribution function to our original coordinate system of (x, y, z)

$$\begin{aligned} f(\vec{X}, H) &\approx f(\vec{X}, H)\Big|_{\frac{v_y}{\Omega_c}=0} + \frac{\partial f(\vec{X}, H)}{\partial \vec{X}}\Bigg|_{\frac{v_y}{\Omega_c}=0} \frac{v_y}{\Omega_c} \\ f(\vec{X}, H) &\approx f(\vec{x}, H) + \frac{\partial f(\vec{x}, H)}{\partial x}\frac{v_y}{\Omega_c}. \end{aligned} \tag{A.10}$$

Now, let the whole distribution be represented by $f = f_0 + \delta f$ where the perturbation (and other perturbed quantities within this model) follows

$$\delta f = \hat{\delta f} \exp\left[i(k_y y + k_z z - \omega t)\right]. \tag{A.11}$$

The Vlasov equation can then be linearized as

$$\begin{aligned} \left[\frac{\partial}{\partial t} + \vec{v}\cdot\frac{\partial}{\partial \vec{x}} + \vec{a}\cdot\frac{\partial}{\partial \vec{v}}\right](f_0 + \delta f) = 0 \\ \left[\vec{v}\cdot\frac{\partial}{\partial \vec{x}} + \vec{a}\cdot\frac{\partial}{\partial \vec{v}}\right] f_0 + \left[\frac{\partial}{\partial t} + \vec{v}\cdot\frac{\partial}{\partial \vec{x}} + \vec{a}\cdot\frac{\partial}{\partial \vec{v}}\right]\delta f = 0 \\ \rightarrow \left[\frac{\partial}{\partial t} + \vec{v}\cdot\frac{\partial}{\partial \vec{x}} + \vec{a_0}\cdot\frac{\partial}{\partial \vec{v}}\right]\delta f = -\vec{\delta a}\cdot\frac{\partial}{\partial \vec{v}} f_0 \\ = \left[\frac{\partial}{\partial t} + \vec{v}\cdot\frac{\partial}{\partial \vec{x}} + \frac{q}{m}\left(\vec{v}\times\vec{B_0} + \frac{\vec{F}}{q}\right)\cdot\frac{\partial}{\partial \vec{v}}\right]\delta f = \frac{q}{m}\nabla\phi\cdot\frac{\partial}{\partial \vec{v}} f_0 \end{aligned} \tag{A.12}$$

where the first-order terms have been grouped to result in our linearized Vlasov equation. The whole operator on the left-hand side of Eq. (A.12) is actual the total time derivative along unperturbed trajectories so that δf can be solved by integrating unperturbed trajectories on the right-hand side. Thus,

$$\delta f(\vec{x}'(t'),\vec{v}'(t'),t') = \int_{-\infty}^{t} dt' \frac{q}{m}\nabla\phi \cdot \left.\frac{\partial f_0}{\partial \vec{v}}\right|_{\vec{x}'(t'),\vec{v}'(t'),t'} \tag{A.13}$$

Since this is not a focus of this thesis, the result of this is simply presented (and can be found in any number of texts)

$$\hat{\delta f} = -\frac{q\hat{\phi}}{T} f_0 \left[1 - (\omega_d' - \omega) \sum_{n,n'=-\infty}^{\infty} \frac{J_n(\frac{k_y v_\perp}{\Omega_c}) J_{n'}(\frac{k_y v_\perp}{\Omega_c}) \exp\left[i(n-n')\theta\right]}{k_z v_z + n\Omega_c + \omega_F - \omega}\right] \tag{A.14}$$

where ω_d' is the drift operator

$$\omega_d' = k_y \frac{T}{qB}\left[\frac{d\ln(n_0)}{dx} + \frac{dT_0}{dx}\frac{\partial}{\partial T_0} - \frac{F}{T_0}\right]. \tag{A.15}$$

This is integrated over velocity-space to yield a perturbed density per species

$$\begin{gathered}\hat{\delta n} = -\frac{q\hat{\phi}}{T} n_0 \left\{1 - (\omega_d' - \omega) \sum_{n=-\infty}^{\infty} \frac{1}{\omega - n\Omega_c - \omega_F}\left[W\left(\frac{\omega - n\Omega_c - \omega_F}{|k_z| v_{th}}\right) - 1\right] \Lambda_n\left(\left(\frac{k_y v_{th}}{\Omega_c}\right)^2\right)\right\} \\ \rightarrow \hat{\delta n} = -\frac{q\hat{\phi}}{T} n_0 \left\{1 + \frac{\omega - \omega_d'}{\omega - \omega_F}\left[W\left(\frac{\omega - \omega_F}{|k_z| v_{th}}\right) - 1\right] \Lambda_0\left(b_{species}\right)\right\}\end{gathered} \tag{A.16}$$

where the left most term on the right-hand side is the adiabatic contribution and the final form assumes that $\omega < \Omega_c$, ie. time-scale of our physics is longer than cyclotron time-scales. The short-hand for the integral is the W dispersion function (which is actually the first derivative of the Z dispersion function, AKA the Faddeeva function),

$$W\left(z\right) = \frac{1}{2\pi}\int_{-\infty}^{\infty} dx \frac{x}{x-z} \exp\left[-x^2/2\right], \tag{A.17}$$

the short-hand for the exponentially scaled, modified Bessel function is

$$\Lambda_n\left(z\right) = \exp\left[-z\right] I_n\left(z\right), \tag{A.18}$$

and the short-hand for the argument inside the scaled modified Bessel function is

$$b_{species} = k_z^2 \rho_{species}^2. \tag{A.19}$$

A.2.1 Drift-wave dispersion

To derive the drift-wave dispersion, we make use of the quasi-neutrality condition. For simplicity, we use the adiabatic electron model as in the fluid derivation. The ion perturbed density can be calculated from Eq. (A.16)

$$\begin{aligned}\delta\hat{n}_i &= -\frac{e\hat{\phi}}{T_i}n_0\left\{1+\frac{\omega-\omega'_{d,i}}{\omega}\left[W\left(\frac{\omega}{|k_z|v_{th,i}}\right)-1\right]\Lambda_0\left(b_i\right)\right\}\\ &= -\frac{e\hat{\phi}}{T_i}n_0\left\{1-\frac{\omega-\omega'_{d,i}}{\omega}\left[\frac{k_z^2v_{th,i}^2}{\omega^2}+1-i\delta\right]\left(1-b_i\right)\right\}\end{aligned}\tag{A.20}$$

where $W(z)\approx-\frac{1}{z^2}+i\sqrt{\frac{\pi}{2}}z\exp[-\frac{1}{2}z^2]$ due to the assumption of cold ions ($z=\frac{\omega}{k_zv_{th,i}}\gg1$) and $\Lambda_0(b)\approx1-b$ due to the assumption of long wavelength ($b_i\ll1$). Putting this into the equation for quasi-neutrality condition

$$\begin{aligned}\delta n_e &= \delta n_i\\ \frac{e\hat{\phi}}{T_e}n_0 &= -\frac{e\hat{\phi}}{T_i}n_0\left\{1-\frac{\omega-\omega'_{d,i}}{\omega}\left[\frac{k_z^2v_{th,i}^2}{\omega^2}+1-i\delta\right]\left(1-b_i\right)\right\}\\ \frac{T_i}{T_e} &= -1+(1-\frac{\omega_{*,i}}{\omega})\left[\frac{k_z^2v_{th,i}^2}{\omega^2}+1-i\delta\right]\left(1-b_i\right).\end{aligned}\tag{A.21}$$

It can be seen that the drift-wave can couple to the ion-acoustic wave from this complicated dispersion relation. The dispersion itself can be checked against the drift-wave dispersion the fluid model by assuming cold ions ($T_i \to 0$) which leads to a simplification of the kinetic dispersion ($k_z^2 v_{th,i}^2 \to 0$ and $b_i = k_\perp^2 \rho_i^2 \to 0$)

$$\begin{aligned}
&\frac{T_i}{T_e} = -1 + (1 - \frac{\omega_{*,i}}{\omega}) \left[\frac{k_z^2 v_{th,i}^2}{\omega^2} + 1 - i\delta \right] (1 - b_i) \\
\to &\frac{T_i}{T_e} = -1 + (1 - \frac{\omega_{*,i}}{\omega}) \left[0 + 1 - i\delta \right] (1 + 0) \\
\to &\frac{T_i}{T_e} = -\frac{\omega_{*,i}}{\omega} \\
&\to \omega = \omega_{*,e}
\end{aligned} \tag{A.22}$$

where only the real components were retained for simplicity and the relation of $-\frac{T_e}{T_i}\omega_{*,i} = \omega_{*,e}$ was used.

Appendix B

Field-aligned ANC verifications

Some of the tests run for the field-aligned version of ANC are shown in this appendix section.

B.1 Marker distribution

In Fig. B.1, the marker distribution is shown for an early time and a later time using relatively large time steps. The top panels show the mean densities (normalized to the analytic distribution in the center column and absolute in the right column) while the bottom panels show the densities on a single toroidal plane.

Going from the early to late times, the marker distribution stays about the same with statistical fluctuations getting larger after time. The fluctuations will decrease with decreased time steps, but a larger time step case is shown to illustrate the changes. This verification confirms the correctness of the particle weighting scheme and the particle pusher.

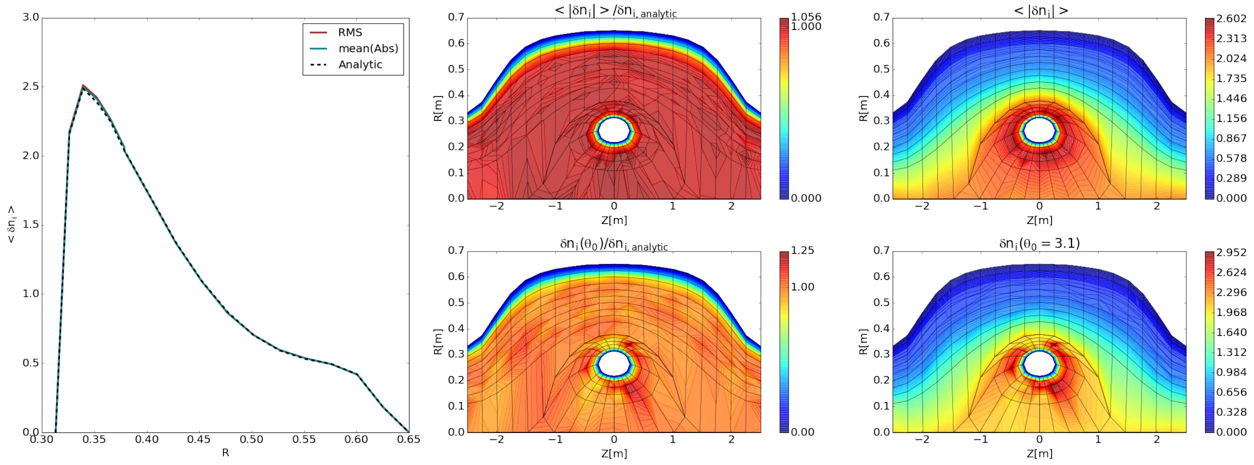

(a) Early distribution of marker particles

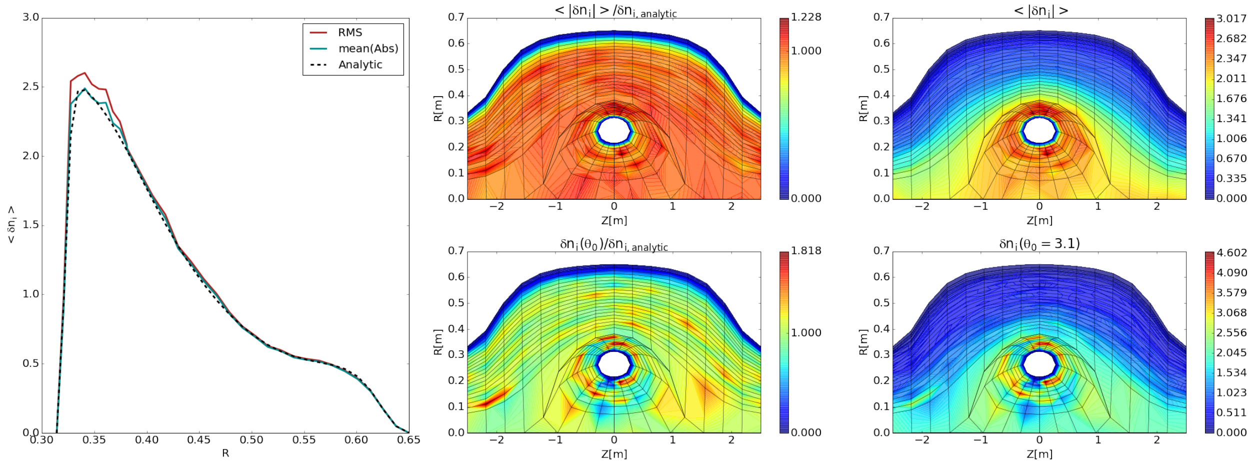

(b) Later distribution of marker particles

Figure B.1: Marker particle distribution does not significantly change, and smaller time steps decrease the fluctuations in later distributions.

B.2 Particle trajectories

In Fig. B.2, particle trajectories for a passing and trapped particle in the core is shown. Using relatively large time steps, the poloidal flux change is shown to be about 0.001% (a proxy for conservation of canonical angular momentum) for both kinds of trajectory. The radial position is also shown for the two particles with no average change. Finally, the parallel velocity is also shown for both particles with no average change (a proxy for conservation of energy).

B.3 Magnetic field

In Fig. B.3, the divergence of the magnetic field in the field-aligned version is plotted. As expected, the divergence remains around machine error, ie. numerically zero. The magnetic field vector in the field-aligned version is also plotted in Fig. B.4. Since the field-aligned version does not modify the routines that handle these magnetic field properties, it was not expected to change. However, it is numerically important to verify that they *do not* change despite the mesh (and some other accompanying routines) having been changed.

B.4 Poisson solver

In Fig. B.5, two different tests of the Poisson solver are shown. The input density is shown in the bottom panels, and the resultant potential found from the solvers is shown in the top panels. The left columns show the solutions from the field-aligned Poisson solver while the right columns show the solutions from the cylindrically regular Poisson solver. The solutions are within comparable magnitudes of each other with slight differences due to

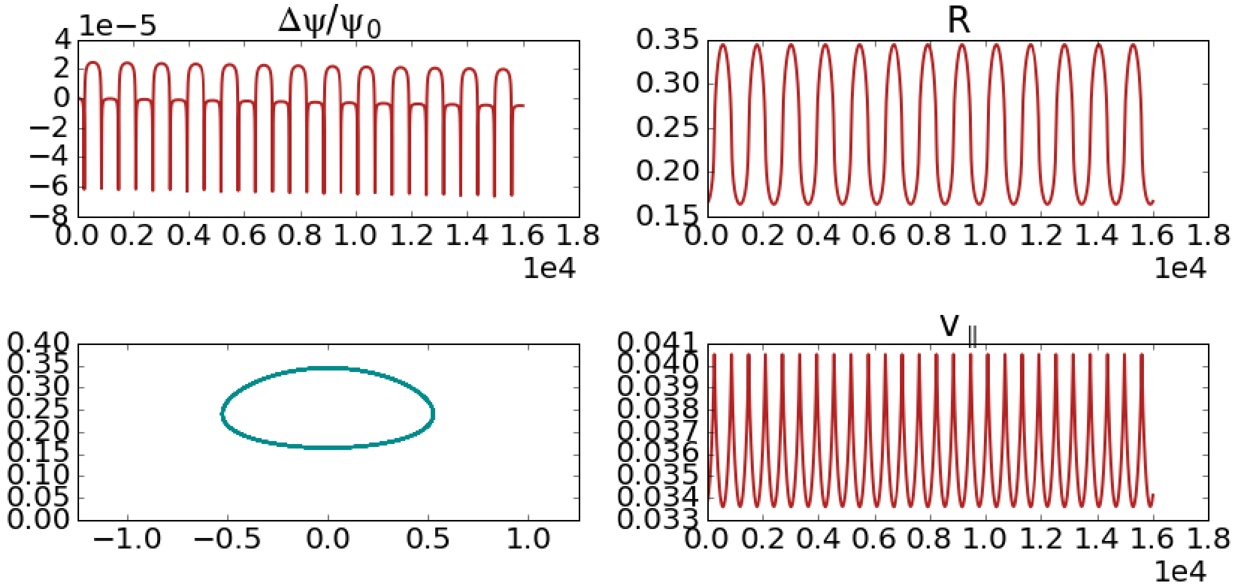

(a) A passing particle

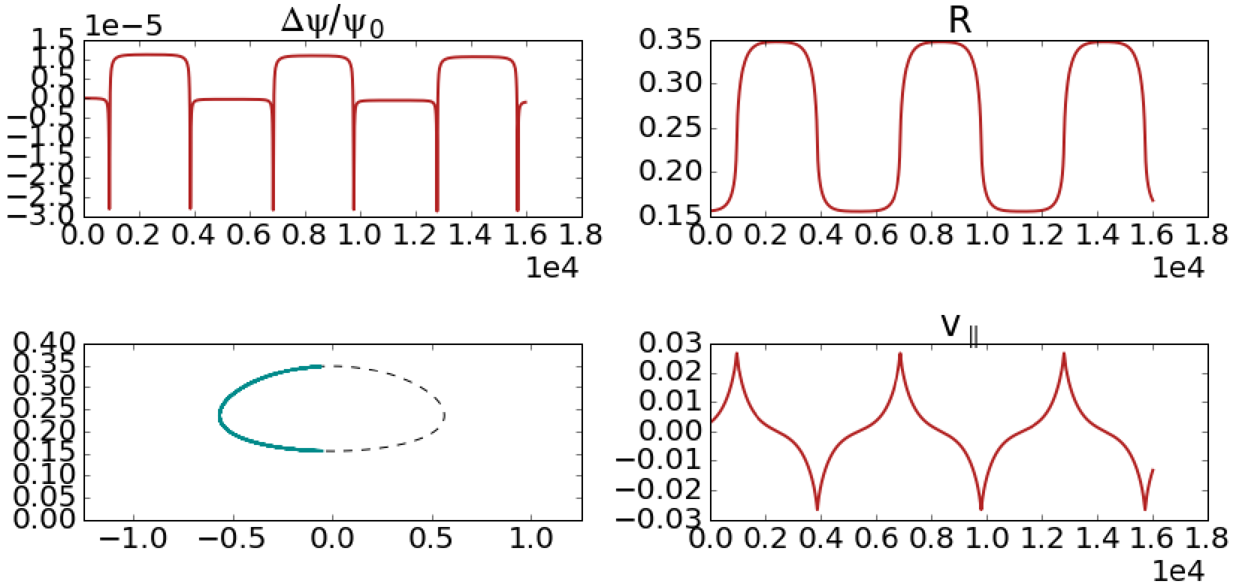

(b) A trapped particle

Figure B.2: Different particle trajectories showing the conservation of canonical angular momentum and energy. The red lines are quantities plotted against simulation time-steps.

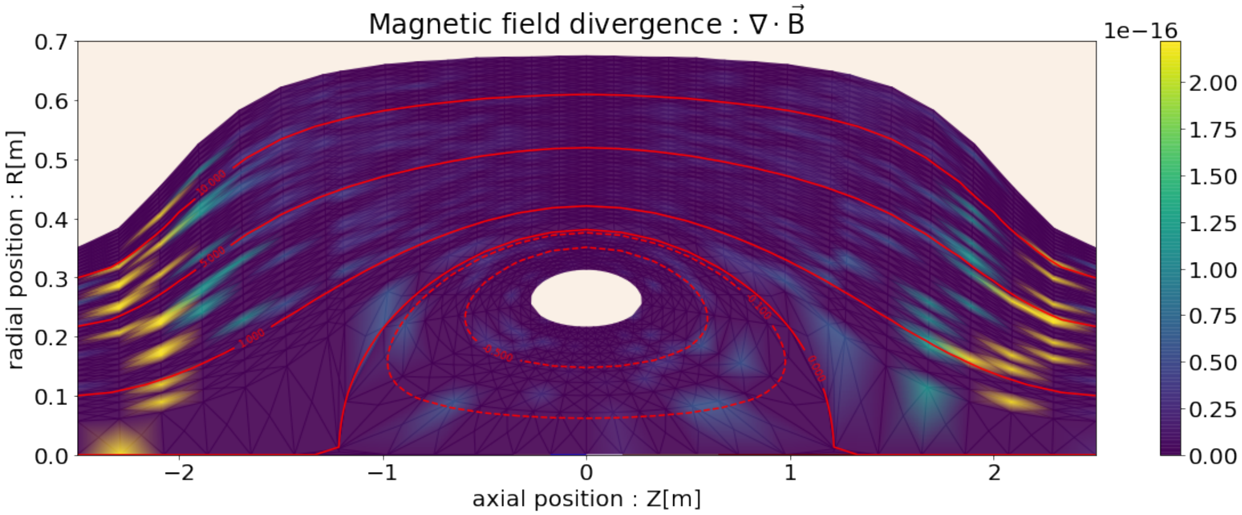

Figure B.3: The divergence of the magnetic field for the field-aligned version is plotted. Several field-lines are plotted in red for reference.

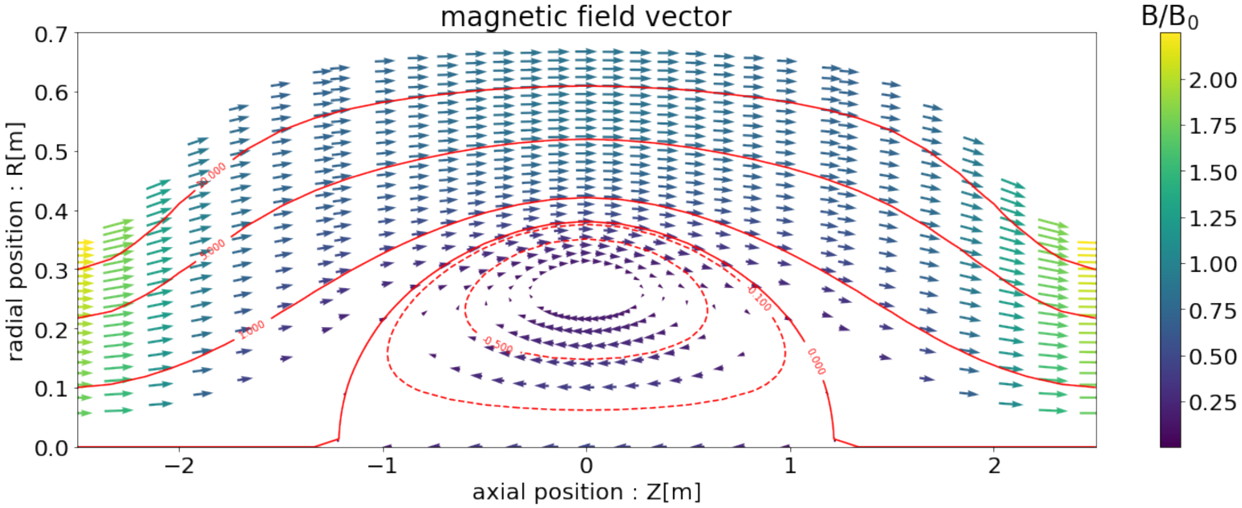

Figure B.4: The magnetic field for the field-aligned version is plotted as a vector field with color and arrow size determined by the magnetic field strength. Several field-lines are plotted in red for reference.

boundary conditions and the inclusion of parallel components in the field-aligned version (for numerical stability).

Since the cylindrically regular Poisson solver has been verified against analytic theory, this shows that the field-aligned version of the Poisson solver is also correct.

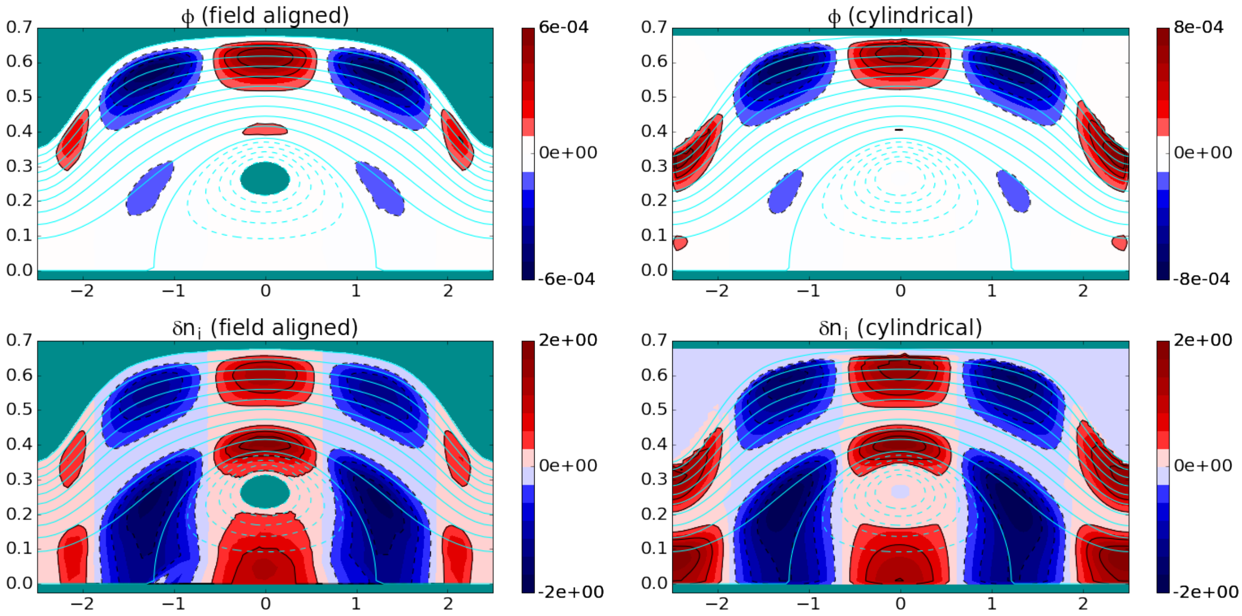

(a) Poisson solver check # 1

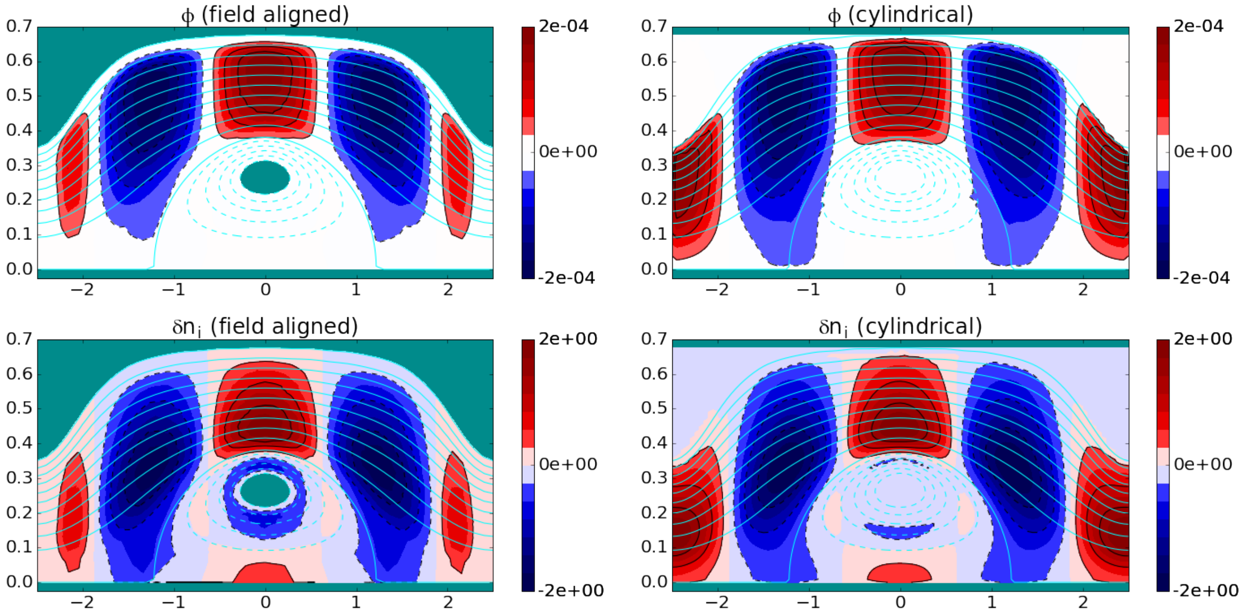

(b) Poisson solver check # 2

Figure B.5: The solutions of the Poisson equation are compared between the field-aligned version and the cylindrically regular version.

Appendix C

ANC numerical tools

C.1 Parallel smoothing

Turbulence simulations are susceptible to high-$k_\parallel$ noise which arise due to numerical aliasing effects. In field-aligned meshes, this is easy to counter by smoothing along the field-line.

In the original cylindrically regular mesh version of ANC, this parallel smoothing is accomplished by finding the neighboring parallel points using the local magnetic field. A weight from a Gaussian blur function is calculated based on the distance away from the point being smoothed. This weight is applied to a value interpolated from the nearest four grid points of these neighboring parallel points. A sample of this process is shown in Fig. C.1 and Fig. C.2. The top panels show a close-up window of the affected grid points: the point being smoothed is the cyan x which is encircled, the neighboring parallel points are the connecting two cyan x's, the blue and red circles are the nearest grid points belonging to the neighboring parallel points, and the dashed black lines are plotted to give a sense of the nearby field-line structures. The bottom panels show the whole R-Z plane to give a better perspective of

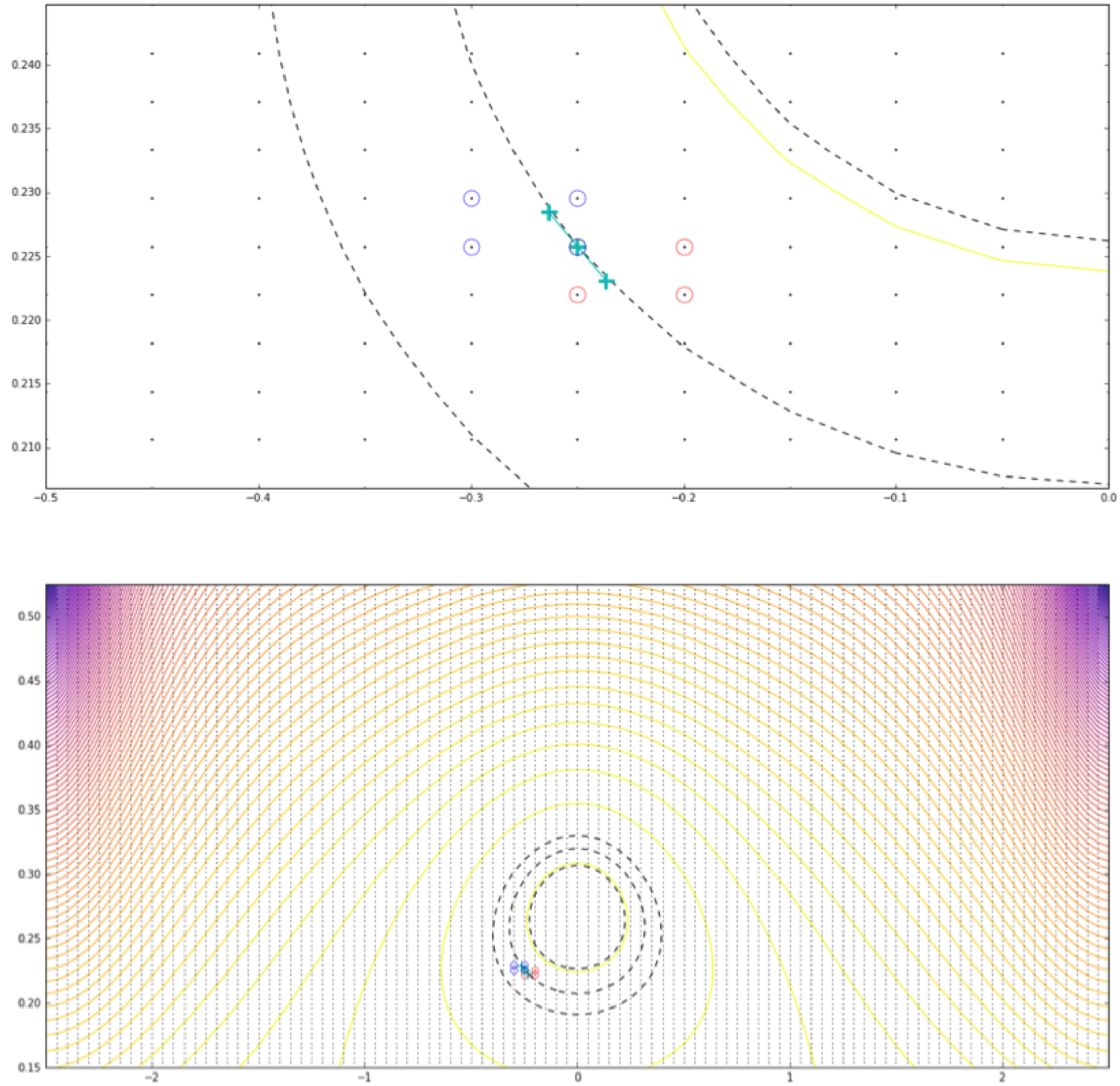

Figure C.1: Smoothing process is shown for the core. Top panel: point being smoothed is encircled cyan x, neighboring parallel points are the connecting cyan x's, blue and red circles are nearest grid points belonging to neighboring parallel points, and dashed black lines are nearby field-lines. Bottom panel: zoomed out plot of top panel to show location of smoothed point.

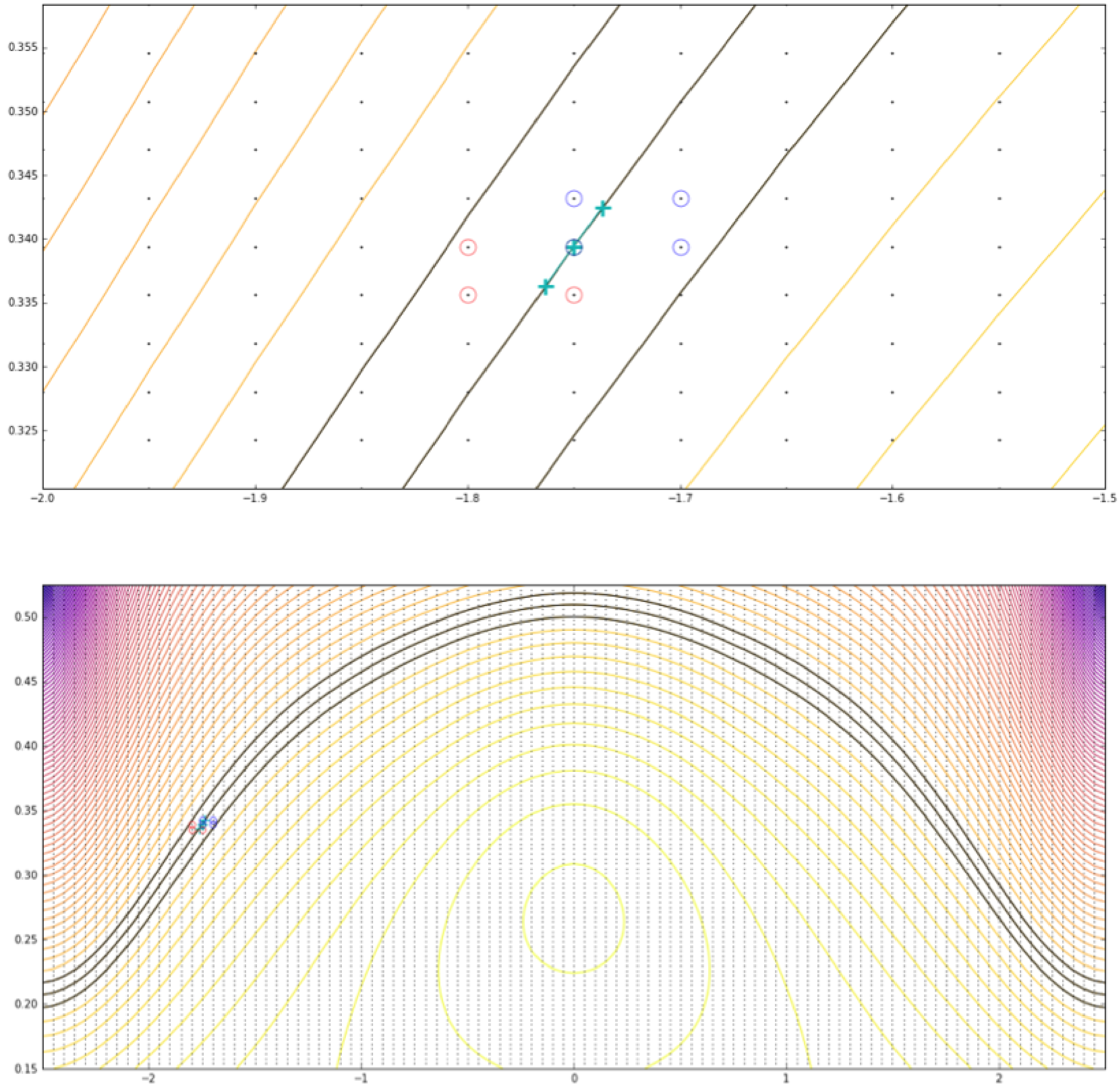

Figure C.2: Smoothing process is shown for the SOL. Top panel: point being smoothed is encircled cyan x, neighboring parallel points are the connecting cyan x's, blue and red circles are nearest grid points belonging to neighboring parallel points, and dashed black lines are nearby field-lines. Bottom panel: zoomed out plot of top panel to show location of smoothed point.

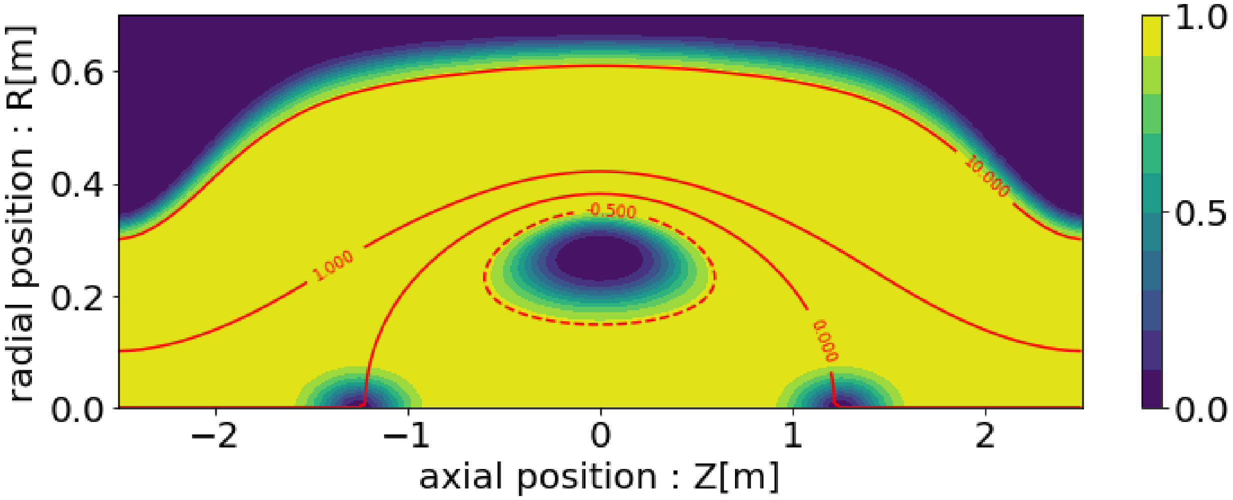

Figure C.3: The yellow regions are non-zero regions and the purple regions are zero regions. The poloidal flux (normalized by the absolute value of the poloidal flux at the O-point) is shown as the red contour lines for reference.

where the close-up smoothing plots are located. This method works for both the core and SOL as seen in the figures.

C.2 Boundaries

In the cylindrically regular mesh version of ANC, choosing to exclude or include different regions is more difficult than just removing the regions from the simulation domains. Instead, an equilibrium quantity for the particle weight is created to smoothly decrease the particle weight to zero for regions away from the areas of interest.

In Fig. C.3, the boundary for the cross-separatrix simulations is shown. The regions of the O-point and X-points are zeroed out. This is the equivalent of taking an assumption of no fluctuations of interest in those regions.

In Fig. C.4, the boundary for the SOL turbulence simulations is shown. Only the SOL region is non-zero for this set of simulations.

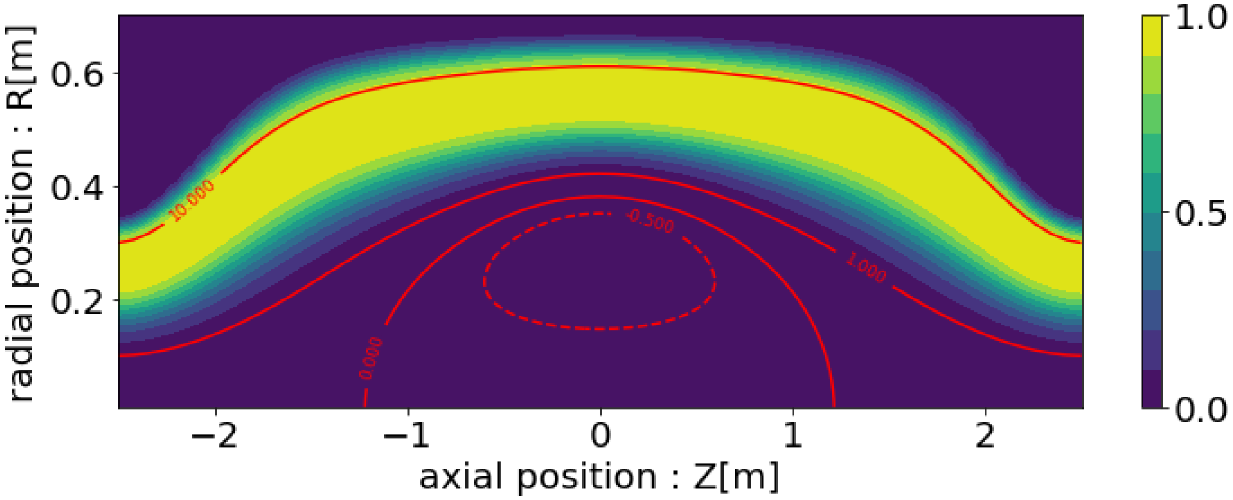

Figure C.4: The yellow regions are non-zero regions and the purple regions are zero regions. The poloidal flux (normalized by the absolute value of the poloidal flux at the O-point) is shown as the red contour lines for reference.